Molecular Imaging of DNA Damage Repair



Claudia Rose Fraser
The Queen's College
University of Oxford

A thesis submitted for the degree of
Doctor of Philosophy
Trinity Term 2022

Table of Contents

Abstract VI

COVID-19 Considerations Statement VII

Acknowledgements VIII

List of Figures X

Abbreviations XV

1 General Introduction 1

1.1 DNA damage and cancer 1

1.1.1 How does DNA damage cause cancer? 1

1.1.2 The DNA damage response 3

1.1.3 Using the DNA damage response to our advantage 5

1.2 Ataxia Telangiectasia Mutated 8

1.2.1 ATM basic function, upstream and downstream targets, and activation 8

1.2.2 ATM and cancer 11

1.2.3 ATM inhibitors 12

1.3 Poly (ADP-Ribose) Polymerase 16

1.3.1 PARP basic function, upstream and downstream targets, and activation 16

1.3.2 PARP and cancer 19

1.3.3 PARP inhibitors 19

1.4 Molecular Imaging in Cancer 24

1.4.1 Medical imaging used in cancer diagnosis 24

1.4.2 Nuclear imaging (PET and SPECT) 25

1.4.3 Current PET/SPECT cancer imaging targets 28

1.4.4 Tumour imaging in the brain 30

1.4.5 What could imaging the DDR tell us? 32

1.5 Aims 34

2 Radiofluorination of a highly potent ATM inhibitor as a potential PET imaging agent 36

2.1 Introduction 36

2.2 Methods 38

2.2.1 Chemical Synthesis 38

2.2.2 Radiosynthesis 39

2.2.3 Cell Culture 40

2.2.4 Western Blot 40

2.2.5 Uptake, retention, and blocking assays 43

2.2.6 *In vivo* mouse models 44

2.2.7 PET/CT imaging 44

2.2.8 Autoradiography and microscopy 45

2.2.9 Statistical Analysis 46
2.3 Results 46
2.3.1 Chemical synthesis 46
2.3.2 Radiochemistry 51
2.3.3 Model characterisation 54
2.3.4 *In vitro* assessment of [^{18}F]1 56
2.3.5 *In vivo* assessment of [^{18}F]1 58
2.4 Discussion 63
2.4.1 General discussion 63
2.4.2 Critical review of project design 66
2.5 Conclusions 68
3 Radiosynthesis of [^{18}F]AZD1390 69
3.1 Introduction 69
3.2 Materials and Methods 71
3.2.1 Chemical Synthesis 71
3.2.2 Radiochemistry 71
3.3 Results 72
3.3.1 Initial attempts towards a nitro-precursor 72
3.3.2 Synthesis of a versatile hydroxy intermediate 75

3.3.3 Tosylate precursor synthesis and radiolabelling 76

3.3.4 Steps towards a boronic ester precursor 78

3.4 Discussion and future work 79

3.4.1 Summary of initial attempts towards [^{18}F]AZD1390 79

3.4.2 Alternative precursor and radiolabelling options for [^{18}F]AZD1390 81

3.4.3 Future of ATM targeted PET imaging 87

3.5 Conclusion 90

4 Towards [^{18}F]A-966492 91

4.1 Introduction 91

4.2 Materials and Methods 96

4.2.1 Chemical Synthesis 96

4.2.2 Cell culture 97

4.2.3 Western Blot 97

4.3 Results 98

4.3.1 Initial design and attempts towards asymmetric precursor synthesis 98

4.3.2 Racemic precursor synthesis progress 100

4.3.3 Characterisation of cell line PARP expression 104

4.4 Discussion and future work 106

4.4.1 Summary of presented work 106

4.4.2 Alternative routes to a boronic ester precursor 107

4.4.3 Alternative radiolabelling and precursor options 112

4.5 Conclusion 113

5 Experimental Write-up 114

5.1 Synthetic analysis 114

5.2 Synthetic experimental for [^{18}F]1 116

5.3 NMR spectra for novel compounds towards [^{18}F]1 130

5.4 Synthetic experimental for [^{18}F]AZD1390 136

5.5 Synthetic experimental for [^{18}F]A-966492 150

6 Discussion and Future Work 159

6.1 General review of presented results 159

6.2 Challenges in designing ^{18}F-radiotracers 160

6.3 ATM vs PARP imaging 162

6.4 Future considerations for imaging the DDR 166

6.5 Concluding remarks 168

7 References 170

Abstract

Nuclear imaging has the ability to non-invasively probe target expression, drug pharmacokinetics, and monitor treatment response. With many cancer therapies inducing DNA damage to overwhelm tumour cells into arrest, there has been a push to investigate the DNA damage response with regards to understanding the key proteins involved and the development of DDR inhibitors to enhance current DNA damaging therapies. The use of DDR inhibitor radiotracers with PET or SPECT could allow scientists to quickly collect information on tumour phenotype, DDRi drug interactions and pharmacokinetics, calculate levels of DNA damage as a result of previous therapies, and could ultimately improve patient stratification. With some key targets of the DDR such as γH2AX and PARP, already under investigation for nuclear imaging, this thesis aimed to investigate ATM as a potential new target for DDR nuclear imaging, as well as expanding the selection of PARPi radiotracers to allow imaging of tumours in the brain. This body of work highlights the key challenges faced in the chemistry and radiochemistry of developing new radiotracers and demonstrates the limitations of ATM as an imaging target. It is the hope that this research will pave the way for further development of ATMi radiotracers to verify whether ATM is a suitable molecular imaging target and to promote the development of BBB-penetrable PARPi tracers.

COVID-19 Considerations Statement

This project was severely disrupted by the impact of the COVID-19 pandemic. The initial lockdown period beginning in March 2020 meant there was no access to lab space for 5 months, only being allowed to return on a part-time basis in mid-August 2020. This disruption so early on in my highly lab intense project (having only begun in mid-October 2019), along with the uncertainty of when we would be able to return meant that there was little alternative work that could be completed from home during this time. This break meant a substantial loss of time towards the compound syntheses reported in this dissertation, and in particular a significant reduction in the level of experimental support towards the project with other more senior lab members leaving the group due to contracts ending soon after our return. Rota work on return also reduced the amount of time and support available to run experiments. Additional implications of the pandemic situation throughout the continuing lockdowns also led to severe delays in deliveries of vital reagents, with a particular impact on the synthesis reported in my fourth chapter, where some key reagents were delayed for nearly four months. Finally, in addition to the physical restrictions enforced, the physical and emotional difficulties during this time (including 3 weeks lost due to recovery from COVID-19) also caused sporadic reductions in work efficiency throughout this three-year project.

Had these situations not arisen, I believe there would be substantially more progress made on my work reported in chapters 3 and 4 and that I would have been able to deliver a more complete and rounded body of work. I hope you are able to take these circumstances into consideration in the assessment of this dissertation.

Acknowledgements

First of all, I would like to thank my supervisor, Bart. Doing a DPhil is hard during normal circumstances, but I think most would agree that doing one during the events of the past three years was bonkers! I can honestly say that the support you have given me both in my project and development as a scientist, but also in personal support during these 'unprecedented times' is what got me through this, particularly in reminding me that 'we were not working from home, but simply at home trying to do some work'. I've thoroughly enjoyed our weekly chats (especially when there were puppy appearances) and the few in person outings we managed to squeeze in along the way. Thanks for all of it.

I would also like to express big thanks to my secondary supervisors, Andy Ryan, Andy Blackford, and Graham Smith. Doing such an interdisciplinary project needed a truly interdisciplinary team of experts, and I have learned a lot from each of you.

I would not have made it through this without such a supportive research group and would like to thank all the BC members, past and present, for the help and fun over my last three years. I'd like to give special thanks to Javi, Gianluca, and Anna for helping me expand my synthetic chemistry and for introducing me to the world of radiochemistry. To Mat, you were right, you did it, and now so have I! And to the BC ladies, thanks for adjusting your lunch schedules to be borderline brunch, for all the kind chats and reassurances, for making the long days in the BMS enjoyable, and most importantly for being the best role models a girl in science could ask for.

While all my amazing friends and family have supported me through this, a special shout out goes to Fiona (my best oncology pal from day one), Alice (for raving to 00s hits with me on those long lab days and bringing me gf brownies when I'd had a bad week), Letitia (ATM for life), Mia (for all the hydrogen and for saving me with a Biotage when I was planning to column 15 g of crude manually…), Olivia (for turning my project into an interpretive dance), and Elliot (who understands 'some of these words').

And finally, onto the biggest thanks of all. First, to Max, you are my rock. Thanks for scooping me up when I had my wobbles, for always being silly and putting a smile on my face, and most importantly, for keeping the flat tidy when I've been too stressed. I probably owe you a good years' worth of chores (and cookies)…

Second, to my amazing mum and dad. You are the reason I'm here, both thanks to your hugely generous support in funding me through this (I still promise to look after you when you're old in return!) and for always being there at the end of the phone or just a drive away when I've needed you. You helped me through the lowest lows and were there to celebrate the highest highs. I love you both and I couldn't have done this without you.

And finally, to Simon. We miss you lots, this is for you.

List of Figures

Figure 1.1 – Cancer formation follows initiation, promotion, progression, and eventually metastasis 2

Figure 1.2 – Examples of DNA damage repair pathways 4

Figure 1.3 – Synthetic lethality 7

Figure 1.4 – (A) Domain map of ATM. (B) Signalling cascade of ATM. 9

Figure 1.5 – (A) Domain map for PARP1, 2, and 3. (B) DNA binding mechanisms of PARP1 18

Figure 1.6 – Schematic of PET imaging 26

Figure 2.1 – Target compound [^{18}F]1 and reported inhibitory data 38

Figure 2.2 – Synthetic pathway for reference [^{19}F]1 and nitro-precursor 2 47

Figure 2.3 – Initial synthetic plan with completed pyridine triflate core 48

Figure 2.4 – Trialled methods towards a 2-nitro-6-(3-(piperidin-1-yl)propoxy)pyridin-3-yl trifluoromethanesulfonate Suzuki coupling partner 49

Figure 2.5 – Late-stage pyridine alkylation gives rise to substitution of both fluoro- and nitro-groups 50

Figure 2.6 – Radiosynthesis of [^{18}F]1 from 2 51

Figure 2.7 – Eckert & Ziegler Modular-Lab schematic for automated radiosynthesis of [^{18}F]1. 52

Figure 2.8 – (A) Example semi-preparatory trace of [^{18}F]1 (radio trace top, UV trace (220 nm) bottom). (B) Example quality control trace of [^{18}F]1. Top trace shows reformulated [^{18}F]1, bottom trace shows co-injection of reformulated [^{18}F]1 with reference [^{19}F]1. Radio trace in black, UV trace (254 nm) in blue. 53

Figure 2.9 – Calibration curve used for molar activity calculation of [^{18}F]1 (error bars too small to be presented). 54

Figure 2.10 – Higher ATM expression is observed in H1299 shGFP knockdown cells compared to H1299 shATM knockdowns. Irradiation of cells (4 Gy) causes an increased expression of pATM, pKAP1, and pCHK2. A decrease in expression of pATM and downstream targets pKAP1 and pCHK2 is observed following treatment of shGFP (4 Gy) cells with different ATM inhibitors. 55

Figure 2.11 – ATM inhibition with [^{19}F]1 in CT26 murine colorectal cancer cells, total ATM Abcam antibody replaced with GTX70107, 1:500 (GeneTex). 55

Figure 2.12 – (A) Cell uptake and (B) retention of [^{18}F]1 in H1299 shATM and shGFP cells. (C) Cell-associated activity in H1299 shATM and shGFP cells after pre-treatment with a range of ATM inhibitors (block) 57

Figure 2.13 – Biodistribution of [^{18}F]1 in C57BL/6 ATM wild type and ATM-knockout mice, 1 h after intravenous administration. Below are shown representative PET/CT MIP images demonstrating the hepatobiliary uptake of tracer in both wild type and ATM-null mice.. 59

Figure 2.14 – In vivo biodistribution of [^{18}F]1 in BALB/c nu/nu mice bearing subcutaneous H1299 wildtype, shATM, or shGFP xenografts. 60

Figure 2.15 – Representative western blot of ex vivo xenograft samples. 61

Figure 2.16 – Autoradiography and H&E staining of xenograft sections (10 µm)..... 62

Figure 2.17 – Autoradiography signal analysis of ex vivo tumour sections. 62

Figure 3.1 – Chemical structures of fluorine containing ATM inhibitors in clinical trials.... 70

Figure 3.2 – (A) Mechanism of cyclisation of 3b demonstrating two possible products. (B) ^{1}H NMR analysis confirms unfavourable 5:1 ratio of products. 74

Figure 3.3 – Synthesis of hydroxy quinoline core 3k 75

Figure 3.4 – Suzuki coupling of 3m and 3k yields 3n and gives a hydroxydeborylated pyridine side product. 76

Figure 3.5 - Proposed radiofluorination of [^{18}F]AZD1390 following titania catalysed radiochemistry reported by van Dam..... 77

Figure 3.6 – Synthesis of key triflate intermediate 3q from 3n..... 78

Figure 3.7 – Comparison of ATM inhibition and selectivity reported for AZD1390, [^{19}F]1, and proposed compound 14. 87

Figure 3.8 – Proposed synthesis and radiosynthesis of [^{18}F]14. 87

Figure 4.1 – Examples of reported ^{18}F-labelled PARP inhibitors. 94

Figure 4.2 – Proposed radiosynthesis of [^{18}F]A-966492 from pinacol ester precursor 4. 99

Figure 4.3 – Proposed asymmetric synthesis towards precursor 4 100

Figure 4.4 – PARP1 K_i and EC_{50} values of A-966492 enantiomers 101

Figure 4.5 – Racemic synthetic pathway towards precursor 4 from methyl-4-bromo-2-hydroxybenzoate 102

Figure 4.6 – Trialled pathway towards precursor 4 from methyl-4-bromo-2-methoxybenzoate 103

Figure 4.7 – Western blot comparing PARP1 and PARP2 expression levels in PSN-1, U87MG, U251MG, MDA-MB-231BR, and MDA-MB-231 wildtype cells. 105

Figure 4.8 – Synthesis proposed by Dr Florian Guibbal towards a boronic pinacol ester precursor for [^{18}F]A-966492. 108

Figure 4.9 – Proposed synthetic route to precursor 4 via TMS protection/deprotection 109

Figure 4.10 – Proposed synthetic route to precursor 4 via benzyl protection/deprotection 110

Figure 4.11 – Alternative retrosynthetic route via C-H activation and photoredox-mediated aryl ring coupling. 112

Figure 5.1 – Synthetic pathway towards [^{19}F]1 and precursor 2 117

Figure 5.2 – Trialled synthesis towards a nitro quinoline core for a precursor to [^{18}F]AZD1390 136

Figure 5.3 – Synthetic steps towards hydroxy intermediate 3k 137

Figure 5.4 – Synthetic steps towards tosylate 3p and boronic ester 3r precursors for [^{18}F]AZD1390 138

Figure 5.5 – Synthetic steps from methyl 4-bromo-2-hydroxybenzoate towards a precursor for [^{18}F]A-966492 150

Figure 5.6 – Synthetic steps from methyl 4-bromo-2-methoxybenzoate towards a precursor for [^{18}F]A-966492 151

Table 1 – ATM inhibitors currently under investigation 13

Table 2 – PARP inhibitors and their status in clinical/preclinical development, with the NAD^+-mimicking pharmacophore highlighted in blue (adapted from ref. [78]) 20

Table 3 - Commonly used PET and SPECT radioisotopes 28

Abbreviations

53BP1 – p53 binding protein 1

ABC – ATR-binding cassette

ADME – Absorption, distribution, metabolism and excretion

ADP – Adenosine diphosphate

A_m – Molar activity

ART – ADP-ribosyl transferase

A-T – Ataxia telangiectasia

ATM – Ataxia telangiectasia mutated

ATP – Adenosine triphosphate

ATR – Ataxia telangiectasia and Rad3 related

BBB – Blood brain barrier

BCA – Bicinchoninic acid

BCRP – Breast cancer resistance protein

BER – Base excision repair

Bn – Benzyl

BOC – *tert*-Butyloxycarbonyl

BRCA – Breast cancer gene

BRCT – BRCA1 C-terminus

BSA – Bovine serum albumin

CAT – C-terminus catalytic domain

CDI - 1,1'-Carbonyldiimidazole

CED – Convection enhanced delivery

CHK1 – Checkpoint kinase 1

CHK2 – Checkpoint kinase 2

CNS – Central nervous system

CT – Computed tomography

dCK – Deoxycytidine kinase

DCM – Dichloromethane

DDR – DNA damage response

dH_2O – Deionised water

DMAP – 4-Dimethylaminopyridine

DMEM – Dulbecco's modified Eagle medium

DMF – *N,N*-dimethylformamide

DMPK – Drug metabolism and pharmacokinetics

DMSO – Dimethyl sulfoxide

DNA – Deoxyribonucleic acid

DNA-PK – DNA-dependent protein kinase

DNA-PKcs – DNA-dependent protein kinase catalytic subunit

DoE – Design of experiments

DSB – Double strand (DNA) breaks

DTT – 1,4-Dithiothreitol

EDTA – Ethylenediaminetetraacetic acid

e.e. – Enantiomeric excess

ESI$^+$ – Positive electrospray ionisation

EtOAc – Ethyl acetate

EtOH – Ethanol

FAC - 1-(2'-deoxy-2'-F-fluoroarabinofuranosyl) cytosine

FAT – FRAP-ATM-TRRAP domain

FATC – FAT catalytic domain

FBS – Foetal bovine serum

F-DOPA - L-6-fluoro-3,4-dihydroxyphenylalnine

FET – Fluoroethyl-L-tyrosine

FDG – 2-Fluoro-2-deoxyglucose

FITC – Fluorescein isothiocyanate

FLT – 3'-Fluoro-3'-deoxythymidine

FTT – Fluorthanatrace

GFP – Green fluorescent protein

GMP – Good manufacturing practice

H2AX – H2A histone family member X

γH2AX – phospho-H2AX^{S139}

H&E – Haematoxylin and eosin

HD – Helical subdomain

HPLC – High-performance liquid chromatography

HR – Homologous recombination

HRMS – High-resolution mass spectrometry

HRP – Horseradish peroxidase

HTS – High throughput screen

IC_{50} – Half maximal inhibitory concentration

ID/g – Injected dose per gram

IHC – Immunohistochemistry

IR – Ionising radiation

K_{222} – Kryptofix® 222

KAP1 – KRAB-associated protein 1

Ku70/80 – NHEJ protein complex Ku70/80

LCMS – Liquid chromatography and mass spectrometry

LED – Light emitting diode

MDR1 – Multidrug resistance protein 1

MeCN – Acetonitrile

MeOH – Methanol

MET – Methionine

MRE11 – DSB repair protein MRE11

MRI – Magnetic resonance imaging

MRN – MRE11-RAD50-NBS1 complex

mRNA – Messenger RNA

mTOR – Mammalian target of rapamycin

NAD^+ – Nicotinamide adenine dinucleotide

NBS – *N*-Bromosuccinimide

NBS1 – Nibrin

NET – Neuroendocrine tumour

NF1 – Neurofibromin 1

NHEJ – Non-homologous end joining

NMR – Nuclear magnetic resonance

***n*-PrOH** – Propan-1-ol

NSCLC – Non-small cell lung cancer

NuMA – Nuclear mitotic apparatus protein

OCT – Optimal cutting temperature compound

p53 – Tumour protein p53

PARP – Poly(ADP-ribose) polymerase

PARylation – Poly ADP-ribosylation

pATM – phospho-ATM^{S1981}

PBS – Phosphate buffered saline

PBST – PBS with Tween-20

pCHK2 – phospho-CHK2^{T68}

PDAC – Pancreatic ductal adenocarcinoma

PDX – Patient derived xenograft

PET – Positron emission tomography

P-gp – P-glycoprotein

PI3K – Phosphatidylinositol 3-kinase

PIKK – PI3K-related kinases

pKAP1 – phospho-KAP1^{S824}

pRAD50 – phospho-RAD50^{S635}

PRD – PIKK regulatory domain

PSG – Penicillin, Streptomycin, L-glutamine mix

PSMA – Prostate specific membrane antigen

PVDF – Polyvinylidene fluoride

RAD50 – DNA repair protein RAD50

RAD51 – DNA repair protein RAD51

RCC – Radiochemical conversion

RCY – Radiochemical yield

RIPA – Radioimmunoprecipitation assay

RNA – Ribonucleic acid

ROS – Reactive oxygen species

RPMI - Roswell Park Memorial Institute

RT – Room temperature

shATM – Short hairpin RNA against ATM

shGFP – Short hairpin RNA against GFP

S_N2 – Substitution nucleophilic bimolecular

S_NAr – Nucleophilic aromatic substitution

SP1 – Transcription factor SP1

SPECT – Single photon emission computed tomography

SSB – Single strand (DNA) break

SSTR – Somatostatin receptor

TBAF – Tetrabutylammonium fluoride

TBS – Tris-buffered saline

TBST – TBS with Tween-20

TEAB – Tetraethylammonium bicarbonate

THF – Tetrahydrofuran

TIP60 – Tat interactive protein-60

TLC – Thin layer chromatography

TMS – Trimethylsilyl

TMZ – Temozolomide

TP53 - Tumour protein p53 gene

US – Ultrasound

UV – Ultraviolet

WEE1 – Protein kinase WEE1

WGR – Tryptophan-glycine-arginine motif

1 General Introduction

1.1 DNA damage and cancer

1.1.1 How does DNA damage cause cancer?

Cancer, described as the uncontrollable proliferation of abnormal cells as a result of mutations within their DNA,[1-3] is one of the leading causes of death globally. These mutations can be either genetic (germline) or spontaneous (somatic) causing alterations in the function of key proteins and changing cell behaviour. Germline mutations are written into our genes before we are born and cannot be prevented through our behaviour, whereas somatic mutations are caused by environmental factors, such as ionising radiation (i.e. UV light), smoking, drinking, and diet. These factors can lead to DNA damage, which when unrepaired can result in the development of cancer.

The steps that follow DNA damaging incidents in the development of somatic mutations and cancer are excellently described in a recent review by Basu.[4] Briefly, the development of malignancies follows three key steps: initiation, promotion, and progression (Figure 1.1). Carcinogenic agents or ionising radiation are responsible for initiation – inducing damaged DNA lesions by making or breaking covalent bonds. Certain compounds are able to bind to the bases of DNA, restricting normal replication during mitosis, resulting in mismatched base pairing and eventual mutation at or around that nucleotide. UV light is another example of a mutagenic agent as it can induce a radical reaction between adjacent pyrimidine bases, resulting in covalent changes in the structure of DNA, again leading to mistakes in replication and introduction of mutations.[5,6] Following initiation is promotion,

the stage in which hyperplasia begins and papillomas begin to form. Promoting agents, such as benzoyl peroxide, croton oil, and okadaic acid, are not carcinogenic on their own, but instead promote the damage and irregular progression of cells after initiation through enhancement of other cellular processes, such as phosphorylations. The final stage of mutagenesis is progression where cells harbouring harmful mutations continue to divide forming malignancies and can eventually metastasise from the original tumour site to other organs.

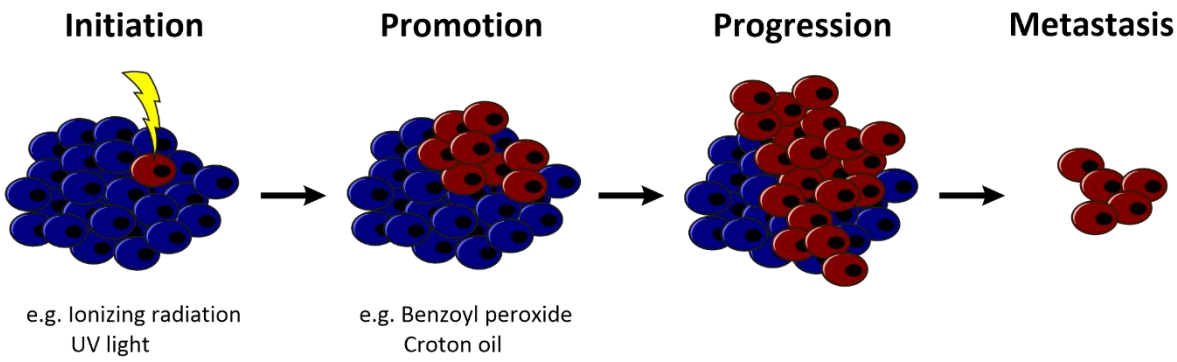


Figure 1.1 – Cancer formation follows initiation, promotion, progression, and eventually metastasis

The effects of these mutations are varied. Harmful damage to DNA can result in nucleotide substitutions, deletions, or chromosomal rearrangements that can lead to gene amplifications, oncogene activation, or gene silencing, all of which change the way the cell behaves. Different processes within the cell can be affected by this, including metabolism and the inability to repair further DNA damage, depending on where the mutation occurs. Since complete avoidance of DNA damaging agents is impossible, the question reverts to why every cell does not become cancerous. All cells undergo tens of thousands of DNA

damaging events every day due to normal side products of cell metabolism, such as the generation of reactive oxygen species (ROS), as well as exogenous insults we are exposed to in normal life including UV light and drug metabolites.[7-10] The reason these damaged DNA lesions do not normally affect us is due to the intricate mechanisms cells have evolved to fix any such damage quickly and effectively, collectively named the DNA damage response (DDR).

1.1.2 The DNA damage response

The DDR encompasses a network of proteins within the cell that collaborate to halt cell replication, allowing time for the repair to take place so as not to pass on any damaged DNA (or mutations) to daughter cells. Two key types of DNA damage lesion are single strand DNA breaks (SSB) and double strand DNA breaks (DSB). While SSBs account for most DNA damage within normal cells and are normally repaired quickly and effectively, DSBs are more deleterious, occurring from both DNA damaging agents and as a result of replication stress. Depending on the stage of the cell cycle and the type of DNA damage sustained, different repair mechanisms and proteins are required. SSBs are repaired most often by Base Excision Repair (BER),[11] while DSBs are repaired mainly by Non-Homologous End Joining (NHEJ)[12] or Homologous Recombination (HR)[13] when NHEJ is not possible (Figure 1.2). Of all the repair pathways available to cells, HR is the least prone to error as it uses template DNA from sister chromatids during S-phase to exactly reproduce the damaged sequence.

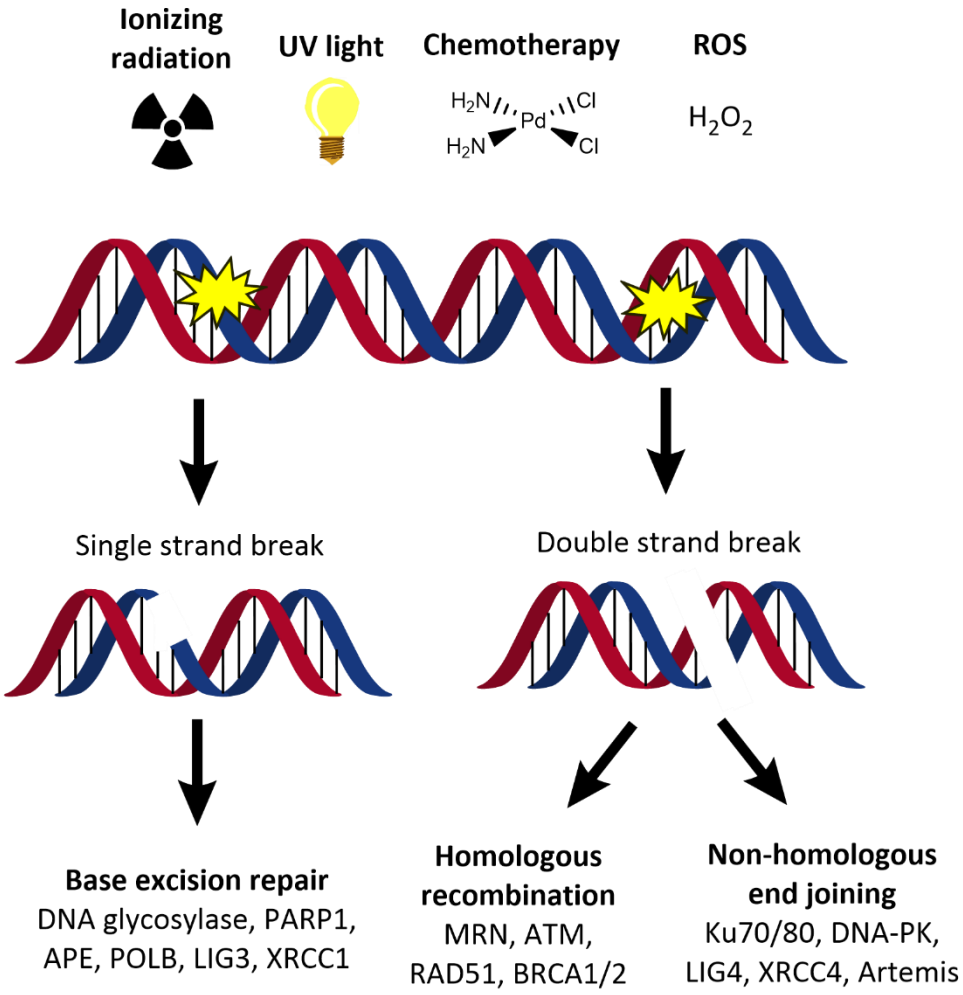


Figure 1.2 – Examples of DNA damage repair pathways

When damage is sustained in the DNA that codes for the proteins required by these repair pathways, the genes may become mutated which can lead to pro-cancerous phenotypes, leave cells less able to repair further DNA damage, and ultimately can result in aberrant protein function that enhances the proliferation of cancer where cells would otherwise initiate cell cycle arrest. Some cancers have specific gene mutations that shift the balance of which proteins/pathways are used to repair damage.

One well researched example is in mutations of the tumour suppressing *BRCA* genes giving rise to dysfunctional BRCA1 or BRCA2 proteins, which are essential to the recruitment and normal function of RAD51 during HR.[14] When BRCA proteins are dysfunctional (due to either germline, or less commonly, somatic mutations), repair of DSBs by HR is dramatically reduced resulting in a higher likelihood of mutagenesis and an increased reliance on parallel repair pathways, such as BER and NHEJ.

Another example commonly linked to high cancer prevalence is mutations within p53. This protein plays a critical role in cell cycle control and has key involvement in many different DDR pathways. Its normal function is regulated by DDR proteins to induce cell cycle arrest and initiation of DNA repair or to signal for apoptosis in irreparable cells. Given this, p53 is considered a tumour suppressor, with mutated p53 linked to a pro-cancer cell phenotype that is often chemotherapy resistant. Somatic mutations in the *TP53* gene (coding for p53) have been reported in almost all types of cancer, with particularly high occurrence in high grade and aggressive tumours.[15,16] A more extreme case of *TP53* mutation is in Li-Fraumeni syndrome, a familial condition resulting in complete functional loss of p53 giving a near 100% lifetime chance of developing cancer.[17]

1.1.3 Using the DNA damage response to our advantage

While DNA damage might cause some cancers, the inability then to recognise and repair damaged DNA effectively is a hallmark of cancer that is exploited in many treatments.[1-3] Radiation therapy and many chemotherapies are used to cause high levels of DNA damage

in cancer cells, overwhelming the cells beyond sustainable repair due to reduced ability to fix damage leading to unsuccessful cell proliferation.[18] These types of therapies are able to somewhat target cancer cells, as any surrounding healthy cells that are damaged by the therapy are more able to repair any damages and resist cell death thanks to a healthy DDR. However, due to the doses of these drugs/radiation therapy required to induce effective DNA damage in cancer cells, there are many off-target effects in healthy cells that can lead to severe side effects. As a result, a large proportion of current research is to look at ways to target cancer cells more specifically with therapy – in both new and combinational chemotherapies, as well as precise delivery of radiotherapies – to reduce drug side effects and radiation absorbed dose required while maintaining efficacy.

Inhibiting proteins of the DDR can provide a way to increase the efficacy of DNA damaging therapies by restricting repair of the induced DNA damage.[19,20] A lower dose of genotoxic therapy may be required for the same response when in combination with DDR inhibitors (DDRi), and this may help reduce harmful side effects resulting from the primary treatment. Inhibiting DDR proteins involved in more error-free repair pathways (e.g. HR) can also lead to reliance of cancer cells on more error-prone repair mechanisms, such as NHEJ, which can cause further genomic instability and promote desirable cell death, enhancing treatment efficacy. Combination therapies with DDR inhibitors are also becoming increasingly important in the development of treatments for therapy resistant cancers.[21]

Specific tumour DDR mutations can also be exploited through the use of synthetic lethality – the act of inhibiting parallel dependant pathways of DNA repair so as to overwhelm the cell with DNA damage beyond repair (Figure 1.3). For example, since tumour cells

harbouring *BRCA* defects are less able to repair DSBs, they rely on sufficient repair of SSBs to avoid further DSB formations. This makes these cells more dependent on SSB repair pathways, such as BER. As a result, drugs that are designed to restrict repair of SSBs (such as PARP inhibitors) are commonly employed in patients with *BRCA* mutated tumours to drive the cells to mitotic catastrophe.[22] The success of this treatment strategy has paved the way to identify other synthetic lethal pathways that could be exploited in cancer treatment, particularly within DDR pathways[23] (e.g. the combined use of ATM or ATR inhibitors with PARP inhibitors[21,24]).

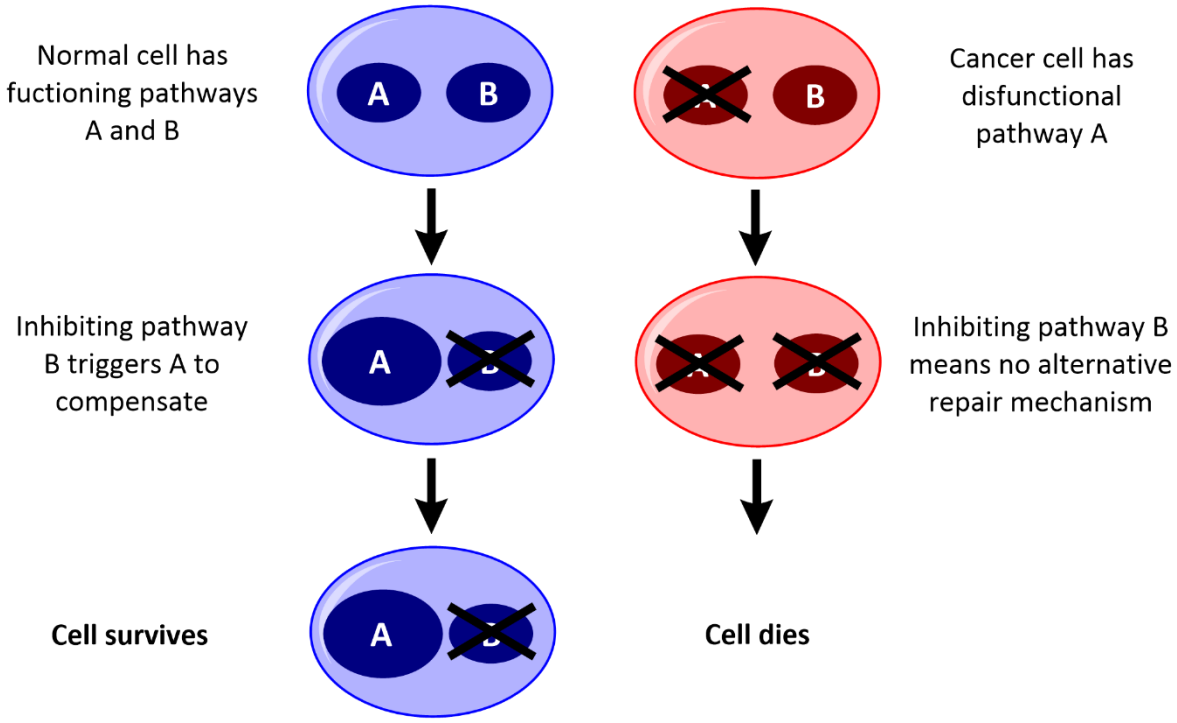


Figure 1.3 – Synthetic lethality

To develop novel inhibitors of the DDR requires a deep knowledge of the target protein in order to understand the underlying mechanisms and key drug binding sites. Described next are the biological mechanisms, importance in cancer, and a brief review on current inhibitors for two central DDR proteins: Ataxia Telangiectasia Mutated (ATM) and Poly (ADP-Ribose) Polymerase (PARP).

1.2 Ataxia Telangiectasia Mutated

1.2.1 ATM basic function, upstream and downstream targets, and activation

Ataxia Telangiectasia Mutated (ATM) is a 350 kDa member of the phosphatidylinositol 3-kinase (PI3K)-related kinases (PIKK) family of serine/threonine protein kinases. It shares sequence homology and domain architecture with other members of the PIKK family (including ATR, DNA-PKcs, and mTOR), comprising of spiral, pincer, FRAP-ATM-TRRAP (FAT), kinase (PIKK), and FATC domains (Figure 1.4 A).[25,26] The condition it is named after – Ataxia Telangiectasia (A-T) – is caused by mutations within and functional loss of the ATM protein that leads to symptoms such as poor muscle coordination (ataxia), slurred speech, poor balance, and red spider veins in the eyes, ears, and cheeks (telangiectasia). A-T patients also have a notably increased susceptibility and predisposition to cancer.[27] It is a central player in the detection of DSBs and subsequent organization and phosphorylation of proteins involved in HR (e.g. BRCA1, RAD51), apoptosis (e.g. CHK2), and cell cycle arrest (e.g. p53) (Figure 1.4 B).

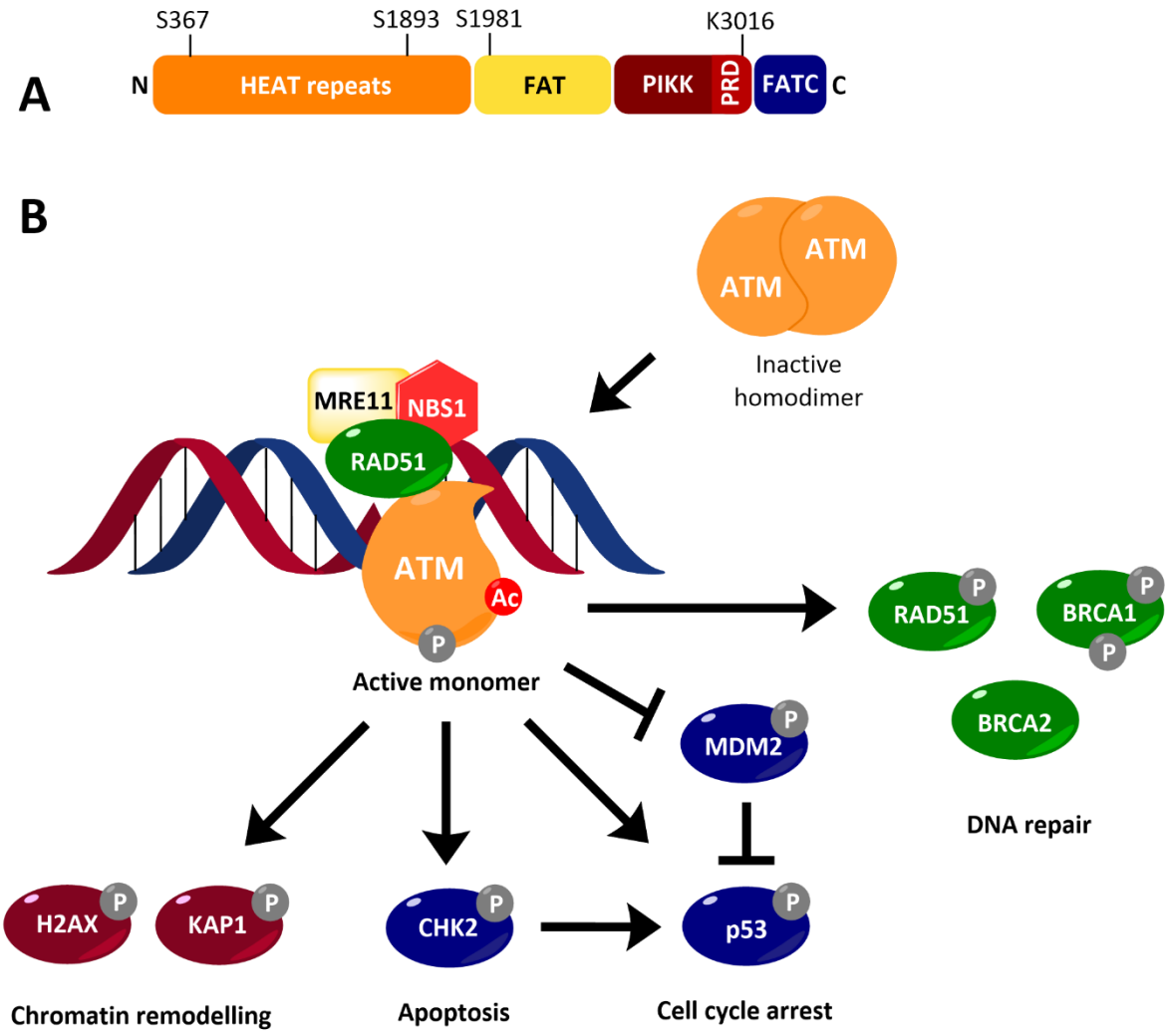


Figure 1.4 – (A) Domain map of ATM. (B) Signalling cascade of ATM.

Although ATM has a crucial role in the DDR, aspects of its activation mechanisms are still not fully understood. In its inactive state ATM exists as a homodimer, with cryo-electron microscopy studies revealing that dimer inactivity may to be due to interactions of PIKK regulatory domains (PRDs). In dimer ATM it appears that the PRD is well ordered and acts

as a pseudo-substrate on its neighbour protomer, but in monomer form it becomes disordered to allow substrate entry to the kinase domain.[26,28,29]

The activity of ATM is post-translationally controlled, with native copy numbers of the protein generally remaining constant and low in all cells across the body.[30-32] With regards to its role in DNA damage repair, it was first thought that ATM activation was dependent on the MRE11-RAD50-NBS1 (MRN) complex detection of DSBs and recruitment to sites of DSBs.[33] It has since been demonstrated that DSB induced ATM activation can occur independently of MRN recruitment, determined experimentally in a model system where the DNA damage sensor responsible for NHEJ (Ku70/80) is defective at the same time as MRN deficiency.[34,35]

The initial and most commonly used definition of ATM activation was described as the rapid intermolecular trans-autophosphorylation of the inactive ATM homodimer at serine-1981, followed by monomerisation,[36] with the monomer form of ATM approximately 10-fold more enzymatically active than its dimer.[29] A range of other amino acids have since been identified as being phosphorylated (e.g. S367, S1893) or acetylated (e.g. K3016) in correlation with activation, making this definition unclear.[37] Studies have also shown that mutation of the canonical ATM phosphorylation site in mice (S1987), alone or in addition to mutation of other known autophosphorylation sites (S367 and S1899), has no effect on the catalytic activity of ATM, questioning the relevance of these particular (auto)phosphorylation events during activation.[38,39] Current theory suggests the process of ATM activation follows acetylation at K3016 by TIP60 in order to open the catalytic domain, followed by a variety of (auto)phosphorylations to maintain an open/monomer form for

active ATM to allow activity on downstream targets.[40] This conformational change from the inactive ATM homodimer to an active open dimer or monomer species is thought to increase ATM-substrate binding, potentially by improving access to the ATP- and substrate-binding pockets, thereby allowing ATM to enact its role as a kinase.[41]

On the other hand, direct oxidation by ROS can lead to activated ATM in its dimer form where it is held in an open conformation by a new disulfide bridge between cysteine-2991 on each protomer.[42] Mutation of this cysteine to a lysine has demonstrated the importance of this residue in forming active ATM, where the C2991L mutant is not activated by peroxide oxidation but instead forms other disulphide bridges between protomers resulting in an inactive ATM species. Additionally, H2AX and KAP1 (involved in chromatin reorganisation for DNA damage repair) are not substrates of ROS activated ATM, demonstrating that ATM activation can be DNA damage independent and highlighting the further role of ATM in regulation of cellular oxidative stress.

1.2.2 ATM and cancer

Cancer cells show increased levels of DSBs, both as a result of their genomic instability and following genotoxic therapies designed to induce DNA damage, such as alkylating agents and ionising radiation. It is therefore predicted that they express higher levels of activated ATM, even though basal *ATM* expression is often unchanged.[43,44] In some cases, however, baseline expression of *ATM* might be increased, as was demonstrated in an *in vitro* model

of radioresistant breast cancer cells developed from repeated exposure to ionizing radiation.[45]

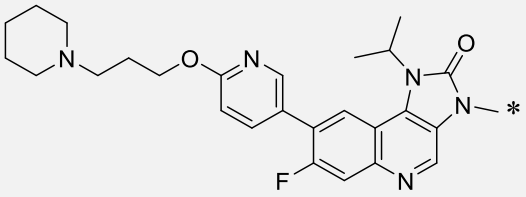
ATM mutations are strongly linked to increased cancer risk: Germline homozygous mutations in *ATM* gives rise to A-T, a condition which is associated with a 25% lifetime chance of developing cancer, particularly haematological cancers,[46] as well as increased radiosensitivity.[27] Heterozygous *ATM* mutations, in which only one *ATM* copy is mutated, are also thought to be linked to higher cancer incidence, but studies have been contradictory, likely as this is dependent on the specific type of mutation being studied.[47,48] In addition to germline mutations, somatic mutations in *ATM* are one of the most common genetic mutations found in a variety of tumour types, with particularly high occurrence in lymphoma and leukemia.[46,49] While germline mutations linked to A-T show direct links to therapy response, somatic missense mutations are less well defined in their impact on ATM function and therapy response. Even though mutations in *ATM* are often linked to increased cancer risk and worse prognosis, in some cases, *ATM* mutations that cause ATM dysfunction with a high heterogeneity score are actually indicators of better prognosis and overall survival, as is the case of metastatic colorectal cancer.[50]

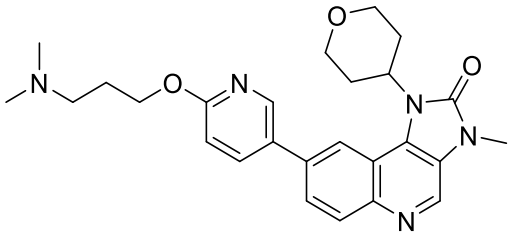
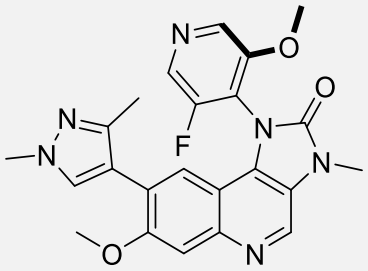
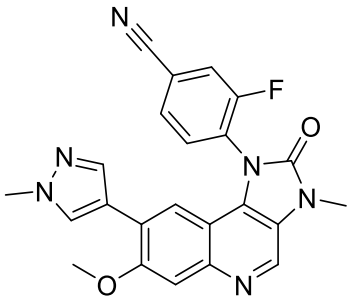
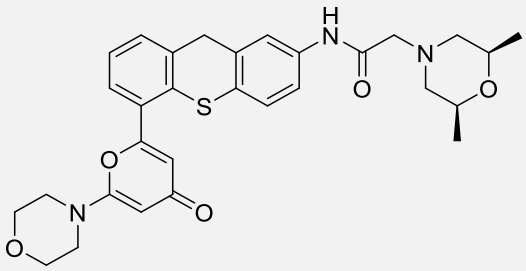
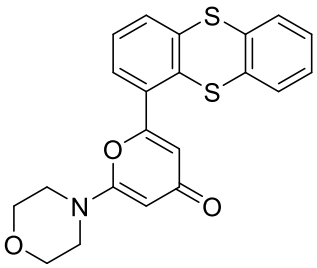
1.2.3 ATM inhibitors

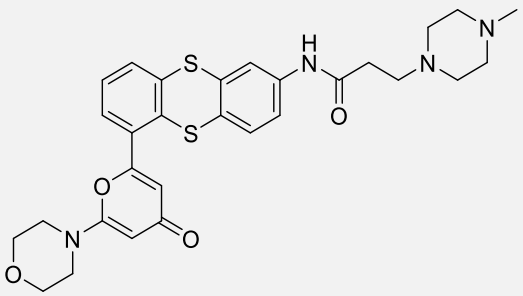
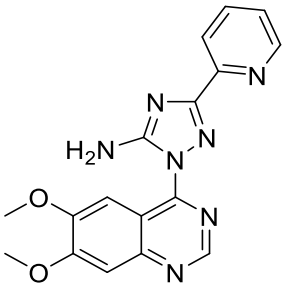
Given the clear importance of ATM with regards to cancer risk and treatment, the volume of research into ways to monitor ATM status/activity and to inhibit ATM is growing.[51] Drugs that inhibit ATM-substrate activity present a method of selectively targeting cancer cells by

reducing their DNA repair function and overloading the cells with damage. Since a precise structure of ATM has not yet been solved and that ATM is known to act on >500 substrates, designing selective inhibitors of the substrate binding site is not yet (and may never be) possible. Inhibitors that bind to the ATP-binding pocket provide an alternative inhibition mechanism. As all PI3K kinases have similar ATP-binding pockets, designing suitable inhibitors that selectively target ATM without inhibiting other kinases is challenging, with such compounds only being developed in the last couple of decades.[52] A range of inhibitors that compete for the ATP-binding pocket of ATM have been investigated, with several currently in clinical trials for a variety of cancers[53] (Table 1).

Table 1 – ATM inhibitors currently under investigation

Name	Structure	ATM IC_{50} (nM)	Status/Key findings
AZD1390		0.78 (Cell-based in HT29 cells)	Phase I clinical trials for brain cancer in combination with radiotherapy.[54,55] Phase I clinical trials for NSCLC and sarcoma in combination with radiotherapy.[56,57] Phase I clinical trial to assess brain PET imaging with ^{11}C-labelled AZD1390 completed (labelled in the starred position).[58-60]

AZD0156		0.58 (Cell-based in HT29 cells)	Phase I clinical trial for advanced solid tumours, alone and in combination with other agents.[24,52,61]
M4076		0.2 (Cell-free)	Phase I clinical trial for advanced solid tumours.[62-64]
M3541		0.5 (Cell-free)	Completed phase I clinical trials for solid tumours in combination with radiotherapy.[64-66]
KU60019		6.3 (Cell-free)	Preclinical *in vitro* evaluation of KU60019 in combination with CHK2 inhibitor, CX4945.[67,68]
KU55933		13 (Cell-free)	First specific ATM inhibitor, demonstrated sensitization of cells to ionizing radiation and topoisomerase inhibitors.[69]

KU59403		3 (Cell-free)	Preclinical investigation in combination with topoisomerase inhibitors and improved pharmacologic properties over previous KuDOS inhibitors.[70]
CP466722		410 (Cell-based in MCF7 cells)	Demonstrated rapid and reversible inhibition of ATM *in vitro*, revealing that only transient ATM inhibition is require for cell sensitization to ionizing radiation.[71,72]

Of these inhibitors, only four have reached clinical trials: AZD1390, AZD0156, M4076, and M3541. The first to enter trials was AZD0156 in 2015 both as a monotherapy and in combination with olaparib, irinotecan, fluorouracil, or folic acid in advanced cancers, although the results of this trial are yet to be published (NCT02588105). Closely following the development of AZD0156 came AZD1390 which retains the same quinoline-based scaffold but was designed and confirmed to be brain penetrable.[59] AZD1390 first entered clinical trials in 2018 for treatment of brain tumours in combination with radiation therapy (NCT03423628) but has since been included in three further trials including for NSCLC, sarcoma, and glioma, both as monotherapy and in combination with radiotherapy (NCT04550104, NCT05182905, NCT05116254). Furthermore, a carbon-11 radiolabelled

version, [^{11}C]AZD1390, has completed phase I trials assessing PET imaging of brain uptake in healthy subjects[60] (NCT03215381). Following the same quinoline scaffold, inhibitors M3541 in combination with radiotherapy and M4076 as monotherapy entered clinical trials in 2017 and 2021 respectively (NCT03225105, NCT04882917). The results of M3541 were recently published demonstrated a manageable toxicity profile but despite promising preclinical data,[64] no dose dependent correlation of PK and PD was observed leading to removal of M3541 from further clinical studies due to its lack of efficacy.[66] M4076 is yet to report any clinical data. These trials demonstrate how the landscape of ATMis is still in its infancy, with clarity of the impact of these inhibitors expected over the next few years as these trials complete.

1.3 Poly (ADP-Ribose) Polymerase

1.3.1 PARP basic function, upstream and downstream targets, and activation

The 17-member family of poly (ADP-ribose) polymerases (PARPs) plays a key role in the DDR, acting via recruitment of other repair proteins to sites of DNA damage, in addition to contributing to other cell maintenance pathways.[73] The major PARP isoform involved in DNA damage repair is PARP1, with PARP2 and PARP3 also shown to be DNA damage dependent. PARP1 consists of three N-terminus zinc finger domains, an auto-modification domain (containing the BRCA1 C-terminus (BRCT) region), a tryptophan, glycine, arginine motif (WGR), and a C-terminus catalytic domain (CAT) comprising of a helical subdomain (HD) and ADP-ribosyl transferase (ART) subdomain. PARP2 and PARP3 retain a similar

domain map but do not contain any zinc finger or BRCT domains (Figure 1.5 A).[74] PARP1 uses its zinc finger domains to detect and bind to sites of SSBs (and DSBs) which in turn destabilises the HD structure, subsequently allowing the substrate nicotinamide adenine dinucleotide (NAD^+) to bind to the ART domain. This allosteric change allows the ART domain to induce poly ADP-ribosylation (PARylation) on target proteins (including PARP itself in both cis and trans, as well as DNA) which signal for recruitment of DNA repair machinery[74] (Figure 1.5 B). Although PARP2 and PARP3 do not have zinc finger domains, the WGR domain is able to detect and bind to DNA damage, undergoing the same activation of ADP-ribosylation. While PARPs are able to bind to different types of DNA damage (including DSBs, SSBs, and stalled replication forks), they are particularly important BER, with expression and activity regulated by SP1 and NF1 at a transcriptional level.[75] Given PARP1 is the most abundant isoform and is predicted to represent over 90% of total PARP protein, from here on, PARP1 will be referred to as “PARP”.

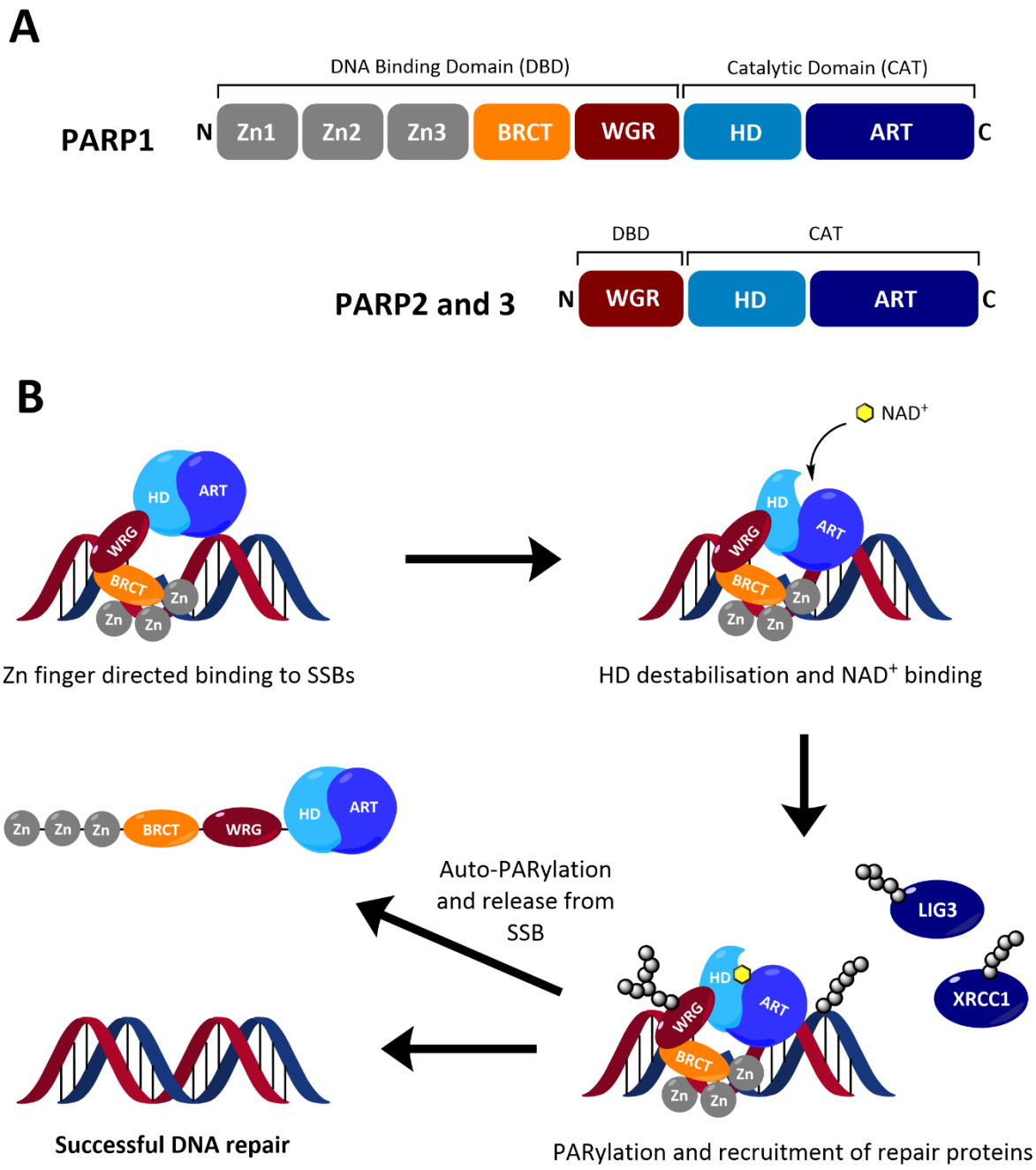


Figure 1.5 – (A) Domain map for PARP1, 2, and 3. (B) DNA binding mechanisms of PARP1

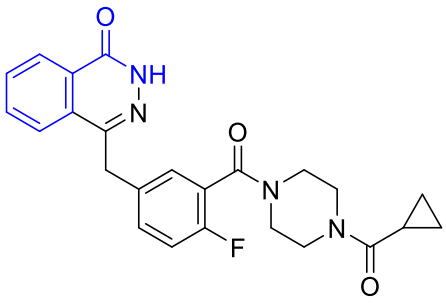
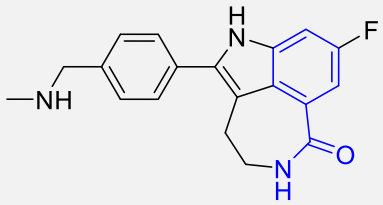
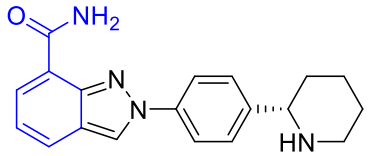
1.3.2 PARP and cancer

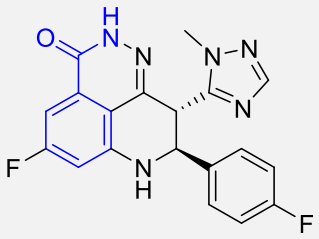
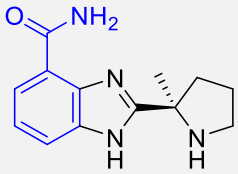
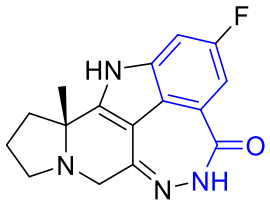
Given the high levels of DNA damage and resulting repair required in cancer cells, PARP is vital as one of the most abundant proteins in the nucleus with very high affinity for damaged DNA,[74] giving it a high profile in cancer biology. One of the biggest themes associated with PARP is synthetic lethality, as PARP is involved in so many types of DNA repair where there may be cancer associated mutations in parallel pathways. As mentioned previously, PARP has been found as a key protein in cases of *BRCA* mutations, as restricting PARP activity in these tumours can induce cell death and affecting tumour treatment. Additionally, PARP inhibitors (PARPis) are being investigated as chemo- and radio-sensitizing drugs to enhance the efficacy of already known treatments by reducing repair of the lesions generated by the primary treatment.[76]

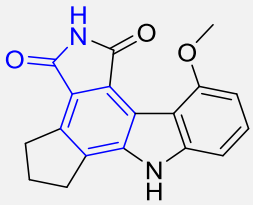
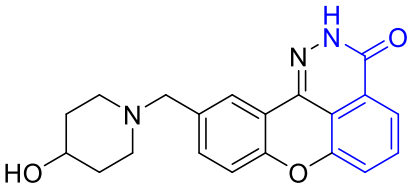
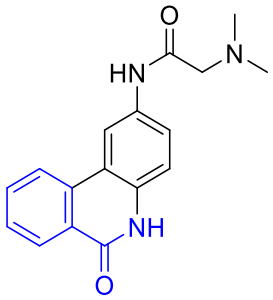
1.3.3 PARP inhibitors

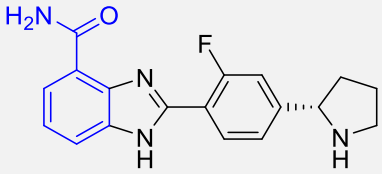
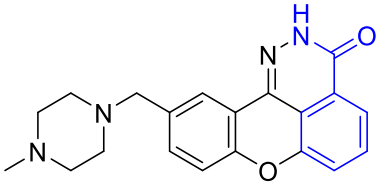
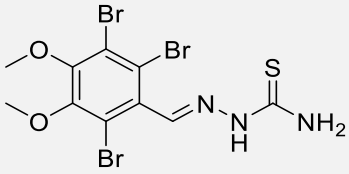
PARP can be inhibited by blocking binding of the native NAD^+ substrate that is required for activity. Given this, many PARP inhibitors have been designed containing a key NAD^+-like benzamide pharmacophore that competes for the NAD^+ binding pocket.[77] A comprehensive list of inhibitors and their current clinical status can be found in Table 2.

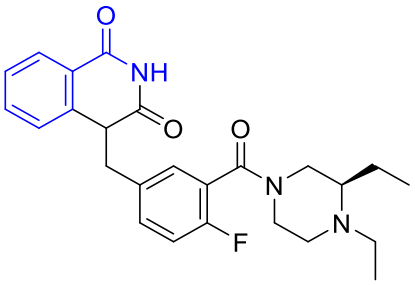
Table 2 – PARP inhibitors and their status in clinical/preclinical development, with the NAD^+-mimicking pharmacophore highlighted in blue (adapted from ref. [78])

Name	Structure	PARP1 (PARP2) IC_{50} (nM)	Status/Key findings
FDA approved			
Olaparib (Lynparza®)		5 (1) (Cell-based in SW620 cells)[79] 1.94 (Cell-free)[80]	Clinically approved for treatment of *BRCA*-mutated breast, ovarian, fallopian tube, and peritoneal cancers. Also approved for *BRCA*-mutated metastatic pancreatic cancer and prostate cancer with HR deficiencies. (Lynparza.com)
Rucaparib (Rubraca®)		0.8 (0.5) (Cell-free)[81] 1.98 (Cell-free)[80]	Clinically approved for treatment of relapsed high-grade platinum responsive, or *BRCA*-mutated ovarian, fallopian tube, or peritoneal cancers. (medicines.org)
Niraparib (Zejula®)		3.8 (2.1) (Cell-based in HeLa cells)[82]	Clinically approved for treatment of advanced or relapsed high-grade platinum responsive ovarian, fallopian tube, or peritoneal cancers. (medicines.org)

Talazoparib (Talzenna®)		0.57 (Cell-free)[80]	Clinically approved for treatment of *BRCA*-mutated (germline) HER-2 negative locally advanced metastatic breast cancer. Also approved for hormone receptor positive patients who are unsuitable for endocrine-based therapy. (medicines.org)
In clinical trials			
Veliparib		4.73 (Cell-free)[80]	Undergoing many phase I-III clinical trials, both as stand-alone treatment, and in combination with radiation therapy and/or DNA damage inducing chemotherapies (e.g. temozolomide (TMZ)), for a range of solid tumour indications. (clinicaltrials.gov)
Pamiparib		1.3 (0.92) (Cell-based in HeLa cells)[83]	Currently being investigated in many phase I—III trials for a range of solid tumours (including brain tumours) as mono- or combination therapy. (clinicaltrials.gov)

CEP-8983 (CEP-9722)		20 (6) (Cell-free)[84]	Prodrug CEP-9722 being investigated in phase I-II for solid tumours as monotherapy and in combination with TMZ, gemcitabine, and/or cisplatin.[85-87]
E7016		~1500 (Cell-based in U251 cells)[88] 40 (Cell-free)[89]	Phase I dose escalation study in combination with TMZ in patients with solid tumours completed.[90] Phase II study in combination with TMZ in patients with grade IV or II (unresectable) melanoma was terminated.[91]
Preclinical			
PJ34		110 (Cell-free)[92]	Huang *et al.* showed PJ34 enhances the effect of cisplatin in liver cancer cells.[93] Doses of PJ34 higher than that required for PARP inhibition but that are able to induce NuMA clustering have also shown significant reduction in tumour size in human PDAC xenograft models.[94]

A-966492		1 (Cell-based in C41 cells)[95]	Initial studies showed A-966492 was BBB-penetrable, could enhance both TMZ and carboplatin treatment in human xenografts models, and was effective as a single agent in a *BRCA1*-deficient xenograft model.[95] Further studies in U87MG glioblastoma spheroids showed the potential for A-966492 in combination with Topotecan to radiosensitize cells.[96]
GPI-15427		13 (Cell-free)[97]	GPI-15427 has been shown to cross the BBB and is able to enhance the antitumour effects of TMZ in CNS tumour models.[98-100] It has also demonstrated increased radiosensitization in head and neck cancer models,[97] and to reduce toxicities associated with Irinotecan used in the treatment of colon cancer.[101]
BTH-8		80 (Cell-free)[102] 2000-26000 (Cell-based)[102]	Showed reduction in tumour growth in breast cancer models.[102] Also lead to development of daughter molecule DHC-1 with a better PARP1 selectivity.[103]

'Compound 24'		0.5 (22) (Cell-free)[104]	Excellent inhibitory effects in combination with TMZ in models of breast and brain cancer, as well as favourable pharmacokinetics and toxicology profile.[104]

While the PARP inhibitors olaparib, rucaparib, niraparib, and talazoparib have been clinically approved with many more in the pipeline, there is an emerging issue with the development of resistance to PARPis in some patients. Resistance can be triggered by standard drug resistant routes, such as overexpression of drug efflux transporters, but also by restoration of HR in previously deficient tumours, either by upregulation of alternative repair pathways (e.g. the downregulation of *TP53* in *BRCA1* mutant cells causes an increase in *BRCA2* dependent HR), or secondary mutations on previously dysfunctional genes (e.g. *BRCA*) that reactivates function.[105,106] Combination of PARPis with other DDR inhibitors including ATR, ATM, and WEE1 inhibitors to limit any HR-recovery resistance mechanisms by further disabling the DDR is one potential solution to PARPi resistance.

1.4 Molecular Imaging in Cancer

1.4.1 Medical imaging used in cancer diagnosis

Computed Tomography (CT), Magnetic Resonance Imaging (MRI), and Ultrasound (US) are the standard imaging modalities used to determine the location, distribution, and spread of tumours. These are normally used for anatomical imaging and are particularly important

for making surgical and radiotherapy plans. However, when it comes to determining chemotherapy treatment plans, these imaging platforms are generally less able to assess the suitability of a certain treatment for a certain tumour. While many chemotherapy drugs are non-specific and designed to enhance the damage caused to tumours (e.g. cisplatin, doxorubicin, TMZ), in order to treat tumours in a more selective and personalised manner, invasive tumour biopsies are often required to gain an understanding of the specific tumour biology. These samples can be very difficult to obtain (such as in difficult to reach cancers e.g. pancreatic, brain) and are unable to fully represent tumour heterogeneity, particularly when there are multiple metastatic sites present. For this reason, techniques for functional imaging have been developed to gain a greater understanding of tumour biology non-invasively and improve diagnosis and treatment planning.

1.4.2 Nuclear imaging (PET and SPECT)

Nuclear imaging is performed following injection of a radiotracer – a radionuclide-tagged small molecule or biologic targeting group, specific to a chosen biological target – then detection of radionuclide concentration and distribution within the body by either Positron Emission Tomography (PET) or Single Photon Emission Computed Tomography (SPECT) (Figure 1.6). In both PET and SPECT, high energy photons (gamma radiation) released by the radionuclide are detected by a series of scintillators coupled to photomultiplier tubes positioned around the body. Reconstruction of these signals is then used to identify the precise location of origin of the decay signal, and therefore of the targeting probe. Visualising the distribution of the targeting probe gives insight into the distribution of the

specific biological target giving real-time information of the tumour biology. Ultimately, the benefits of nuclear imaging encompass the ability to study the biology of tumour sites non-invasively to assist with diagnosis, staging, and patient stratification in treatment selection. It can also be used to predict and monitor therapy response, in addition to supporting novel drug development by providing detailed pharmacokinetics information and confirming target engagement using drug radioisotopologues.

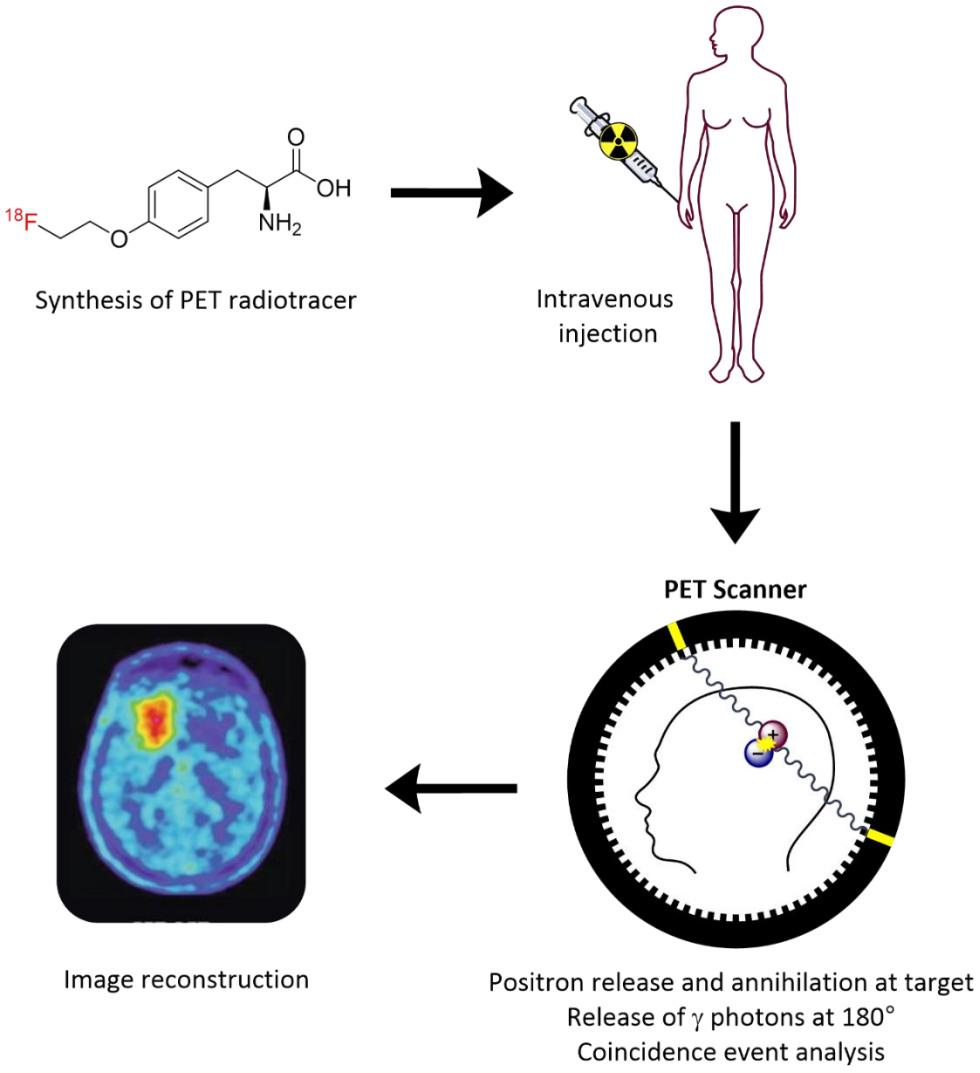


Figure 1.6 – Schematic of PET imaging

Although the resolution of PET (low mm) and SPECT (3-5 mm) are less than that of MRI (100-500 μm), these nuclear imaging modalities are more sensitive in being able to visualize biological targets at lower concentrations (nM), such as enzyme expression, than MRI (mM).[107] The difference in resolution and sensitivity in PET and SPECT comes down to the detection of specific radionuclide decay, as well at the way the radioactivity is detected. In PET, detection is of two high energy (511 keV) gamma photons released at a 180° angle resulting from positron-electron annihilation emanating from the selected positron emitting radionuclide. These can be detected in their respective pairs by stationary ring scintillation detectors using electronic collimation and coincidence processing, allowing for more simple background radiation/noise reduction and more precise localization of the radiotracer. SPECT on the other hand uses radionuclides with generally longer half-lives that release one gamma photon. This gamma decay is detected by rotating scintillation detectors collecting emission data at multiple angles and requires physical collimation, resulting in slightly poorer detection efficiency, and more complex background correction. Some common radionuclides used in PET and SPECT are detailed in Table 3.

Alongside imaging modality comes the choice of radiotracer. The ideal radiotracer must be highly specific to its target with high binding affinity (preferably in the sub-nM range), must be highly stable *in vivo*, must be structurally amenable to incorporation of a radionuclide, and ideally will be quick and easy to synthesise, particularly when labelling with radionuclides that have short half-lives. While the radiotracers are designed to interact with the specified biological system in order to probe target function, they are dosed at sub-

therapeutic concentrations whereby they do not impose a biological response, known as the radiotracer principle.

Table 3 - Commonly used PET and SPECT radioisotopes

Imaging Modality	Radionuclide	Decay modality	Half-life	Gamma energy detected (keV)
PET	^{11}C	β^+	20 min	511
	^{18}F	β^+	110 min	
	^{13}N	β^+	10 min	
	^{15}O	β^+	2 min	
	^{68}Ga	β^+	68 min	
SPECT	^{99m}Tc	γ	6 hours	140
	^{123}I	γ	13 hours	159
	^{131}I	γ	192.5 hours	364
	^{111}In	Auger e^-	67 hours	173 / 247

1.4.3 Current PET/SPECT cancer imaging targets

For nuclear imaging to be useful, a suitable target or process must be chosen for analysis that is disease specific or shows a change in expression/function compared to normal tissue in order to give good signal-to-noise ratio upon imaging. In oncology, the target will ideally be ubiquitous across different tumour types to expand the usefulness of the radiotracer to multiple tumour indications, however this is not a necessity. The target must also be accessible for engagement with the designed radiotracer in useful concentrations. Most importantly, a target must be chosen that will give useful read-out information from the

acquired image, for example, by increasing understanding of target expression and distribution, or by improving understanding of pharmacokinetics and tumour engagement of novel drug-based radiotracers.

The most common nuclear imaging used in oncology is [^{18}F]fluorodeoxyglucose (FDG) PET imaging. [^{18}F]FDG is a radioactive analogue of glucose which images cancer by taking advantage of the Warburg effect – an alteration in glucose metabolism seen in most cancer cells that results in an increased uptake of glucose (and therefore of [^{18}F]FDG).[108] While [^{18}F]FDG benefits from being able to detect most tumours and is particularly useful in staging, it can sometimes give poor tumour delineation due to high uptake in the brain, heart, and urinary tract, as well as increased uptake in areas of inflammation and infection.[109] Other processes that are often abnormal in cancer have been harnessed for oncology PET and SPECT include amino acid transport,[110] hypoxia,[111] dopamine metabolism, and lipid and fatty acid metabolism.[112]

Away from quantification of biological processes, some proteins are known to be overexpressed in some types of tumours. Prostate specific membrane antigen (PSMA) was identified on the surface of prostate cancer cells, with high expression correlating with higher staging and poorer survival rates. It has been the target of many PET studies, with [^{68}Ga]Ga-PSMA-11 approved for clinical assessment of prostate cancer in 2020.[113] The success of this tracer has also led to the development of radionuclide therapies targeting PSMA,[114] with recent FDA approval of the β-emitting [^{177}Lu]Lu-PSMA-617 in March 2022 for treatment of metastatic castration resistant prostate cancer. Similarly, neuroendocrine tumours (NETs) often overexpress somatostatin receptors (SSTRs) and radiolabelled

somatostatin analogues such as [^{68}Ga]Ga-DOTATATE are currently used in clinic for imaging these NETs.[115]

1.4.4 Tumour imaging in the brain

Brain tumours continue to be some of the hardest cancers to treat. While primary brain tumours account for <2% of all cancer types (World Cancer Research Fund, 2020), the percentage of brain tumours resulting from metastasising non-brain primary tumours is harder to determine with current data estimating brain metastases to be anywhere between 1.6-10 times more prevalent than primary brain tumours.[116,117] Breast, lung, and skin cancers are responsible for up to 80% of all brain metastases,[118] and incidence of brain metastases from these types of cancer appear to be increasing with the improvement of treatment of the primary tumour – likely linked to longer survival frames, as well as improved detection and monitoring of disease.[119]

The standard of care for brain tumours involves surgery (where possible), along with TMZ and radiotherapy,[120] however, drug treatment of brain tumours is challenging due to the presence of the blood-brain barrier (BBB). The BBB is made up of a series of tight-junctions, adherens junctions, and gap junctions that together selectively allow vital substances (e.g. glucose, oxygen) to permeate the brain, while protecting it from harmful substances and infection.[121] With this tight regulation by restrictive transcellular influx and highly effective efflux of compounds, there are very few drugs that are able to reach the brain in doses high enough to kill tumours. During the development of primary brain tumours and particularly

in the invasion of the brain by metastatic cancer cells, however, the BBB is often disrupted and thought to be more leaky allowing greater drug delivery to tumours, as evidenced by the efficacy of treatments for glioblastoma.[122]

A lot of current research is focusing on novel methods to deliver drugs to the brain, for example the use of ultrasound to disrupt the BBB and make it more permeable to drugs in the bloodstream.[123] Medicinal chemists also work on the careful design of suitable drugs that are able to cross the BBB effectively. Such drugs are often small, lipophilic, rigid, and are designed not to be substrates of key efflux transporters in the brain (e.g. BCRP and MDR1). Assessing a novel drug's BBB permeability generally requires highly invasive and technically complex *in vivo* studies, recently reviewed by Chowdhury *et al*.[124]

Nuclear imaging can provide a non-invasive way to visualise dynamic drug-brain uptake and can be repeated in longitudinal studies, reducing the need for more invasive evaluation. PET and SPECT are used in a variety of brain diseases such as neuroinflammation and metabolism (with [^{18}F]FDG) and neurodegeneration (with 6-[^{18}F]-L-fluoro-L-3, 4-dihydroxyphenylalanine, [^{18}F]F-DOPA).[125] In neuro-oncology, very few currently investigated oncology radiotracers are BBB penetrable, hindering their use in probing brain cancer biology.[126] While [^{18}F]FDG is able to cross the BBB and is frequently used in the diagnosis of glioma, the glucose requirement of normal brain tissue is high making tumour delineation poor. Additionally, areas of inflammation in the brain demonstrate high [^{18}F]FDG uptake, reducing tumour diagnostic performance.[127] Beyond [^{18}F]FDG, amino acid PET radiotracers such as [^{18}F]fluoroethyl-L-tyrosine ([^{18}F]FET), [^{18}F]F-DOPA, and [^{11}C]methionine ([^{11}C]MET) visualising increased protein metabolism are frequently used in

brain imaging,[110] the use of which is guided by the Response Assessment in Neuro-Oncology working group (RANO).[128] Nucleoside analogues have also been investigated for neuro-oncology PET with deoxy-[^{18}F]fluorothymidine ([^{18}F]FLT) for imaging tumour proliferation, however normal BBB penetration is poor.[129] In parallel, activity of P-glycoprotein (P-gp) as one of the main efflux transporters in the BBB restricting brain drug bioavailability[126] has been investigated with PET[130] and could help in understanding P-gp expression and function when assessing brain cancer treatments.

1.4.5 What could imaging the DDR tell us?

While recent developments in the field of DDR inhibitors are promising, there remains an issue of finding the right patients for the right treatments. Identifying tumours with particular mutations (e.g. *ATM*, *BRCA*) normally requires invasive tumour biopsy followed by assessment by pathology, or more expensive DNA sequencing, and may not represent the heterogeneity of tumour phenotypes across the whole tumour or indeed any metastatic lesions. Being able to characterise tumour phenotype and any druggable mutations in a more holistic way will assist in the selection of patients who are likely to respond well to selected DDR inhibitors or identify those who may be more suited to alternative therapies quicker.

Research into nuclear imaging of DDR proteins began in the past two decades, beginning with the development of radiolabelled PARP inhibitors. The first reported radiolabelled PARPi was [^{11}C]PJ34 in 2005, and demonstrated the ability of this tracer to image levels of

high PARP1 expression *in vivo* in diabetic rat pancreases in comparison to normal pancreas tissue.[131] Following this, many other PARPi radiotracers, mostly labelled with fluorine-18 or iodine radionuclides have been developed[132-134] with two, [^{18}F]fluorthanatrace (FTT)[135] and [^{18}F]PARPi,[136] reaching clinical trials.

In addition to PARP, other DDR proteins have been targeted in recent radiotracer development, as discussed in a recent review by Everix *et al.*[137] A radiofluorinated analogue of the ATR inhibitor Ve-821 was developed and assessed in U251MG glioblastoma cells demonstrating ATR target engagement through blocking experiments *in vitro* and *in vivo*, although reduction in tracer binding was minimal, with no further evaluation of this tracer reported.[138] ATM inhibitors AZD1390 and AZD0156 were each labelled with carbon-11 for assessment of BBB penetration in non-human primates,[59] with [^{11}C]AZD1390 recently completing phase I clinical trial showing excellent brain exposure in healthy participants.[60] The radiosynthesis of ^{11}C-labelled chromen-4-one based DNA-PK inhibitors for use in PET imaging has also been described, however no biological data has been reported.[139]

While not used for imaging, it is common to develop carbon-14 or tritium labelled drugs to assist in their regulatory approval. For example, the ^{14}C-labelled CHK1/CHK2 inhibitors LY2606368 (Prexasertib) and LY2603618 (Rabusertib) were investigated in the clinic alongside the non-labelled equivalents to evaluate their ADME properties,[140,141] and ^{14}C-labelled LY3023414 (Samotolisib), a dual DNA-PK/mTOR inhibitor, was used to investigate DMPK and ADME properties.[142] Studies such as these demonstrate the enhanced dataset that can be collected using radiopharmaceuticals, and drug radioisotopologues in particular, in the development and understanding of novel drugs in a clinical setting.[143] By

selecting appropriate radionuclides, these properties can be applied to PET/SPECT imaging probes where they may gain additional benefits of non-invasive imaging for assessment of tumour biology on top of their use for DMPK/ADME studies.

1.5 Aims

The use of DDRi drugs in the treatment of cancer is a rapidly growing research area with many new inhibitors entering clinical trials over the last decade. With the development of new drugs, particularly a new class of drugs, comes the need to understand which patients will benefit most from these therapies. Nuclear imaging has demonstrated the ability to probe biological characteristics of heterogenous tumour tissues and assist in patient therapy selection. PET imaging of DDR proteins with radiolabelled DDRis proposes a way to investigate tumour characteristics and DDRi pharmacokinetics, as well as the potential use in monitoring and understanding the response to DNA damaging therapies.

Hypothesis 1: Is ATM a useful target for PET imaging with novel ^{18}F-labelled small molecule ATM inhibitors?

The critical role of ATM in mediating the DNA damage response to double strand DNA breaks as well as the recent introduction of small molecule ATM inhibitors into phase I clinical trials makes it an intriguing PET target, both for imaging areas of high DNA damage and for investigating ATMi pharmacokinetics and ATMi-target engagement non-invasively. Additionally, in contrast to the two ^{11}C-labelled ATMis that are restricted by a very short half-life of 20 min, synthesis of a fluorine-18 labelled ATMi with its longer half-life may be

more useful in investigating the activation mechanisms of ATM that are currently incompletely understood. Chapter 2 reports the first radiofluorinated ATMi ([^{18}F]**1**) and its subsequent biological assessment.

A second and more challenging target, [^{18}F]AZD1390, was proposed as a useful tracer for comparison with [^{18}F]**1**. Additionally, given AZD1390 being investigated clinically in the treatment of brain tumours, [^{18}F]AZD1390 could provide a radiotracer to visualise brain tumour engagement of AZD1390 that would ultimately be transportable across multiple hospital sites, unlike the currently investigated [^{11}C]AZD1390. Chapter 3 reports the synthesis and radiolabelling trials towards [^{18}F]AZD1390, with accompanying review on the challenges of radiofluorination of electronically neutral arenes and reflections on ATM as a PET target.

Hypothesis 2: Would a BBB-penetrable ^{18}F-labelled PARP inhibitor be useful for PET imaging of brain tumours?

Finally, given the challenges faced in imaging ATM and radiofluorinating the BBB-penetrable [^{18}F]AZD1390, PARP was proposed as an alternative target for DDR imaging in the brain. Although there have been many reports of radiofluorinated PARP inhibitors that have demonstrated the ability to image PARP expression in pre-clinical studies, none of the reported tracers have demonstrated BBB-penetrability, reducing their ability for brain tumour imaging of PARPi engagement. Chapter 4 investigates the synthesis towards [^{18}F]A-966492 as a BBB-penetrable PARPi radiotracer.

2 Radiofluorination of a highly potent ATM inhibitor as a potential PET imaging agent

The majority of the work presented in this chapter has recently been published with myself as first author:

Fraser CR, Ajenjo J, Veal M, et al. Radiofluorination of a highly potent ATM inhibitor as a potential PET imaging agent. *EJNMMI Res*. 2022;12(1):50

2.1 Introduction

Ataxia Telangiectasia Mutated (ATM) is a key mediator of the DNA damage response with a crucial role in maintaining genomic integrity, making it significant in the study and therapy of cancer. When ATM is activated in the presence of double stranded DNA breaks (DSBs) resulting from genomic instability, replication stress, or external stimuli such as radio- or chemotherapy, it undergoes monomerization and autophosphorylation at S1981. Its central role in DNA damage repair signalling has led to a variety of ATM inhibitors (ATMi) being developed to reduce ATM enzymatic activity, restricting repair of harmful lesions and cell cycle arrest, resulting in mitotic catastrophe and cell death (Table 1, page 13).[53,144] Although there are a handful of ATM inhibitors currently undergoing clinical trials, none have been approved for use in patients yet.

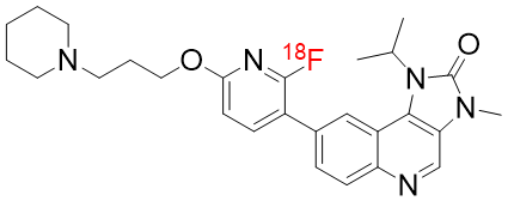
The study of ATM both mechanistically and as a therapeutic target has led to the development of a range of techniques to visualise ATM, recently reviewed.[51] Investigations into the activation mechanisms of ATM have historically used classical techniques such as

immunoblotting to identify ATM activation and the effects on downstream targets of ATM, aided by the use of increasingly selective ATM inhibitors. Due to the complexity of ATM mechanisms, the study of proteins associated with ATM have also been used to assess its activity indirectly. One elegant example is the use of PET with ^{18}F-labelled 1-(2'-deoxy-2'-^{18}F-fluoroarabinofuranosyl) cytosine ([^{18}F]FAC) to image the expression of deoxycytidine kinase (dCK), an enzyme that is phosphorylated by ATM, activating its role in nucleotide salvage for DNA damage repair.[145] More recently, direct imaging of the biodistribution of an ATM inhibitor using a ^{11}C-labelled version, [^{11}C]AZD1390, has demonstrated that particular inhibitor's ability to cross the blood-brain barrier in a phase I clinical trial.[59,60]

Radiolabelled analogues of investigational drugs add enormous value for the study of pharmacokinetics, can aid preclinical development, and act as companion biomarkers assisting patient stratification.[146] PET/SPECT imaging with these radiopharmaceuticals can be used to non-invasively assess tumour/tissue uptake and aid dose calculations and scheduling for each patient prior to treatment with the therapeutic, assisting the move to more personalised medicine. [^{11}C]AZD1390 demonstrated some of these benefits, however the relatively short half-life of ^{11}C (20 min) does limit the clinical applicability of ^{11}C-labelled small molecules.

The need for an ATM inhibitor labelled with a radionuclide that correlates with the pharmacokinetics of the inhibitor itself led to this work to create the first ^{18}F-labelled ATM inhibitor, utilising fluorine-18 as a radioisotope with a longer decay half-life of 110 min. The compound was chosen from a series of ATM inhibitors reported by Baalam *et al.* that includes a number of highly potent and selective molecules containing fluorine moieties in

their structures.[147] Based on the structures and ATM inhibition data reported in this series (with regards to ease of synthesis, likelihood of ^{18}F-labelling, and ATM selectivity), we developed a synthetic route to access an ^{18}F-labelled ATM inhibitor, [^{18}F]**1** (Figure 2.1). Herein we report the synthesis of a nitro-precursor molecule **2** that is suitable for nucleophilic radiofluorination to afford [^{18}F]**1** and biological assessment of [^{18}F]**1** *in vitro* and *in vivo,* investigating its potential as an ATM PET imaging agent.



[^{18}F]**1**

Cellular IC_{50} by catalytic inhibition reported for [^{19}F]**1**	ATM	< 0.000453 µM
	ATR	> 30 µM
	PI3K	5.75 µM
	mTOR	> 5.19 µM

Figure 2.1 – Target compound [^{18}F]1 and reported inhibitory data

2.2 Methods

2.2.1 Chemical Synthesis

The synthesis of the non-radioactive ^{19}F version of compound **1** followed methods reported by patent,[147] with minor modifications (Figure 2.2). The synthesis of nitro-precursor **2** followed the same route as for [^{19}F]**1**. Full synthetic details are presented in chapter 5 (sections 5.2 and 5.3, page 116).

2.2.2 Radiosynthesis

Manual radiolabelling reactions were performed using aliquots of [^{18}F]fluoride (approx. 200 MBq) supplied by Alliance (UK) that were azeotropically dried with acetonitrile with addition of K_2CO_3 (1 mg) and K_{222} (5 mg) before the subsequent labelling reactions.

Automation of the radiosynthesis of [^{18}F]**1** was performed on an Eckert & Ziegler Modular-lab system. Briefly, [^{18}F]fluoride (5-10 GBq, supplied by the Positron Emission Tomography Imaging Centre (PETIC, Cardiff) or Alliance, UK) was trapped on a QMA carbonate cartridge (Waters, preconditioned with 2 mL deionised H_2O) and eluted to the reaction vessel with a solution of Kryptofix®222 (30 mg) and K_2CO_3 (6 mg) in H_2O (0.1 mL) and acetonitrile (0.9 mL), driven by vacuum. The [^{18}F]fluoride was azeotropically dried with three further additions of anhydrous acetonitrile (3 × 0.5 mL) at 120°C under vacuum and nitrogen air flow, before addition of precursor **2** (1 mg) in DMF (300 µL) and reaction at 120°C for 10 min. The reaction was allowed to cool to 35°C then diluted by addition of 0.1% formic acid in water (4.5 mL) before loading onto a Luna 10u C18(2) 100 Å 250 × 10 mm semi-preparative column. The product was eluted with 25% acetonitrile in 0.1% formic acid buffer (isocratic) at a flow rate of 3 mL/min. The product peak was redirected and diluted in a flask containing dH_2O (15 mL). The diluted product was then driven with nitrogen and trapped on a C18 light cartridge (Waters, preconditioned with 10 mL EtOH then 10 mL dH_2O). The C18 cartridge was washed with dH_2O (1 mL) before eluting to the final vial with ethanol absolute (1.5 mL) which was then dried at 100°C under vacuum until dry. The dried product was reformulated in a solution of 10% DMSO/0.9% saline (typically at 0.5-1 GBq/mL) and 20 µL sample used for quality control performed on a ThermoScientific

UltiMate™ 3000 system with a Luna Omega 5µm Polar C18 100 Å LC 250 × 4.6 mm analytical column, eluting with 25% acetonitrile in 0.1% formic acid buffer (isocratic) at a flow rate of 1 mL/min. A secondary sample (10 µL) was co-injected with a solution of reference [^{19}F]**1** to confirm product identity.

2.2.3 Cell Culture

H1299 non-small cell lung cancer cells, either wildtype, or stably transfected with short hairpin RNA for ATM (shATM) or GFP (shGFP, as a control) expression knockdown, were kindly gifted by Dr Anderson Ryan at the University of Oxford.[148] All cells were cultured at 37°C and 5% CO_2 in Dulbecco's Modified Eagle Medium (DMEM) supplemented with 10% Foetal Bovine Serum (FBS) (Gibco, USA), 2 mM L-glutamine, 100 units/mL penicillin and 100 µg/mL streptomycin (PSG) (Sigma Aldrich); knockdown cell lines were additionally supplemented with 0.5 µg/mL puromycin dihydrochloride (Merck Life Science, UK). Cells were originally purchased from ATCC, were authenticated by the provider and by STR profiling. Cells were tested regularly for the absence of mycoplasma contamination and were cultured for a maximum of 20 passages after resuscitation from liquid nitrogen storage.

2.2.4 Western Blot

Western blot analysis was performed to compare the total ATM expression between cell models, in addition to expression of phospho-ATM^{S1981} (pATM), phospho-KAP1^{S824} (pKAP1),

and phospho-CHK2^{T68} (pCHK2) expression to assess the effect of irradiation and ATM inhibition on ATM catalytic activity. Cells were irradiated (4 Gy; 0.75 Gy/min) or sham-irradiated and incubated at 37°C for one hour before harvesting cells for lysis and blotting. Where required, inhibitors were added to cells at the stated concentration from DMSO stock solutions (reaching no greater than 10% DMSO final concentration) with incubation for one hour prior to irradiation/sham-irradiation.

After exposure to the required chemicals, cell culture medium was removed and cells were washed once with ice cold phosphate buffered saline (PBS). Cells were then lysed in radioimmunoprecipitation assay (RIPA) buffer (50 mM Tris-HCl, 150 mM NaCl, 1% NP-40, 0.5% sodium deoxycholate, and 0.1% sodium dodecyl sulfate, in dH_2O, pH 8) containing protease inhibitor (cOmplete EDTA-free, Roche) and phosphatase inhibitor (PhosStop, Roche) and collected by scraping. Lysates were kept on ice with agitation for 20 min then centrifuged at 20,000 rcf, 4°C for 20 minutes and supernatant (lysate) isolated.

Before lysis, frozen xenografts were weighed and supplemented RIPA buffer added (20 µL/mg sample) immediately following thaw. Tissue was mechanically broken up using a scalpel and by passing through 19G and 21G needles. The lysates were agitated via vortex and sonicated (3 × 10 s) periodically while keeping on ice for 20 min before being centrifuged at 20,000 rcf, 4°C for 20 minutes and supernatant (lysate) isolated.

Lysates were normalised against BSA standards via BCA assay before reduction and denaturation in NuPage LDS sample buffer (Invitrogen) containing DTT at 100 mM final concentration for 10 min at 70°C. Samples were run at ~30 mg per well on NuPage® 3-8%

Tris-Acetate gel in Tris-acetate Running Buffer (both Novex) at 150 V. Gels were blotted onto PVDF membranes using the iBlot2 system (Invitrogen) (20 V for 1 min, 23 V for 3 min, 25 V for 5 min) and recovered into tris-buffered saline (TBS, Santa Cruiz).

Blots were then probed with a variety of antibodies using the following sequence: Blots were blocked for one hour at room temperature in 5% milk/TBST (TBS with 0.1% Tween-20) solution, then submerged in a solution of primary antibody at the required dilution in block solution and incubated at 4°C overnight. Blots were then washed 3 × 15 min in TBST. If required, blots were then incubated for one hour at room temperature in a solution of HRP-conjugated secondary antibody in block solution, then washed 3 × 15 min in TBST. Blots were rinsed in TBS, then incubated at room temperature using a SuperSignal™ West Pico PLUS chemiluminescence kit (Thermo Scientific) for 5 min before imaging on a Li-Cor C-DiGit Blot Scanner. After imaging, blots were recovered in TBS and washed 3 × 15 min in TBST before blocking, repeating the same sequence with additional primary antibodies. Separate identical blots were used to probe for phosphorylated proteins and their total protein counterparts, with protein standards stained for on each blot to compare loading. Blots were cut along ~170 kDa to separate ATM bands, allowing for separate, simultaneous staining.

The following antibodies and dilutions were used in this work: Phospho-ATM S1981 (ab81292, 1:5000, Abcam); phospho-KAP1 S824 (ab133440, 1:10,000, Abcam); phospho-CHK2 T68 (#2661, 1:1000, Cell Signalling Technologies); Total ATM (ab32420, clone [Y170], 1:500, Abcam); Total KAP1 (ab10483, 1:1000, Abcam); Total CHK2 (05-649, 1:1000, Merck Millipore); HRP-conjugated Tubulin (ab197740, clone [YL1/2], 1:4000, Abcam); HRP-

conjugated β-Actin (clone 13E5, 1:1000, Cell Signalling Technologies), HRP-conjugated anti-rabbit secondary (HAF008, 1:1000, R&D Systems); HRP-conjugated anti-mouse secondary (HAF007, 1:1000, R&D Systems). All blots were repeated on at least two separate occasions with new cell lysates for validation.

2.2.5 Uptake, retention, and blocking assays

To assess cellular uptake of [^{18}F]**1**, aliquots of H1299 shATM or shGFP cells were plated with 1×10^5 cells per well in 24-well plates in 500 µL complete growth medium and incubated overnight to allow cells to adhere. Cell culture medium was removed, cells washed with PBS and media replaced with DMEM (no additives). Cells were irradiated (4 Gy; 0.75 Gy/min) or sham-irradiated and incubated for one hour before addition of [^{18}F]**1**, followed by incubation at 37°C and 5% CO_2 for the indicated time. Supernatant cell culture medium was collected, and cells were washed twice with PBS, after which they were lysed with 0.1 M sodium hydroxide (200 µL) for 30 min. The amount of ^{18}F-activity associated with each fraction was determined using a Wizard2 Automatic Gamma Counter (PerkinElmer).

Retention assays followed the same procedure with a one hour incubation of cell with [^{18}F]**1**, but after culture medium was aspirated and cells washed with PBS (2 × 500 µL), it was replaced (500 µL DMEM) and cells incubated at 37°C and 5% CO_2 for the desired time. The amount of ^{18}F-activity retained in cells was then determined as above.

Blocking studies followed the same procedure as uptake with one hour tracer incubation, however the replacement media contained the blocking agent at the indicated

concentrations in no greater than 10% DMSO, and a DMSO control was also run in parallel at the highest DMSO concentration used, followed by incubation at 37°C and 5% CO_2 for one hour before irradiation.

2.2.6 *In vivo* mouse models

All animal procedures were performed in accordance with the UK Animals (Scientific Procedures) Act 1986 and with local ethical committee approval. Mice were bred from parent C57BL/6J mice heterozygous for a targeted mutation in the $ATM^{tm1Awbl}$ allele to produce ATM-null ($ATM^{-/-}$) mice (Jackson laboratory). Wild type mice ($ATM^{+/+}$) from this breeding program were used as controls. In a separate study, tumour xenografts were created in BALB/c *nu/nu* mice (8-weeks old) via subcutaneous injection of H1299 wildtype, shATM knockdown, or shGFP knockdown cells in a 1:1 PBS/Matrigel® formulation on both sides of the hind flank. Total tumour volumes were allowed to reach an average of 600 mm^3 (range 330-930 mm^3) before imaging and/or biodistribution studies (approx. 6-10 weeks after inoculation).

2.2.7 PET/CT imaging

Animals were anaesthetised by 4% isoflurane gas (0.5 L/min O_2) and maintained at approx. 2% and 37°C throughout the imaging session. C57BL/6 $ATM^{+/+}$ and $ATM^{-/-}$ mice were administered [^{18}F]**1** (83 ng; 0.5-4.6 MBq, molar activity range of 3.2-24.2 GBq/µmol with a standard deviation of 6.5 GBq/µmol)) via intravenous bolus injection in the lateral tail vein.

Xenograft bearing BALB/c *nu/nu* mice were administered [^{18}F]**1** (0.5 µg; 0.7-9.6 MBq, molar activity range of 0.62-9.8 GBq/µmol with a standard deviation of 3.0 GBq/µmol) via intravenous bolus injection to the lateral tail vein. PET/CT scanning was completed using a VECTor4CT scanner (MILabs, Utrecht, the Netherlands) for one hour and was immediately followed by culling, dissection and gamma counting of selected organs. Reconstruction of both CT and PET images was performed with the MILabs reconstruction analysis using a γ-ray energy window of 467–571 keV (background weight 2.5 %), 0.8 mm^3 voxel size, 8 subsets and 5 iterations using the manufacturer's SROSEM reconstruction type. PET images were each registered to CT, attenuation corrected, calibrated by imaging a phantom containing a fluorine-18 standard solution, and analysed using PMod software package (Version 3.807, PMOD Technologies).

2.2.8 Autoradiography and microscopy

After PET/CT imaging, tumour tissue was immediately flash frozen in liquid nitrogen and mounted in OCT before producing 10 µm thick sections for digital autoradiography analysis. The same sections were analysed by H&E staining to identify tumour heterogeneity: Frozen tissue section slides were allowed to air dry for 10 min at room temperature before washing in PBS (2 × 3 min) to remove any residual OCT. Slides were then submerged in 4% formaldehyde in PBS for 10 min to fix. Slides were washed in deionised water (3 × 2 min) before submerging in 0.1% Mayers Haematoxylin Solution (Sigma Aldrich) for 8 min at room temperature. Slides were then rinsed in cool running tap water for 6 min followed by rinsing in deionised water (2 × 2 min). Slides were dipped in Eosin Y-Solution 0.5% alcoholic (Merck)

for 3.5 min then washed in distilled water for 2 min. Slides were dehydrated by dipping in ethanol solutions (70%, 90%, then 100%, 30 sec each) and cleared in xylene (30 sec) before mount and coverslip with DPX. Mounted slides were allowed to dry overnight before imaging at 20x on a Leica Aperio slide scanner.

2.2.9 Statistical Analysis

Statistical analysis was performed using GraphPad Prism v9 (GraphPad Software, San Diego, CA, USA). In each case, a 1-way or 2-way ANOVA was performed with multiple comparisons using Šidák's or Tukey's test, with significance denoted as * $p<0.05$, ** $p<0.01$, *** $p<0.001$, **** $p<0.0001$, or ns $p>0.05$.

2.3 Results

2.3.1 Chemical synthesis

The synthesis of reference compound [^{19}F]**1** was completed with an overall yield of 10% over 12 steps. Nitro-precursor **2** was prepared with a yield of 12% over 12 steps (Figure 2.2).

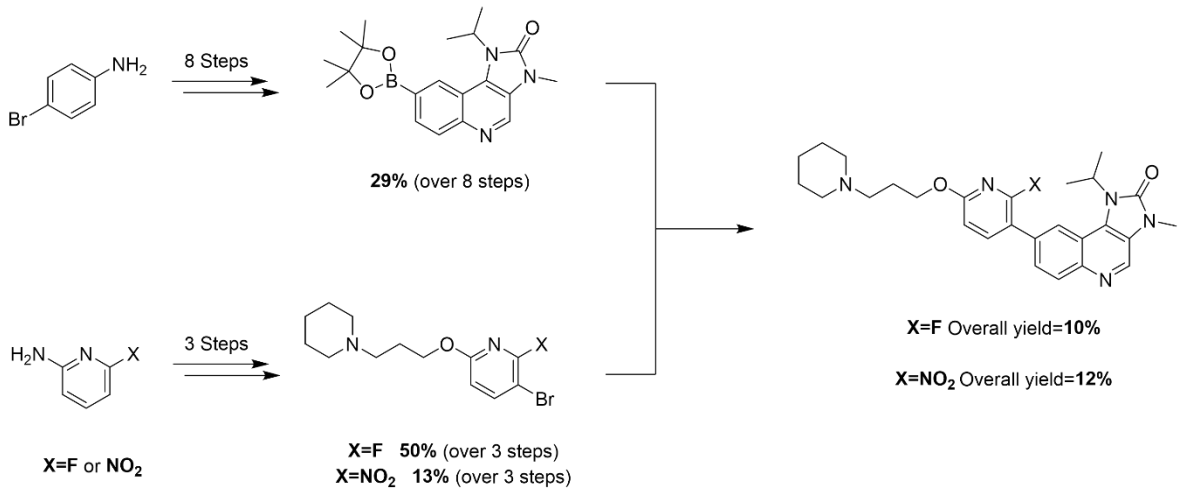


Figure 2.2 – Synthetic pathway for reference [^{19}F]1 and nitro-precursor 2

The synthesis of the ^{19}F-reference compound was changed marginally compared to the patent reported synthesis: the Suzuki coupling pair was reversed, and slight changes were made to the addition of the alkoxy group to the pyridine moiety. The Suzuki pair reversal was considered because while we were having difficulties accessing the nitro-pyridine core for the precursor, borylation of the quinoline core was investigated in parallel and was successful with 82% yield and clean product isolated without the need for column chromatography (which is known to sometimes cause degradation of boronic esters). This reduced the number of synthetic steps required for the already challenging pyridine core. The addition of the 3-(piperidin-1-yl)propyl alkyl chain to both reference and precursor pyridine cores was also performed before the final Suzuki coupling using less harsh basic conditions by simple S_N2 substitution from the 3-bromo-6-hydroxypyridine with 1-(3-chloropropyl)piperidine, as opposed to the patent reported final step fluoride S_NAr substitution with 3-(piperidin-1-yl)propan-1-ol and sodium hydride.

The choice to synthesise a nitro-precursor, **2**, was decided given the activated *ortho*-position in the pyridyl moiety of the compound, predicted to be easily substituted by ^{18}F-fluoride via nucleophilic aromatic substitution (S_NAr) during radiolabelling, with many reports of similar successful radiofluorinations of this moiety.[149-152] Alternative precursor leaving groups considered included a trimethyl ammonium salt or halide (chloro, bromo, and iodo), however radiofluorination from halides is generally less robust, with lower radiochemical yields, and synthesis of a trimethyl ammonium salt was initially thought to be more complex than of a nitro-precursor.

The initial synthetic route devised for the nitro-pyridine core involved coupling of a completed pyridine triflate core containing the piperidyl moiety to the boronic ester quinoline core (Figure 2.3). However, many conditions and reaction routes for nitration, alkylation, and triflation of 6-fluoro-3-hydroxypyridine starting material were trialled, yet yields were too low with no successful scalable synthesis of the final core (Figure 2.4).

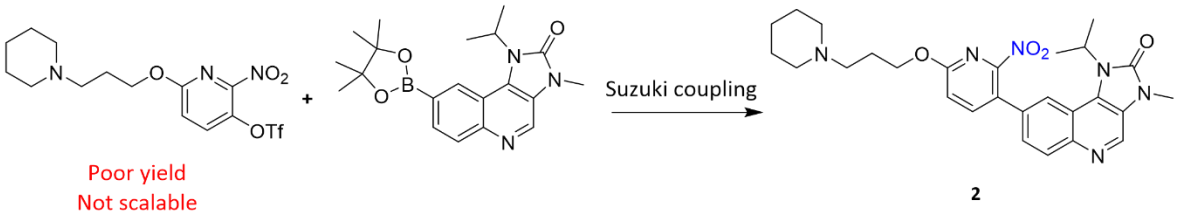


Figure 2.3 – Initial synthetic plan with completed pyridine triflate core

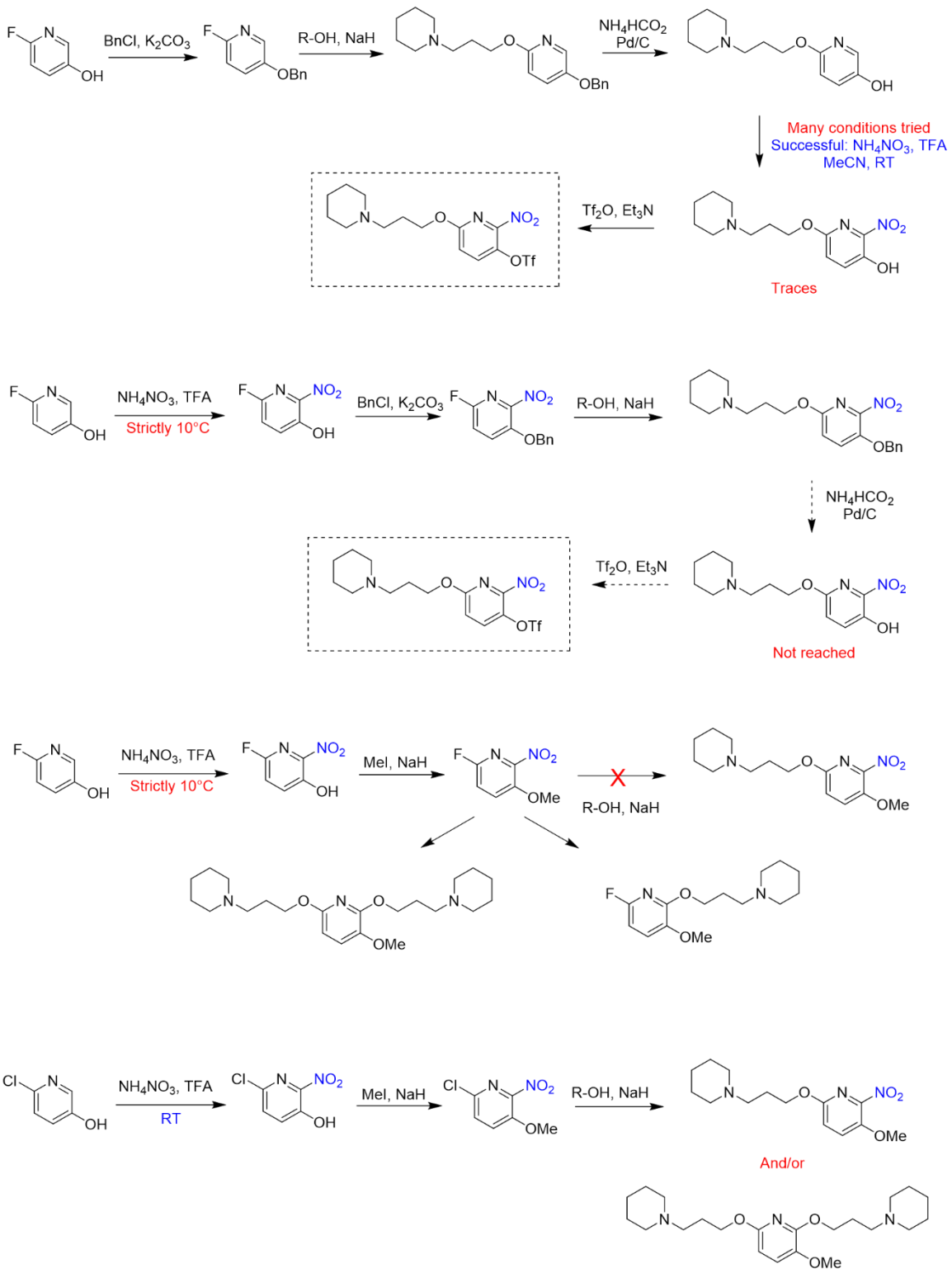


Figure 2.4 – Trialled methods towards a 2-nitro-6-(3-(piperidin-1-yl)propoxy)pyridin-3-yl trifluoromethanesulfonate Suzuki coupling partner

An alternative route to the final precursor was trialled in parallel, with the piperidyl alkyl chain aromatic substitution performed as the final step after Suzuki coupling of 6-fluoro-2-nitropyridin-3-yl trifluoromethanesulfonate with the boronic ester quinoline core, more closely following the patent reported synthesis (Figure 2.5). Unfortunately, this gave rise to a doubly substituted pyridine core through substitution of first the nitro-group followed by the fluoro-group, even under mild conditions. The reason for this is unknown and not reported in literature, however, we hypothesise that this unexpected regioselectivity is likely due to the specific electronics of this pyridine core, and/or geometry of the nitro-group if positioned orthogonally to the ring, potentially reducing C-NO_2 bond strength and increasing leaving group ability.

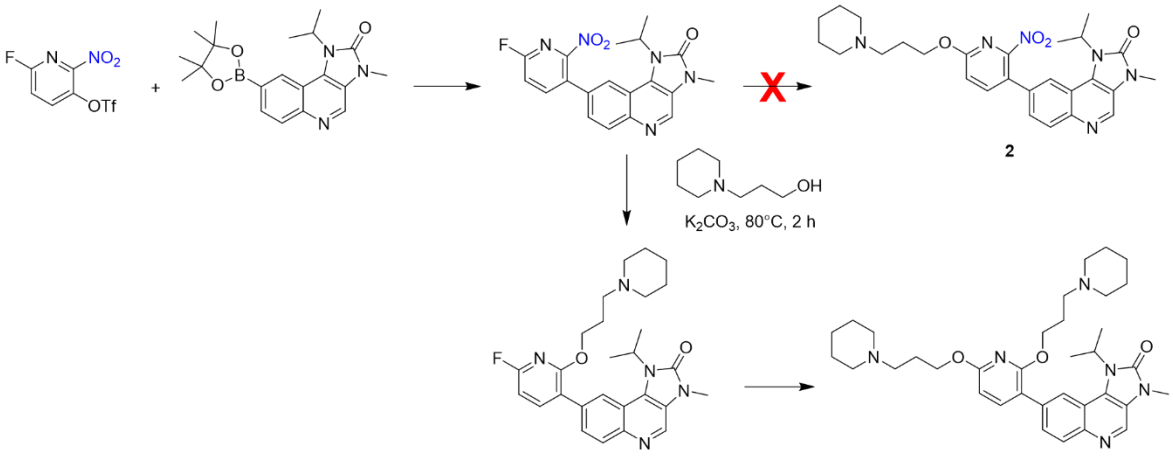


Figure 2.5 – Late-stage pyridine alkylation gives rise to substitution of both fluoro- and nitro-groups

Following attempts of these syntheses, we found that the reagent 2-amino-6-nitropyridine had become commercially available and had discovered the method reported by AstraZeneca for the preferential bromination in the 5-position of this substrate.[153] Fortunately, we were able to repeat this method, allowing successful completion of our nitro-pyridine core and final Suzuki coupling to yield our full nitro-precursor molecule **2**.

2.3.2 Radiochemistry

Reaction condition screening during manual radiofluorination of precursor **2** revealed the best radiochemical conversion was obtained in DMF at 120°C for 10 min. The automated radiosynthesis of [^{18}F]**1**, performed on an Eckert & Ziegler Modular-Lab, was completed in 80 ± 13 min with a radiochemical yield of 20 ± 13% (decay-corrected), radiochemical purity >99% and molar activity up to 79.5 GBq/µmol (n=11) (Figure 2.6-Figure 2.9).

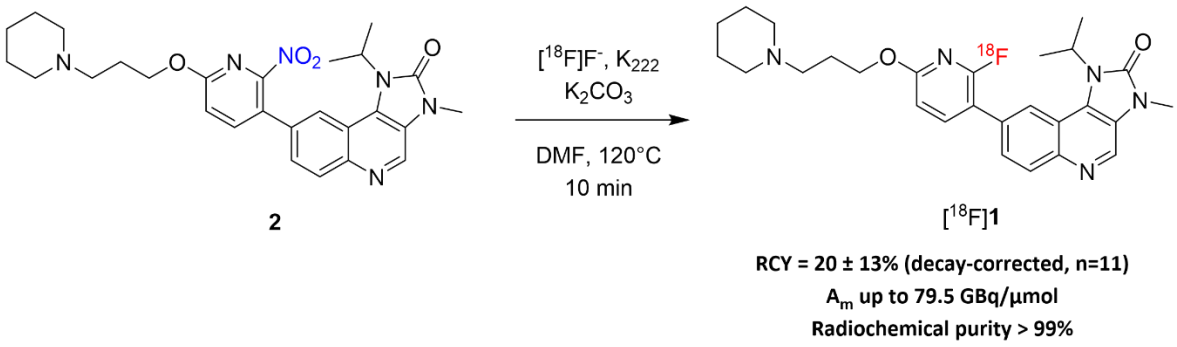


Figure 2.6 – Radiosynthesis of [^{18}F]1 from 2

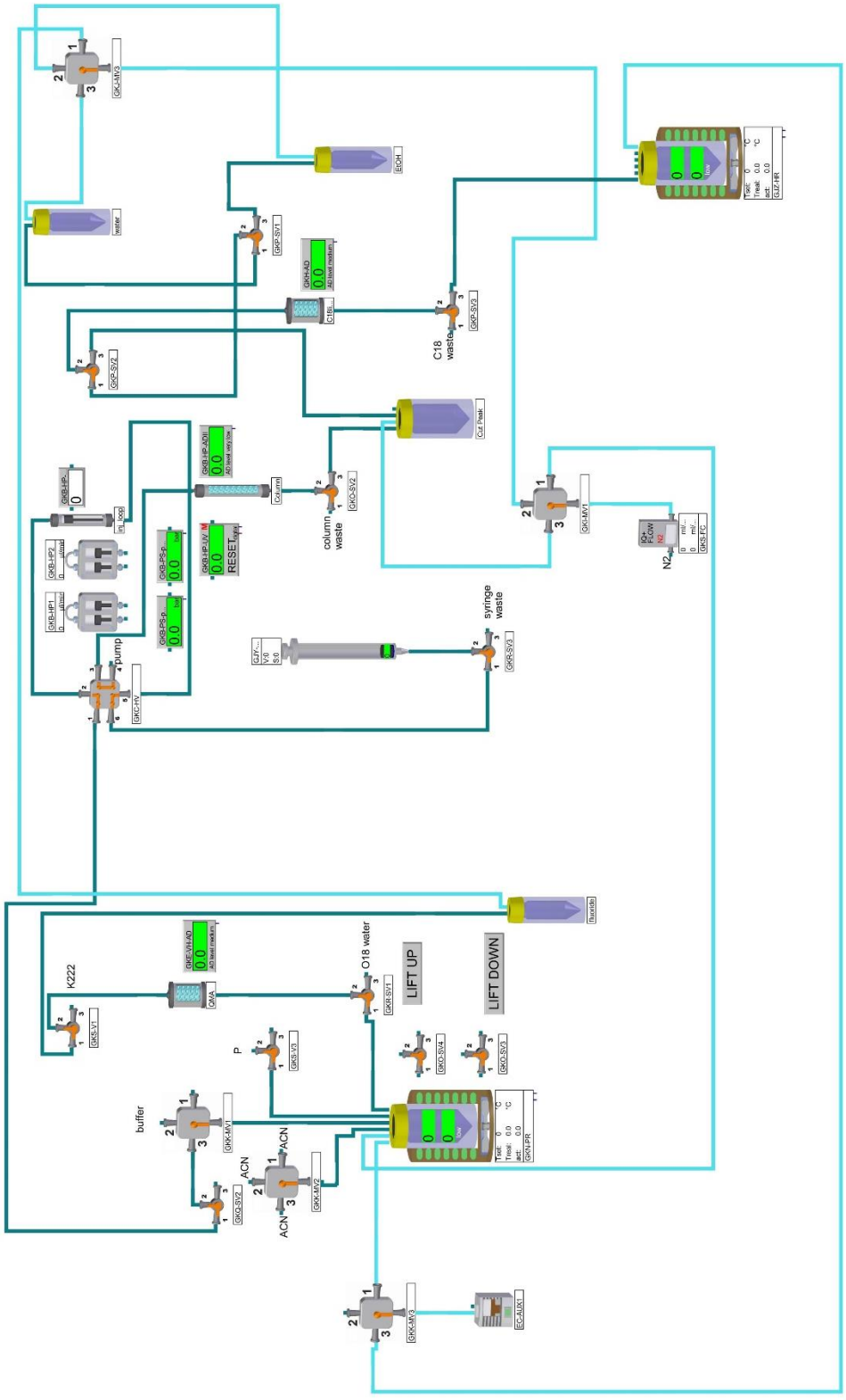


Figure 2.7 – Eckert & Ziegler Modular-Lab schematic for automated radiosynthesis of [^{18}F]1.

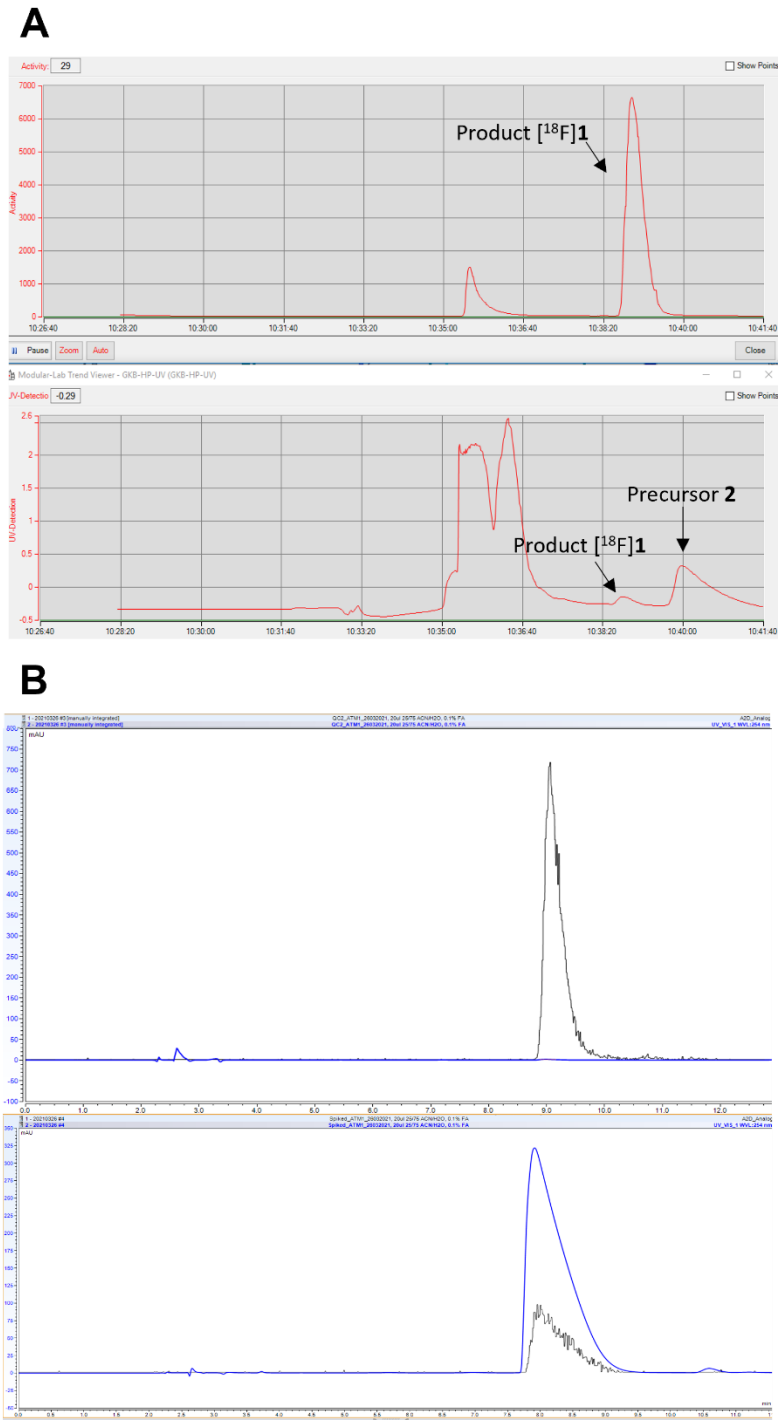


Figure 2.8 – (A) Example semi-preparatory trace of [^{18}F]1 (radio trace top, UV trace (220 nm) bottom). (B) Example quality control trace of [^{18}F]1. Top trace shows reformulated [^{18}F]1, bottom trace shows co-injection of reformulated [^{18}F]1 with reference [^{19}F]1. Radio trace in black, UV trace (254 nm) in blue.

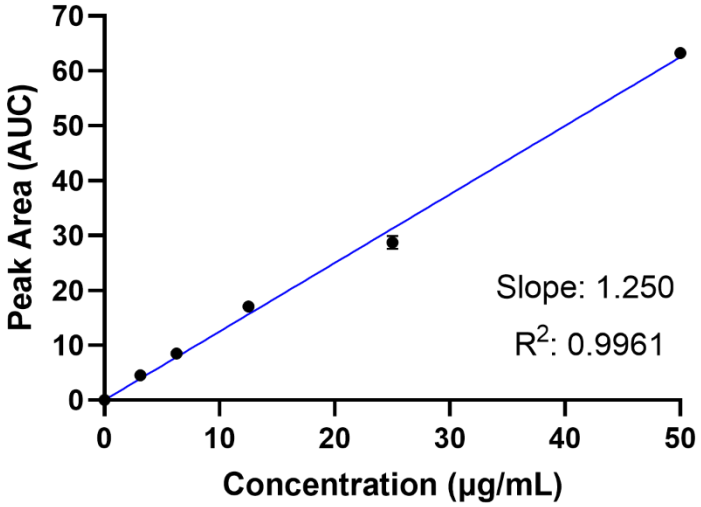


Figure 2.9 – Calibration curve used for molar activity calculation of [^{18}F]1 (error bars too small to be presented).

2.3.3 Model characterisation

Western blot analysis confirmed a reduced total-ATM expression in the shATM knockdown H1299 cells compared to the shGFP knockdown H1299 cells, and reduced phospho-ATM^{S1981} (pATM) expression in irradiated shATM cells compared to irradiated shGFP cells. In irradiated shGFP knockdown cells, ATM inhibition with known ATM inhibitors AZD1390, [^{19}F]**1**, AZD0156, KU60019, as well as precursor **2**, were confirmed by a decrease in pATM expression, as well as expression of downstream targets of pATM, pKAP1 and pCHK2, relative to a DMSO control (Figure 2.10).

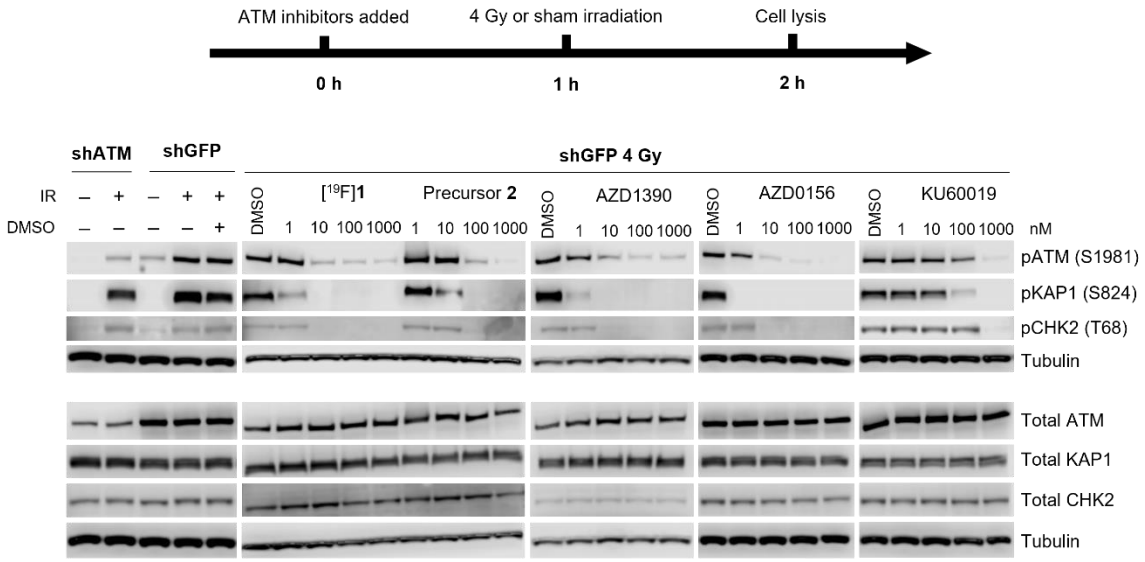


***Figure 2.10* – Higher ATM expression is observed in H1299 shGFP knockdown cells compared to H1299 shATM knockdowns. Irradiation of cells (4 Gy) causes an increased expression of pATM, pKAP1, and pCHK2. A decrease in expression of pATM and downstream targets pKAP1 and pCHK2 is observed following treatment of shGFP (4 Gy) cells with different ATM inhibitors.**

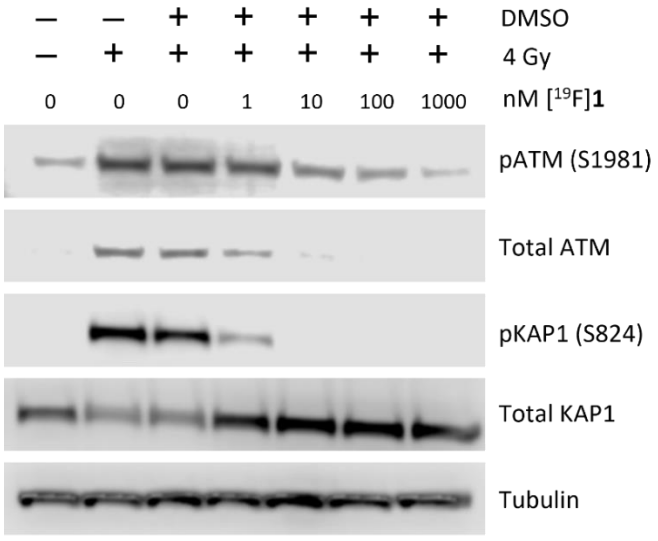


Figure 2.11 – ATM inhibition with [19F]1 in CT26 murine colorectal cancer cells, total ATM Abcam antibody replaced with GTX70107, 1:500 (GeneTex).

Additionally, a comparison of murine ATM inhibition by [^{19}F]**1** was needed to validate the usefulness of ATM-null vs wildtype mouse models for *in vivo* imaging. Although murine ATM is different to human ATM,[38] it retains much of the same structure and many of the same phosphorylation sites. We were able to demonstrate murine pATM inhibition by **1** in CT26 murine colorectal cancer cells (and reduction of downstream target pKAP1) using western blot, indicating binding of **1** to murine ATM (Figure 2.11). Surprisingly this blot shows an apparent change in total ATM expression with response to inhibition by [^{19}F]**1**. However, this is likely to be caused by a technical error in stripping the pATM antibody from the blot before staining for total ATM and a poor staining efficiency of the total ATM antibody leading to observation of a carry-over of pATM signal and little to no total ATM signal.

2.3.4 *In vitro* assessment of [^{18}F]1

Uptake of [^{18}F]**1** in cells showed an increase in cell associated activity over one hour followed by a plateau. Retention of [^{18}F]**1** in the same cells revealed a gradual decrease in cell associated activity of approximately 50% over two hours. No significant differences between cell associated activity were observed between the different cell lines/irradiation conditions. Nonetheless, significant blocking was observed with increasing concentrations of the ATM inhibitor KU60019, demonstrating some specific binding of [^{18}F]**1** to ATM and revealing high levels of non-specific uptake. Surprisingly, addition of some known ATM inhibitors AZD1390, AZD0156, or [^{19}F]**1** resulted in an initial blocking effect at lower concentrations of the inhibitor (0.1-10 nM), but an increase in cell-associated activity at higher concentrations (Figure 2.12).

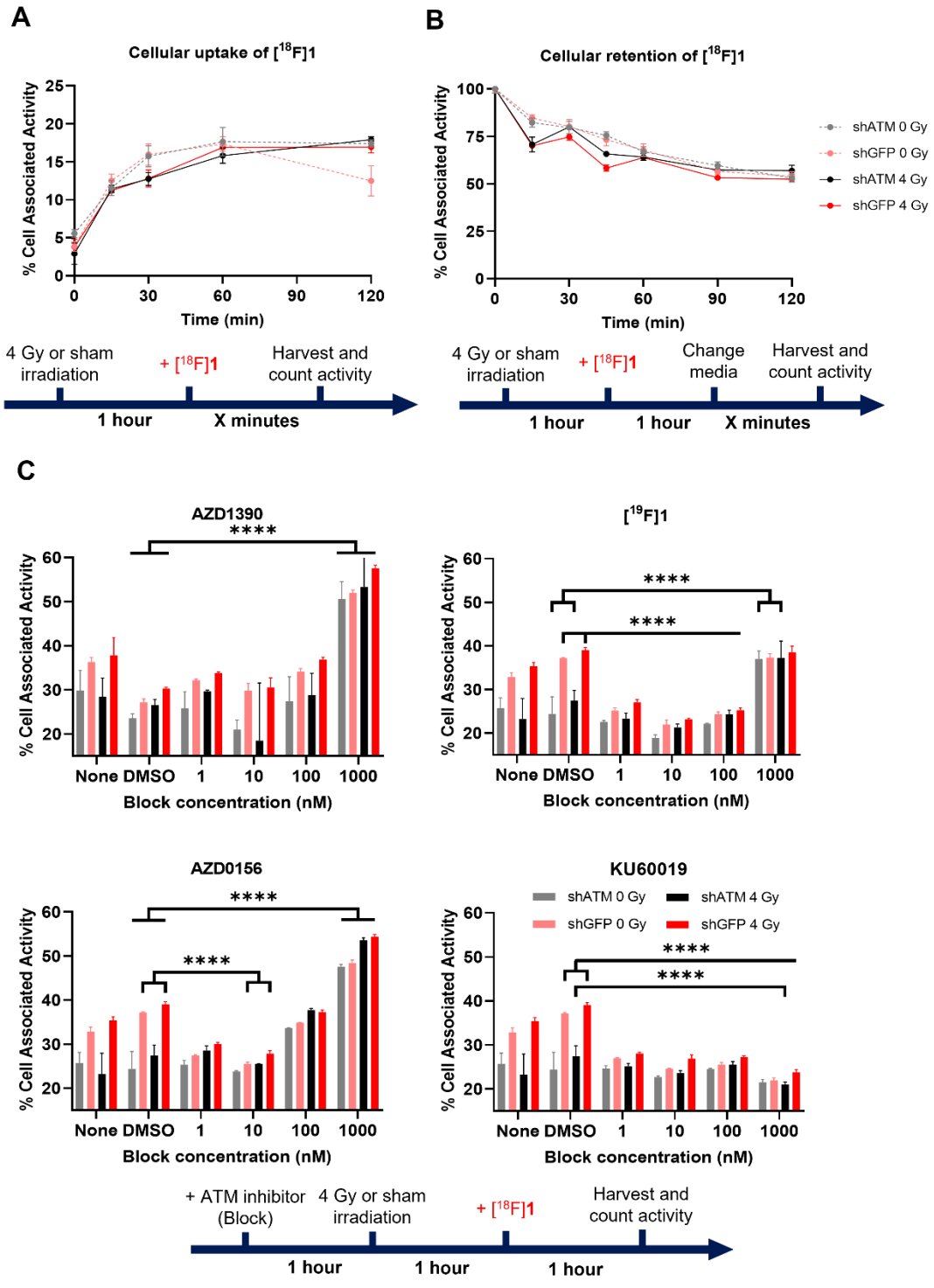


Figure 2.12 – (A) Cell uptake and (B) retention of [^{18}F]1 in H1299 shATM and shGFP cells. (C) Cell-associated activity in H1299 shATM and shGFP cells after pre-treatment with a range of ATM inhibitors (block)

2.3.5 *In vivo* assessment of [^{18}F]1

PET/CT imaging and *ex vivo* biodistribution of [^{18}F]**1** in wildtype and ATM-null C57BL/6 mice one hour after intravenous administration revealed hepatobiliary clearance (Figure 2.13). Significant differences in uptake between the two mice were only observed in the kidneys and liver. Challenges due to [^{18}F]**1** adhering to the walls of long canula lines during intravenous injection meant that short canula lines were necessary to administer the dose, resulting in a delayed start of dynamic PET imaging (starting approx. 10 minutes after injection of the tracer) by which point tissue activity concentrations remained near constant, preventing pharmacokinetic analysis.

Biodistribution of [^{18}F]**1** in BALB/c *nu/nu* mice was comparable to C57BL/6 mice. Uptake in H1299 tumour xenografts was measured as 0.38 ± 0.12%ID/g (wildtype), 0.35 ± 0.14%ID/g (shGFP), and 0.35 ± 0.10%ID/g (shATM) (Figure 2.14). No significant differences were observed in tumour uptake between the different tumour types, reflecting our *in vitro* results, despite confirmation of xenograft ATM knockdown status by *ex vivo* western blot (Figure 2.15).

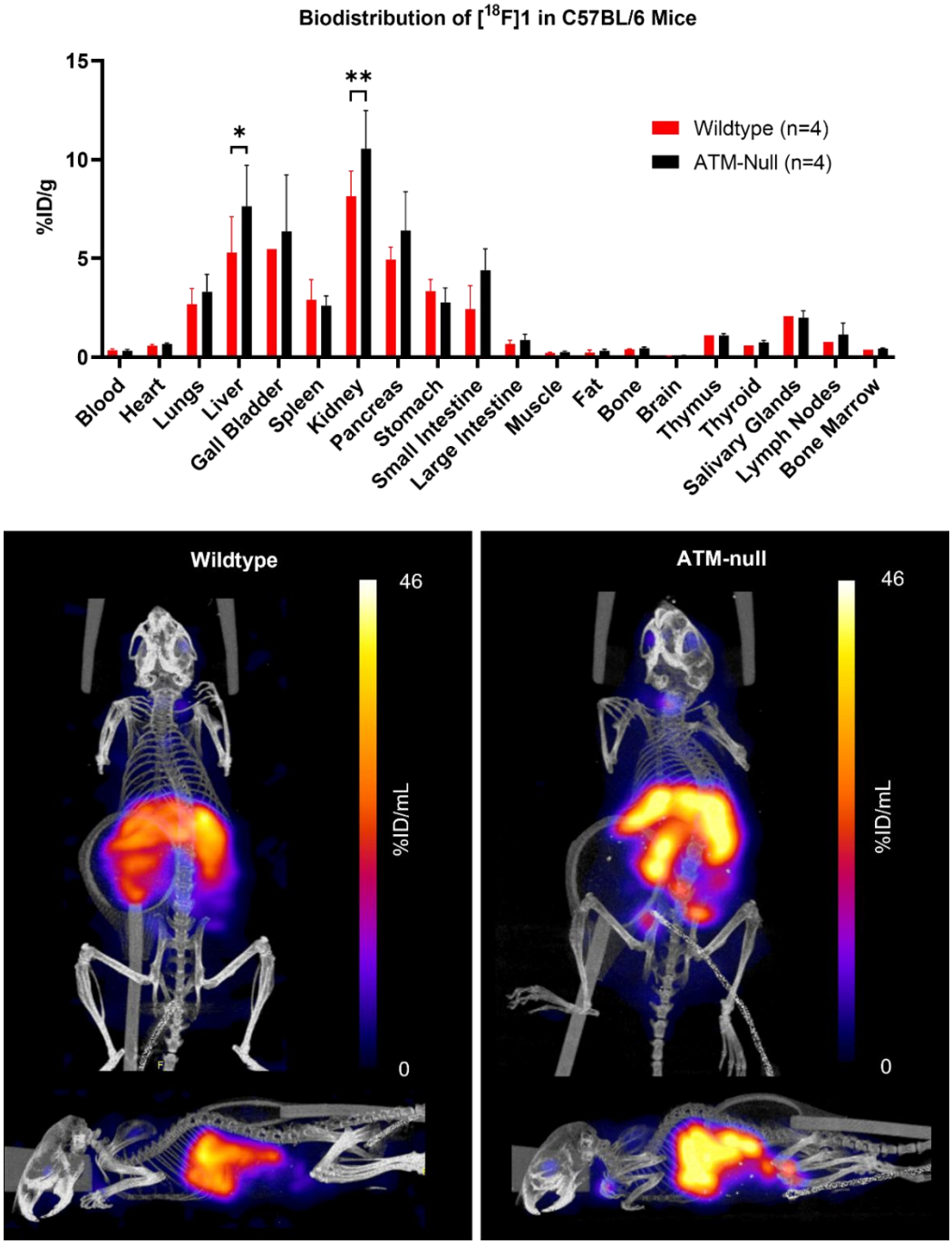


Figure 2.13 – Biodistribution of [^{18}F]1 in C57BL/6 ATM wild type and ATM-knockout mice, 1 h after intravenous administration. Below are shown representative PET/CT MIP images demonstrating the hepatobiliary uptake of tracer in both wild type and ATM-null mice.

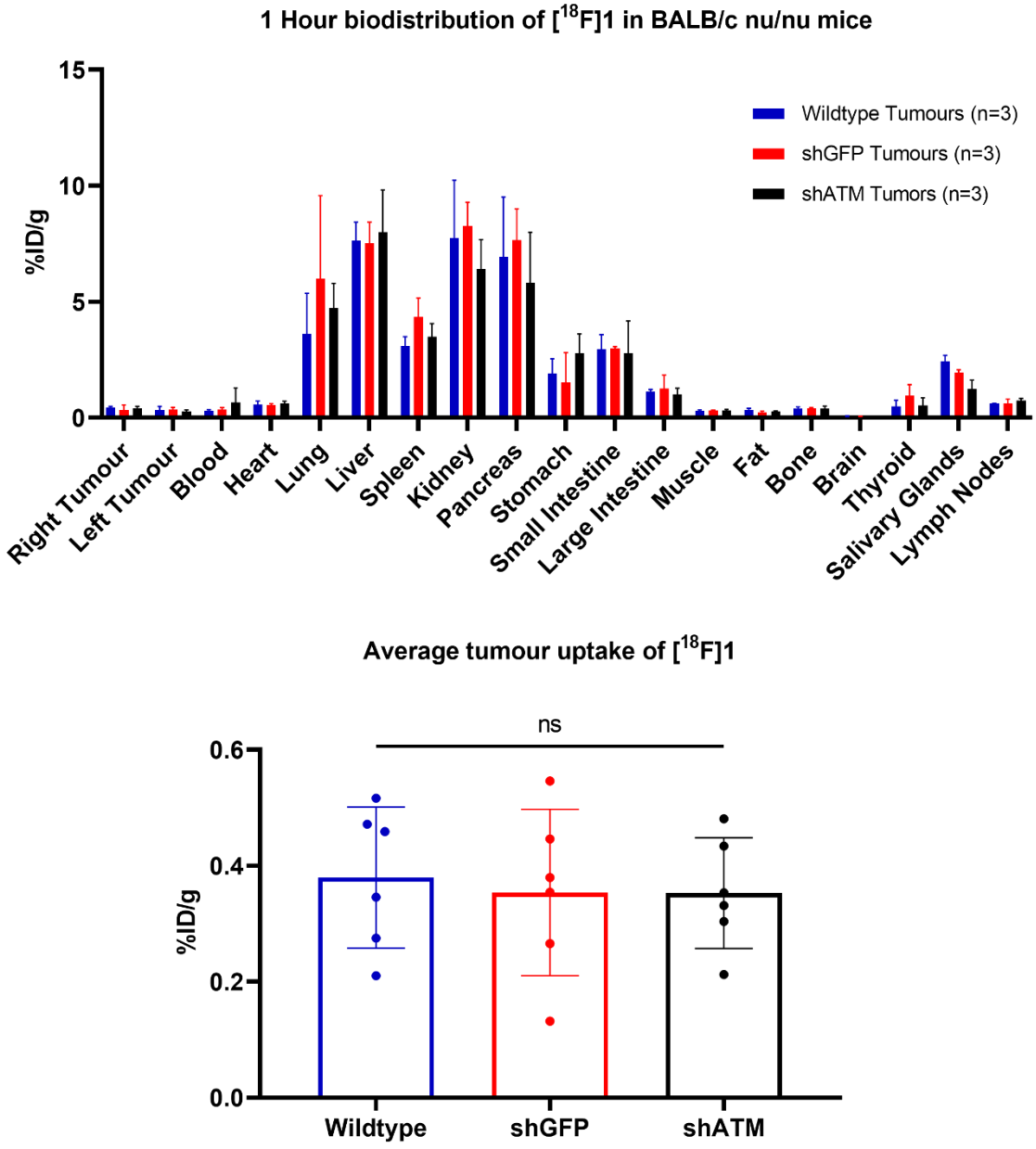


Figure 2.14 – In vivo **biodistribution of [^{18}F]1 in BALB/c nu/nu mice bearing subcutaneous H1299 wildtype, shATM, or shGFP xenografts.**

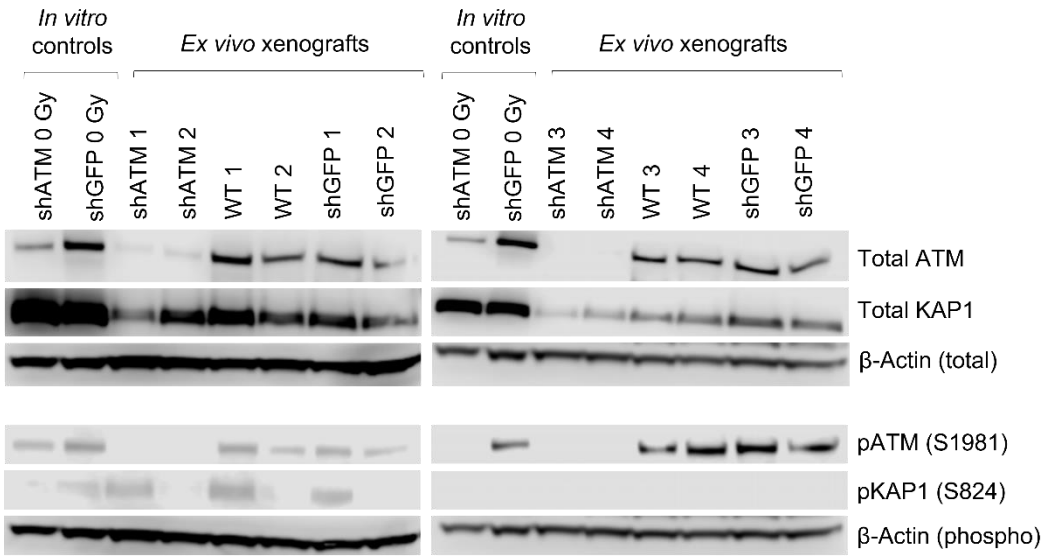


Figure 2.15 – Representative western blot of ex vivo xenograft samples.

Autoradiography of tumour sections revealed heterogeneous uptake across the xenografts that was not specific to tumour type. H&E staining of the same tumour sections revealed regions of tissue lacking nuclei (possibly suggesting necrosis) that matched autoradiography low signal regions of the tumour, indicating uptake of the tracer only in viable cells (Figure 2.16). The few tumours revealed to have necrotic centres did not have significantly different uptake (%ID/g) compared to the more viable tumours. Autoradiography analysis of viable cell regions (i.e. excluding areas of necrosis) revealed no significance in %ID/cm^2 between xenograft type (Figure 2.17).

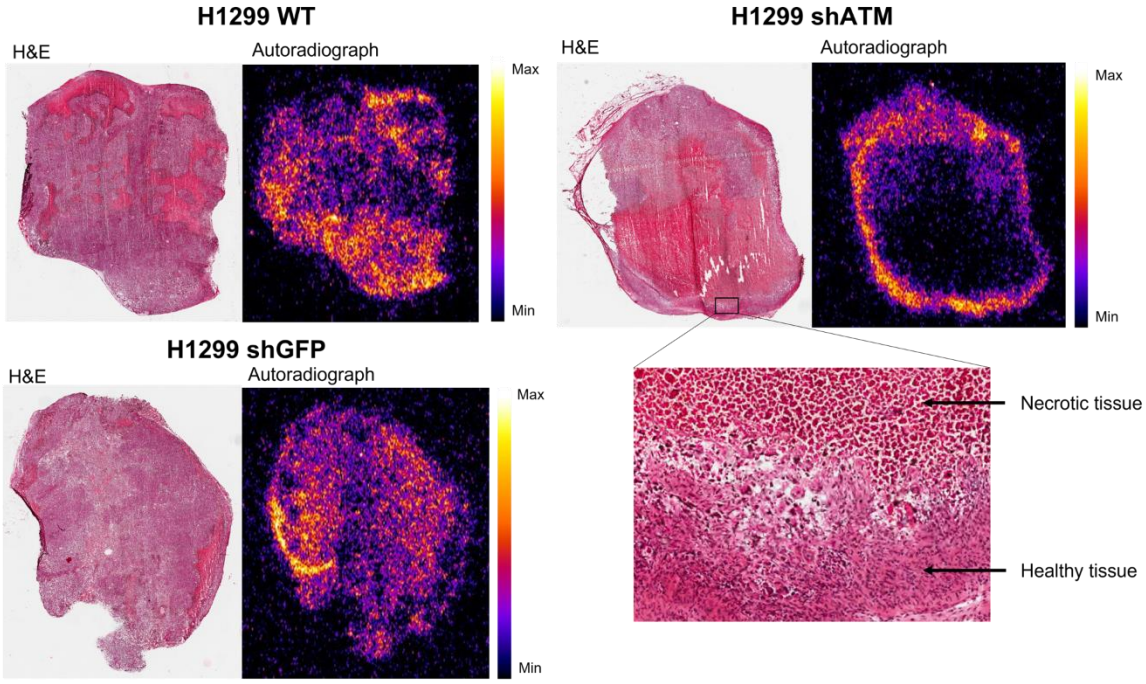


Figure 2.16 – Autoradiography and H&E staining of xenograft sections (10 µm).

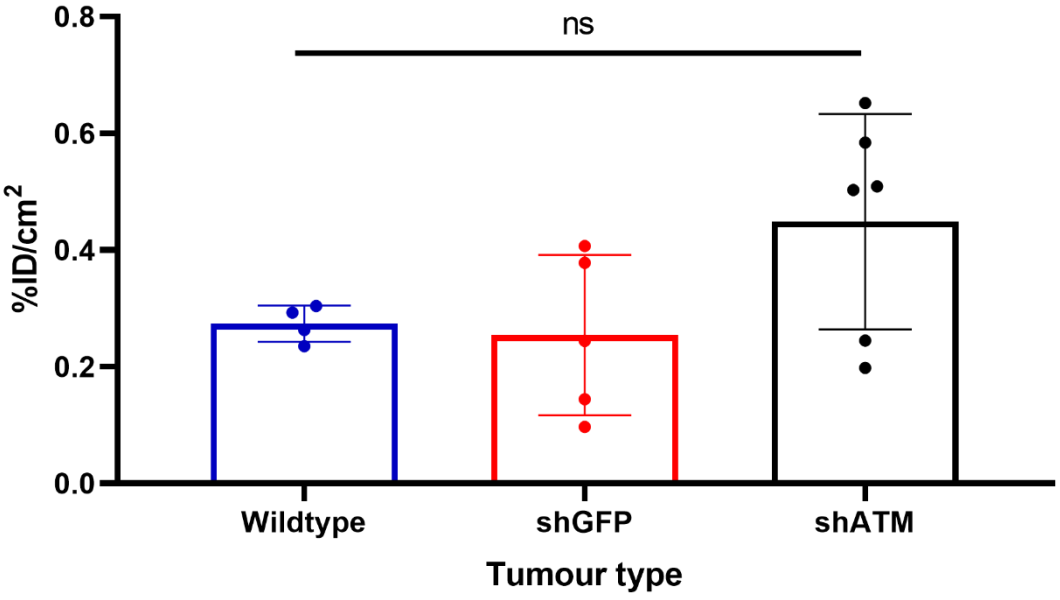


Figure 2.17 – Autoradiography signal analysis of ex vivo tumour sections.

2.4 Discussion

2.4.1 General discussion

ATM inhibitors are an up-and-coming treatment for cancer. While there are four inhibitors currently undergoing human trials (Table 1, page 13), none are currently approved for clinical use. A host of preclinical studies have demonstrated the potential of these inhibitors for cancer treatment, most in combination with other DNA damaging therapies.[25,70] However, many drugs fail to reach or progress through this vital stage of drug development due to lack of understanding of the drug efficacy. Studying the pharmacokinetics of experimental drugs provides vital information that can aid the transition into clinical evaluation. Drug pharmacokinetics are generally measured through the sampling of blood, urine, and tissue biopsies over time, which can be invasive and cannot reveal drug biodistribution across the whole body or in heterogeneous tissues, or indeed the tumour target distribution.

The use of nuclear imaging can provide a clearer picture of drug pharmacokinetics across the whole body non-invasively with the use of radiolabelled drug analogues.[146] This technique can assist in designing treatment plans for patients (e.g. calculating drug dosage) but can also assist the clinical development of novel drugs. A radiolabelled ATM inhibitor promises to visualise and quantify drug distribution, while also having the potential to give insight into ATM tissue distribution. The previously reported [^{11}C]AZD1390 has shown in clinical studies how radiopharmaceuticals can aid these measurements, however the short half-life of ^{11}C reduces the scope of using ^{11}C-labelled drug variants due to the requirement of on-site cyclotrons in hospitals. Where the radiochemistry is available and able to target

binding properties, the use of ^{18}F-radiotracers can overcome this issue. Hence, we radiofluorinated potent ATM inhibitor **1**, as a tool to investigate ATM PET imaging.

Our *in vitro* model system demonstrated the ability of **1** to inhibit ATM activity through inhibition of ATM Serine-1981 phosphorylation and the phosphorylation of its downstream targets of ATM, KAP1 and CHK2. This showed **1** to have ATM inhibitory properties comparable to other ATM inhibitors such as AZD1390, AZD0156, and KU60019, confirming its reported sub-nM IC_{50} value of ATM inhibition.[147] This data indicates that **1** binds to and inhibits ATM in live cells and reinforces the proposal that [^{18}F]**1** could be used to image ATM.

While some specific binding to ATM of [^{18}F]**1** was observed, as evident from statistically significant reductions of cell associated activity after exposure to an excess of the ATM inhibitor KU60019 ($P<0.0001$), high levels of non-ATM specific cell association were also revealed. This relatively low level of ATM specific uptake relative to the non-specific uptake is likely due to the innately low cellular expression of ATM[30-32] which may lead to only slight observable changes in [^{18}F]**1** uptake, in addition to the highly lipophilic nature of the inhibitor which aides passive transport of the compound into the cell. This low ratio of specific to non-specific binding may be masking any differences in uptake that are expected between cell lines with highly varying ATM expression levels, as well as the effects of irradiation (and therefore increased expression of active, phosphorylated ATM) on the uptake of [^{18}F]**1**. This result demonstrates the limits of [^{18}F]**1** for mechanistic studies of ATM.

Surprisingly, blocking [^{18}F]**1** uptake with high molar excess (1000 nM) of the ATM inhibitors AZD1390, AZD0156, or [^{19}F]**1** resulted in an increase in cell associated activity of [^{18}F]**1**, compared to a DMSO control, despite demonstration by western blot that total ATM protein levels were not affected by the same doses of the blocking agents. Since ATM expression levels remain constant in these blocking conditions, it is not yet clear what caused this effect. Quinoline-based ATM inhibitors are highly lipophilic compounds, so it may be hypothesised that at high concentrations the blocking compounds could be altering cell membrane permeability, increasing cellular infiltration of [^{18}F]**1**. An alternative hypothesis could be that the high blocking concentrations are binding to and blocking drug efflux transporter proteins that expel compound **1**, meaning that [^{18}F]**1** is becomes trapped in the cell non-specifically. Similarly, the excess blocking agents may be impacting the expression of other kinases unrelated to ATM expression, resulting in increased off-target specific binding of [^{18}F]**1.** Further work is needed to determine the binding affinity of [^{19}F]**1** to known drug efflux proteins and/or kinases to investigate this theory, and the potential for [^{18}F]**1** to image proteins other than ATM.

In vivo, the comparison in biodistribution of [^{18}F]**1** in wildtype versus ATM-null mice showed significant differences in the liver and kidney uptake (Figure 2.13). Given the observed hepatobiliary and renal clearance (demonstrated by high uptake in the liver, small intestine, and kidneys), it may be hypothesised that the lower uptake in these organs of the wildtype mice could be due to an 'ATM sink' effect, where there may be increased specific binding of [^{18}F]**1** to ATM across the rest of the body, slowing the hepatobiliary clearance of the tracer (therefore reducing hepatobiliary organ uptake of [^{18}F]**1**) relative to the ATM-null

mice. Alternatively, this difference could be due to fundamental differences in metabolism between the two mouse strains, i.e. ATM wildtype vs. ATM-null. It should be noted that the ATM-null mice were of smaller size and weight than wildtype mice, although *ex vivo* organ weight as a percentage of body weight was comparable.

Similar hepatobiliary clearance of [^{18}F]**1** was observed in xenograft-bearing BALB/c *nu/nu* mice, but there was no significant difference between uptake in any of the organs or tumours across the different tumour models (Figure 2.14). This lack of differential uptake in the H1299 tumour xenografts mimics our *in vitro* uptake results in the same cells, indicating that the use of a radiolabelled ATMi for imaging ATM status may be challenging in a clinical setting, but still demonstrates the usefulness of [^{18}F]**1** to non-invasively measure whole body drug biodistribution and quantify tumour-drug uptake.

2.4.2 Critical review of project design

In review of this body of work there are several improvements to experimental design that could be considered for future investigation. Firstly, while the yield of the precursor synthesis was reasonable it could be greatly improved by refinement of the final Suzuki coupling conditions. Additionally, improving the peak separation during prep-HPLC of [^{18}F]**1** and the precursor could improve the radiochemical yield. Finally, further optimisation of precursor loading for the radiosynthesis may improve molar activities.

With regards to the *in vitro* H1299 model system, alternative cell lines could be considered from different tissues in case of specific H1299 characteristics impacting the uptake and

blocking results. Additionally, cells in which ATM has been knocked out (via CRISPR[154]) or expression of ATM has been increased[45] could be included for a system with more extreme ATM expression changes compared to the shATM/GFP knockdown system used. For *in vitro* assays, chemical induction of DNA damage may also be interesting to investigate as a comparison to IR induced damage. *In vivo*, although the ATM-null mouse model served as a useful tool for investigating target engagement, it would be interesting to investigate the effects of using excess ATMi to block [^{18}F]**1** uptake, particularly in xenograft models, and to see if results are comparable to those seen in *in vitro* blocking studies. Furthermore, irradiated tumour models could also be investigated to probe for any effects of pATM expression on [^{18}F]**1** uptake *in vivo* for comparison with the *in vitro* dataset.

Working with [^{18}F]**1** in plastic vessels (e.g. 24-well plates) revealed that the radiotracer was very lipophilic. We found high activity remaining in plates after PBS washes and that there was much higher removal of activity from the plates when using the more lipophilic RIPA buffer for cell lysis compared to aqueous sodium hydroxide. This lipophilicity was problematic when using long canula lines in dynamic imaging studies where the cannula line sequestered most of the injected dose even after PBS flush. Less lipophilic materials (such as glass) could have a positive impact on radiotracer delivery and should be used for future similar studies where possible.

2.5 Conclusions

To the best of our knowledge, radiolabelled compound [^{18}F]**1** is the first reported radiofluorinated ATM inhibitor. We were able to demonstrate the cellular uptake of [^{18}F]**1** *in vitro* and revealed the challenges in determining specific binding to ATM, likely due to low ATM expression in cells in comparison to a high non-specific uptake. *In vivo*, no significant difference in uptake between tumour xenografts expressing different levels of ATM was observed, but we were able to demonstrate whole body drug biodistribution and the hepatobiliary clearance of [^{18}F]**1**. Taken together, these results show the potential challenges in using radiotracers to assess ATM status but highlight the potential benefit of developing similar radiofluorinated ATM inhibitors for the non-invasive assessment of drug pharmacokinetics and tumour distribution.

3 Radiosynthesis of [^{18}F]AZD1390

3.1 Introduction

Following the work completed with [^{18}F]**1**, the main questions raised were (1) why no significant differences of tracer uptake seen with regards to differing ATM expression, and (2) whether small molecule imaging of ATM is useful to investigate further. While it was hypothesised that the lack of correlation could be linked to the fundamentally low expression of ATM, with no other radiolabelled ATMis for comparison this is difficult to confirm and could alternatively be a result of the tracer structure and binding, rather than target expression. The only other reported radiolabelled ATM inhibitor that could potentially serve to test this hypothesis is [^{11}C]AZD1390, however the short half-life of ^{11}C being only 20 minutes restricts its use in probing ATM biology. Therefore, we hypothesised that the results shown in chapter 2 could be due to chemical structure and aimed to compare the same experiments with an alternative ^{18}F-labelled ATM inhibitor.

While there are several libraries of compounds and individual candidate molecules reported to inhibit ATM,[61,68-70,147,155,156] it would ultimately be most useful to focus efforts on those containing fluorine in their structures (to synthesise radioisotopologue rather than radioanalogues) and those being investigated in clinical trials currently (Table 1, page 13), so as to increase the clinical usefulness of a synthesised tracer should the biological results prove to be promising. The candidate molecules containing fluoride moieties that are currently in clinical trials limit this selection to M3541, M4076, and AZD1390 (Figure 3.1).

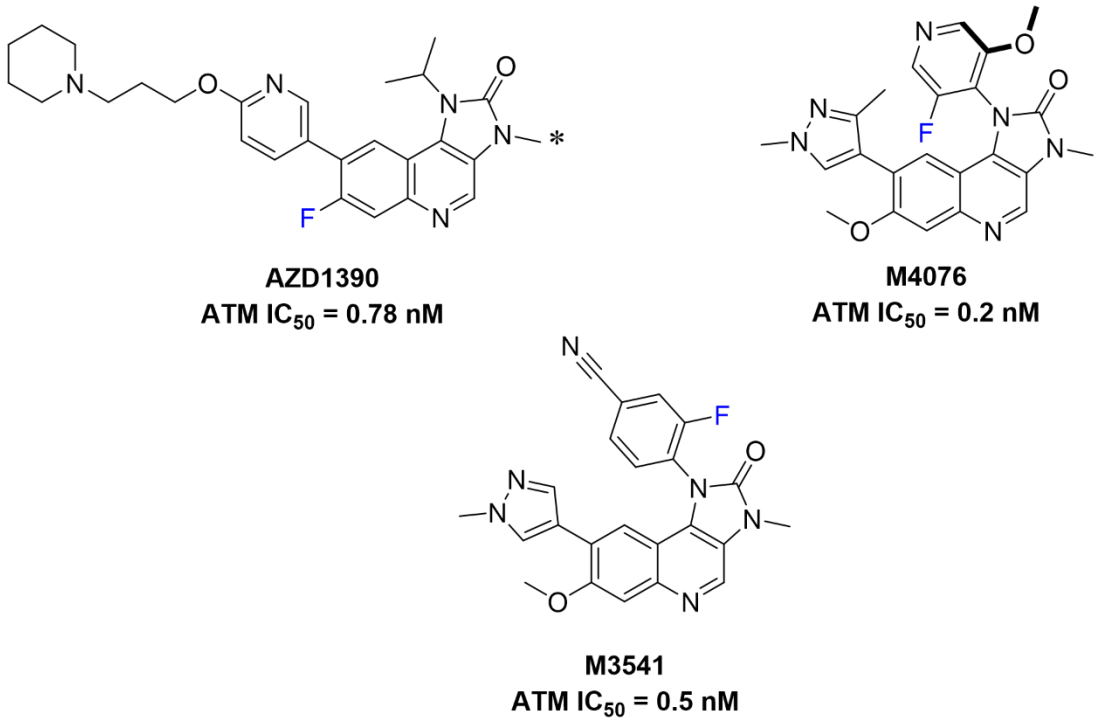


Figure 3.1 – Chemical structures of fluorine containing ATM inhibitors in clinical trials

While the location of the fluorine moiety in M3541 and M4076 may be more amenable to reported radiolabelling methodologies using boronic esters or diaryliodonium salt precursors,[157-159] phase I clinical trial results from M3541 demonstrated no observable dose-response relationship and unfavourable pharmacokinetics, resulting in its withdrawal from clinical development.[66] The promising clinical results of [^{11}C]AZD1390, which had already been reported,[60] made [^{18}F]AZD1390 the preferred compound for investigation. Additionally, with brain tumours showing a high incidence of DDR defects, the reported blood-brain barrier penetrability of AZD1390[59] adds to the potential of [^{18}F]AZD1390 for imaging changes in ATM expression (and therefore levels of DNA damage) in the brain, in addition to assessing drug uptake and pharmacokinetics of AZD1390 in the brain.

While the radiosynthesis of [^{18}F]**1** presented in chapter 2 followed highly robust S_NAr radiochemistry, radiofluorination of [^{18}F]AZD1390 is likely to require a more complex radiosynthesis as there are few reported radiofluorinations in the 7-position of quinoline[160] or similar substrates, especially where there is a group *ortho* to the labelling position. As this is not an electronically activated position, it is likely that classical S_NAr [^{18}F]fluoride substitution will not be successful, therefore more recent techniques and precursors would need to be investigated. This chapter presents the initial work towards synthesis of [^{18}F]AZD1390, the challenges encountered in the development of a suitable precursor molecule, the proposed future steps that could be taken in the synthesis of [^{18}F]AZD1390, and a discussion on the future of ATM as a target for nuclear imaging.

3.2 Materials and Methods

3.2.1 Chemical Synthesis

Full synthetic details on the synthesis towards [^{18}F]AZD1390 precursor molecules are presented in chapter 5 (section 5.4, page 136).

3.2.2 Radiochemistry

Manual radiolabelling reactions were performed using aliquots of [^{18}F]KF (approx. 200 MBq) supplied by the Positron Emission Tomography Imaging Centre (PETIC, Cardiff). For titania catalysed reactions, a stock solution of [^{18}F]fluoride in tetraethylammonium bicarbonate (TEAB) was prepared by adding equal volumes of a 75 mM aqueous TEAB solution with the delivered aqueous [^{18}F]fluoride. For these reactions, a preincubation of

the tosylate precursor **3l** (1.5 mg) with titanium oxide (1.1 mg) in 1:1 acetonitrile/ethanol or acetonitrile/*n*-propanol (30 µL) for one hour at RT was performed before addition of the [^{18}F]TEAB/fluoride solution (10 µL) and heating the reaction at 130°C or 150°C. After 20 min, the reactions were cooled and diluted with methanol (100 µL) before injecting a sample for radio-HPLC analysis. Reactions following this procedure without the addition of titania were also performed.

For reactions without titanium oxide, a stock of azeotropically dried [^{18}F]fluoride was prepared by trapping aqueous [^{18}F]KF (200 µL, approx. 300 MBq) on a QMA carbonate cartridge (Waters, preconditioned with 2 mL deionised H_2O) and eluting with a solution of K_2CO_3 (6 mg) and Kryptofix®222 (30 mg) in 9:1 acetonitrile/water (1 mL), and azeotropically drying with two additions of acetonitrile (2 × 1 mL) before the subsequent labelling reactions.

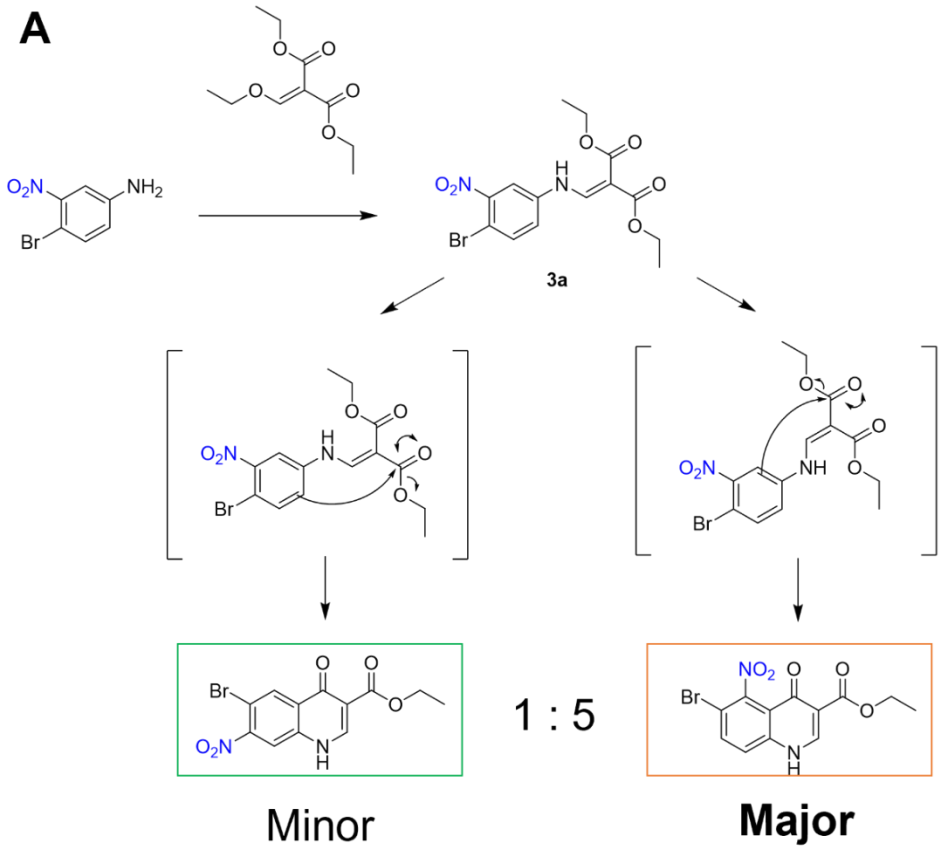
Radio-HPLC analysis was performed on a ThermoScientific UltiMate™ 3000 system with a Luna Omega 5µm Polar C18 100 Å LC 250 × 4.6 mm analytical column, eluting with 20-33% acetonitrile in 0.1% formic acid buffer over 15 min at a flow rate of 1 mL/min. Radio-TLC was performed using a Scan-RAM (LabLogic) detector.

3.3 Results

3.3.1 Initial attempts towards a nitro-precursor

While direct S_NAr radiofluorination of [^{18}F]AZD1390 was predicted to be challenging, attempts were made towards a nitro-precursor in the hopes of testing standard

[^{18}F]fluoride/Kryptofix®222 labelling. The nitro-group could also act as a versatile synthetic handle that could allow development of alternative precursors (e.g. trimethyl ammonium salts). Synthesis towards the nitro-precursor followed a similar synthetic route reported for AZD1390,[147] but starting with commercially available 4-bromo-3-nitroaniline. While the first coupling of the aniline with the malonate was successful, the regioselectivity of the subsequent cyclisation of intermediate **3a** step led to an unfavourable 5:1 ratio of 5-nitro and 7-nitro products, identified by ^{1}H NMR (Figure 3.2).



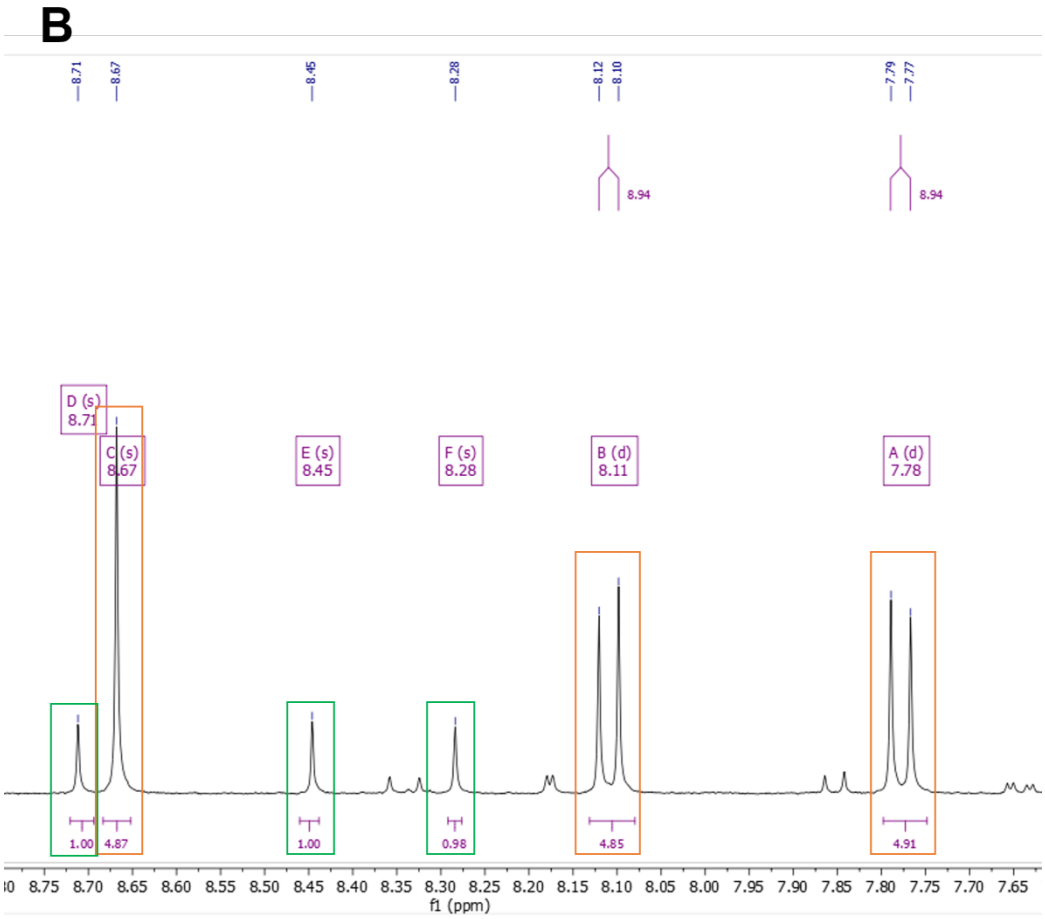


Figure 3.2 – (A) Mechanism of cyclisation of 3b demonstrating two possible products. (B) ^{1}H NMR analysis confirms unfavourable 5:1 ratio of products.

Given the unfavourable ratio of isomers from this key first step in the synthesis, no further attempts were made to isolate the desired isomer due to the scale that would be required for substantial production of the minor product, along with difficulties in separating these isomers which have very poor solvent solubilities.

3.3.2 Synthesis of a versatile hydroxy intermediate

Alternative precursors with fewer potential issues during the initial cyclisation of the quinoline were investigated. The titania catalysed radiofluorination reported by the van Dam group proposed an interesting method that could be tested for radiofluorinating [^{18}F]AZD1390, requiring the synthesis of a tosylate precursor.[161] While this method was developed with the aim of radiofluorination in aqueous media to reduce the need for time consuming azeotropic drying required by most nucleophilic radiofluorinations, the substrate scope presented, while not including a 7-fluoroquinoline, is reasonable including some electronically neutral arenes with good RCYs. Additionally, synthesis of a hydroxy compound suitable for tosylation would also provide a useful intermediate for investigating other precursors if required.

To synthesise this key hydroxy intermediate **3k**, a methoxy quinoline core was first synthesised following methods adapted from patent[63] that followed the same pathway as the AZD1390 reported synthesis with a final demethylation with BBr_3 (Figure 3.3).

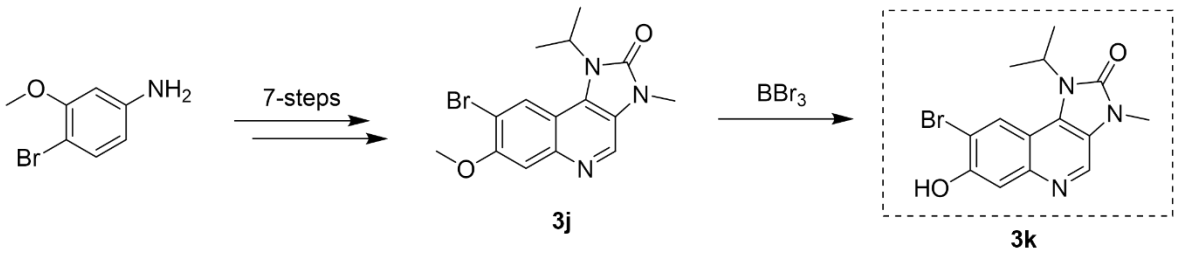


Figure 3.3 – Synthesis of hydroxy quinoline core 3k

The Suzuki coupling with the pyridine core **3m** (synthesised following patent[147]) was relatively low yielding (max. yield 38%) requiring a large catalyst loading (25%), and difficult purification due to the presence of the hydroxy group resulting in high affinity to silica during chromatography. Notably, purification by normal-phase silica chromatography resulted in the need for 100% methanol to elute the product and led to coelution of the hydroxydeborylated pyridine side product (Figure 3.4). Optimisation with regards to catalyst choice, base, temperature, solvent system, or alternate purifications were not tested during the timescale of this project.

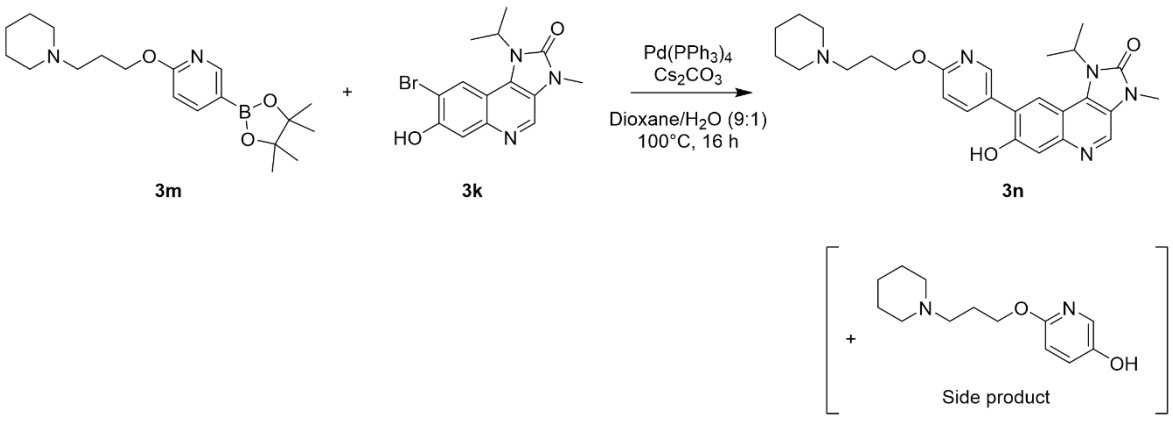


Figure 3.4 – Suzuki coupling of 3m and 3k yields 3n and gives a hydroxydeborylated pyridine side product.

3.3.3 Tosylate precursor synthesis and radiolabelling

With the hydroxy intermediate **3n** in hand, a final tosylation step was required before the titania-catalysed radiofluorination could be tested. Given the low yielding Suzuki coupling, only limited material was available for testing tosylation conditions. Conversion of **3n** to the

desired tosylate by reaction with tosyl chloride in pyridine at 65°C overnight gave good, clean conversion by LCMS and TLC, however NMR revealed some aromatic impurities, likely some tosylic acid and traces of tosylated pyridine (from the hydroxydeborylated by-product of the Suzuki coupling).

Following the isolation of the tosylate **3p**, radiolabelling was trialled following the conditions set out by the van Dam group[161] (Figure 3.5). Initial labelling tried by Dr Gianluca Destro in the Cornelissen group showed a hint of radiolabelled product by radio-HPLC, later confirmed as [^{18}F]AZD1390 by HPLC. Subsequent attempts to repeat this result in the same conditions unfortunately showed only free [^{18}F]fluoride by radio-HPLC and radio-TLC. The same van Dam reaction performed without the titania, and with a non-nanoparticle TiO_2 was also attempted with no conversion seen. Given that tosylate can be a good leaving group for S_NAr reactions, labelling reactions using azeotropically dried [^{18}F]fluoride/K_{222} were also attempted in DMF, MeCN and MeCN/*n*-PrOH solvent systems, however no conversion was observed.

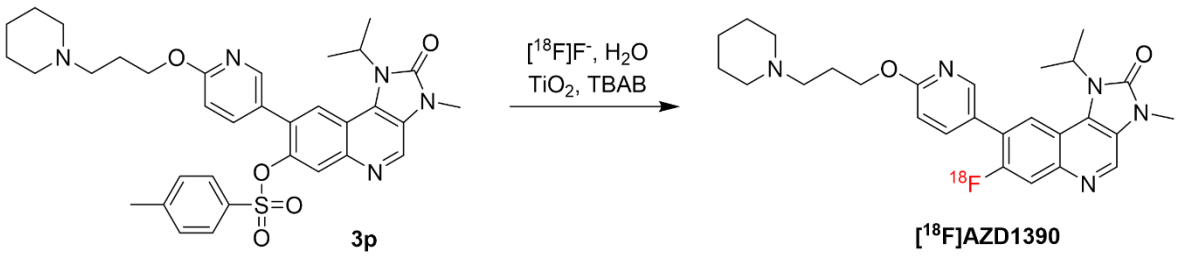
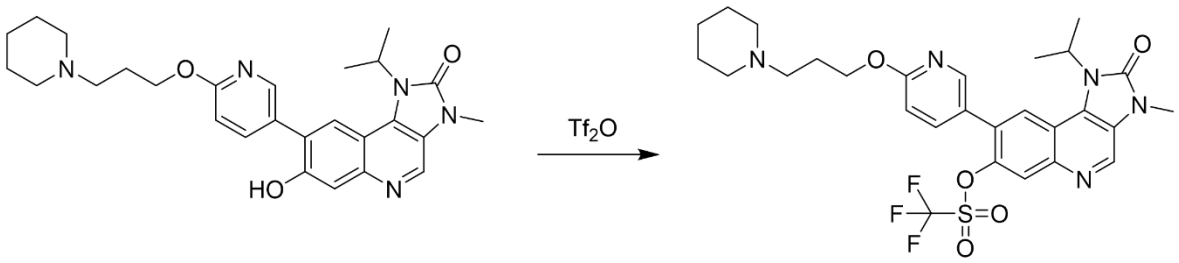


Figure 3.5 - Proposed radiofluorination of [^{18}F]AZD1390 following titania catalysed radiochemistry reported by van Dam.

3.3.4 Steps towards a boronic ester precursor

After the unfortunate results from the titania catalysed radiosynthesis trials, alternative radiolabelling routes and precursors were explored. One radiolabelling method that has proven successful in the labelling of electronically neutral aromatic compounds is the copper-mediated technique applied to boronic acid/ester precursors, developed in the Gouverneur group.[162] Therefore, the synthesis of a boronic ester precursor to test copper-mediated radiofluorination was investigated.

Boronic esters and acids are commonly synthesised via Miyaura borylation of the respective halide.[163] Insertion of a suitable halide in the 7-position during the quinoline synthesis for later borylation would likely interfere with the desired Suzuki coupling and lead to unwanted side products. Miyaura borylations have however been successful on triflate leaving groups.[163] Fortunately, the previously synthesised hydroxide intermediate **3n** provided a synthetic handle for synthesis of a triflate, with compound **3q** isolated in reasonable yields (Figure 3.6). Unfortunately, column chromatography gave coelution of the desired **3q** along with the triflated pyridine, resulting from triflation of residual hydroxydeborylated pyridine from the previous Suzuki coupling step.



3n **3q**

Figure 3.6 – Synthesis of key triflate intermediate 3q from 3n.

Attempts were then made to synthesise the final boronic ester following standard Miyaura borylation conditions (B_2pin_2, KOAc, 1,4-dioxane). Conversion of the triflate starting material into product boronic ester was tracked by LCMS, with triflate concentration decreasing over 12 hours, and the production of a compound with m/z 587 increasing. This m/z was thought to be corresponding to the product boronic ester $[M+H]^+$ adduct, despite being 1 mass unit larger than predicted by its molecular mass (585.35 $gmol^{-1}$), initially thought to occur due to the low resolution of the LCMS machine used. High resolution mass spectrometry of the crude material containing predominantly this species however failed to confirm this as the boronic ester product. Time restrictions and diminished stocks of key intermediates meant that alternative reaction conditions could not be tested further.

3.4 Discussion and future work

3.4.1 Summary of initial attempts towards [^{18}F]AZD1390

Following the recent successful synthesis and phase I studies with a ^{11}C-labelled ATMi [^{11}C]AZD1390, an ^{18}F-labelled radioisotopologue of AZD1390 was proposed as a more clinically useful tracer due to the longer half-life of ^{18}F (110 min) versus ^{11}C (20 min). The BBB-penetrable properties of AZD1390 demonstrated by AZD1390 added further interest for the use of [^{18}F]AZD1390 to investigate ATM expression levels in brain tumours, where there is a high occurrence of DDR defects and therefore a potential increase in ATM expression to mediate higher levels of DNA damage. While the work presented in chapter 2 presented the radiofluorination of an AZD1390 isomer, it also demonstrated the potential

limitations in using radiolabelled ATMis for detecting changes in ATM expression. The work presented in this chapter towards [^{18}F]AZD1390 hoped to further validate or challenge the results presented in chapter 2 with regards to quantifying ATM expression levels, but with the further aim to synthesise a radiotracer that could be used to investigate drug pharmacokinetics and drug-target engagement of the current clinical candidate AZD1390 via non-invasive PET imaging.

Initial design of a suitable precursor molecule for radiofluorination of [^{18}F]AZD1390 considered the variety of radiolabelling options available for similar substrates that are not electronically activated and less suited for traditional S_NAr radiofluorination. Synthesis of a nitro-precursor was however initially investigated in the hopes of trialling S_NAr labelling as well as providing a nitro-group that could serve as a useful synthetic handle for investigating other precursors. Regioselectivity issues very early in the synthesis however restricted this pathway. Following this, a hydroxy intermediate was synthesised to provide a synthetic handle for a tosylate precursor for testing titania-catalysed radiofluorination. Unfortunately, radiolabelling trials were unsuccessful in yielding any radioactive products. The same hydroxy intermediate was used to synthesise a triflate intermediate for Miyaura borylation to give a boronic ester precursor for testing the well reported copper-mediated radiofluorination developed by the Gouverneur group.

Although time restricted the development of successful conditions for synthesis of this boronic ester precursor, the intermediates reported in this chapter have paved the way towards [^{18}F]AZD1390. The immediate next steps for the synthesis of a boronic ester precursor would require optimised conditions for the Miyaura borylation (with regards to

temperature, catalyst, solvent and base),[164] in addition to improvements to the previous Suzuki coupling yield and purification of the hydroxy and triflate intermediates. In the case that a boronic ester precursor may not be suitable for copper-mediated radiofluorination, alternative pathways that could be considered in the development of [^{18}F]AZD1390 with regards to alternative radiolabelling methods and precursors are described in the next section.

3.4.2 Alternative precursor and radiolabelling options for [^{18}F]AZD1390

The native fluorine of the AZD1390 quinoline core was predicted to be a poor position for traditional late-stage S_NAr radiofluorination due to the lack of electron withdrawing groups from this aromatic ring. Additionally, there are very few reported reactions to substitute this 7-quinoline position with a fluorine (both ^{18}F and ^{19}F), of which require halogen exchange and/or long reaction times.[165] Notably, there is one reported electrophilic radiofluorination of quinoline in the 7-position via [^{18}F]acetyl hypofluorite gas directly from 5-chloro-8-hydroxyquinoline (example 10) or tin derivative 5-chloro-8-*t*-butoxycarbonyloxy-7-trimethylstannylquinoline (example 15).[160] This type of radiochemistry was not considered due to lack of reported substrate scope, as well as the specialist facilities required and higher risk associated with handling gaseous radiofluorine. One reported radiofluorination method considered was the use of diaryliodonium salts or ylids as precursors as these have demonstrated efficient labelling of electron-rich arenes, as well as potential labelling enhancement in precursors with ortho-substituents.[150] This method was however disregarded due to the difficulties in inserting an iodine moiety in the

labelling position, as well as the low stability of these compounds and potential issues in the oxidation of iodo-molecules required for precursor synthesis, particularly in the presence of our required quinoline and pyridine moieties.

The decision to first investigate the van Dam titania catalysed chemistry was made regarding both the accessibility of a suitable tosylate precursor and the apparent substrate scope demonstrating this type of radiochemistry can be effective on electronically neutral aromatic precursors.[161] The purpose of this radiochemistry was to demonstrate conditions that allow nucleophilic radiofluorination in the presence of water and remove the need for time-costing azeotropic drying, a key improvement upon many radiochemical methods. There is however only one further report of this method being considered for radiofluorination, although the authors abandoned it due to instability of their precursor in the presence of TBAF that would be generated in situ with this type of radiochemistry.[166] The lack of repeated reports using this method may suggest it is perhaps not a robust method, reflected in the difficulties faced here using it for labelling [^{18}F]AZD1390.

A different phenol-based precursor labelling method considered was that described by Neumann *et.al.*, in which phenol substrates are reacted with a PhenoFluor derivative to give uronium salt precursors, promoting a concerted substitution with [^{18}F]fluoride.[167] While the substrate scope reported ^{19}F mechanistic studies demonstrate suitability of this method for both electron poor and rich arenes, the ^{18}F-labelling scope mostly covers electron deficient aromatic systems, not reflecting the requirements for [^{18}F]AZD1390. Additionally, with none of the reported substrates demonstrating fluorination in compounds with *ortho*-groups, like in the precursor that would be required for

[^{18}F]AZD1390, the synthesis of the uronium salt required for labelling may also pose difficulties with regards to steric requirements as well as potential need to freshly synthesise the salts before each labelling in case of poor stability. For these reasons, this method was not pursued for [^{18}F]AZD1390.

The move towards copper-mediated radiofluorination for [^{18}F]AZD1390 was considered worthwhile given the accessibility of a suitable boronic ester precursor and the broad scope reported for this radiochemistry including electron-rich and neutral substrates.[162] This method has become well-established, with many reports of its use in radiofluorination of pharmaceutically relevant tracers.[168-173] If the boronic ester precursor for [^{18}F]AZD1390 can be prepared, the main query with this type of radiolabelling is whether the *ortho*-pyridine substituent will restrict the reaction, given the scope of this reaction did not report any substrates with *ortho*-groups. With regards to steric hinderance, if the boronic ester is accessible via palladium catalysed substitution, then there may be fewer concerns surrounding potential steric hinderance during the copper-mediated substitution. With this route not yet tested, consideration into other radiolabelling methods is practical.

Radiofluorination of electron-rich and neutral arenes is one of the key issues being addressed in current radiolabelling methodology research. This is in part due to the broad range of (often fluorine containing) compounds that are desirable as potential PET probes. Traditional fluorination of aromatic compounds often involves insertion of the desired fluorine-moiety early in the synthesis via a range of nucleophilic, electrophilic, and radical substitutions. Translation of these methods to radiofluorination are however often restricted by the fluorine-18 half-life (enforcing late-stage fluorination), use of specific

fluorinating reagents not yet available with fluorine-18, and effectiveness at the reduced stoichiometry imposed by radiofluorination.[174] One method of bypassing these issues is by using isotopic exchange of ^{19}F-containing compounds with ^{18}F in the presence of [^{18}F]F$^-$/potassium carbonate/Kryptofix®222 or [^{18}F]TBAF. However, for efficient labelling these methods require electron-withdrawing groups in the *ortho/para* positions and result in inherently low molar activities.[175]

Recently, the use of photoredox-mediated halogen exchange with ^{18}F-fluoride has been applied to electron-rich halo(hetero)arenes with decent radiochemical yields.[176] Chen *et al.* proposed that single electron oxidation would enable directed ^{18}F-exchange directly from electron-rich fluoro- or chloro-(hetero)arene precursors – leaving groups that have previously shown poor reactivity in electron-rich systems and when compared to bromo- and iodo-precursor equivalents. This work however demonstrated higher radiochemical conversion (RCC) of chloro (up to 75.3%) and often even higher of fluoro (up to 79.7%) (hetero)arene precursors compared to the bromo and iodo equivalents (up to 46.5% and 5.1% respectively). The high RCC of the demonstrated Cl/^{18}F and ^{19}F/^{18}F exchange is of particular significance as this would allow for direct radiofluorination of desirable electron-rich fluorine or chlorine containing target molecules without the need for complex precursor synthesis, an area where current S_NAr radiochemistries are lacking. This was demonstrated for a variety of known bioactive compounds through both Cl/^{18}F (3.9-43.9%) and ^{19}F/^{18}F (10.1-72%) exchange, with the scope including ^{19}F/^{18}F exchange applied to the radiosynthesis of [^{18}F]F-DOPA from a methyl and BOC protected ^{19}F-DOPA precursor. The latter was achieved on a clinically relevant 37 GBq scale with >30% RCC and >99% e.e., albeit

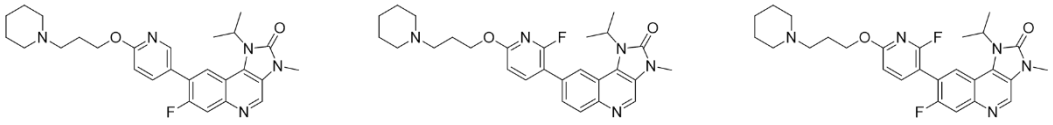
with a low A_m of 1.51 GBq/µmol. Notably, no additional molar activities were reported other than for Cl/^{18}F exchange yielding [^{18}F]1-fluoro-4-methoxybenzene with A_m of 71.25 GBq/µmol, raising a question of feasibility of this method for radiotracers with high molar activity requirements.

Given the demonstrated success of this photoredox-mediated radiofluorination for ^{19}F/^{18}F exchange in electron-rich (hetero)arenes, it could be considered as a method to access [^{18}F]AZD1390 from the commercially available AZD1390. However, if successful, given the high binding affinity of AZD1390 to ATM and the low target expression, molar activity may need to be improved to reduce any blocking effects from ^{19}F-AZD1390 in the formulation. Should increasing molar activity be an issue for direct ^{19}F/^{18}F exchange, the substrate scope also reports radiofluorination through exchange of triflate (albeit only one example with a RCC of only 11.6%) which could be attempted from the already synthesised intermediate **3q**. Alternatively, similar photoredox-mediated radiofluorination has been reported by the same group employing deoxyfluorination[177] and could be explored for [^{18}F]AZD1390. The main drawback of these methods however is the need for specialist catalysts and laser/LED setups as well as the limited reported substrate scope of only simple (hetero)arene systems and currently restricted translatability to automated/GMP synthesis.

Other recent methods that have demonstrated successful radiolabelling of electron-rich and neutral arenes worth mentioning includes the use of electrochemistry,[178] however again this requires specialist setups and current methods still suffer from poor regioselectivity. Electrophilic radiofluorination may be considered, however, these methodologies are generally less safe with most electrophilic fluorine sources being

gaseous (e.g. $[^{18}F]F_2$, $[^{18}F]XeF_2$, $[^{18}F]FClO_3$, $[^{18}F]CH_3COOF$). Alternative, safer sources of electrophilic fluorine that also show higher selectivity include [^{18}F]*N*-F fluorination agents such as [^{18}F]Selectfluor *bis*(triflate),[179] [^{18}F]*N*-fluoropyridinium triflate,[180] and [^{18}F]*N*-fluorobenzenesulfonamide.[181] These reagents however are still not commercially available (all requiring specialist equipment to synthesise from $[^{18}F]F_2$), limiting their use for developing [^{18}F]AZD1390.

Beyond alternative radiolabelling methods, a parallel project based on the work presented in this and the previous chapter could consider the synthesis of a doubly fluorinated, singly labelled ATMi hybrid molecule, in which the patent reported 7-fluoroquinoline AZD1390 scaffold could be linked to the previously synthesised nitropyridine **2c** with subsequent S_NAr radiofluorination as presented in chapter 2. With these quinoline-based ATMis binding to the ATP-binding site of ATM via the quinoline nitrogen, the location of the 7-fluoroquinoline group on this proposed molecule, as in AZD1390, may play a significant role in the binding to ATM. This could considerably affect the selectivity against other kinases and therefore may yield different uptake results to [^{18}F]**1**. This doubly fluorinated compound is reported in the same patent describing AZD1390 (compound 14, ref.[147]) with a whole cell ATM IC_{50} of 3.51 nM and excellent selectivity against ATR, mTOR and PI3Kα, making it a suitable compound worth investigation for ATM imaging (Figure 3.7). A proposed pathway for radiosynthesis of this compound is shown in Figure 3.8.



	AZD1390	[^{19}F]1	'Compound 14'
ATM	< 0.000787 μM	< 0.000453 μM	0.00351 μM
ATR	> 30 μM	> 30 μM	> 30 μM
PI3Kα	>12 μM	5.75 μM	>30 μM
mTOR	> 30 μM	> 5.19 μM	> 30 μM

Figure 3.7 – Comparison of ATM inhibition and selectivity reported for AZD1390, [^{19}F]1, and proposed compound 14.

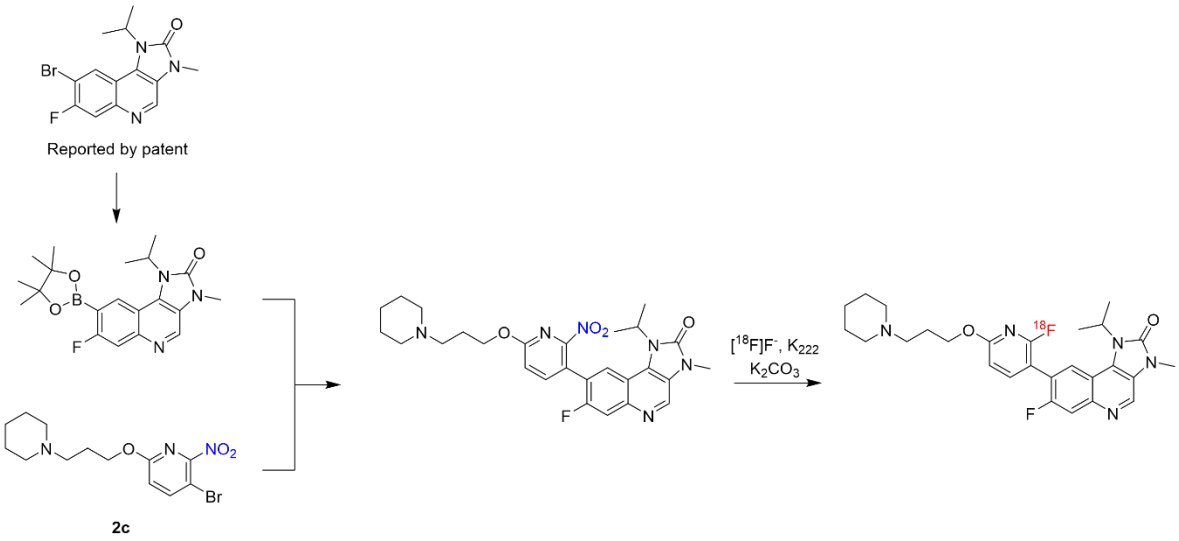


Figure 3.8 – Proposed synthesis and radiosynthesis of [^{18}F]14.

3.4.3 Future of ATM targeted PET imaging

ATM is an attractive target for nuclear imaging due to its critical role in sensing and organising DSB repair. High levels of DNA damage, and DSBs in particular, are seen in

tumour cells meaning levels of active ATM may be increased. Being able to detect ATM activity levels non-invasively through nuclear imaging could give insight into tumour cell biology, help to stratify patients who may benefit from ATM inhibitor or related therapy, and potentially monitor ongoing DNA damaging treatments such as radiotherapy.

Previous research conducted by Dr Mathew Veal in the Cornelissen group had investigated the use of an ^{111}In-labelled anti-phospho-ATM antibody as a potential SPECT imaging probe in evaluating levels of phospho-ATM^{S1981} (pATM) expression, the canonical marker of ATM activity.[182] Unfortunately, the results of this study showed no significant difference in uptake in cells expressing variable levels of pATM, as mimicked by the results of [^{18}F]**1** presented in chapter 2. While the hypothesis drawn for these results was that the innately low copy numbers of ATM and pATM makes imaging changes in uptake against high background inherently difficult, the lack of alternative ATM-targeted radiotracers makes this difficult to confirm.

The ATM inhibitors AZD1390 and AZD0156 were the first two small molecules to be radiolabelled, with their main use as demonstrating BBB-penetrability of [^{11}C]AZD1390 in comparison to the lack of brain uptake of [^{11}C]AZD0156.[59] While [^{11}C]AZD1390 has begun clinical evaluation to assess the potential of uptake of AZD1390 therapy in the brain, little more is reported of this tracer with regards to understanding ATM biology, and in particular being able to assess levels of ATM activity. Unfortunately, the short 20-minute half-life of ^{11}C means that extensive preclinical biological evaluation using this tracer for assessing ATM activity levels are limited. Hence it was proposed to synthesise the more useful ^{18}F-labelled

AZD1390 to investigate ATM activity, particularly in the context of brain tumour imaging, as well as for further justifying the hypotheses drawn from the results in chapter 2.

With ATM inhibitors only being developed as therapeutics in the last two decades, there are limited targeting species characterised that could serve as nuclear imaging agents, other than those investigated in this thesis. Aside from their recent development, one of the main reasons for the reduced number and characterisation of ATM inhibitors is the reduced understanding of ATM biology itself, stemming partly from the lack of a full crystal structure of ATM due to its large size. There is however an increasing database of ATM structures becoming available, with high resolution electron microscopy allowing the development of better molecular dynamics models.[26,41] Hopefully these advances will help in the design of new ATM inhibitors in the future, however, there will likely remain difficulty in finding inhibitors that are suitable for radiofluorination for in depth biological investigations and PET imaging. Designing such radiotracers comes with developing suitable precursor syntheses and labelling techniques that are simple, cheap, and translatable, ideally to a GMP-validated level so as to increase clinical usefulness. As highlighted in this chapter, these factors are not trivial and often require years of development.

Taken together, the recent and presented work on the development of ATM radiotracers have demonstrated little success in measuring differing ATM expression levels, with a common hypothesis suggesting the inherently low expression/copy numbers of ATM may make it an unsuitable target for nuclear imaging. Additionally, even though ATM plays a central role in the DDR giving it high relevance in cancer research, correlation of ATM levels and cancer outcome are rarely reported except in the case of AT patients where lack of

functional ATM results in a higher susceptibility to cancer. Therefore, given these preliminary findings suggesting ATM levels are too low to detect, alongside the few reports on the clinical relevance of ATM expression in cancer, further development of ATM-targeted radiotracers for measuring ATM levels with PET may not be warranted. Furthermore, while the development of radiotracers based on current ATMi clinical candidates could be useful in assessing patient specific drug pharmacokinetics, the cost of developing radiofluorinated tracers purely for understanding ATMi pharmacokinetics may ultimately outweigh their usefulness in the clinic.

3.5 Conclusion

In summary, here is reported the first steps towards the synthesis and radiolabelling of [^{18}F]AZD1390. The first steps in the development towards a nitro-precursor were revealed to have regioselectivity issues in the crucial formation of the quinoline. A second tosylate-precursor was synthesised in reasonable yields, however radiolabelling of this compound proved difficult, with no radioactive products observed in the conditions trialled. A final pathway towards a boronic ester precursor suitable for copper-mediate radiofluorination was devised, with successful synthesis of a triflate prerequisite compound, however more work is needed to achieve the final borylation step and to improve yield and purification of the later intermediates. Extended discussion on alternative synthetic and radiolabelling methods that could be suitable for [^{18}F]AZD1390, as well as discussion on the future of ATM molecular imaging were presented.

4 Towards [^{18}F]A-966492

4.1 Introduction

PARP proteins play a key role in the repair of DNA damage, with PARP1, PARP2, and PARP3 involved in the recruitment of other members of the DDR by the synthesis of covalent ADP-ribosylated proteins. Several PARP inhibitors (PARPi) have been developed for use in cancer therapy, with four currently approved for use in clinic and many more at the preclinical stage (Table 2, page 20). Their use as cancer therapies has stemmed mainly from their ability to induce synthetic lethality in cancers presenting defects in homologous recombination (e.g. *BRCA* mutants).[22]

Brain tumours have become an interesting target for PARPi treatment as there are limited treatment options currently available and brain tumours have a high prevalence of HR defects.[183] Finding drugs that can reach brain tumours in sufficient concentrations is complex, in part due to the blood-brain barrier (BBB) that only allows paracellular transport of compounds into the brain and is home to a host of efflux transporters designed to protect the brain from harmful agents. While some PARPis have been evaluated in the treatment of brain tumours, many are substrates for these efflux transporters, such as P-glycoproteins (P-gp) and ATP-binding cassette transporters (ABC), which often results in poor brain uptake. Rucaparib for example showed increased efficacy in combination with TMZ *in vitro* and in PDX models of GBM, however, had no effect in orthotopic mouse models treated with TMZ as it was shown to be a substrate for BCRP1 and MDR1 (P-gp) efflux transporters.[184]

Some PARPis, such as niraparib[185] are not substrates of the key BBB efflux transporters and therefore are able to penetrate the intact BBB in concentrations suitable for effective tumour dosing. Additionally, in many cases of larger brain tumours and brain metastases, the BBB is compromised and therefore may allow better passage of non-BBB penetrable drugs into the tumour. For example, olaparib was shown to be an ABCB1 efflux substrate leading to inadequate brain delivery in some cases,[78,186] however mass spectrometry on resected glioblastoma samples in the OPARATIC phase I clinical trial demonstrated good distribution and concentrations within the tumour core and tumour margins that would be sufficient for radiosensitisation.[187,188] Since brain tumours lead to variable levels of BBB-disruption, with high grade gliomas normally highly disruptive and lower grade tumours less so, it would be useful to be able to predict how well a PARPi would penetrate the brain and the resulting drug concentration in brain tumours.

Currently, patients who might respond well to PARPi treatment are generally selected following identification of HR deficiencies, such as *BRCA1* and *BRCA2* mutations, determined via genetic testing. Identification of biomarkers other than *BRCA* mutations that may indicate PARPi suitability are being investigated, such as immunohistochemistry staining for RAD51 where high expression may indicate PARPi resistance,[189] but none are in routine use in clinic.[190] Within patients expressing PARPi favourable mutations, it would be useful to identify those who have tumours with increased PARP expression itself since this may be indicative of increased reliance of the cancer cells on PARP for DNA damage repair[191] and has been associated with worse prognosis.[192-195] Determining PARP expression can be performed by analysis of tumour biopsies by immunohistochemistry or by

measuring mRNA expression levels of PARP, however these techniques are not necessarily representative of all tumour tissue (including metastatic sites), rely on potentially difficult to retrieve tumour biopsies (e.g from brain or pancreatic tissue), and may not yield quantitative data.

Molecular imaging of PARP has the potential to semi-quantitatively identify PARP expression of tumours and identify tumour-PARPi engagement, with PARP inhibitor radiotracers under investigation since the early-2010s. The first reported radiofluorinated PARP inhibitor was an analogue of Olaparib, [^{18}F]BO, designed following the success of a fluorescently tagged olaparib derivative to image PARP expression in live cells.[196] The following decade has shown a whole range of radiofluorinated PARPi-based tracers put into development (Figure 4.1), as well as radioiodine, astatine, and copper-labelled radiotracers.[133,134,197]

Notably, two PARP radiotracers, [^{18}F]fluorthanatrace (FTT) and [^{18}F]PARPi, have reached clinical trials for the evaluation of tracer uptake in a range of tumour presentations, with preliminary results from both showing good tolerability, tumour uptake, and high tumour/blood ratios.[135,198-200] While these clinical investigations have demonstrated the usefulness of developing PARP PET radiotracers for the evaluation of PARP expression and PARPi tumour uptake, since they are both radioanalogues of approved PARP inhibitors, they are not able to accurately represent tumour-drug uptake or drug pharmacokinetics of the parent drugs (rucaparib and olaparib, respectively) due to their chemically different

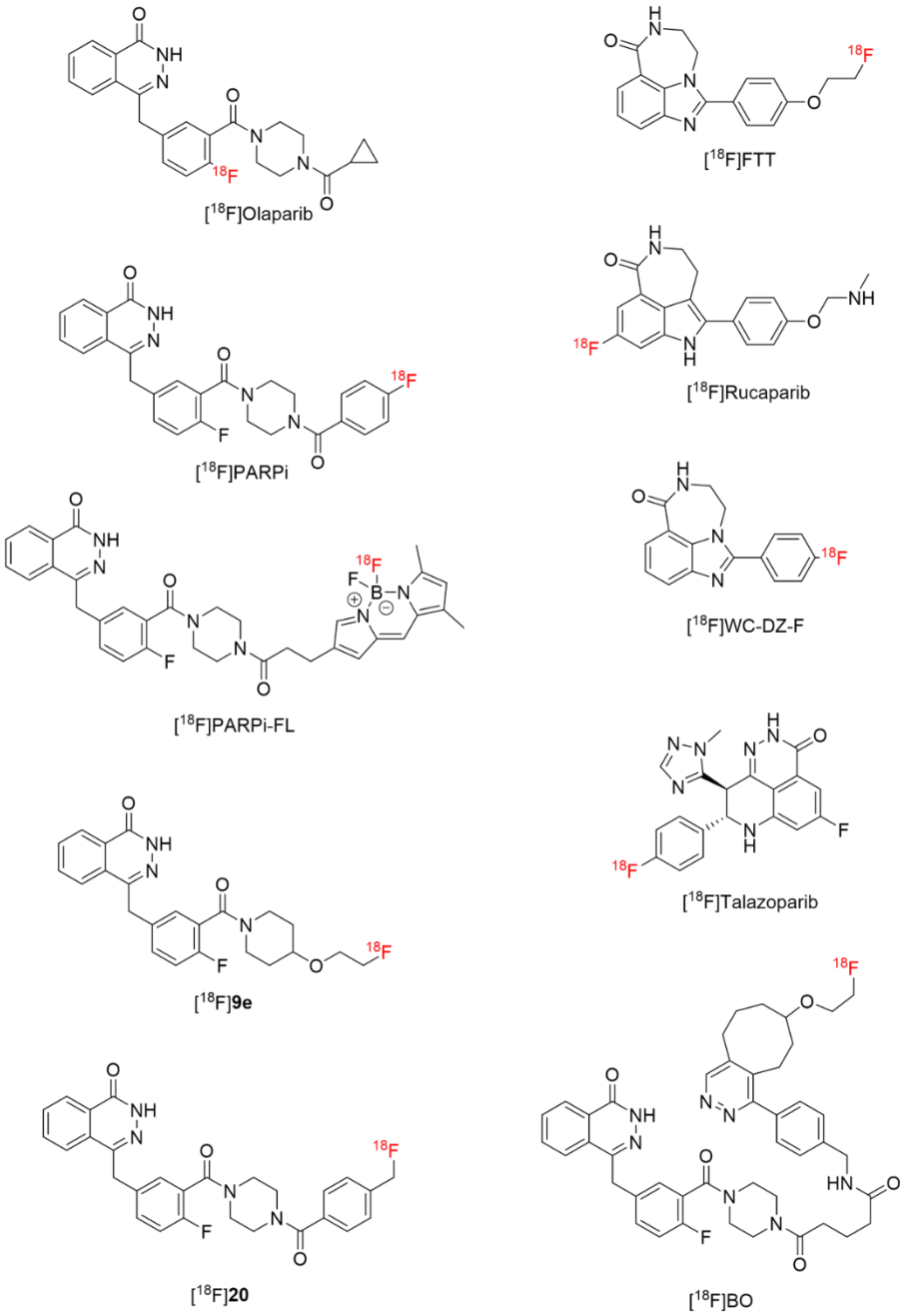


Figure 4.1 – Examples of reported ^{18}F-labelled PARP inhibitors.

structures that may differ in protein binding, membrane permeability, lipophilicity, and bioavailability. Radioisotopologues – where the chemical structure of the parent drug is retained only exchanging a single atom with a radioisotope of the same element – are

however able to predict parent drug pharmacokinetics and tumour uptake more accurately. Three of the clinically approved PARP inhibitors have been labelled as isotopologues with ^{18}F; [^{18}F]Olaparib,[173,201] [^{18}F]Rucaparib,[172,202] and [^{18}F]Talozoparib,[203,204] all of which have shown good uptake in correlation with PARP expression and selectivity to PARP in preclinical studies. An isotopologue of the PARP inhibitor [^{18}F]AZD2461 was also developed and showed how different PARP isoform binding profiles reflect the different blocking abilities of AZD2461 and olaparib.[205]

With regards to imaging PARPi uptake in the brain, several ^{18}F-labelled PARPi radiotracers have been tested and/or designed to explore brain tumour imaging. With [^{18}F]FTT demonstrated as a potent substrate of P-gp with poor brain uptake, the Mach group developed an ^{18}F-labelled AZD2461 analogue, [^{18}F]SWR-4-127 (structure not disclosed), demonstrated its higher uptake in mouse brains, and confirmed its low binding to P-pg by comparison using P-gp knockout mouse models.[206] Further studies by the same group however demonstrated that [^{18}F]**9e** (likely the same compound, however structure of the former was not disclosed) could not cross the BBB in non-human primates and was metabolically unstable.[207] Conversely, [^{18}F]F-PARPi showed promising results in a pilot study involving 8 patients with brain tumours (primary and metastatic), suggesting that [^{18}F]F-PARPi uptake correlated with PARP expression (visualised by IHC on surgical samples) and was able to differentiate between active cancer and treatment-related changes, however the sample size was small.[136] Additional studies in mice bearing brain tumours following co-injection of [^{18}F]F-PARPi and non-BBB penetrable FITC-dextran were used to investigate whether [^{18}F]F-PARPi is BBB-penetrable. *Ex vivo* IHC and autoradiography

showed higher brain uptake of the radiotracer compared to the FTIC-dextran, with the authors suggesting that these results indicate that [^{18}F]PARPi uptake in brain tumours is a result of BBB-penetrability rather than of a disrupted BBB. The small sample size alongside the inherent disruption of the BBB during orthotopic tumour inoculation does however raise the need for further validation.

Altogether, these results highlight the previous success of imaging PARP as an indicator of DNA damage in cancer, and how the use of PARP-targeted PET could be used for visualising PARPi-target engagement. The additional relevance of PARP in brain cancer along with the recent results of [^{18}F]PARPi in imaging brain tumours further demonstrates the value of developing BBB-penetrable PARPi radiotracers. Therefore, with regards to the reported PARP1 inhibition (1 nM, cell-free) and plasma-to-brain ratios of ~2:1, [^{18}F]A-966492 proposed a useful target molecule for imaging PARP expression in the brain.[95] Here is reported the first synthetic steps towards a suitable precursor for [^{18}F]A-966492 and preliminary biological characterisation of brain cancer cell lines that would be suitable for future biological evaluation of the tracer.

4.2 Materials and Methods

4.2.1 Chemical Synthesis

Full synthetic details on the synthesis towards [^{18}F]A-966492 are presented in chapter 5 (section 5.5, page 150).

4.2.2 Cell culture

The cell lines used in this work were PSN-1, U87MG, U251MG (purchased from ATCC, UK), MDA-MB-231 and MDA-MB-231BR (kindly gifted from Prof. Nicola Sibson at the University of Oxford). PSN-1 cells were cultured in Roswell Park Memorial Institute media (RPMI), with the others cultured in DMEM, each supplemented with 10% Foetal Bovine Serum (FBS) (Gibco, USA), 2 mM L-glutamine, 100 units/mL penicillin and 100 µg/mL streptomycin (PSG) (Sigma Aldrich). Cells were not used beyond 20 passages after resuscitation from liquid nitrogen. Cells were authenticated by the supplier and STR profiling and tested regularly for the absence of mycoplasma.

4.2.3 Western Blot

Approximately 1×10^6 cells were washed with PBS, detached with Trypsin-EDTA solution, and pelleted before vortexing in ice cold PBS, removal of PBS, and addition of 100 µL of cold RIPA buffer containing protease inhibitor (cOmplete EDTA-free, Roche). The lysates were sonicated on ice for 5 seconds then left on ice for 10 min before centrifugation at 20,000 rcf, 4°C for 20 min then supernatants (lysates) were isolated. Protein concentration was determined with the BCA assay against BSA standards and normalised to 1.7 mg/mL diluting in RIPA buffer. Lysates were denatured by addition of NuPage LDS loading buffer (Invitrogen) and heated to 95°C for 1 min before loading 30 µg per well to a NuPage 4-12% bis-tris gel (ThermoFisher). The gel was run in MOPS running buffer (Invitrogen) at 120 V for approximately two hours then transferred to a PVDF membrane at 20 V for 10 min using an iBlot2 system (Invitrogen). The membrane was recovered in PBS and cut to isolate

proteins >100 kDa (for PARP1 staining), 55-100 kDa (for PARP2 staining), and <55 kDa (for β-Actin loading control). Membranes were blocked in 5% milk in PBST (PBS with 0.1% Tween-20) for one hour, then incubated with primary antibodies in blocking buffer at 4°C overnight. Membranes were washed 3 × 10 min with PBST, then incubated (where necessary) with secondary antibody in blocking buffer at RT for one hour, followed by 3 × 10 min wash in PBST. Membranes were rinsed in PBS before imaging with SuperSignal™ West Pico PLUS chemiluminescence kit (Thermo Scientific) on a Leica Odyssey FC system. The antibodies used in this work and their dilutions are as follows: PARP1 (MPA045168, 1:500, Atlas Antibodies); PARP2 (MPA052003, 1:300, Atlas Antibodies); HRP-conjugated β-Actin (clone 13E5, 1:1000, Cell Signalling Technologies).

4.3 Results

4.3.1 Initial design and attempts towards asymmetric precursor synthesis

The precursor chosen for radiolabelling of [^{18}F]A-966492 was a boronic pinacol ester **4**, with plans for the subsequent copper-catalysed radiofluorination (Figure 4.2).[162] Synthetic pathways were designed to reach a triflate intermediate that would be suitable for Miyaura borylation[163] to give this precursor.

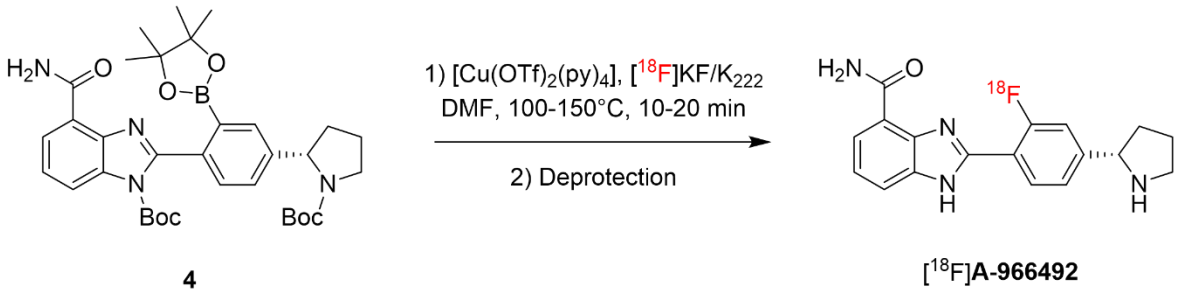


Figure 4.2 – Proposed radiosynthesis of [^{18}F]A-966492 from pinacol ester precursor 4.

Although the reported synthesis for A-966492 enrolled chiral-HPLC for separation of enantiomers following a Suzuki coupling,[95] the first synthetic pathway trialled for the synthesis of precursor **4** followed an initial enantioselective Negishi coupling to remove the need for expensive chiral-HPLC separation. Given the likely interference of a phenol in the Negishi coupling, a methoxy derivative was chosen with the aim of demethylation later in the synthesis to release a phenol for triflation and borylation (Figure 4.3). While this reaction on very similar substrates has been reported both racemically[208] and enantiomerically,[209] unfortunately no product was seen in trials of this reaction, likely due to issues with the *sec*-BuLi which was visually quite cloudy, suggesting significant levels of LiH and deactivation of the reagent. Further exploration of this pathway was paused while there were supply issues for new reagents.

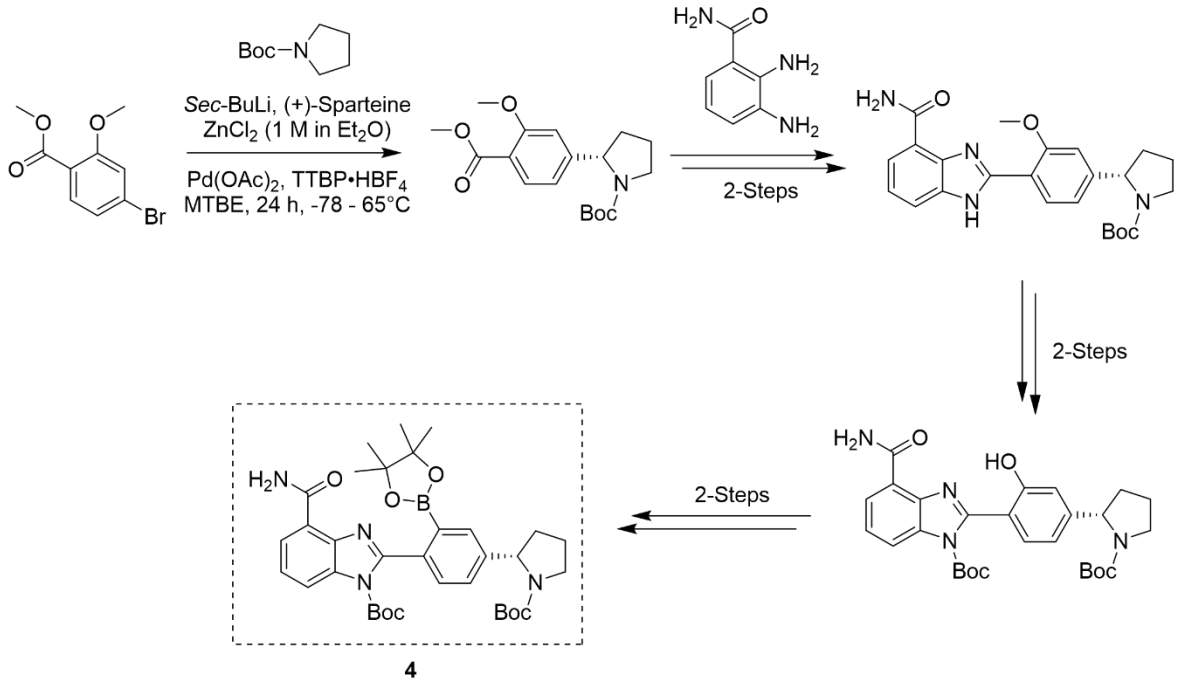
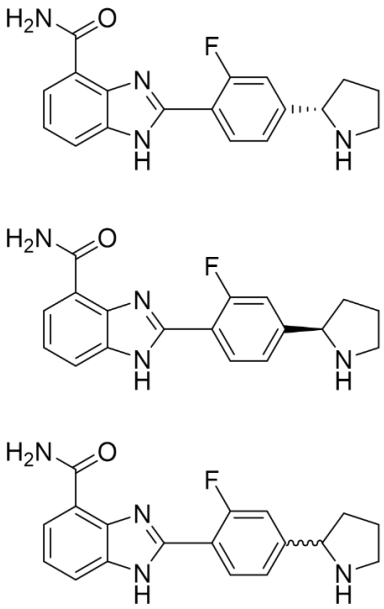


Figure 4.3 – Proposed asymmetric synthesis towards precursor 4

4.3.2 Racemic precursor synthesis progress

A new synthetic route was devised to synthesise the racemic precursor in lieu of the necessary reagents for the enantiomeric synthesis. Revisiting the published data on A-966492 showed that the PARP1 binding profiles and IC_{50} values of the *R*-enantiomer and the racemic compound were comparable with the desired *S*-enantiomer, along with similar brain:plasma ratios of the two enantiomers[95] (Figure 4.4). While ultimately an enantiomerically selective synthesis would be preferred to remove any variables from the biological characterisation, the racemic synthesis is useful to perfect the conditions required and confirm a suitable pathway before using costly enantiomeric ligands (as would

be required for the Negishi coupling). Additionally, if the enantiomeric synthesis proves ineffective, chiral separation during the racemic synthesis could be explored.



	PARP1 K_i (μM)	Cellular EC_{50} (μM)
	0.001	0.001
	0.004	0.009
	0.003	0.004

Figure 4.4 – PARP1 K_i and EC_{50} values of A-966492 enantiomers

The racemic pathway devised followed the reported synthesis of A-966492 uses an initial Suzuki coupling followed by hydrogenation to give **4b**, in place of what would be the single step enantiomeric Negishi coupling (Figure 4.5). Given the scope of Suzuki couplings often proceeding successfully in the presence of hydroxy groups, the synthesis with both hydroxy and methoxy benzene starting materials were performed in parallel in case an extra synthetic step could be saved by using the free hydroxy, or by having a methyl protection in case of complications with the later synthetic steps.

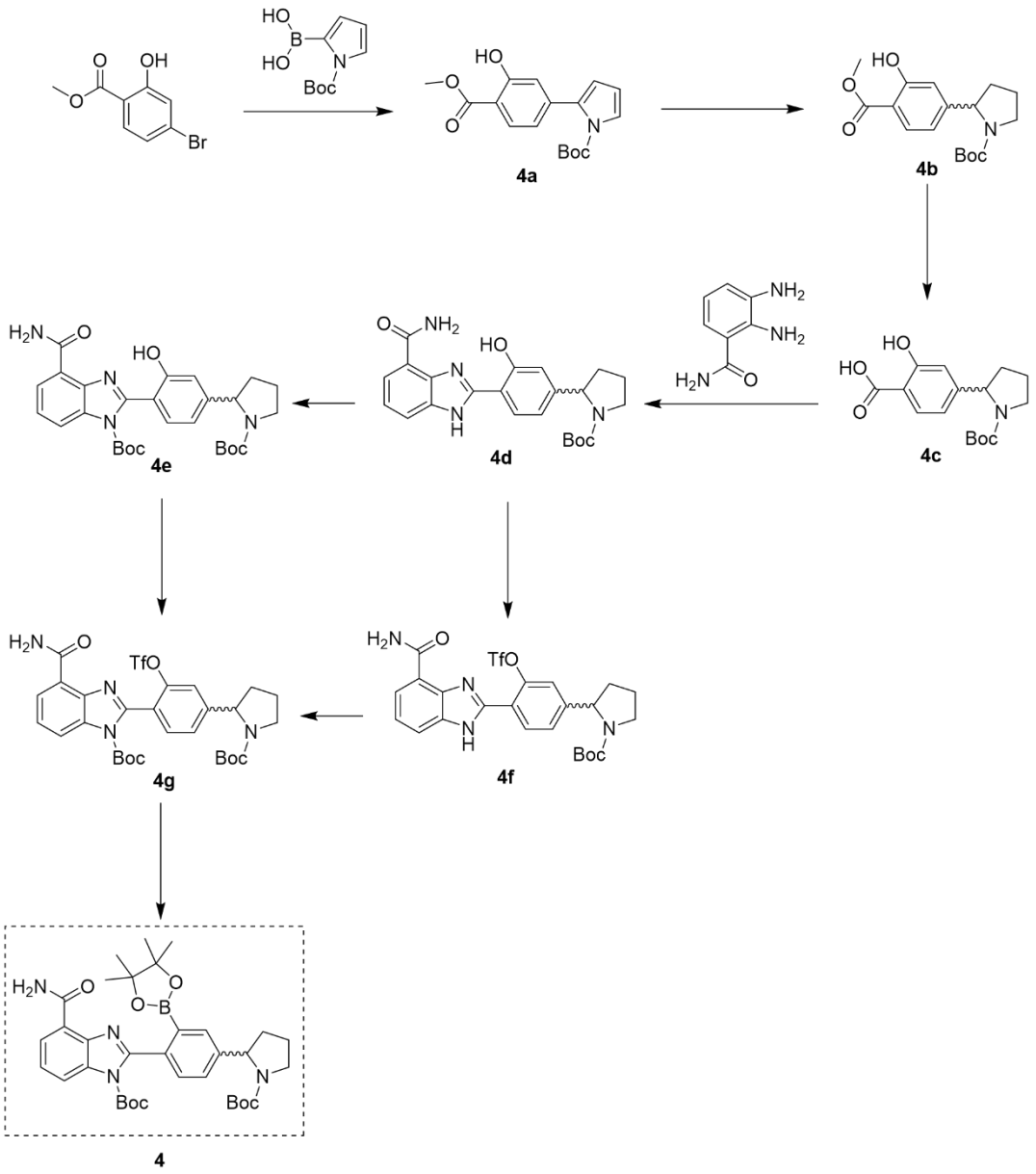


Figure 4.5 – Racemic synthetic pathway towards precursor 4 from methyl-4-bromo-2-hydroxybenzoate

The synthesis from the methoxy starting material showed to have better yields (over 4-steps: methoxy = 34%, hydroxy = 6.7%), however a test demethylation reaction after the benzimidazole formation using BBr_3 showed only BOC deprotection (as expected from the

acidic conditions but could be subsequently re-protected) with no demethylation observed by LCMS (Figure 4.6). Additionally, even though the synthesis from the hydroxy starting material had slightly lower yields, the hydroxy group did not interfere with the key benzimidazole coupling. Therefore, the hydroxy synthesis was prioritised for scale-up and subsequent development.

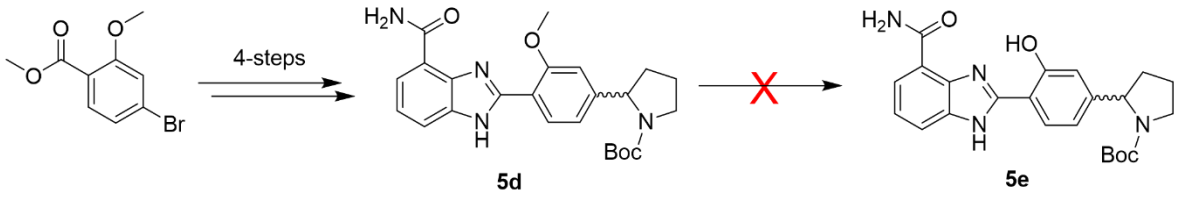


Figure 4.6 – Trialled pathway towards precursor 4 from methyl-4-bromo-2-methoxybenzoate

Issues arose when it came to BOC protection of the resulting benzimidazole given there are three nucleophilic groups on compound **4d**, imidazole-NH, benzamide-NH_2, and phenol-OH, all of which have the potential be become BOC protected. Trial reactions with varying equivalents of BOC-anhydride, triethylamine and DMAP, as well as different temperatures, showed varying levels of single and double protected species (evaluated by LCMS). Given the small scale of these reactions, the location of the BOC protections were not confirmed by NMR. As nitrogen is less electronegative than oxygen, the secondary amine lone pair is more available with nitrogen considered to be a better nucleophile, therefore it is predicted that the reactivity of the three nucleophilic moieties would follow NH > OH > $CONH_2$. However, comparison of the primary amide versus the phenol nucleophilicity is harder to

predict due to delocalisation of the reactive lone pairs into the carbonyl and phenyl moieties respectively, and BOC protection could be happening on the amine and/or amide, as opposed to the phenol. If BOC protection is occurring on the amide, it should in theory be hydrolysable by acid deprotection after the radiolabelling step. Further trial reactions to determine whether performing the triflation before BOC protection could give a cleaner selectivity profile, however in the few conditions trialled, there was a high level of double and triple triflation reactions occurring. Time constraints left further development of this synthesis on hold.

4.3.3 Characterisation of cell line PARP expression

In preparation for future biological testing of [^{18}F]A-966492, multiple cell lines were characterised for their PARP1 and PARP2 expression. The cell lines chosen for comparison were based on data from previous studies in the Cornelissen group, in addition to choosing brain tumour relevant models. PSN-1 cells were chosen as a highly PARP1 expressing control, as determined in previous studies.[201,202] The brain tumour cell lines U87MG and U251MG were chosen to represent high grade glioma as they have previously been used in similar radiotracer studies with good *in vivo* growth.[210] Additionally, MDA-MB-231BR cells were chosen as a representative brain metastasis model with well-reported protocols for *in vivo* models of brain metastases,[211,212] with the parent MDA-MB-231 wildtype cells also assessed for comparison.

Western blot confirmed the high PARP1 expression of PSN-1 cells and revealed lower PARP1 expression in the other four cell lines (Figure 4.7). Interestingly, the MDA-MB-231BR cells showed comparatively more PARP1 than the parent MDA-MB-231 wildtype cells. Given this western blot is comparing expression levels across different cell lines, the B-actin housekeeping protein controls show variation in expression that may not correctly represent protein loading.

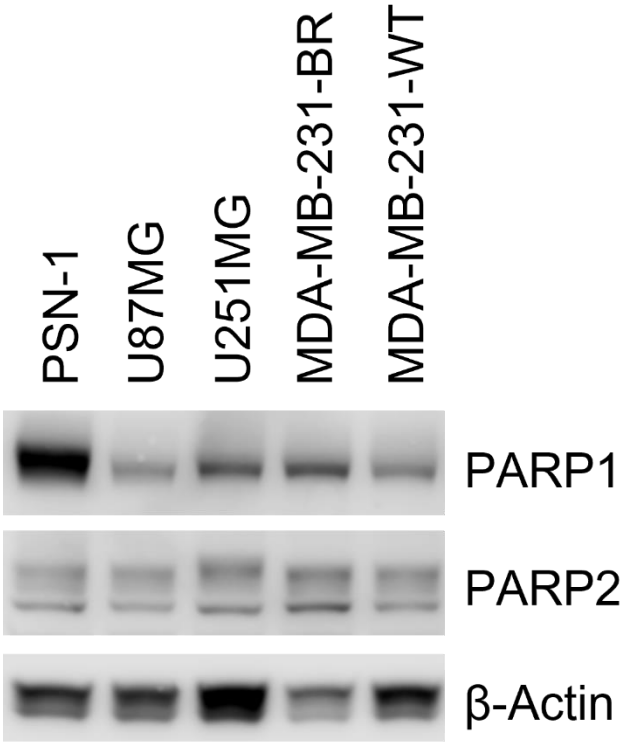


Figure 4.7 – Western blot comparing PARP1 and PARP2 expression levels in PSN-1, U87MG, U251MG, MDA-MB-231BR, and MDA-MB-231 wildtype cells.

4.4 Discussion and future work

4.4.1 Summary of presented work

This work presents the initial stages in the development of BBB-penetrable PARP targeted radiotracer [^{18}F]A-966492. A boronic ester precursor was chosen due to the diverse range of these substrate molecules amenable to ^{18}F-labelling, including from less electronically activated aromatic positions as is the case for A-966492. The first synthetic route designed included an enantioselective Negishi coupling to try and preserve the *S*-stereochemistry present in A-966492, however after a few attempts following reported conditions, no coupling was observed. Further optimisation of this step would likely enable access.

The choice to move to a racemic synthetic pathway was initially due to difficulties in accessing reagents required for the Negishi coupling, but with the reported PARP binding profiles for the *R*-enantiomer and the racemic compound being comparable to the desired *S*-enantiomer, the racemic compound was also considered valuable, in addition to its use for later characterisation of synthesised enantiomers. Chiral separation of the precursor enantiomers could also be considered. The racemic synthesis was trialled both with a free phenol and an *O*-methyl protection, with both routes able to form the benzimidazole. Given the free phenol route was comparable to the *O*-methyl protected route, and the high likelihood of deprotecting the BOC-pyrrole during any demethylation procedures, only the free phenol route was investigated further.

The final steps required to reach the desired BOC protected boronic ester – amine BOC protection, phenol triflation, borylation of the triflate – proved to have several

regioselectivity challenges. While the secondary amine requiring BOC protection is theoretically the strongest nucleophile available in the molecule, the phenol and/or primary amide demonstrated reactivity towards BOC-anhydride with LCMS of the reaction progress showing the main product mass correlating to that of double BOC addition. An alternative route was also tested to triflate the phenol before BOC protection, however even with a tightly controlled triflic anhydride stoichiometry, the major products of this reaction seen by LCMS unsurprisingly showed double and triple triflation. In case of poor labelling with the unprotected amide, a trityl protection could be considered. With the complexities arising from this synthetic route, potential alternative routes have been devised, presented in section 4.4.2.

4.4.2 Alternative routes to a boronic ester precursor

An initial synthetic plan designed by Dr Florian Guibbal (Gouverneur and Cornelissen groups) proposed the incorporation of a pinacol ester in the first stages of the synthesis (Figure 4.8). This synthesis was proposed to follow an enantioselective Negishi coupling with a pinacol ester starting material that would otherwise be unsuitable for the alternative Suzuki coupling pathway reported due to the potential for significant homocoupling. The reason this synthesis was not initially tested was due to the uncertainty of whether the boronic ester, which while generally quite chemically stable, could potentially degrade over the course of the remaining three synthetic steps and their purifications and could still interfere with the first metal coupling. Additionally, the suggested TIPS protection could result in [^{18}F]TIPSF as a by-product during radiofluorination, reducing radiochemical yield.

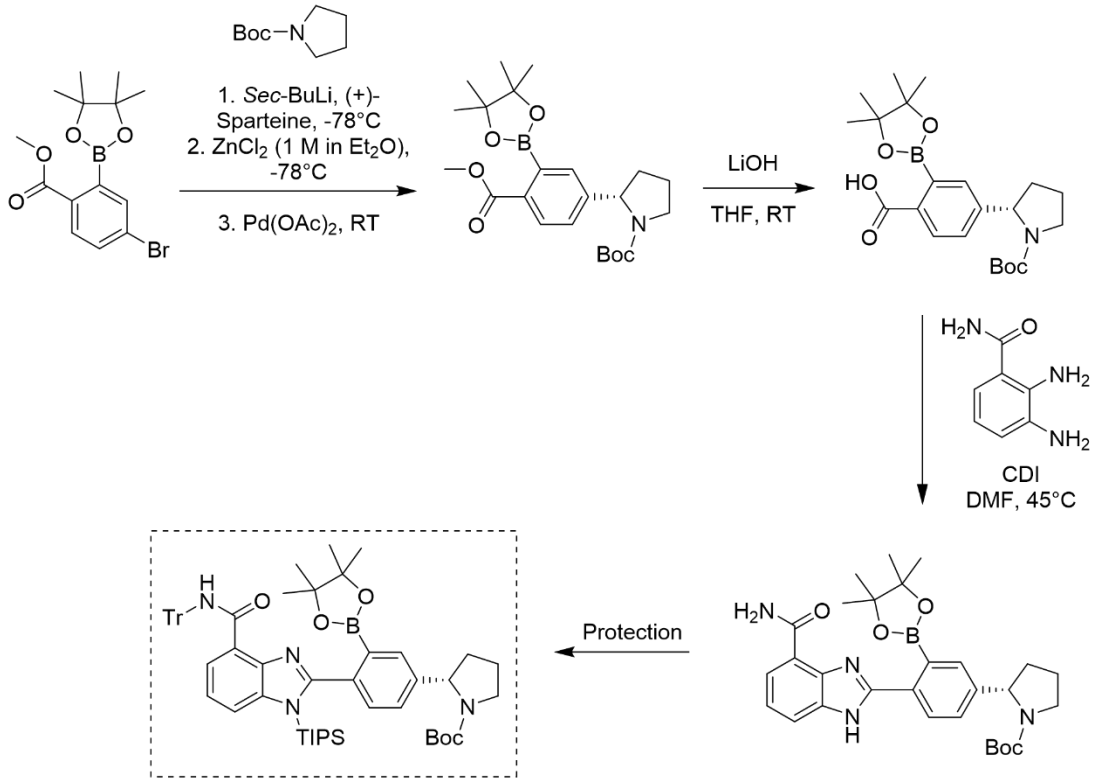


Figure 4.8 – Synthesis proposed by Dr Florian Guibbal towards a boronic pinacol ester precursor for [^{18}F]A-966492.

Another route to be considered following the presented route is one using an alternative hydroxy protecting group that could be deprotected in non-acidic conditions until after BOC protection. Base-labile groups could be more complex given the base hydrolysis conditions needed for the ester hydrolysis step, however they could potentially be added to the benzoic acid species itself before the formation on the benzimidazole. One protecting group to be considered is trimethylsilyl (TMS) that has been reported to protect hydroxide in the presence of carboxylic acids[213] (although there are contradicting reports[214]) and can be deprotected in basic conditions, or more commonly in the presence of fluoride (Figure 4.9).

The main reservation from this synthesis would be whether the TMS group would double protect the phenol and the benzoic acid, and whether TMS deprotection after BOC protection would be successful.

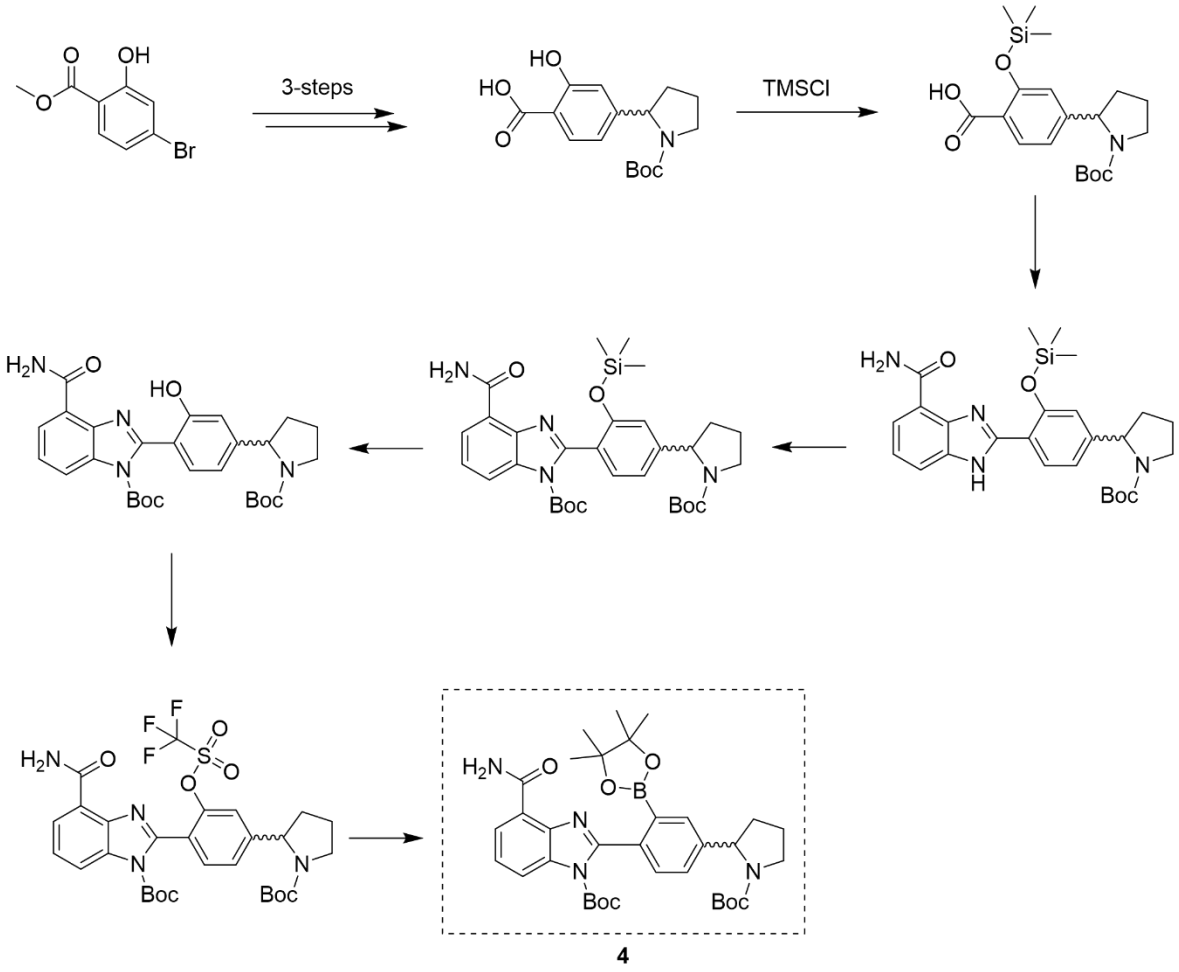


Figure 4.9 – Proposed synthetic route to precursor 4 via TMS protection/deprotection

Another route could use a benzyl (Bn) protection, which could subsequently be deprotected by hydrogenation, potentially being incorporated into the same step as the pyrrole hydrogenation (Figure 4.10). The uncertainty in this pathway is whether the hydrogenation

conditions required would also reduce the imidazole ring, however no literature is reported for such a reduction in a benzimidazole system.

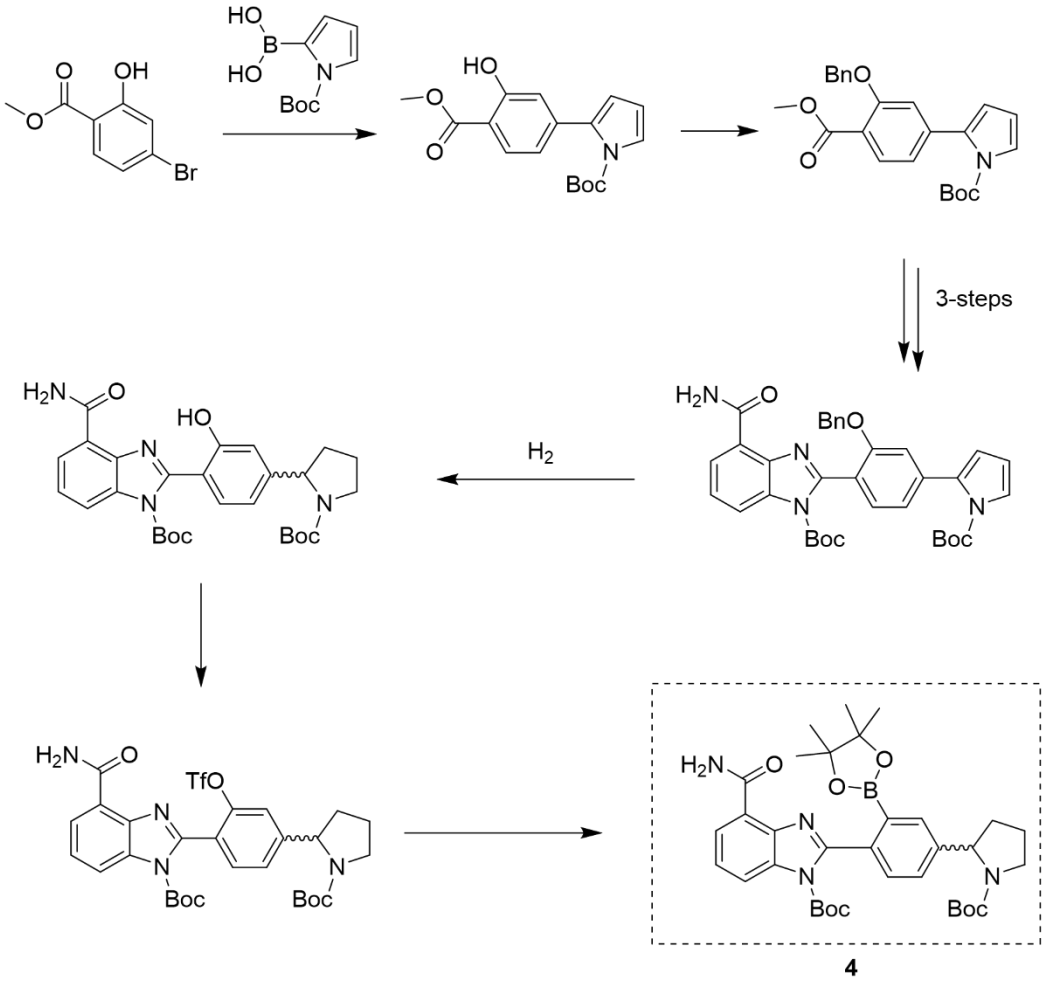


Figure 4.10 – Proposed synthetic route to precursor 4 via benzyl protection/deprotection

Alternatively, different disconnections could be used in the retrosynthetic design of a suitable intermediate to access the desired boronic ester precursor. Coupling of a fully formed BOC (and potentially amide trityl) protected benzimidazole to a suitable aryl core

via C-H activation with an NHC-Pd(II) catalyst could be considered following methods reported by Gu *et al.* on a small scope of benzimidazole compounds.[215] This methodology could be applied for this precursor to a chlorobenzene derivative that is already coupled to the pyrrolidine ring (Figure 4.11). There may however be some selectivity issues that arise from the synthesis of the chlorobenzene-pyrrolidine motif as this preparation would require metal-catalysed coupling of the two cores, likely needing a 1-chloro-4-bromobenzene or 1-chloro-4-iodobenzene coupling partner, where the chloro- moiety required for the subsequent benzimidazole coupling remains intact. Some syntheses have been reported for these substrates coupling to BOC protected pyrrolidine or proline by employing a photoredox iridium catalyst in the presence of a nickel catalyst, selectively coupling in the bromo or iodo position while leaving a chloro-group unaffected (70% and 77% from 1-bromo-4-chlorobenzene and 1-chloro-4-iodo-benzene respectively).[216,217] Substitutions at the 3-position (as would be required for the precursor) on aryl bromide substrates also revealed no steric effects with efficient coupling. Whether the presence of a hydroxy group required in this position for later triflation and borylation would impact either of these coupling reactions has not been reported but could cause interference. Using a bromobenzene intermediate for borylation could be a possibility, however inserting the bromo group before the coupling reactions will again likely interfere with the other halogen-coupling reactions. A later bromination (e.g. with NBS) after the coupling reactions would likely give further regioselectivity issues given the five separate aromatic sites where bromination could occur.

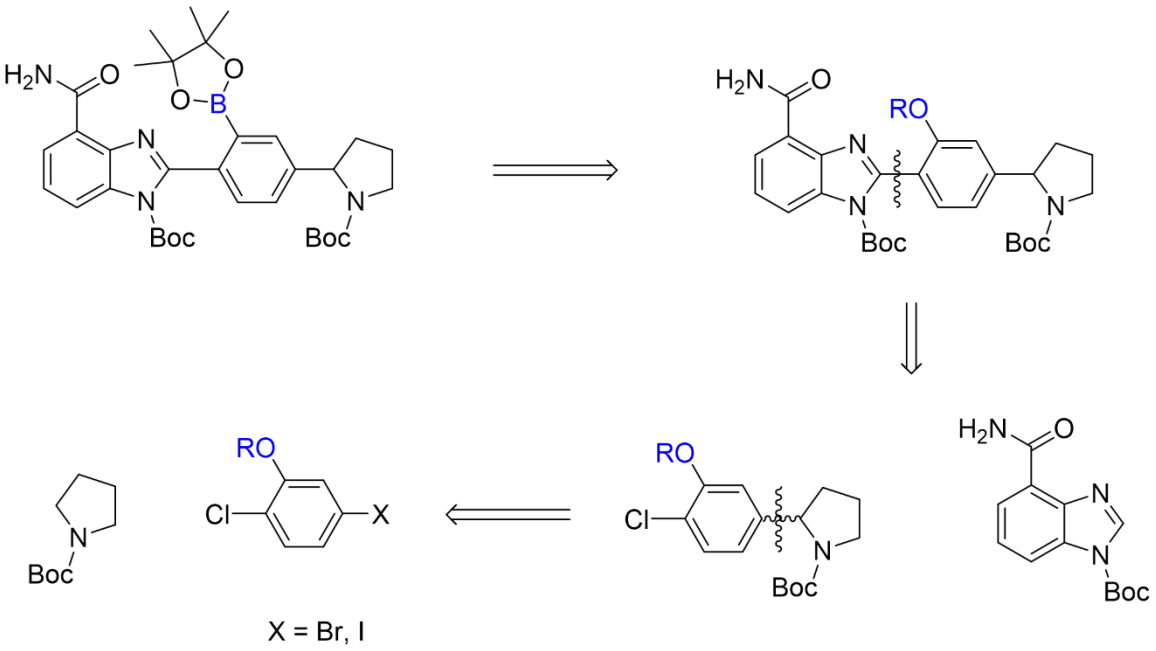


Figure 4.11 – Alternative retrosynthetic route via C-H activation and photoredox-mediated aryl ring coupling.

4.4.3 Alternative radiolabelling and precursor options

As was the case for [^{18}F]AZD1390 in chapter 3, the position to be labelled on [^{18}F]A-966492 is not electronically activated for nucleophilic radiofluorination, reducing the number of radiofluorination methods available. Copper-mediated radiofluorination from a boronic ester precursor was considered the most promising method due to the synthetic accessibility and stability of the boronic ester, as well as the broad substrate scope that have been tested with this methodology, including substrates that are electronically neutral.[162] Alternative methodologies considered were Ritter's ^{18}F-deoxyfluorination[167,218] from the appropriate phenol-uronium salt, or labelling of a diaryliodonium salt precursor,[150] however steric hindrance and stability would likely be an issue for both of these methods

as well as difficulties in inserting an iodine to the molecule for the latter. Further methods that could be investigated for radiofluorination of [^{18}F]A-966492 include those that are discussed for [^{18}F]AZD1390 within chapter 3 (section 3.4.2, page 81).

4.5 Conclusion

While there is still significant work to be done to complete the synthesis and radiolabelling of [^{18}F]A-966492, this work presents the initial steps in precursor synthesis and characterisation of a suitable range of cell lines for future biological evaluation once radiolabelling is achieved. Given the electronically neutral position of radiolabelling is likely not suited to traditional S_NAr radiofluorination methods, multiple precursors may need to be tested using a range of ^{18}F-labelling strategies. Although the target molecule in this report is for a boronic ester precursor with the ultimate aim of copper-mediated radiofluorination, the key triflate intermediate may allow for a range of other leaving groups suitable for alternative [^{18}F]fluoride substitution chemistries to be synthesised.

5 Experimental Write-up

5.1 Synthetic analysis

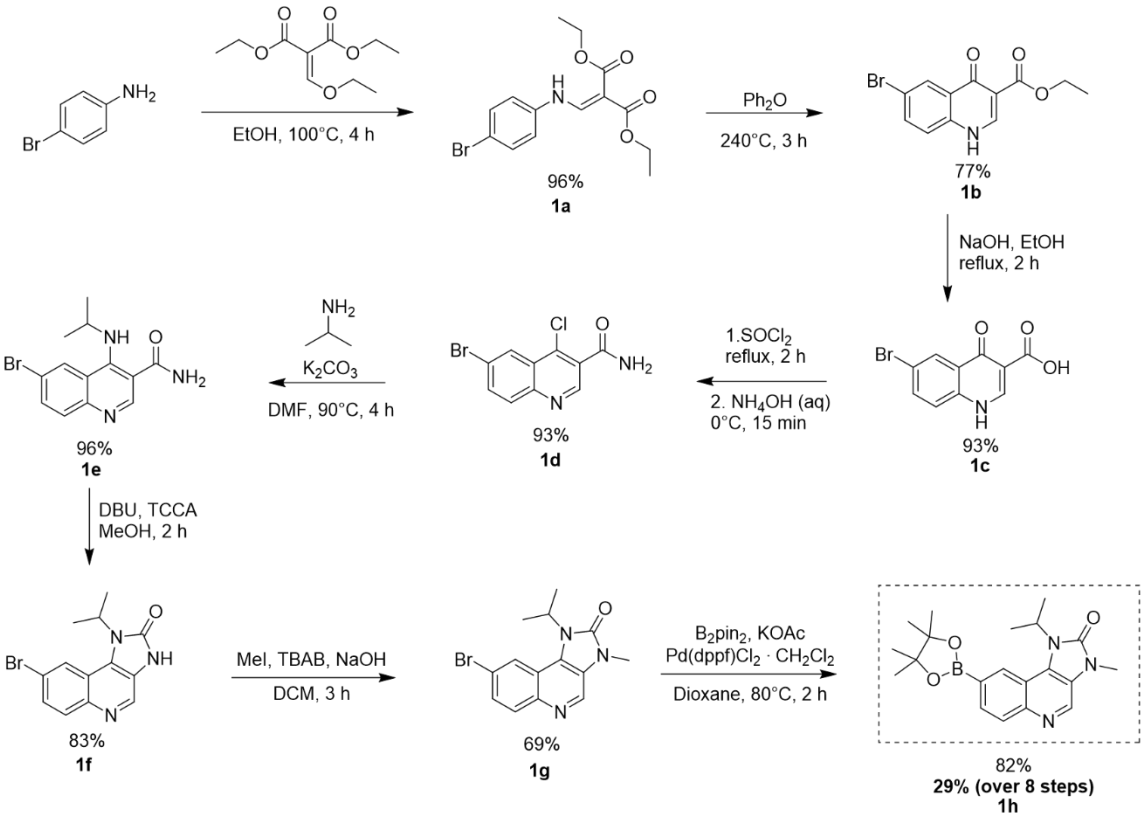
All reagents used in the chemical synthesis described were purchased from commercial sources: Sigma Aldrich, Merck, Alfa Aesar, Fluorochem, Across Organics, Manchester Organics, Fisher Scientific and used without further purification. Moisture sensitive reactions were carried out using purchased dry solvents (Sigma Aldrich). Reactions were monitored by liquid chromatography mass spectrometry (LCMS, Waters HPLC and Acquity QDa Mass detection system), thin layer chromatography (TLC) on silica gel pre-coated aluminium sheets (ALUGRAM® SIL G/UV_{254}, Macherey-Nagel). Visualization was accomplished by irradiation with UV light at 254 nm. Flash column chromatography was performed on silica gel (60A, particle size 35-70 micron, Fluorochem).

All NMR spectra were recorded on a 400 MHz Bruker Ascend™. ^{1}H and ^{13}C NMR spectral data are reported as chemical shifts (δ) in parts per million (ppm) relative to the solvent peak using the Bruker internal referencing procedure (edlock). ^{19}F NMR spectra were used to confirm presence of single species, with spectral data reported as chemical shifts (δ) in parts per million (ppm) relative to an internally calibrated trifluorotoulene standard. Data are reported as follows: chemical shift, multiplicity (s = singlet, d = doublet, t= triplet, q = quartet, p = pentet, m = multiplet), coupling constants (Hz) and integration. NMR spectra were processed with MestReNova 11.0 or higher. Novel compounds in the synthesis of [^{18}F]**1** were characterised by ^{1}H, ^{13}C, ^{19}F NMR and high-resolution mass spectrometry (HRMS) on a Thermo Exactive High-Resolution Orbitrap FTMS using the HESI-II probe for

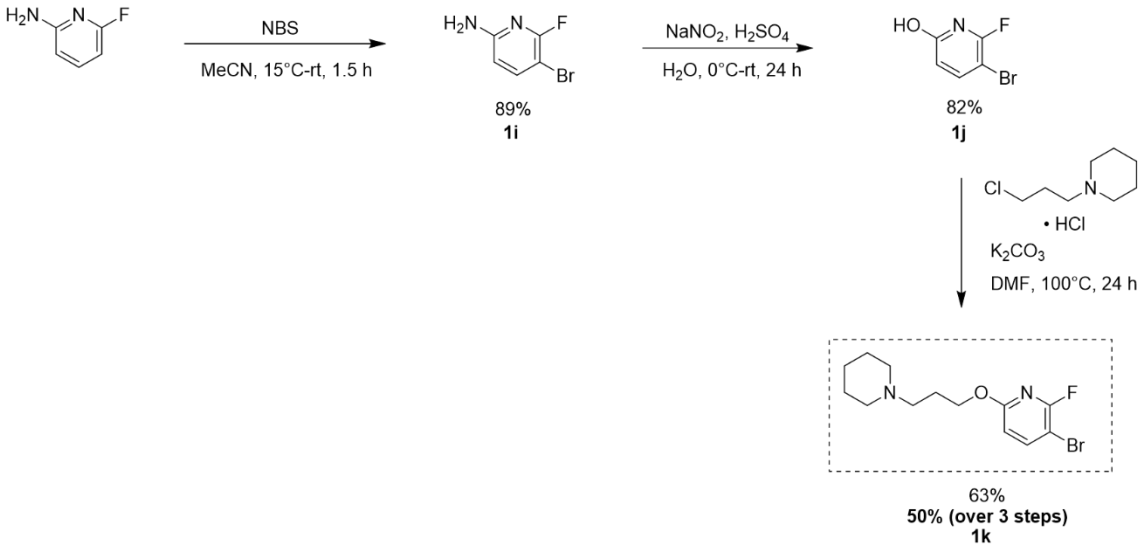
positive electrospray ionisation (ESI^+). Some novel compounds reported in sections 5.4 and 5.5 are only reported with ^1H NMR and low-resolution mass spectrometry data from LCMS and have not been analysed with ^{13}C NMR, therefore structures are not fully confirmed and should be considered as tentative. Some isolated compounds might contain traces of impurities which did not affect the sequential steps and were labelled in the NMR spectra.

5.2 Synthetic experimental for [^{18}F]1

Quinoline core synthesis



Fluoropyridine Core Synthesis



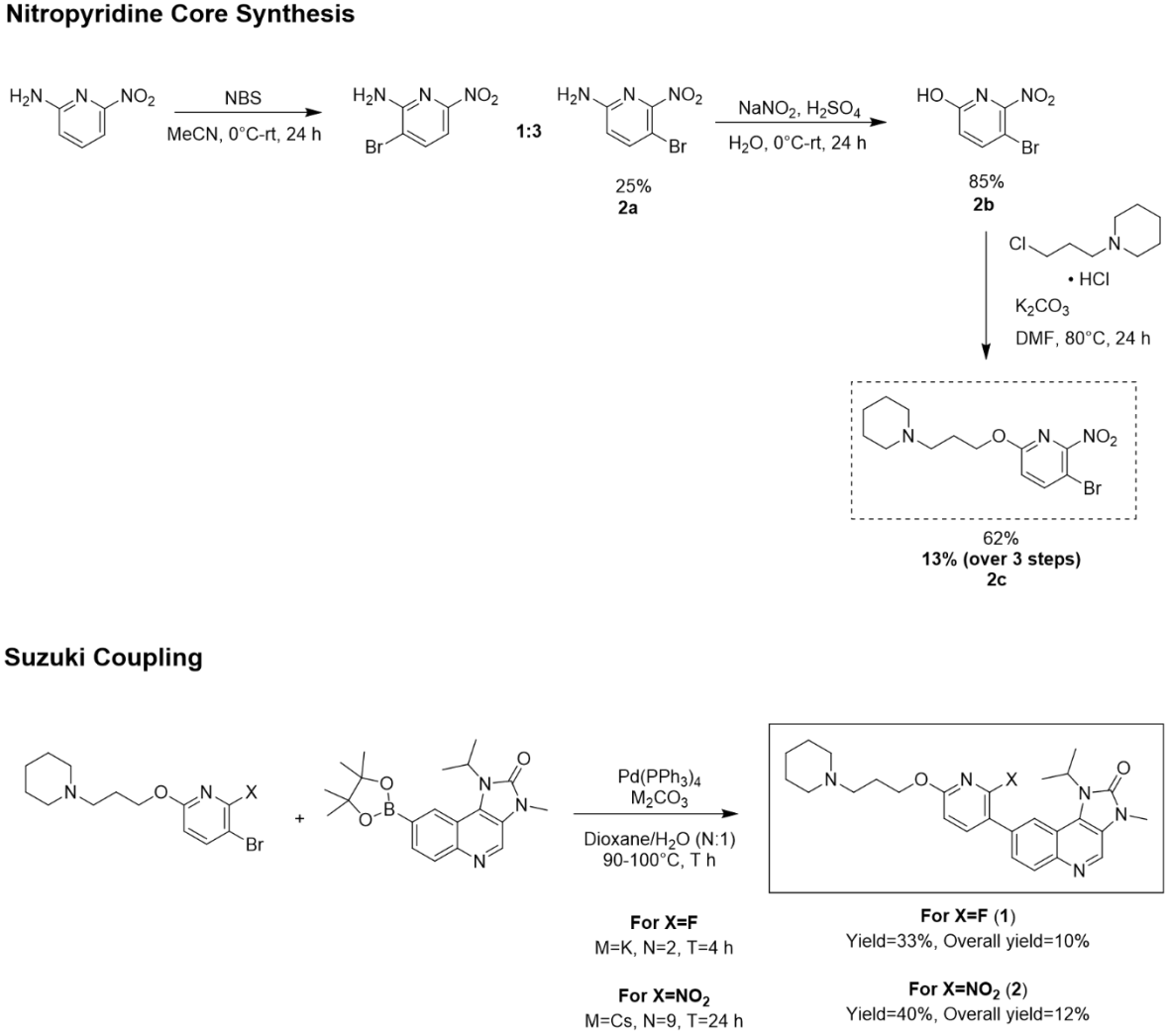
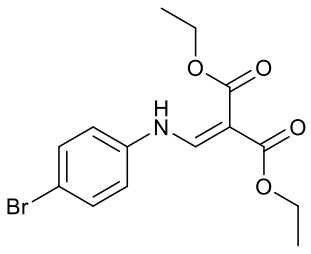


Figure 5.1 – Synthetic pathway towards [^{19}F]1 and precursor 2

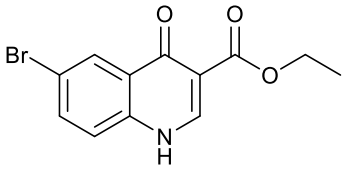
Diethyl 2-(((4-bromophenyl)amino)methylene)malonate (**1a**)



A solution of 4-bromoaniline (15.0 g, 87.2 mmol, 1.00 eq) and diethyl 2-(ethoxymethylene)malonate (20.7 g, 95.9 mmol, 1.10 eq) in EtOH (100 mL) was stirred at 85°C for 4 hours. The reaction was allowed to cool and was filtered to isolate diethyl 2-(((4-bromophenyl)amino)methylene)malonate (28.8 g, 96%) as a white crystalline solid.

^{1}H NMR (400 MHz, DMSO-d_6) δ 10.64 (d, *J* = 13.3 Hz, 1H), 8.35 (d, *J* = 13.5 Hz, 1H), 7.55 (d, *J* = 8.9 Hz, 2H), 7.36 (d, *J* = 8.9 Hz, 2H), 4.20 (q, *J* = 7.1 Hz, 2H), 4.12 (q, *J* = 7.1 Hz, 2H), 1.24 (q, *J* = 7.2 Hz, 6H); **LCMS** (ES+) m/z: $[M+H]^+$ 344. Data is in accordance with known literature.[147]

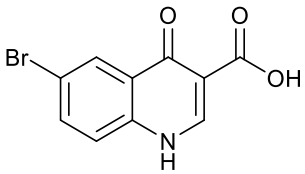
Ethyl 6-bromo-4-oxo-1,4-dihydroquinoline-3-carboxylate (**1b**)



A solution of diethyl 2-(((4-bromophenyl)amino)methylene)malonate (50.5 g, 148 mmol, 1.00 eq) in diphenyl ether (250 mL) was heated to 250°C and stirred for 4 hours open-flask. The reaction was allowed to cool to room temperature and the precipitate was filtered to isolate ethyl 6-bromo-4-oxo-1,4-dihydroquinoline-3-carboxylate (33.5 g, 76.5%) as a beige powder.

^{1}H NMR (400 MHz, DMSO-d_6) δ 8.60 (s, 1H), 8.22 (d, *J* = 2.4 Hz, 1H), 7.76 – 7.69 (m, 1H), 7.58 – 7.51 (m, 1H), 4.19 (q, *J* = 7.0 Hz, 2H), 1.27 (t, *J* = 7.1 Hz, 3H); **LCMS** (ES+) m/z: $[M+H]^+$ 298. Data is in accordance with known literature.[147]

6-Bromo-4-oxo-1,4-dihydroquinoline-3-carboxylic acid (**1c**)

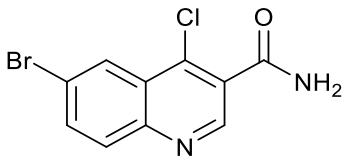


To a stirred solution of ethyl 6-bromo-4-oxo-1,4-dihydroquinoline-3-carboxylate (8.80 g, 29.7 mmol, 1.00 eq) in EtOH (50 mL) was added a solution of NaOH (5.90 g, 149 mmol, 5.00 eq) in water (40 mL) at ambient temperature. The reaction was heated to 80°C and

stirred for 2 hours before cooling to 0°C and adjusting to pH 4 with HCl (12 M). The precipitate formed was isolated by filtration affording 6-bromo-4-oxo-1,4-dihydroquinoline-3-carboxylic acid (7.46 g, 93%) as a pink solid.

^{1}H NMR (400 MHz, DMSO-d_6) δ 14.98 (s, 1H), 13.62 (s, 1H), 8.92 (s, 1H), 8.35 (d, *J* = 2.3 Hz, 1H), 8.03 (dd, *J* = 8.9, 2.4 Hz, 1H), 7.79 (d, *J* = 8.9 Hz, 1H); **LCMS** (ES+) m/z: $[M+H]^+$ 270. Data is in accordance with known literature.[147]

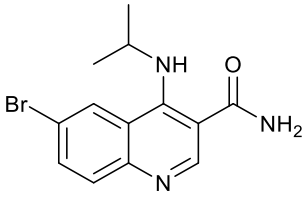
6-Bromo-4-chloroquinoline-3-carboxamide (**1d**)



DMF (100 µL) was added to a stirred suspension of 6-bromo-4-oxo-1H-quinoline-3-carboxylic acid (9.49 g, 35.4 mmol, 1.00 eq) in thionyl chloride (50.0 mL, 686 mmol, 19.4 eq) at 0°C and the mixture slowly heated to 75°C reflux, stirring for 2 hours. The reaction was allowed to cool to ambient temperature, concentrated *in vacuo* and the residue dried twice as an azeotrope with anhydrous hexane to afford a yellow solid, which was added portion-wise to saturated aqueous ammonium hydroxide (50 mL) at 0°C. The resulting suspension was stirred for 15 minutes before isolating the solid by filtration and washing with water to afford 6-bromo-4-chloroquinoline-3-carboxamide (9.46 g, 93%) as a beige solid.

^{1}H NMR (400 MHz, DMSO-d_6) δ 8.91 (s, 1H), 8.43 (dd, *J* = 1.9, 0.8 Hz, 1H), 8.23 (s, 1H), 8.08 – 8.05 (m, 2H), 8.01 (s, 1H); **LCMS** (ES+) m/z: $[M+H]^+$ 287. Data is in accordance with known literature.[147]

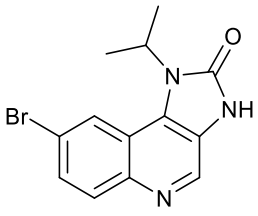
6-Bromo-4-(isopropylamino)quinoline-3-carboxamide (**1e**)



Propan-2-amine (1.03 mL, 12.6 mmol, 1.20 eq) was added to a suspension of 6-bromo-4-chloroquinoline-3-carboxamide (3.00 g, 10.5 mmol, 1.00 eq) and K_2CO_3 (4.35 g, 31.5 mmol, 3.00 eq) in DMF (20 mL) and the mixture stirred at 90°C for 4 hours. The reaction was cooled to ambient temperature and water (100 mL) was added forming a white precipitate that was collected by filtration, washed with pentane and further dried under vacuum to afford 6-bromo-4-(isopropylamino)quinoline-3-carboxamide (3.11 g, 96%) as an off-white powder.

^{1}H NMR (400 MHz, DMSO-d_6) δ 8.60 (s, 1H), 8.48 (d, *J* = 1.8 Hz, 1H), 8.03 (s, 2H), 7.78 (dd, *J* = 8.9, 2.0 Hz, 1H), 7.74 (d, *J* = 8.9 Hz, 1H), 7.50 (s, 1H), 4.13 (s, 1H), 1.23 (d, *J* = 6.3 Hz, 6H); **LCMS** (ES+) m/z: $[M+H]^+$ 310. Data is in accordance with known literature.[147]

8-Bromo-1-isopropyl-3*H*-imidazo[4,5-*c*]quinolin-2-one (**1f**)

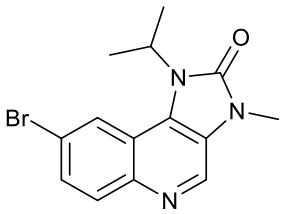


6-Bromo-4-(isopropylamino)quinoline-3-carboxamide (9.18 g, 29.8 mmol, 1.00 eq) and 1,8-diazabicyclo[5.4.0]undec-7-ene (8.90 mL, 59.6 mmol, 2.00 eq) were suspended in MeOH (61.2 mL) and cooled to 0°C before adding a solution of trichloroisocyanuric acid (3.46 g, 14.9 mmol, 0.50 eq) in methanol (20 mL) dropwise over 10 minutes. The reaction was returned to ambient temperature and stirred for 20 hours before filtering, isolating 8-bromo-1-isopropyl-3*H*-imidazo[4,5-*c*]quinolin-2-one (5.08 g) as a cream solid. Further material was isolated by

concentrating the filtrate and resuspending in water (50 mL) before adjusting to pH 3 (HCl, 1 M) and filtering the resulting precipitate (3.51 g). Overall yield 8.59 g, 94%.

^{1}H NMR (400 MHz, DMSO-d_6) δ 11.54 (s, 1H), 8.66 (s, 1H), 8.40 (d, *J* = 1.9 Hz, 1H), 7.95 (d, *J* = 9.0 Hz, 1H), 7.72 (dd, *J* = 9.0, 2.0 Hz, 1H), 5.12 (hept, *J* = 6.7 Hz, 1H), 1.62 (d, *J* = 6.8 Hz, 6H); **LCMS** (ES+) m/z: $[M+H]^+$ 308. Data is in accordance with known literature.[147]

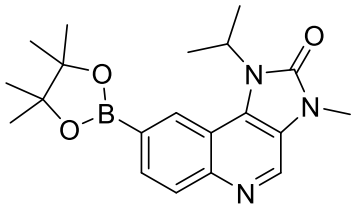
8-Bromo-1-isopropyl-3-methyl-1,3-dihydro-2*H*-imidazo[4,5-*c*]quinolin-2-one (**1g**)



8-Bromo-1-isopropyl-1,3-dihydro-2*H*-imidazo[4,5-*c*]quinolin-2-one (7.80 g, 25.5 mmol, 1.00 eq), tetrabutylammonium bromide (821 mg, 2.55 mmol, 0.100 eq) and methyl iodide (3.20 mL, 51.0 mmol, 2.00 eq) were suspended in DCM (100 mL) before adding a solution of NaOH (1.53 g, 38.2 mmol, 1.50 eq) in water (50 mL) and stirring vigorously at ambient temperature for 3 hours. The reaction was concentrated removing DCM *in vacuo* before diluting with MeOH (30 mL) and filtering to isolate 8-bromo-1-isopropyl-3-methyl-1,3-dihydro-2*H*-imidazo[4,5-*c*]quinolin-2-one (6.86 g, 84%) as a white powder.

^{1}H NMR (400 MHz, DMSO-d_6) δ 8.92 (s, 1H), 8.44 (s, 1H), 7.99 (d, *J* = 9.1 Hz, 1H), 7.75 (dd, *J* = 9.2, 2.0 Hz, 1H), 5.19 (hept, *J* = 6.8 Hz, 1H), 3.49 (s, 3H), 1.63 (d, *J* = 6.7 Hz, 6H); **LCMS** (ES+) m/z: $[M+H]^+$ 322. Data is in accordance with known literature.[147]

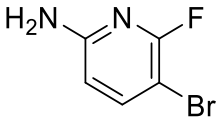
1-isopropyl-3-methyl-8-(4,4,5,5-tetramethyl-1,3,2-dioxaborolan-2-yl)-1,3-dihydro-2*H*-imidazo[4,5-*c*]quinolin-2-one (**1h**)



In a flame-dried two-necked 25 mL round bottom flask, 8-bromo-1-isopropyl-3-methyl-1,3-dihydro-2*H*-imidazo[4,5-*c*]quinolin-2-one (500 mg, 1.56 mmol, 1.00 eq), potassium acetate (460 mg, 4.68 mmol, 3.00 eq) and bis(pinacolate)diboron (594 mg, 2.34 mmol, 1.50 eq) were dissolved in anhydrous 1,4-dioxane (25 mL) under an argon atmosphere. The mixture was stirred and flushed with argon for 15 minutes before adding $Pd(dppf)Cl_2 \cdot CHCl_2$ (64.0 mg, 5% mol) and flushing for a further 15 minutes. The reaction was heated to 80°C, stirred for 24 hours, then allowed to cool to room temperature and filtered through Celite (3 cm) eluting with EtOAc (500 mL). The filtrate was reduced to a fifth of its volume before partitioning with water (100 mL) and the aqueous phase re-extracted with further EtOAc (100 mL). The combined organics were washed with brine (100 mL), dried over $MgSO_4$ and concentrated *in vacuo* to a crude brown solid. The solid was suspended in *n*-pentane (40 mL), sonicated and filtered to afford 1-isopropyl-3-methyl-8-(4,4,5,5-tetramethyl-1,3,2-dioxaborolan-2-yl)-1,3-dihydro-2*H*-imidazo[4,5-*c*]quinolin-2-one (470 mg, 82%) as a brown powder.

^{1}H NMR (400 MHz, $CDCl_3$) δ 8.73–8.66 (m, 2H), 8.10 (d, *J* = 8.4 Hz, 1H), 7.94 (dd, *J* = 8.5, 1.3 Hz, 1H), 5.31 (p, *J* = 6.9 Hz, 1H), 3.55 (s, 3H), 1.78 (d, *J* = 7.0 Hz, 6H), 1.38 (s, 12H). **^{13}C NMR** (101 MHz, $CDCl_3$) δ 153.8, 146.8, 133.0, 131.4, 130.2, 129.7, 129.1, 123.0, 115.3, 84.3, 67.2, 27.3, 25.0, 20.6. **HRMS** (ESI) for $C_{20}H_{26}BN_3O_3$ $[M+H]^+$ requires 368.2141 found 368.2141.

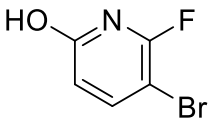
5-Bromo-6-fluoropyridin-2-amine (**1i**)



N-bromosuccinimide (16.7 g, 93.7 mmol, 1.05 eq) was added portion-wise over 25 minutes to a solution of 6-fluoropyridin-2-amine (10.0 g, 89.2 mmol, 1.00 eq) in acetonitrile (80 mL) maintained at 10-20°C. The reaction was stirred at ambient temperature for 1.5 hours then concentrated *in vacuo* to a brown residue which was triturated in water (100 mL) and the solid filtered to isolate 5-bromo-6-fluoropyridin-2-amine (15.1 g, 89%) as a pale brown solid.

^{1}H NMR (400 MHz, $CDCl_3$) δ 7.59 (dd, *J* = 8.9, 8.3 Hz, 1H), 6.25 (dd, *J* = 8.3, 1.4 Hz, 1H), 3.84 (s, 2H). **LCMS** (ES) m/z: $[M + H]^+$ 192. Data is in accordance with known literature.[147]

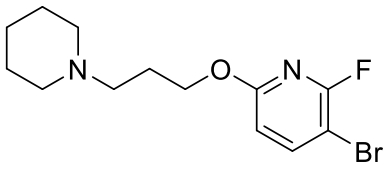
5-Bromo-6-fluoropyridin-2-ol (**1j**)



5-Bromo-6-fluoropyridin-2-amine (4.00 g, 20.9 mmol, 1.00 eq) was suspended in a solution of H_2SO_4 (18 M, 11.6 mL, 209 mmol, 10.0 eq) in water (30 mL) and cooled to 0°C before adding a solution of $NaNO_2$ (4.34 g, 62.8 mmol, 3.00 eq) in water (10 mL) dropwise over 1 hour, maintaining the temperature below 5°C. The reaction was then stirred at 0°C for 1 hour before allowing it to warm to room temperature and stirring overnight for a total of 24 hours. The precipitate was then collected by filtration to isolate 5-bromo-6-fluoropyridin-2-ol (3.30 g, 82%) as a brown solid.

^{1}H NMR (400 MHz, $CDCl_3$) δ 10.16 (s, 1H), 7.85 (t, *J* = 8.7 Hz, 1H), 6.59 (dd, *J* = 8.5, 0.7 Hz, 1H); **LCMS** (ES) m/z: $[M + H]^+$ 192. Data is in accordance with known literature.[147]

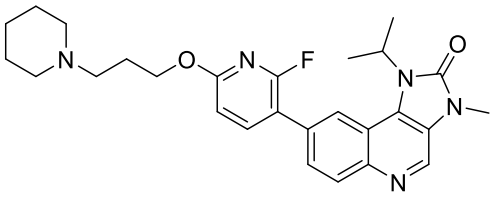
3-Bromo-2-fluoro-6-(3-(piperidin-1-yl)propoxy)pyridine (**1k**)



5-Bromo-6-fluoropyridin-2-ol (2.62 g, 13.6 mmol, 1.00 eq) was dissolved in DMF (80 mL), then 1-(3-chloropropyl)piperidine monohydrochloride (3.35 g, 16.4 mmol, 1.20 eq) and K_2CO_3 (5.66 g, 40.9 mmol, 3.00 eq) were added and the mixture stirred at 100°C for 24 hours. The reaction was cooled to room temperature before adding water (100 mL) and extracting with EtOAc (4 × 30 mL). Combined organics washed with aqueous LiCl (1 M, 100 mL) then brine (100 mL), dried over $MgSO_4$ and concentrated to a red oil. The extracted crude was purified by silica gel chromatography, eluting with 0-2% 2 N methanolic ammonia in ethyl acetate to isolate 3-bromo-2-fluoro-6-(3-(piperidin-1-yl)propoxy)pyridine (2.71 g, 63%) as a red oil.

^{1}H NMR (400 MHz, $CDCl_3$) δ 7.73 (t, *J* = 8.8 Hz, 1H), 6.51 (dd, *J* = 8.4, 0.9 Hz, 1H), 4.27 (t, *J* = 6.5 Hz, 2H), 2.45–2.30 (m, 6H), 1.99–1.88 (m, 2H), 1.57 (p, *J* = 5.6 Hz, 6H), 1.47–1.37 (m, 2H). **HRMS** (ESI) for $C_{13}H_{18}BrFN_2O$ $[M+H]^+$ requires 319.0639, found 319.0634. Data is in accordance with known literature.[147]

8-(2-fluoro-6-(3-(piperidin-1-yl)propoxy)pyridin-3-yl)-1-isopropyl-3-methyl-1,3-dihydro-2*H*-imidazo[4,5-*c*]quinolin-2-one (**1**)

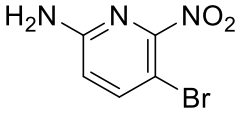


In a two neck 25 mL round bottom flask, 3-bromo-2-fluoro-6-(3-(piperidin-1-yl)propoxy)pyridine (104 mg, 0.328 mmol, 1.00 eq), was added and dissolved in 1,4-dioxane (3.60 mL) and water (1.80 mL). 1-sopropyl-3-methyl-8-(4,4,5,5-tetramethyl-1,3,2-dioxaborolan-2-yl)-1,3-dihydro-2*H*-imidazo[4,5-*c*]quinolin-2-one (132 mg, 0.361 mmol, 1.10 eq) and K_2CO_3 (136 mg, 0.984 mmol, 3.00 eq) were added and flushed with argon for 5 min before adding tetrakis(triphenylphosphine)palladium(0) (19.0 mg, 0.016 mmol, 0.05 eq) and heating to 100°C reflux for 24 hours. The reaction was allowed to cool before passing through Celite, eluting with acetone (150 mL) and drying to a brown crude oil. The crude was suspended in water and extracted with EtOAc (3 × 50 mL), combined organics were washed with brine (100 mL), dried over $MgSO_4$ and concentrated *in vacuo* to a yellow residue (110 mg). The extracted crude was purified by silica gel chromatography, first eluting impurities with MeOH, then the product was eluted in 4% 2 N methanolic ammonia in DCM, isolating 8-(2-fluoro-6-(3-(piperidin-1-yl)propoxy)pyridin-3-yl)-1-isopropyl-3-methyl-1,3-dihydro-2*H*-imidazo[4,5-*c*]quinolin-2-one (51 mg, 33%) as a white crystalline solid.

^{1}H NMR (400 MHz, $CDCl_3$) δ 8.69 (s, 1H), 8.43 (s, 1H), 8.19 (d, *J* = 8.8 Hz, 1H), 7.90 (dd, *J* = 10.2, 8.2 Hz, 1H), 7.72 (d, *J* = 8.9 Hz, 1H), 6.77 (dd, *J* = 8.2, 1.0 Hz, 1H), 5.26 (p, *J* = 7.0 Hz, 1H), 4.38 (t, *J* = 6.5 Hz, 2H), 3.58 (s, 3H), 2.52–2.44 (m, 2H), 2.41 (s, 4H), 2.06–1.99 (m, 2H), 1.76 (d, *J* = 6.9 Hz, 6H), 1.59 (p, *J* = 5.6 Hz, 4H), 1.44 (q, *J* = 6.0 Hz, 2H). **^{13}C NMR** (101 MHz,

$CDCl_3$) δ 162.34 (d, *J* = 13.9 Hz), 159.9, 157.5, 153.7, 144.5, 142.8 (d, *J* = 4.3 Hz), 132.6, 131.8 (d, *J* = 5.4 Hz), 131.6, 129.3, 126.8 (d, *J* = 1.8 Hz), 123.3, 115.6, 113.7 (d, *J* = 26.3 Hz), 108.4 (d, *J* = 5.2 Hz), 65.6, 55.9, 54.6, 27.3, 26.3, 25.7, 24.3, 20.5. **^{19}F NMR** (376 MHz, $CDCl_3$) δ -73.3 (d, *J* = 10.1 Hz) (potential rotamer). **HRMS** (ESI) for $C_{27}H_{32}FN_5O_2$ $[M+H]^+$ requires 478.2613, found 478.2610. Data is in accordance with known literature.[147]

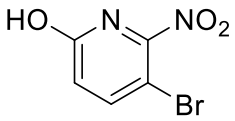
5-Bromo-6-nitropyridin-2-amine (**2a**)



A solution of 6-nitropyridin-2-amine (3.03 g, 21.7 mmol, 1.00 eq) in acetonitrile (200 mL) was cooled to 0°C and protected from light before adding *N*-bromosuccinimide (3.87 g, 21.7 mmol, 1.00 eq) portion-wise over 1.5 h. The reaction was allowed to reach room temperature overnight before addition of saturated aqueous $Na_2S_2O_3$ (50 mL) and water (100 mL) and extraction into EtOAc (3 × 100 mL). The combined organic fractions were washed with brine (100 mL), dried over magnesium sulphate, and concentrated *in vacuo* to afford a yellow solid. The product was purified by silica gel chromatography eluting with 10-50% EtOAc in *n*-pentane, affording pure 5-bromo-6-nitropyridin-2-amine (1.20 g, 25%).

^{1}HNMR (400 MHz, DMSO) δ 7.84 (d, *J* = 8.8 Hz, 1H), 7.01 (s, 2H), 6.66 (d, *J* = 8.8 Hz, 1H). **HRMS** (ESI) for $C_5H_4BrN_3O_2$ $[M+H]^+$ requires 218.9223 found 218.9224. Data is in accordance with known literature.[153]

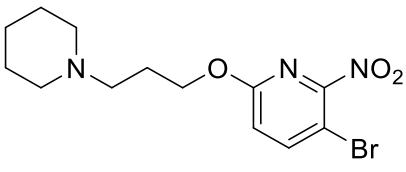
5-Bromo-6-nitropyridin-2-ol (**2b**)



A solution of 5-Bromo-6-nitropyridin-2-amine (2.11 g, 9.69 mmol, 1.00 eq) in water (150 mL) was cooled to 0°C before addition of H_2SO_4 (18 M, 5.40 mL, 97.20 mmol, 10.0 eq). A cooled solution of $NaNO_2$ (2.01 g, 29.1 mmol, 3.00 eq) in water (25 mL) was then added portion-wise. The resulting suspension was stirred vigorously for at 0°C for 45 min, then allowed to return to room temperature, stirring overnight. The precipitate was then collected by filtration and dried with pentane to isolate 5-bromo-6-nitropyridin-2-ol (1.79 g, 85%) as a brown solid.

^{1}H NMR (400 MHz, Acetone) δ 10.83 (s, 1H), 8.20 (d, *J* = 8.6 Hz, 1H), 7.05 (d, *J* = 8.6 Hz, 1H). **^{13}C NMR** (101 MHz, Acetone) δ 162.9, 156.19, 147.6, 116.4, 99.1. **HRMS** (ESI) for $C_5H_3BrN_2O_3$ $[M-H]^-$ requires 218.9223, found 218.9224.

3-Bromo-2-nitro-6-(3-(piperidin-1-yl)propoxy)pyridine (**2c**)

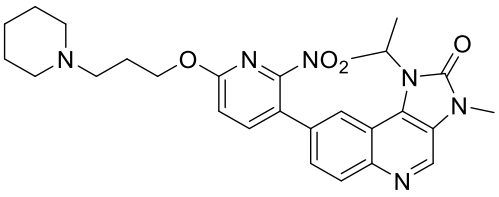


5-Bromo-6-nitropyridin-2-ol (100 mg, 0.457 mmol, 1.00 eq) was dissolved in DMF (8 mL), then 1-(3-chloropropyl)piperidine monohydrochloride (112 mg, 0.548 mmol, 1.20 eq) and K_2CO_3 (189 mg, 1.37 mmol, 3.00 eq) were added and the mixture stirred at 80°C for 24 hours. The reaction was cooled to room temperature before adding water (8 mL) and extracting with ethyl acetate (4 × 7 mL). Combined organics washed with aqueous LiCl (1 M, 20 mL) then brine (20 mL), dried over $MgSO_4$ and concentrated to a brown oil. The extracted crude was purified by silica gel chromatography, eluting with 2-

10% MeOH in DCM to isolate 3-bromo-2-nitro-6-(3-(piperidin-1-yl)propoxy)pyridine (98.0 mg, 62%) as a brown oil.

^{1}H NMR (400 MHz, Acetone-d_6) δ 8.21 (d, *J* = 8.8 Hz, 1H), 7.11 (d, *J* = 8.8 Hz, 1H), 4.37 (t, *J* = 6.6 Hz, 2H), 2.44 – 2.29 (m, 6H), 1.93 (p, *J* = 6.8 Hz, 2H), 1.51 (p, *J* = 5.5 Hz, 4H), 1.40 (q, *J* = 6.0 Hz, 2H). **^{13}C NMR** (101 MHz, $CDCl_3$) δ 162.0, 155.0, 145.6, 116.7, 100.2, 66.6, 55.9, 54.7, 26.3, 26.1, 24.5. **HRMS** (ESI) for $C_{13}H_{18}BrN_3O_3$ $[M+H]^+$ requires 346.0595, found 346.0579.

1-Isopropyl-3-methyl-8-(2-nitro-6-(3-(piperidin-1-yl)propoxy)pyridin-3-yl)-1,3-dihydro-2*H*-imidazo[4,5-*c*]quinolin-2-one (2)



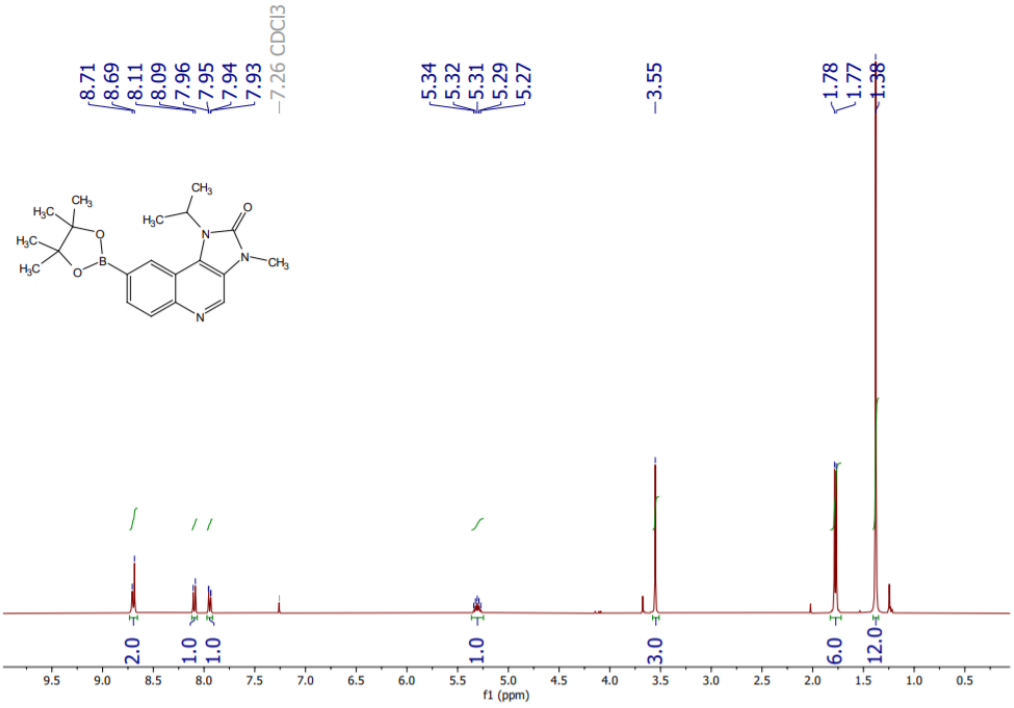
In a two neck 25 mL round bottom flask, 3-bromo-2-nitro-6-(3-(piperidin-1-yl)propoxy)pyridine (248 mg, 0.720 mmol, 1.00 eq), was added and dissolved in 1,4-dioxane (11.7 mL) and water (1.3 mL). 1-Isopropyl-3-methyl-8-(4,4,5,5-tetramethyl-1,3,2-dioxaborolan-2-yl)-1,3-dihydro-2*H*-imidazo[4,5-*c*]quinolin-2-one (529 mg, 1.44 mmol, 2.00 eq) and Cs_2CO_3 (704 mg, 2.16 mmol, 3.00 eq) were added and flushed with argon for 10 min before adding tetrakis(triphenylphosphine)palladium(0) (250 mg, 0.216 mmol, 0.300 eq), flushed with argon for a further 10 min, then heated to 90°C reflux for 15 hours. The reaction was allowed to cool before passing though celite eluting with EtOAc (50 mL), the collected organic washed with water (60 mL) and brine (60 mL), dried over $MgSO_4$ and concentrated *in vacuo* to a yellow residue (610 mg). The extracted crude was purified by silica gel chromatography eluting with 0-20% MeOH in DCM, isolating 1-

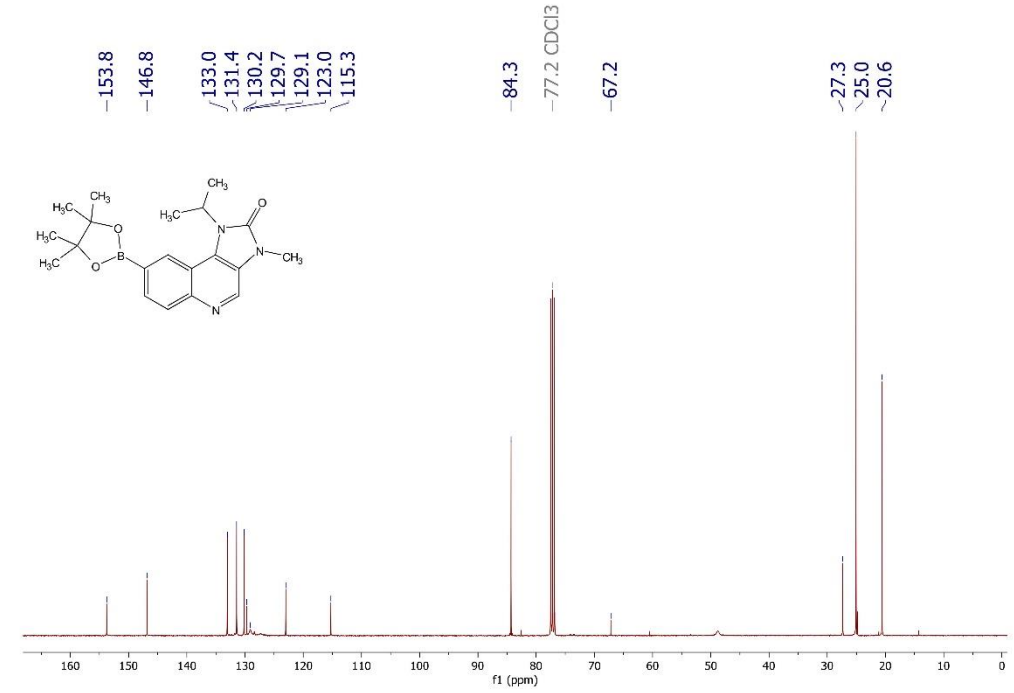
isopropyl-3-methyl-8-(2-nitro-6-(3-(piperidin-1-yl)propoxy)pyridin-3-yl)-1,3-dihydro-2*H*-imidazo[4,5-*c*]quinolin-2-one (102 mg, 28%) as a yellow crystalline solid.

^{1}H NMR (400 MHz, $CDCl_3$) δ 8.72 (s, 1H), 8.21 (d, *J* = 8.8 Hz, 1H), 8.12 (d, *J* = 1.9 Hz, 1H), 7.87 (d, *J* = 8.4 Hz, 1H), 7.54 (dd, *J* = 8.7, 1.9 Hz, 1H), 7.09 (d, *J* = 8.5 Hz, 1H), 5.19 – 5.04 (m, 1H), 4.45 (t, *J* = 6.4 Hz, 2H), 3.57 (s, 3H), 2.62 – 2.40 (m, 6H), 2.07 (p, *J* = 6.6 Hz, 2H), 1.73 (d, *J* = 6.9 Hz, 6H), 1.66 (p, *J* = 5.7 Hz, 4H), 1.51 – 1.43 (m, 4H). **^{13}C NMR** (101 MHz, $CDCl_3$) δ 162.3, 155.1, 153.6, 144.9, 143.3, 133.1, 132.3, 132.3, 129.3, 126.5, 123.6, 121.4, 115.6, 115.4, 66.0, 55.7, 54.5, 31.0, 29.8, 27.4, 25.9, 25.5, 24.1, 20.6. **HRMS** (ESI) for $C_{27}H_{32}N_6O_4$ $[M+H]^+$ requires 505.2558, found 505.2557.

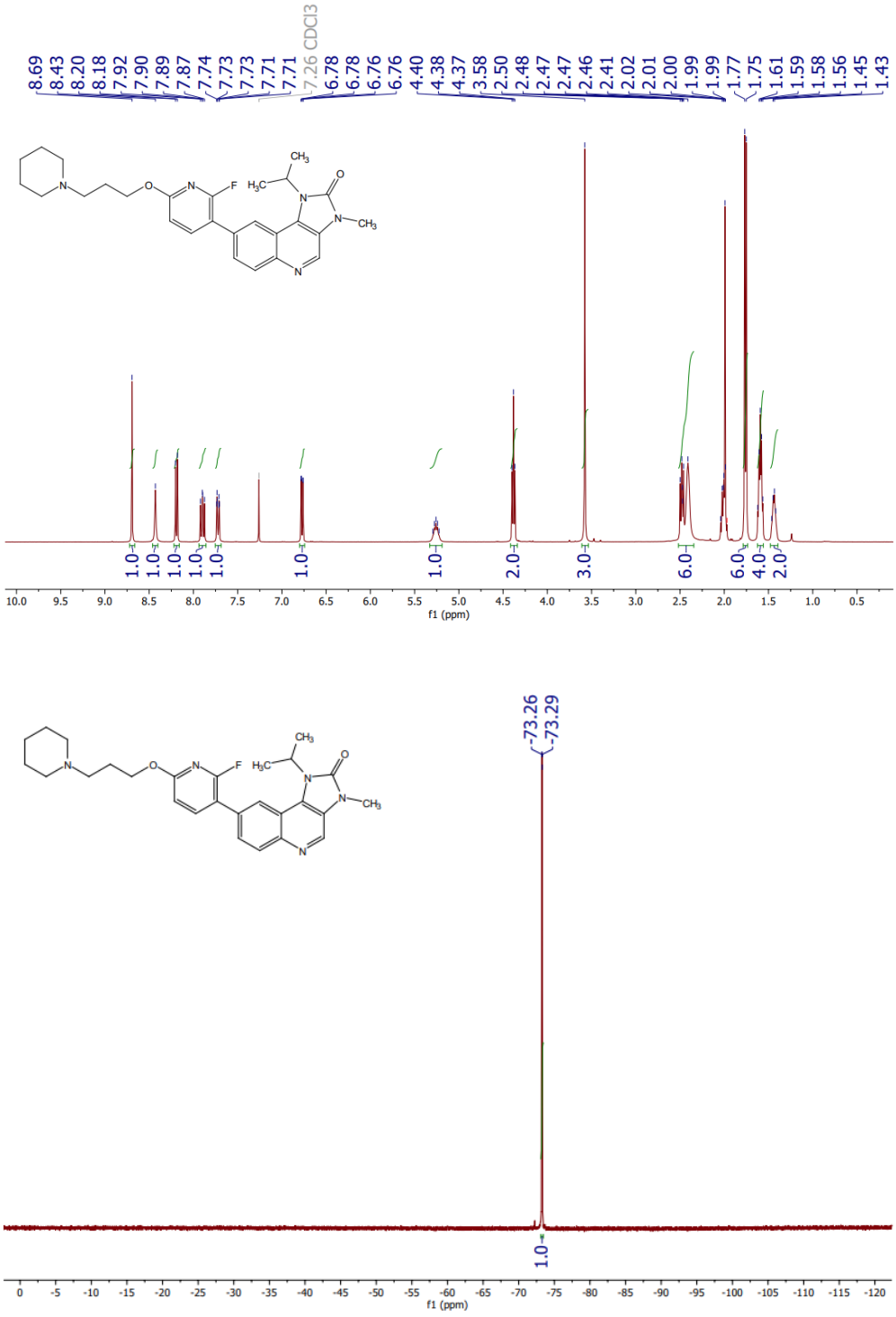
5.3 NMR spectra for novel compounds towards [^{18}F]1

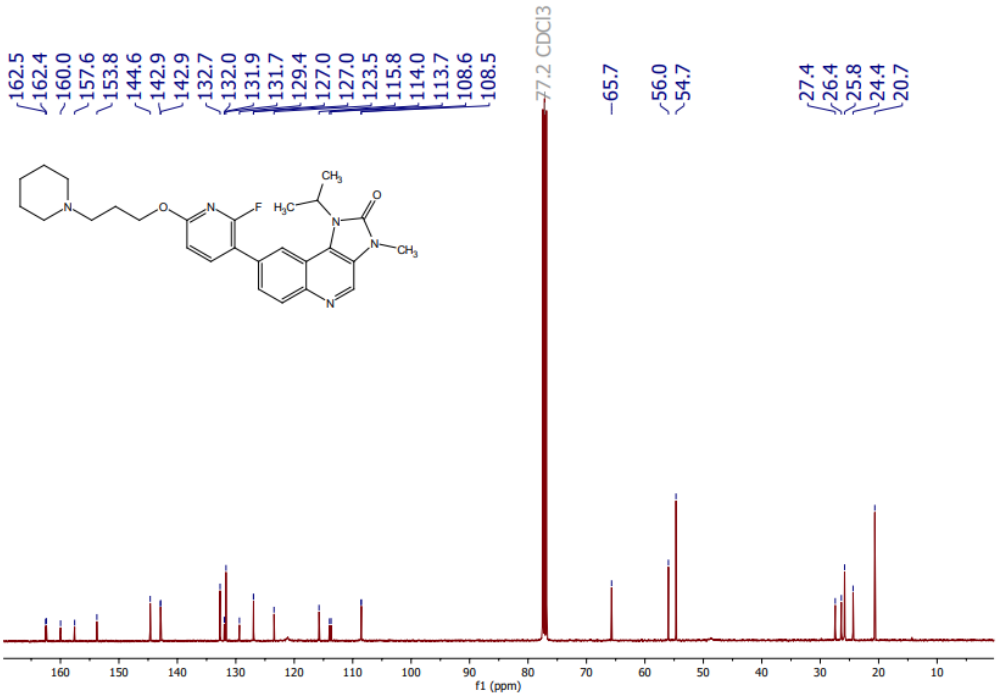
1-isopropyl-3-methyl-8-(4,4,5,5-tetramethyl-1,3,2-dioxaborolan-2-yl)-1,3-dihydro-2*H*-imidazo[4,5-*c*]quinolin-2-one (**1h**)



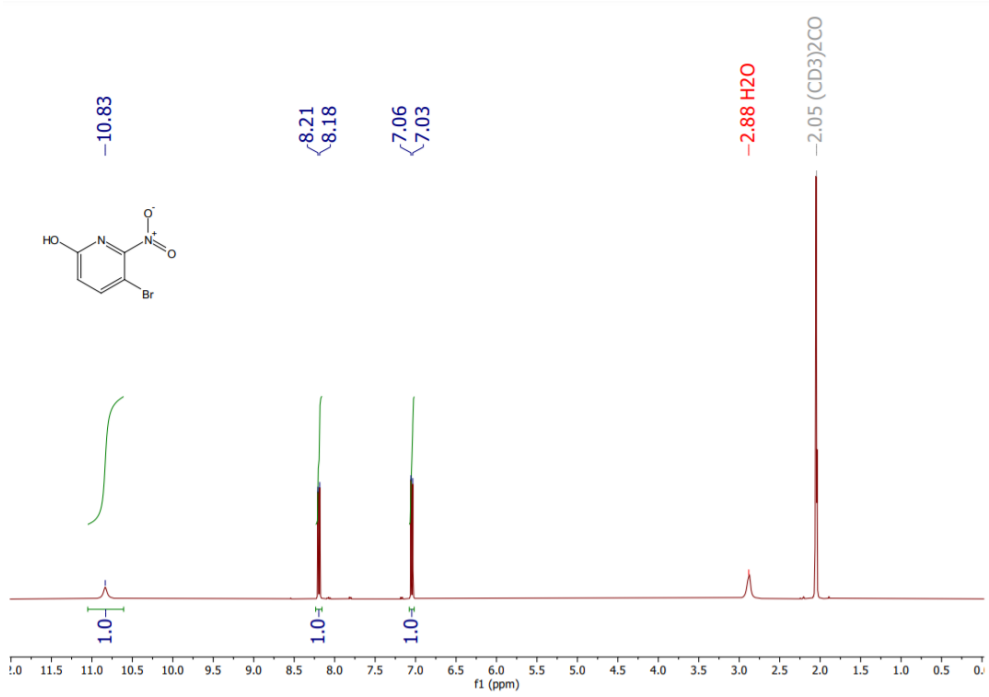


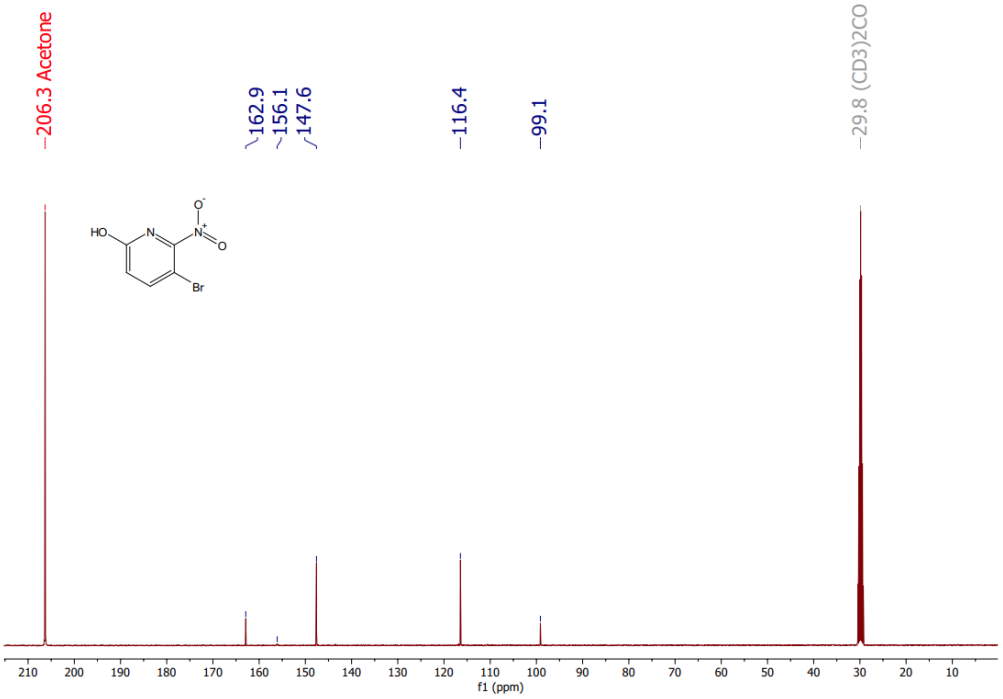
8-(2-fluoro-6-(3-(piperidin-1-yl)propoxy)pyridin-3-yl)-1-isopropyl-3-methyl-1,3-dihydro-2*H*-imidazo[4,5-*c*]quinolin-2-one (**1**)



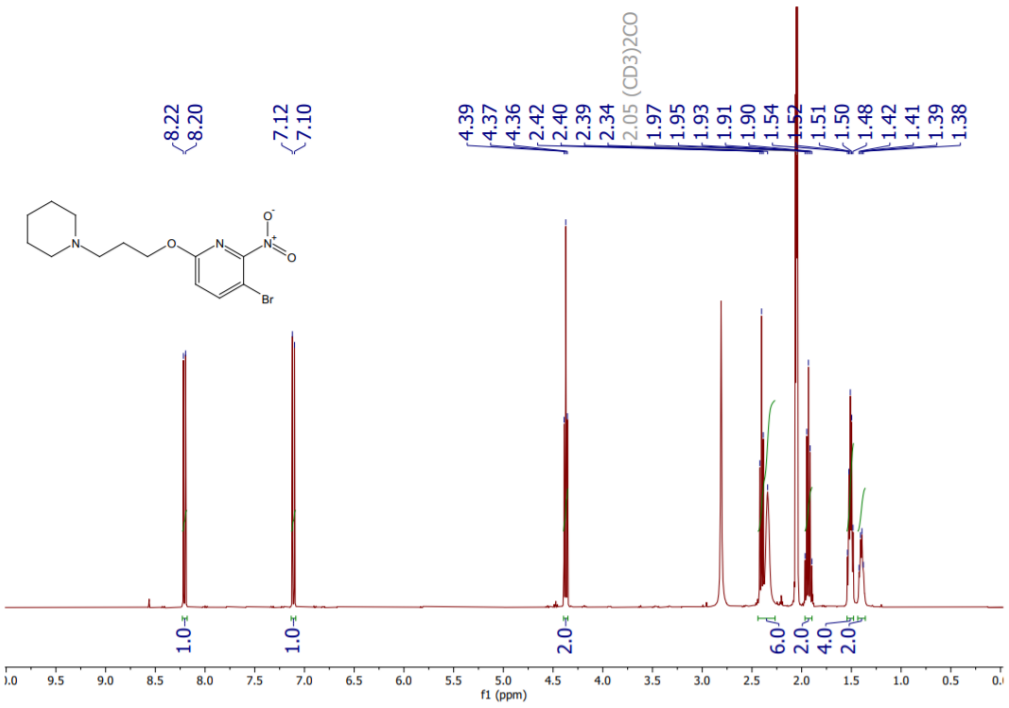


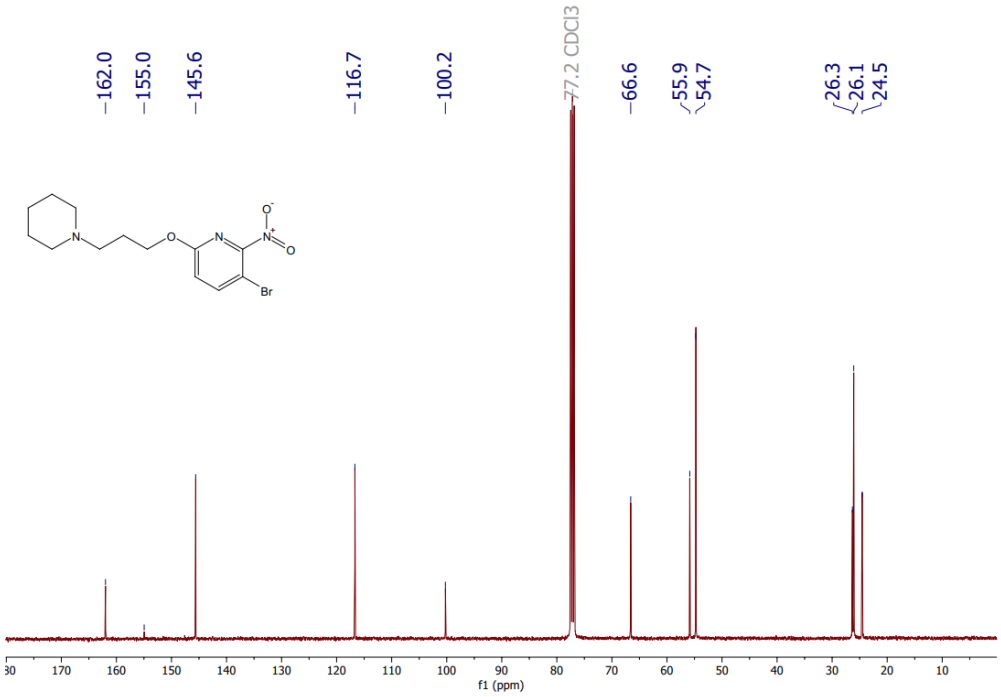
5-Bromo-6-nitropyridin-2-ol (**2b**)



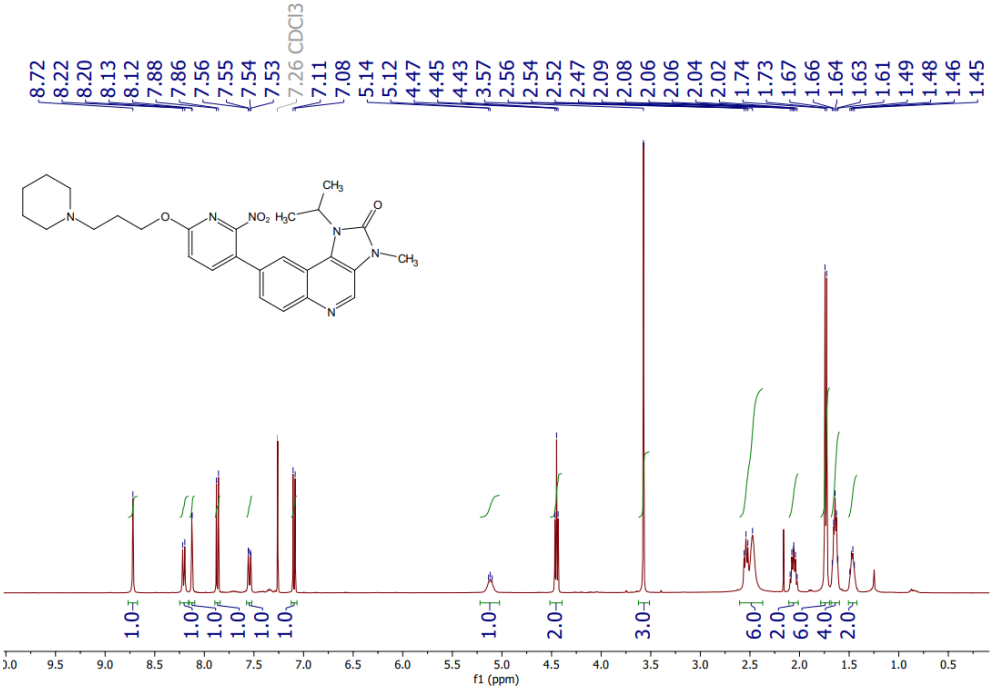


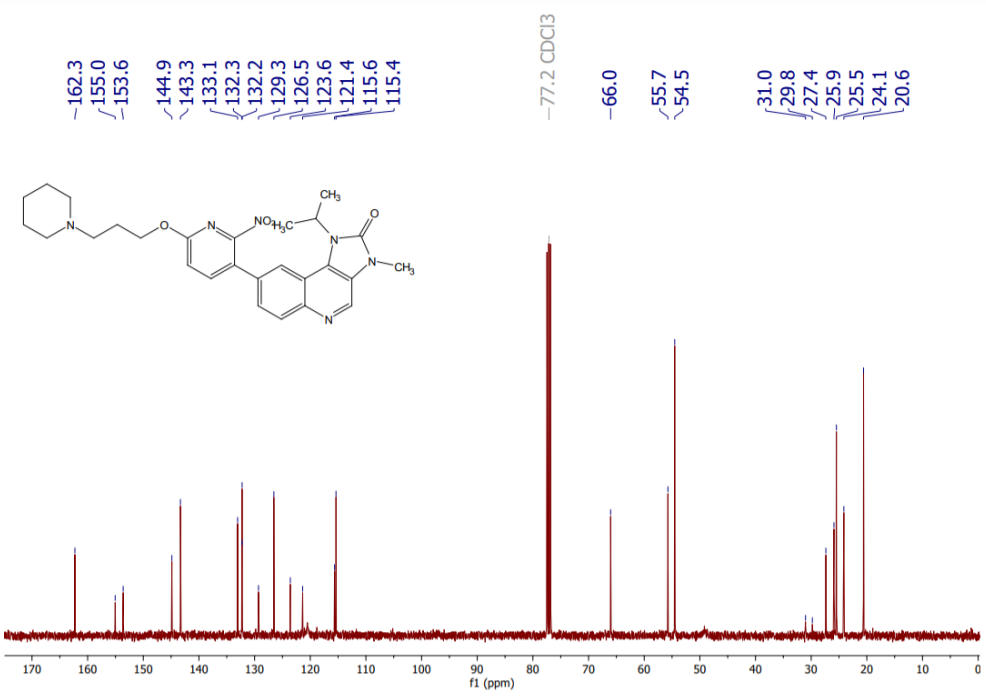
3-Bromo-2-nitro-6-(3-(piperidin-1-yl)propoxy)pyridine (**2c**)





1-Isopropyl-3-methyl-8-(2-nitro-6-(3-(piperidin-1-yl)propoxy)pyridin-3-yl)-1,3-dihydro-2*H*-imidazo[4,5-*c*]quinolin-2-one (**2**)




162.3
155.0
153.6
144.9
143.3
133.1
132.3
132.2
129.3
126.5
123.6
121.4
115.6
115.4
77.2 CDCl3
66.0
55.7
54.5
31.0
29.8
27.4
25.9
25.5
24.1
20.6
f1 (ppm)

5.4 Synthetic experimental for [^{18}F]AZD1390

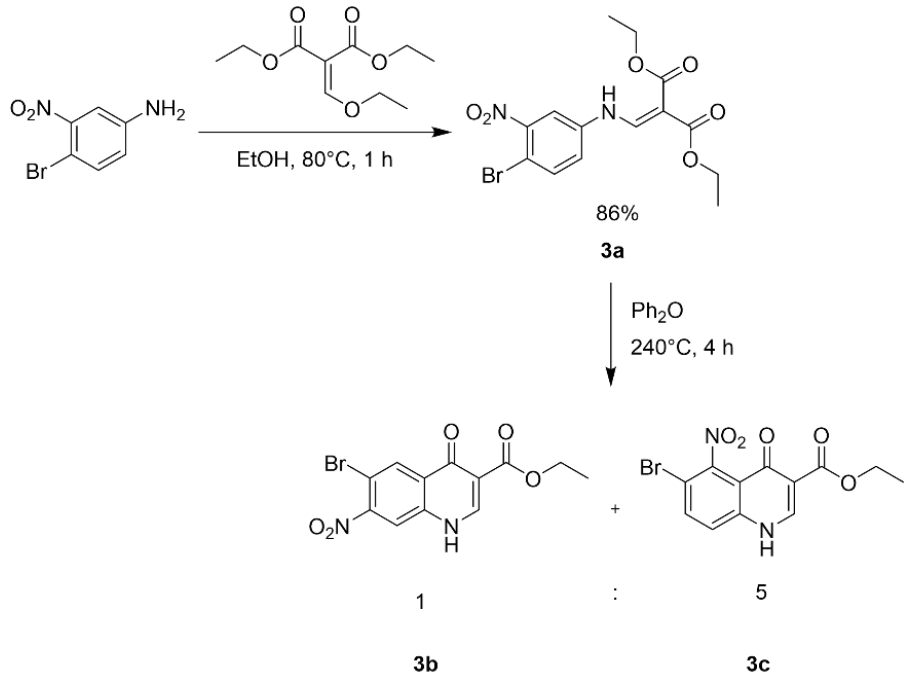


Figure 5.2 – Trialled synthesis towards a nitro quinoline core for a precursor to [^{18}F]AZD1390

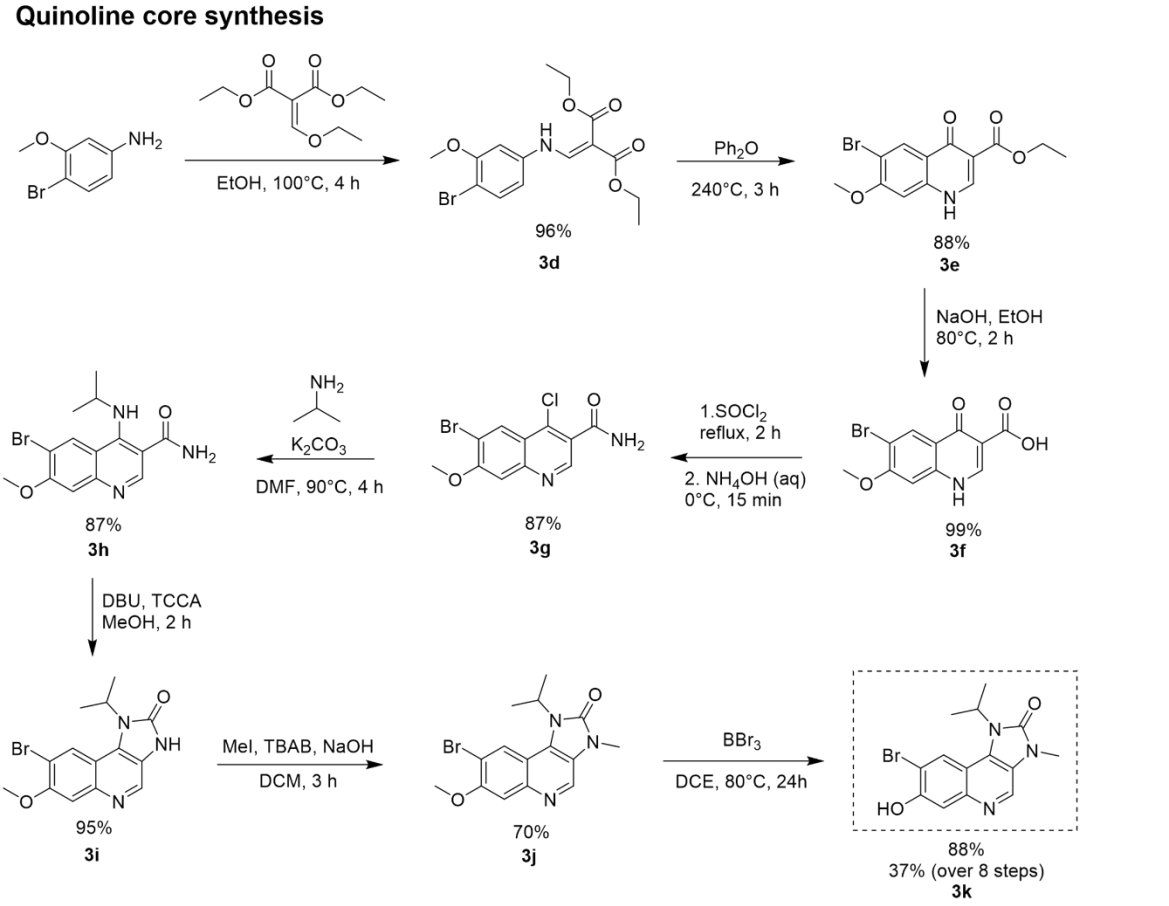
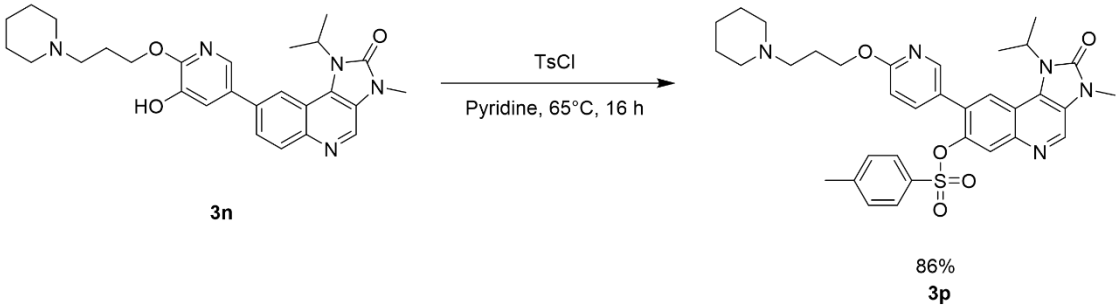


Figure 5.3 – Synthetic steps towards hydroxy intermediate 3k

Tosylate precursor synthesis



Boronic ester precursor synthesis

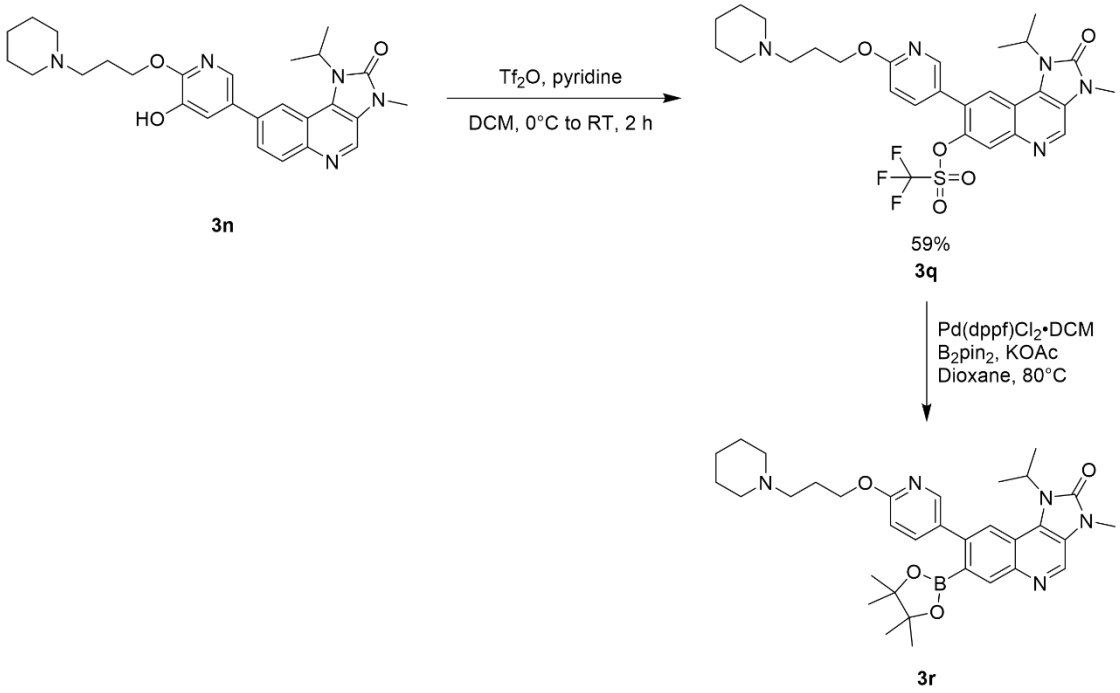
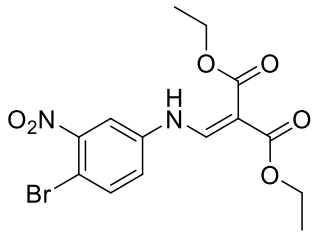


Figure 5.4 – Synthetic steps towards tosylate 3p and boronic ester 3r precursors for [^{18}F]AZD1390

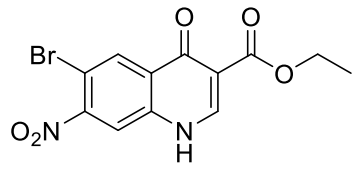
Diethyl 2-(((4-bromo-3-nitrophenyl)amino)methylene)malonate (3a)



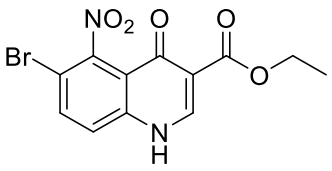
A solution of 4-bromo-3-nitroaniline (5.00 g, 23.0 mmol, 1.00 eq) and diethyl 2-(ethoxymethylene)malonate (3.34 g, 25.3 mmol, 1.10 eq) in EtOH (40 mL) was stirred at 80°C for 1 h. The reaction was allowed to cool to room temperature and then filtered, washing the precipitate with water and pentane to isolate diethyl 2-(((4-bromo-3-nitrophenyl)amino)methylene)malonate (7.72 g, 86%) as a brown solid.

^{1}H NMR (400 MHz, DMSO-d_6) δ 10.67 (s, 1H), 8.33 (s, 1H), 8.16 (d, *J* = 2.7 Hz, 1H), 7.83 (d, *J* = 8.8 Hz, 1H), 7.62 (dd, *J* = 8.8, 2.7 Hz, 1H), 4.21 (q, *J* = 7.1 Hz, 2H), 4.14 (q, *J* = 7.1 Hz, 2H), 1.25 (q, *J* = 6.9 Hz, 6H).); **^{13}C NMR** (101 MHz, DMSO-d6) δ 166.6, 164.8, 150.2, 149.8, 140.3, 135.3, 122.4, 114.3, 106.6, 96.0, 59.9, 59.8, 14.2, 14.1. **LCMS** (ES+) m/z: $[M+H]^+$ 387.

Ethyl 6-bromo-7-nitro-4-oxo-1,4-dihydroquinoline-3-carboxylate (3b) and ethyl 6-bromo-5-nitro-4-oxo-1,4-dihydroquinoline-3-carboxylate (3c)



3b



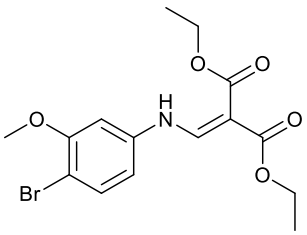
3c

A solution of diethyl 2-(((4-bromo-3-nitrophenyl)amino)methylene)malonate (7.67 g, 19.8 mmol, 1.00 eq) in diphenyl ether (50 mL) was heated to 240°C and stirred for 4 hours at reflux. The reaction was allowed to cool to ~70°C then filtered, washing with acetone to

isolate a mixture of ethyl 6-bromo-7-nitro-4-oxo-1,4-dihydroquinoline-3-carboxylate (**3b**) and ethyl 6-bromo-5-nitro-4-oxo-1,4-dihydroquinoline-3-carboxylate (**3c**) (5.49 g, 81%) as a pale brown solid, shown to be in a 1:5 ratio by ^{1}H NMR.

^{1}H NMR (400 MHz, DMSO-d_6) δ 12.83 (s, 1H, **3c**), 10.67 (d, *J* = 13.7 Hz, 1H, **3b**), 8.71 (s, 1H, **3b**), 8.67 (s, 1H, **3c**), 8.45 (s, 1H, **3b**), 8.28 (s, 1H, **3b**), 8.11 (d, *J* = 8.9 Hz, 1H, **3c**), 7.78 (d, *J* = 8.9 Hz, 1H, **3c**), 4.22 (q, *J* = 7.2 Hz, 4H, **3b** and **3c**), 1.33 – 1.21 (m, 6H, **3b** and **3c**). **LCMS** (ES+) m/z: $[M+H]^+$ 341.

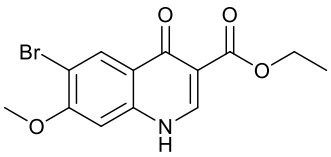
Diethyl 2-(((4-bromo-3-methoxyphenyl)amino)methylene)malonate (3d)



A solution of 4-bromo-3-methoxyaniline (25.0 g, 124 mmol, 1.00 eq) and diethyl 2-(ethoxymethylene)malonate (29.5 g, 137 mmol, 1.10 eq) in MeCN (150 mL) was stirred at room temperature overnight. The solvent was then concentrated *in vacuo*, trituated with pentane (50 mL) and filtered to isolate diethyl 2-(((4-bromo-3-methoxyphenyl)amino)methylene)malonate (48.8 g, 105%, wet) as a grey powdery solid.

^{1}H NMR (400 MHz, $CDCl_3$) δ 11.01 (d, *J* = 13.5 Hz, 1H), 8.45 (d, *J* = 13.5 Hz, 1H), 7.49 (d, *J* = 8.4 Hz, 1H), 6.65 (dd, *J* = 8.5, 2.5 Hz, 1H), 6.60 (d, *J* = 2.5 Hz, 1H), 4.30 (q, *J* = 7.1 Hz, 2H), 4.25 (q, *J* = 7.1 Hz, 2H), 3.90 (s, 3H), 1.37 (t, *J* = 7.1 Hz, 3H), 1.32 (t, *J* = 7.1 Hz, 3H). **LCMS** (ES+) m/z: $[M+H]^+$ 373. Data is in accordance with known literature.[219]

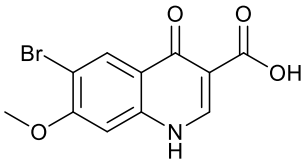
Ethyl 6-bromo-7-methoxy-4-oxo-1,4-dihydroquinoline-3-carboxylate (**3e**)



A solution of diethyl 2-(((4-bromo-3-methoxyphenyl)amino)methylene)malonate (48.8 g, 131 mmol, 1.00 eq) in diphenyl ether (180 mL) was heated to 250°C and stirred for 4 hours at reflux. The reaction was allowed to cool to room temperature, poured into hexane (400 mL) and the precipitate was filtered, washing with further hexane (100 mL) to isolate ethyl 6-bromo-7-methoxy-4-oxo-1,4-dihydroquinoline-3-carboxylate (37.7 g, 88%) as a brown powder.

NMR Compound too insoluble for NMR analysis; **LCMS** (ES+) m/z: $[M+H]^+$ 326. Data is in accordance with known literature.[219,220]

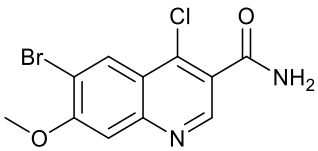
6-Bromo-7-methoxy-4-oxo-1,4-dihydroquinoline-3-carboxylic acid (**3f**)



To a stirred solution of ethyl 6-bromo-7-methoxy-4-oxo-1,4-dihydroquinoline-3-carboxylate (37.4 g, 115 mmol, 1.00 eq) in ethanol (50 mL) was added a solution of NaOH (23.0 g, 574 mmol, 5.00 eq) in water (150 mL) at ambient temperature. The reaction was heated to 100°C reflux and stirred overnight before cooling to 0°C and adjusting to pH 4 with HCl (12 M). The precipitate formed was isolated by filtration affording 6-bromo-7-methoxy-4-oxo-1,4-dihydroquinoline-3-carboxylic acid (33.8 g, 99%) as a beige solid.

^{1}H NMR (400 MHz, DMSO-d_6) δ 15.18 (s, 1H), 13.38 (s, 1H), 8.85 (s, 1H), 8.36 (s, 1H), 7.33 (s, 1H), 4.00 (s, 3H); **LCMS** (ES+) m/z: $[M+H]^+$ 298.

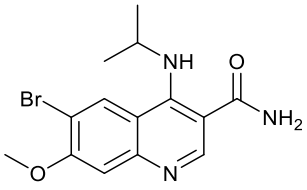
6-Bromo-4-chloro-7-methoxyquinoline-3-carboxamide (**3g**)



6-Bromo-7-methoxy-4-oxo-1,4-dihydroquinoline-3-carboxylic acid (33.6 g, 113 mmol, 1.00 eq) was suspended in thionyl chloride (150.0 mL, 2.57 mol, 18.2 eq) at 0°C before adding DMF (1 mL, 13.0 mmol, 0.12 eq). The mixture was slowly heated to 75°C reflux, stirring for 4 hours. The reaction was allowed to cool to ambient temperature, concentrated *in vacuo* and the residue dried twice as an azeotrope with pentane to afford a yellow solid, which was added portion-wise to saturated aqueous ammonium hydroxide (50 mL) at 0°C. The resulting suspension was stirred for 15 minutes before isolating the solid by filtration and washing with water to afford 6-bromo-4-chloro-7-methoxyquinoline-3-carboxamide (30.4 g, 85%) as a beige solid.

^{1}H NMR (400 MHz, DMSO-d_6) δ 8.84 (s, 1H), 8.46 (s, 1H), 8.18 (s, 1H), 7.93 (s, 1H), 7.62 (s, 1H), 4.06 (s, 3H); **LCMS** (ES+) m/z: $[M+H]^+$ 315.

6-Bromo-4-(isopropylamino)-7-methoxyquinoline-3-carboxamide (**3h**)

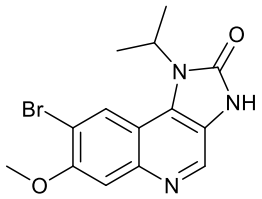


Propan-2-amine (2.00 mL, 23 mmol, 1.20 eq) was added to a suspension of 6-bromo-4-chloro-7-methoxyquinoline-3-carboxamide (6.00 g, 19 mmol, 1.00 eq) and K_2CO_3 (7.88 g, 57 mmol, 3.00 eq) in DMF (60 mL) and the mixture stirred at 90°C overnight. The reaction was cooled to ambient temperature and water (200 mL) was added forming a white precipitate that was collected by filtration, washed with diethyl ether (80 mL) and further dried under

vacuum to afford 6-bromo-4-(isopropylamino)-7-methoxyquinoline-3-carboxamide (5.57 g, 87%) as an off-white powder.

^{1}H NMR (400 MHz, DMSO-d_6) δ 8.63 (s, 1H), 8.48 (s, 1H), 8.34 (d, *J* = 9.0 Hz, 1H), 8.05 (s, 1H), 7.42 (s, 1H), 7.32 (s, 1H), 4.13 (m, 1H), 3.98 (s, 3H), 1.24 (d, *J* = 6.3 Hz, 6H); **LCMS** (ES+) m/z: $[M+H]^+$ 338.

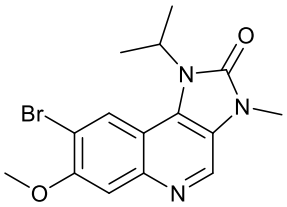
8-Bromo-1-isopropyl-7-methoxy-1,3-dihydro-2*H*-imidazo[4,5-*c*]quinolin-2-one (**3i**)



6-Bromo-4-(isopropylamino)-7-methoxyquinoline-3-carboxamide (7.50 g, 22.2 mmol, 1.00 eq) and 1,8-diazabicyclo[5.4.0]undec-7-ene (6.60 mL, 44.4 mmol, 2.00 eq) were suspended in MeOH (50 mL) and cooled to 0°C before adding a solution of trichloroisocyanuric acid (2.58 g, 11.1 mmol, 0.50 eq) in methanol (50 mL) dropwise over 10 minutes. The reaction was returned to ambient temperature and stirred for 20 hours before filtering through a fine pore frit, isolating 8-bromo-1-isopropyl-7-methoxy-1,3-dihydro-2*H*-imidazo[4,5-*c*]quinolin-2-one (7.10 g, 95%) as a cream solid.

^{1}H NMR (400 MHz, DMSO-d_6) δ 11.42 (s, 1H), 8.58 (s, 1H), 8.44 (s, 1H), 7.52 (s, 1H), 5.09 (p, *J* = 6.9 Hz, 1H), 3.97 (s, 3H), 1.61 (d, *J* = 6.7 Hz, 6H); **LCMS** (ES+) m/z: $[M+H]^+$ 336.

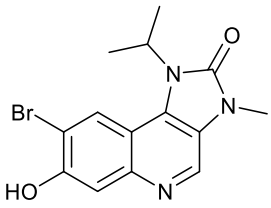
8-Bromo-1-isopropyl-7-methoxy-3-methyl-1,3-dihydro-2*H*-imidazo[4,5-*c*]quinolin-2-one (**3j**)



8-bromo-1-isopropyl-7-methoxy-1,3-dihydro-2*H*-imidazo[4,5-*c*]quinolin-2-one (6.77 g, 20.0 mmol, 1.00 eq), tetrabutylammonium bromide (649 mg, 2.00 mmol, 0.100 eq) and methyl iodide (2.50 mL, 40.0 mmol, 2.00 eq) were suspended in DCM (80 mL) before adding a solution of NaOH (1.61 g, 40.0 mmol, 2.00 eq) in water (40 mL) and stirring vigorously at ambient temperature overnight. The reaction was filtered to isolate 8-Bromo-1-isopropyl-7-methoxy-3-methyl-1,3-dihydro-2*H*-imidazo[4,5-*c*]quinolin-2-one (4.93 g, 70%) as a beige powder.

^{1}H NMR (400 MHz, DMSO-d_6) δ 8.80 (s, 1H), 8.46 (s, 1H), 7.54 (s, 1H), 5.13 (p, *J* = 6.8 Hz, 1H), 3.99 (s, 3H), 3.45 (s, 3H), 1.62 (d, *J* = 6.7 Hz, 6H); **LCMS** (ES+) m/z: $[M+H]^+$ 350.

8-Bromo-7-hydroxy-1-isopropyl-3-methyl-1,3-dihydro-2*H*-imidazo[4,5-*c*]quinolin-2-one (**3k**)

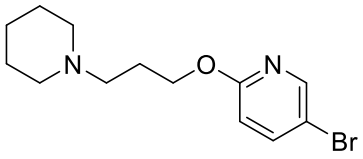


Boron tribromide 1.0 M in hexanes (14.4 mL, 14.4 mmol, 5 eq) was added dropwise to a solution of 8-bromo-1-isopropyl-7-methoxy-3-methyl-1,3-dihydro-2*H*-imidazo[4,5-*c*]quinolin-2-one (1.01 g, 2.89 mmol, 1.00 eq) in anhydrous dichloroethane (25 mL). The reaction was stirred at 80°C reflux overnight, then water (100 mL) added and filtered, isolating 8-bromo-7-hydroxy-1-isopropyl-3-methyl-1,3-dihydro-2*H*-imidazo[4,5-*c*]quinolin-2-one (0.765 g, 79%) as a brown

solid. When required, silica gel chromatography was performed, dry loading the sample on celite and eluting with 2.5-5% MeOH/DCM.

^{1}H NMR (400 MHz, $CDCl_3$) δ 12.14 (s, 1H), 9.14 (s, 1H), 8.71 (s, 1H), 7.63 (s, 1H), 5.30 (p, *J* = 6.7 Hz, 1H), 3.49 (s, 3H), 1.64 (d, *J* = 6.7 Hz, 6H). **LCMS** (ES+) m/z: $[M+H]^+$ 336.

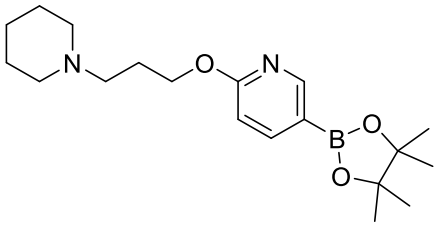
5-Bromo-2-(3-(piperidin-1-yl)propoxy)pyridine (**3l**)



To a solution of 3-(piperidin-1-yl)propan-1-ol (0.946 mL, 6.24 mmol, 1.20 eq) in anhydrous DMF (10 mL) at 0°C was added NaH (60% dispersion in mineral oil, 0.312 g, 7.80 mmol, 1.50 eq), stirring for 10 min at 0°C then 20 min at room temperature until bubbling ceased. 5-Bromo-2-chloropyridine (1.00 g, 5.20 mmol, 1.00 eq) was then added and reaction heated to 90°C for 30 min. The reaction was allowed to cool to room temperature and poured onto cold water (40 mL) then extracted with EtOAc (3 × 20 mL), combined organics washed with 1 M LiCl (50 mL) and brine (50 mL), before drying over MgSO4 and concentrating in vacuo to a yellow oil (1.231 g). The crude material was purified by silica chromatography, eluting with 2-5% 2 N methanolic ammonia in EtOAc, isolating 5-bromo-2-(3-(piperidin-1-yl)propoxy)pyridine (0.904 g, 58%) as a pink crystalline solid.

^{1}H NMR (400 MHz, $CDCl_3$) δ 8.17 (dd, *J* = 2.6, 0.6 Hz, 1H), 7.62 (dd, *J* = 8.8, 2.6 Hz, 1H), 6.64 (dd, *J* = 8.8, 0.7 Hz, 1H), 4.28 (t, *J* = 6.5 Hz, 2H), 2.49 – 2.30 (m, 6H), 2.02 – 1.90 (m, 2H), 1.64-1.52 (m, 4H), 1.46 – 1.41 (m, 2H). **LCMS** (ES+) m/z: $[M+H]^+$ 299. Data is in accordance with known literature.[147]

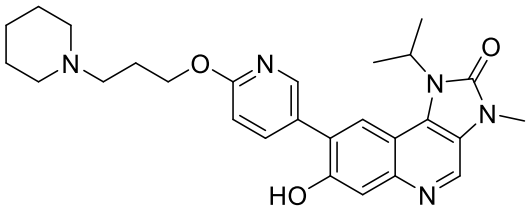
2-(3-(Piperidin-1-yl)propoxy)-5-(4,4,5,5-tetramethyl-1,3,2-dioxaborolan-2-yl)pyridine (**3m**)



In a flame-dried two-necked 25 mL round bottom flask, 5-bromo-2-(3-(piperidin-1-yl)propoxy)pyridine (208 mg, 0.696 mmol, 1.00 eq), potassium acetate (205 mg, 2.09 mmol, 3.00 eq) and bis(pinacolate)diboron (265 mg, 1.04 mmol, 1.50 eq) were dissolved in anhydrous 1,4-dioxane (8 mL) under an argon atmosphere. The mixture was stirred and flushed with argon for 15 minutes before adding $Pd(dppf)Cl_2 \cdot CH_2Cl_2$ (56.8 mg, 10% mol) and flushing for a further 15 minutes. The reaction was heated to 90°C, stirred overnight, then allowed to cool to room temperature and filtered through Celite (1.5 cm) eluting with EtOAc (50 mL). The filtrate was reduced to a fifth of its volume before partitioning with water (10 mL) and the aqueous phase re-extracted with further EtOAc (10 mL). The combined organics were washed with brine (20 mL), dried over $MgSO_4$ and concentrated *in vacuo* to afford 2-(3-(piperidin-1-yl)propoxy)-5-(4,4,5,5-tetramethyl-1,3,2-dioxaborolan-2-yl)pyridine (255 mg, 105 %, wet) as a brown oily solid, used without further purification.

^{1}H NMR (400 MHz, DMSO-d_6) δ 8.38 (dd, *J* = 2.1, 0.8 Hz, 1H), 7.85 (dd, *J* = 8.3, 2.0 Hz, 1H), 6.78 (dd, *J* = 8.3, 0.9 Hz, 1H), 4.28 (t, *J* = 6.7 Hz, 2H), 2.33 (dd, *J* = 15.6, 8.3 Hz, 6H), 1.84 (p, *J* = 6.9 Hz, 2H), 1.47 (p, *J* = 5.5 Hz, 4H), 1.41 – 1.32 (m, 2H), 1.29 (s, 12H); **LCMS** (ES+) m/z: $[M+H]^+$ 347. Data is in accordance with known literature.[147]

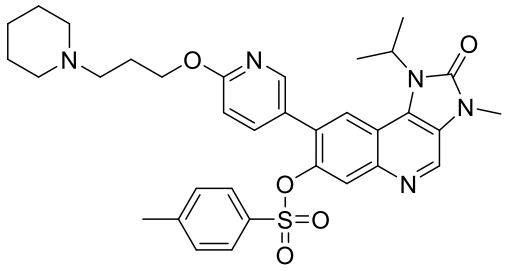
7-Hydroxy-1-isopropyl-3-methyl-8-(6-(3-(piperidin-1-yl)propoxy)pyridin-3-yl)-1,3-dihydro-2*H*-imidazo[4,5-*c*]quinolin-2-one (3n)



In a two neck 25 mL round bottom flask, 8-bromo-7-hydroxy-1-isopropyl-3-methyl-1,3-dihydro-2*H*-imidazo[4,5-*c*]quinolin-2-one (56.0 mg, 0.167 mmol, 1.00 eq), was added and dissolved in 1,4-dioxane (9 mL) and water (1 mL). 2-(3-(Piperidin-1-yl)propoxy)-5-(4,4,5,5-tetramethyl-1,3,2-dioxaborolan-2-yl)pyridine (133 mg, 0.384 mmol, 2.00 eq) and Cs_2CO_3 (162 mg, 0.500 mmol, 3.00 eq) were added and flushed with argon for 5 min before adding tetrakis(triphenylphosphine)palladium(0) (19.2 mg, 0.017 mmol, 0.10 eq) and heating to 100°C reflux overnight. The reaction was allowed to cool before passing through Celite (1.5 cm), eluting with ethyl acetate (150 mL) and washing the organic with water (2 × 100 mL) and dried over $MgSO_4$ and concentrated *in vacuo* to a brown residue (228 mg). The extracted crude was purified by silica gel chromatography, eluting with 0-100% MeOH in DCM, isolating 7-hydroxy-1-isopropyl-3-methyl-8-(6-(3-(piperidin-1-yl)propoxy)pyridin-3-yl)-1,3-dihydro-2*H*-imidazo[4,5-*c*]quinolin-2-one (15 mg, 19%) as a white solid.

^{1}H NMR (400 MHz, DMSO-d_6) δ 8.63 (s, 1H), 8.45 (d, *J* = 2.4 Hz, 1H), 8.05 (s, 1H), 7.64 (d, *J* = 3.0 Hz, 1H), 7.40 (s, 1H), 6.61 (d, *J* = 8.8 Hz, 1H), 5.19 (p, *J* = 6.8 Hz, 1H), 4.12 (t, *J* = 6.6 Hz, 3H), 3.43 (s, 3H), 2.42 – 2.25 (m, 23H) (overlapping with impurity), 1.94 – 1.76 (m, 8H) (overlapping with impurity), 1.61 (d, *J* = 6.7 Hz, 6H), 1.52 – 1.44 (m, 17H) (overlapping with impurity), 1.40 – 1.34 (m, 8H) (overlapping with impurity). **LCMS** (ES+) m/z: $[M+H]^+$ 476.

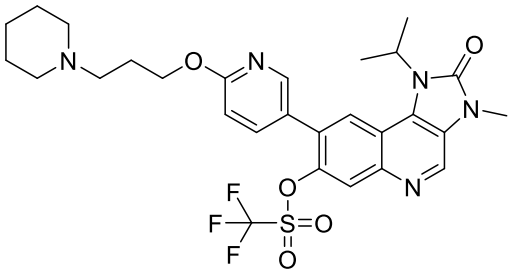
1-Isopropyl-3-methyl-2-oxo-8-(6-(3-(piperidin-1-yl)propoxy)pyridin-3-yl)-2,3-dihydro-1*H*-imidazo[4,5-*c*]quinolin-7-yl 4-methylbenzenesulfonate (**3p**)



Para-toluenesulfonyl chloride (18.0 mg, 0.095 mmol, 3.00 eq) was added to a solution of 7-hydroxy-1-isopropyl-3-methyl-8-(6-(3-(piperidin-1-yl)propoxy)pyridin-3-yl)-1,3-dihydro-2*H*-imidazo[4,5-*c*]quinolin-2-one (15.0 mg, 0.032 mmol, 1.00 eq) in pyridine (1 mL) and stirred at 65°C overnight. The reaction was diluted with EtOAc (10 mL), washed with water (2 × 10 mL) and brine (10 mL), dried over $MgSO_4$ and concentrated to crude, isolating 1-isopropyl-3-methyl-2-oxo-8-(6-(3-(piperidin-1-yl)propoxy)pyridin-3-yl)-2,3-dihydro-1*H*-imidazo[4,5-*c*]quinolin-7-yl 4-methylbenzenesulfonate (17.0 mg, 86%) as a pale yellow crystalline solid. If required, silica chromatography was performed eluting with 10% MeOH in DCM.

^{1}H NMR (400 MHz, DMSO-d_6) δ 8.94 (s, 1H) (*p*-toluenesulfonic acid impurity), 8.14 (s, 1H), 8.04 (d, *J* = 2.5 Hz, 1H), 7.84 (s, 1H), 7.75 – 7.70 (m, 1H), 7.52 – 7.45 (m, 3H), 7.35 (d, *J* = 8.2 Hz, 2H) (*p*-toluenesulfonic acid impurity), 7.24 (d, *J* = 8.2 Hz, 2H) (*p*-toluenesulfonic acid impurity), 7.11 (d, *J* = 7.8 Hz, 2H), 6.83 (d, *J* = 8.7 Hz, 1H), 5.19 (p, *J* = 6.8 Hz, 1H), 4.37 (t, *J* = 6.2 Hz, 3H), 3.49 (s, 3H), 2.39 (s, 3H) (*p*-toluenesulfonic acid impurity), 2.27 (s, 3H), 2.19 – 1.97 (m, 3H), 1.90 (s, 1H), 1.68 (q, *J* = 6.0 Hz, 6H), 1.58 (d, *J* = 6.7 Hz, 6H), 1.50 (s, 4H). **LCMS** (ES+) m/z: $[M+H]^+$ 630.

1-Isopropyl-3-methyl-8-(6-(3-(piperidin-1-yl)propoxy)pyridin-3-yl)-7-((trifluoromethyl)sulfonyl)-1,3-dihydro-2*H*-imidazo[4,5-*c*]quinolin-2-one (**3q**)



To an ice cold solution of 7-hydroxy-1-isopropyl-3-methyl-8-(6-(3-(piperidin-1-yl)propoxy)pyridin-3-yl)-1,3-dihydro-2*H*-imidazo[4,5-*c*]quinolin-2-one (53.0 mg, 0.111 mmol, 1.00 eq) in anhydrous DCM (2.5 mL) and anhydrous pyridine (12.0 µL, 0.123 mmol, 1.10 eq) at 0°C under argon atmosphere was added triflic anhydride (21.0 µL, 0.123 mmol, 1.10 eq). The reaction was stirred at RT for 2 h before diluting in DCM (10 mL) and washing with sat. $NaHCO_3$ (aq, 10 mL), brine (10 mL), drying over $MgSO_4$ and concentrating to a crude orange oil. The crude was purified by silica gel chromatography, eluting with 0-100% MeOH in DCM, isolating 1-isopropyl-3-methyl-8-(6-(3-(piperidin-1-yl)propoxy)pyridin-3-yl)-7-((trifluoromethyl)sulfonyl)-1,3-dihydro-2*H*-imidazo[4,5-*c*]quinolin-2-one (40 mg, 59%) as a yellow crystalline solid.

^{1}H NMR (400 MHz, $CDCl_3$) δ 8.77 (s, 1H), 8.33 (dd, *J* = 2.6, 0.7 Hz, 1H), 8.22 (s, 1H), 8.18 (s, 1H), 8.09 (d, *J* = 2.9 Hz, 1H) (impurity), 7.80 (dd, *J* = 8.6, 2.5 Hz, 1H), 7.49 (dd, *J* = 9.1, 3.0 Hz, 1H) (impurity), 6.89 (dd, *J* = 8.6, 0.7 Hz, 1H), 6.77 (d, *J* = 9.1 Hz, 1H) (impurity), 5.18 (s, 1H), 4.44 (t, *J* = 6.3 Hz, 2H), 4.35 (t, *J* = 6.3 Hz, 3H) (impurity), 3.60 (s, 3H), 2.75 – 2.46 (m, 15H) (overlapping with impurity), 2.22 – 2.12 (m, 2H), 2.07 (p, *J* = 6.4 Hz, 2H) (impurity), 1.80 – 1.64 (m, 17H) (overlapping with impurity), 1.56 – 1.44 (m, 5H) (overlapping with impurity). **^{19}F NMR** (376 MHz, $CDCl_3$) δ -72.47 (impurity), -73.48. **HRMS** (ESI) for $C_{28}H_{32}F_3N_5O_5S$ $[M+H]^+$ requires 608.2149, found 608.2188.

5.5 Synthetic experimental for [^{18}F]A-966492

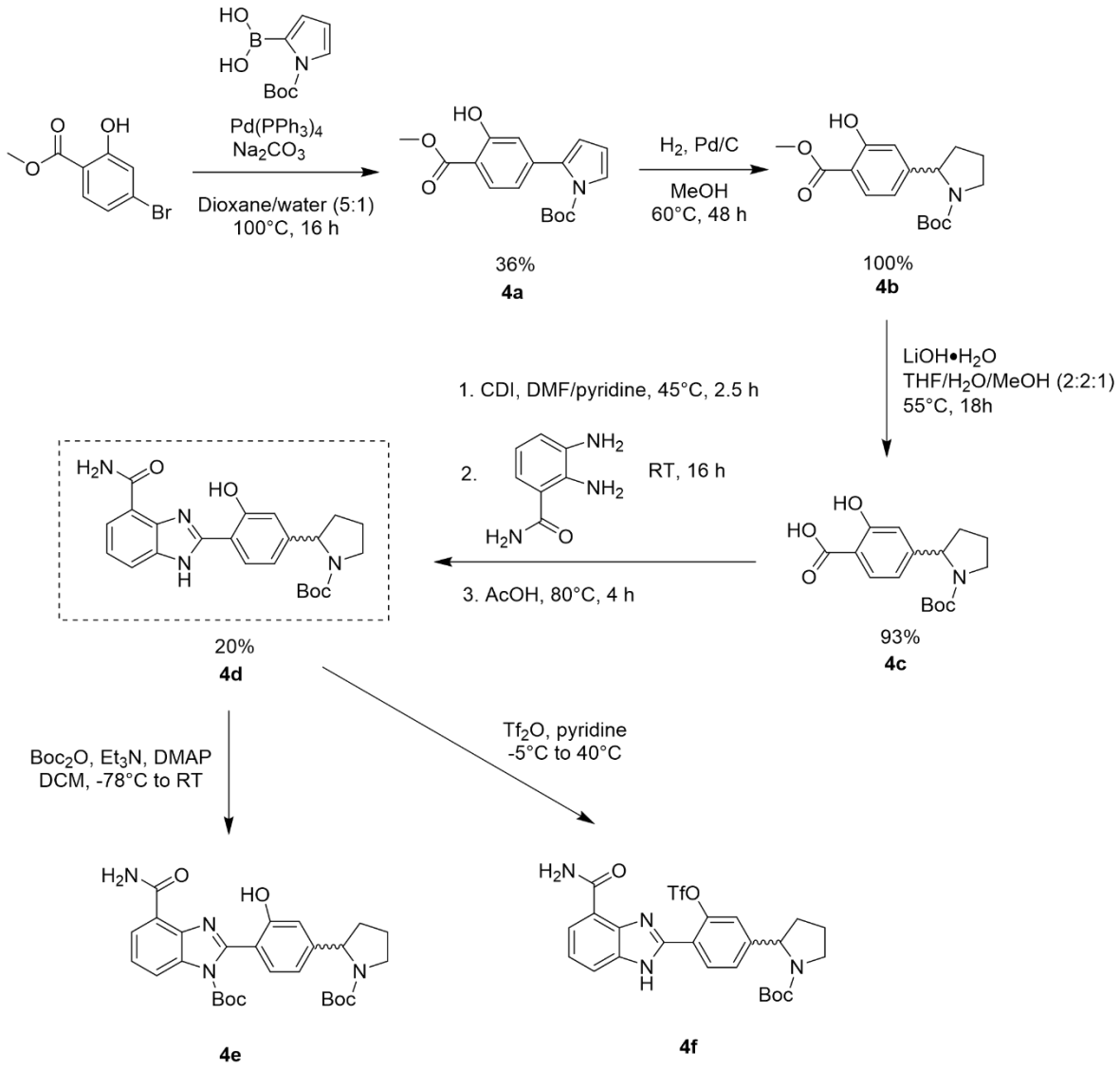


Figure 5.5 – Synthetic steps from methyl 4-bromo-2-hydroxybenzoate towards a precursor for [^{18}F]A-966492

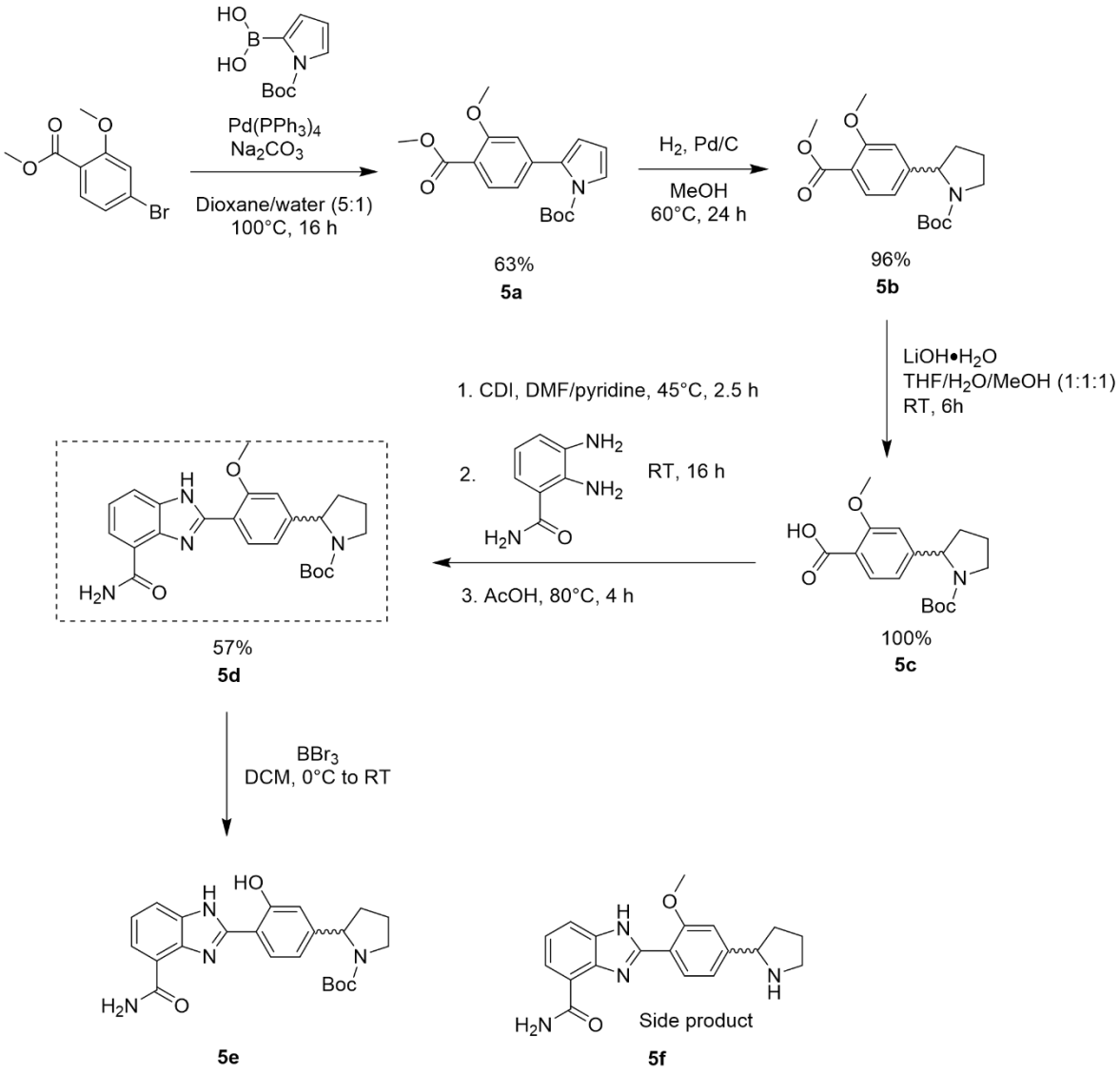
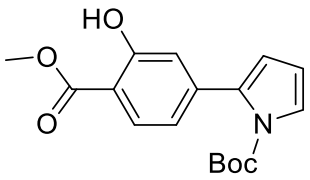


Figure 5.6 – Synthetic steps from methyl 4-bromo-2-methoxybenzoate towards a precursor for [^{18}F]A-966492

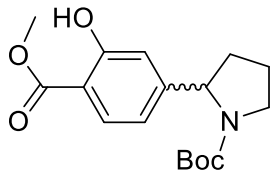
Tert-butyl 2-(3-hydroxy-4-(methoxycarbonyl)phenyl)-1*H*-pyrrole-1-carboxylate (**4a**)



Two 5 g scale reactions were setup in parallel: A solution of methyl 4-bromo-2-hydroxybenzoate (5.00 g, 21.6 mmol, 1.00 eq), 1-(boc)pyrrole-2-boronic acid (4.80 g, 22.7 mmol, 1.05 eq), and Na_2CO_3 (6.88 g, 64.9 mmol, 3.00 eq) in 1,4-dioxane (100 mL) and water (20 mL) was degassed with argon for 10 min before adding tetrakis(triphenylphosphine)palladium(0) (1.25 g, 1.08 mmol, 0.05 eq) and stirring at 100°C reflux for 20 h. The reaction was cooled to RT and passed through ~5 cm celite, washing with EtOAc (500 mL). The filtrates from each reaction were combined and concentrated *in vacuo* to ~200 mL, then partitioned with water (250 mL) and brine (250 mL), dried over $MgSO_4$ and concentrated *in vacuo* to a dark brown crude oil. The crude was purified over two runs on a Biotage Isolera system loaded with a 100 g silica cartridge, eluting the product on a 0-10% gradient of EtOAc in cyclohexane over 15 CV. *Tert*-butyl 2-(3-hydroxy-4-(methoxycarbonyl)phenyl)-1*H*-pyrrole-1-carboxylate (4.90 g, 36%) was isolated as a thick pale-yellow oil.

^{1}H NMR (400 MHz, $CDCl_3$) δ 10.76 (s, 1H), 7.79 (d, *J* = 8.3 Hz, 1H), 7.37 (dd, *J* = 3.3, 1.8 Hz, 1H), 6.98 (d, *J* = 1.7 Hz, 1H), 6.87 (dd, *J* = 8.2, 1.7 Hz, 1H), 6.28 (dd, *J* = 3.3, 1.8 Hz, 1H), 6.23 (t, *J* = 3.3 Hz, 1H), 3.96 (s, 3H), 1.41 (s, 9H); **^{13}C NMR** (101 MHz, $CDCl_3$) δ 170.6, 161.1, 149.2, 141.8, 133.8, 129.0, 123.9, 120.4, 117.7, 115.7, 111.0, 84.3, 52.4, 27.8, 27.1; **LCMS** (ES+) m/z: $[M+H]^+$ 318.

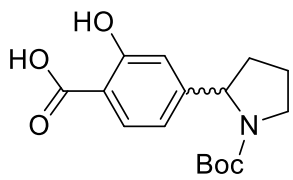
Tert-butyl 2-(3-hydroxy-4-(methoxycarbonyl)phenyl)pyrrolidine-1-carboxylate (**4b**)



To a solution of *tert*-butyl 2-(3-hydroxy-4-(methoxycarbonyl)phenyl)-1*H*-pyrrole-1-carboxylate (4.90 g, 15.4 mmol, 1.00 eq) in MeOH (120 mL) was added 10% Pd/C (1.47 g, 0.30 eq). The reaction was purged with hydrogen and stirred at 60°C for 24 h. Reaction showed no progression, so further 10% Pd/C (1.47 g, 0.30 eq) was added and stirred for a further 24 h at 60°C. The reaction showed full conversion by LCMS, was cooled to RT, and passed through ~ 5 cm celite washing with methanol and concentrated *in vacuo* to give *tert*-butyl 2-(3-hydroxy-4-(methoxycarbonyl)phenyl)pyrrolidine-1-carboxylate (5.00 g, 100%) as a thick opaque oil, which was used without further purification.

^{1}H NMR (400 MHz, $CDCl_3$) δ 10.73 (s, 1H), 7.75 (d, *J* = 8.2 Hz, 1H), 6.78 (d, *J* = 1.7 Hz, 1H), 6.69 (d, *J* = 8.2 Hz, 1H), 4.95 – 4.64 (m, 1H), 3.93 (s, 3H), 3.65 – 3.54 (m, 2H), 2.39 – 2.20 (m, 1H), 1.95 – 1.74 (m, 3H), 1.50 – 1.40 (m, 3H), 1.21 (s, 6H) (boc-group rotamers); **^{13}C NMR** (101 MHz, $CDCl_3$) δ 170.6, 161.8, 154.5, 154.2, 130.0, 116.6, 114.5, 110.9, 79.7, 61.3, 52.3, 47.2, 35.7, 28.3, 23.4; **LCMS** (ES+) m/z: $[M+H]^+$ 322.

4-(1-(*Tert*-butoxycarbonyl)pyrrolidin-2-yl)-2-hydroxybenzoic acid (**4c**)

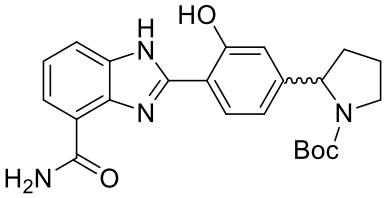


A solution of *tert*-butyl 2-(3-hydroxy-4-(methoxycarbonyl)phenyl)pyrrolidine-1-carboxylate (5.00 g, 15.6 mmol, 1.00 eq) and lithium hydroxide monohydrate (1.96 g, 46.7 mmol, 3.00 eq) in THF (60 mL), water (60 mL) and MeOH (30 mL) was stirred at 55°C for 16

h. The reaction was then cooled on ice and brought to pH 2 with 1 M HCl before extracting with EtOAc (3 × 20 mL), combined organics washed with brine (60 mL), dried over $MgSO_4$ and concentrated *in vacuo* to give 4-(1-(*tert*-butoxycarbonyl)pyrrolidin-2-yl)-2-hydroxybenzoic acid (4.16 g, 87%) as a beige solid, which was used without further purification.

^{1}H NMR (400 MHz, DMSO-d_6) δ 11.24 (s, 1H), 7.72 (d, *J* = 8.1 Hz, 1H), 6.79 – 6.64 (m, 2H), 4.80 – 4.63 (m, 1H), 3.54 – 3.42 (m, 2H), 2.36 – 2.19 (m, 1H), 1.85 – 1.74 (m, 2H), 1.73 – 1.61 (m, 1H), 1.38 (s, 3H), 1.11 (s, 6H); **LCMS** (ES+) m/z: $[M+H]^+$ 308.

Tert-butyl 2-(4-(4-carbamoyl-1*H*-benzo[*d*]imidazol-2-yl)-3-hydroxyphenyl)pyrrolidine-1-carboxylate (**4d**)

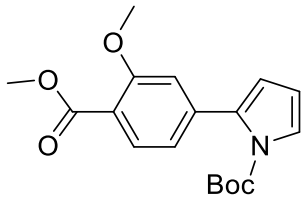


To a solution of 4-(1-(*tert*-butoxycarbonyl)pyrrolidin-2-yl)-2-hydroxybenzoic acid (4.10 g, 13.3 mmol, 1.00 eq) in DMF (40 mL) and pyridine (40 mL) was added CDI (2.38 g, 14.7 mmol, 1.10 eq), and the resulting mixture stirred at 45°C for 2.5 h. The reaction was cooled to RT before adding 2,3-diaminobenzamide (2.22 g, 14.7 mmol, 1.10 eq) and stirring at RT for 16 h. The reaction was concentrated *in vacuo* to a thick red oil before adding glacial acetic acid (80 mL) and stirring the reaction at 80°C for 4h. The reaction was concentrated *in vacuo* and resolved in EtOAc (80 mL) before washing with sat. $NaHCO_3$ (aq, 100 mL), back extracting from the aqueous with EtOAc (2 × 40 mL), then combined organics washed with brine (100 mL), dried over $MgSO_4$, and concentrated *in vacuo* to a crude oily orange solid.

The crude was purified on a Biotage Isolera system loaded with a 100 g silica cartridge, eluting the product on a 0-5% gradient of methanol in DCM over 20 CV, isolating *tert*-butyl 2-(4-(4-carbamoyl-1*H*-benzo[*d*]imidazol-2-yl)-3-hydroxyphenyl)pyrrolidine-1-carboxylate (1.10 g, 20%) as a pale yellow crystalline solid.

^{1}H NMR (400 MHz, $CDCl_3$) δ 10.83 (s, 1H), 9.96 – 9.86 (m, 1H), 8.53 – 8.41 (m, 1H), 8.17 – 8.08 (m, 1H), 7.70 – 7.59 (m, 1H), 7.38 – 7.28 (m, 2H), 7.02 – 6.93 (m, 1H), 6.91 – 6.84 (m, 1H), 6.09 (s, 1H), 5.04 – 4.77 (m, 1H), 3.73 – 3.57 (m, 2H), 2.37 (s, 1H), 1.91 (dq, *J* = 12.9, 6.8 Hz, 3H), 1.79 (s, 4H), 1.48 (s, 3H), 1.23 (s, 6H). **LCMS** (ES+) m/z: $[M+H]^+$ 423.

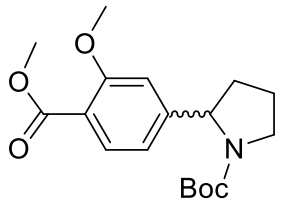
Tert-butyl 2-(3-methoxy-4-(methoxycarbonyl)phenyl)-1*H*-pyrrole-1-carboxylate (5a)



A solution of methyl 4-bromo-2-methoxybenzoate (2.00 g, 8.16 mmol, 1.00 eq), 1-(boc)pyrrole-2-boronic acid (1.72 g, 8.16 mmol, 1.00 eq), and Na_2CO_3 (2.60 g, 24.4 mmol, 3.00 eq) in 1,4-dioxane (40 mL) and water (8 mL) was degassed with argon for 10 min before adding tetrakis(triphenylphosphine)palladium(0) (0.472 g, 0.408 mmol, 0.05 eq) and stirring at 100°C reflux for 20 h. The reaction was cooled to RT and passed through ~1 cm celite, washing with EtOAc (100 mL) then the organic filtrate partitioned with water (100 mL) and brine (100 mL), dried over $MgSO_4$ and concentrated *in vacuo* to an orange crude oil. The crude was purified by silica gel chromatography, eluting with 10-12% EtOAc in *n*-pentane, isolating *tert*-butyl 2-(3-methoxy-4-(methoxycarbonyl)phenyl)-1*H*-pyrrole-1-carboxylate (1.70 g, 63%) as a colourless oil.

^{1}H NMR (400 MHz, $CDCl_3$) δ 7.81 (d, *J* = 8.4 Hz, 1H), 7.37 (dd, *J* = 3.3, 1.8 Hz, 1H), 7.00 – 6.91 (m, 2H), 6.29 – 6.20 (m, 2H), 3.91 (s, 3H), 3.89 (s, 3H), 1.38 (s, 9H). **LCMS** (ES+) m/z: $[M+H]^+$ 332.

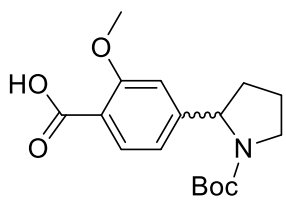
Tert-butyl 2-(3-methoxy-4-(methoxycarbonyl)phenyl)pyrrolidine-1-carboxylate (**5b**)



To a solution of *tert*-butyl 2-(3-methoxy-4-(methoxycarbonyl)phenyl)-1*H*-pyrrole-1-carboxylate (1.60 g, 4.82 mmol, 1.00 eq) in MeOH (40 mL) was added 10% Pd/C (0.450 g, 0.30 eq). The reaction was purged with hydrogen and stirred at 60°C for 18 h. The reaction showed full conversion by LCMS, was cooled to RT, and passed through ~ 5 cm celite washing with methanol and concentrated *in vacuo* to give *tert*-butyl 2-(3-methoxy-4-(methoxycarbonyl)phenyl)pyrrolidine-1-carboxylate (1.55 g, 96%) as a thick opaque oil, which was used without further purification.

^{1}H NMR (400 MHz, $CDCl_3$) δ 7.75 (d, *J* = 7.9 Hz, 1H), 6.80 – 6.74 (m, 2H), 4.99 – 4.71 (m, 1H), 3.89 – 3.84 (m, 6H), 3.66 – 3.58 (m, 2H), 2.33 (s, 1H), 1.94 – 1.75 (m, 3H), 1.48 – 1.41 (m, 3H), 1.19 (s, 6H). **LCMS** (ES+) m/z: $[M+H]^+$ 336.

4-(1-(*Tert*-butoxycarbonyl)pyrrolidin-2-yl)-2-methoxybenzoic acid (**5c**)

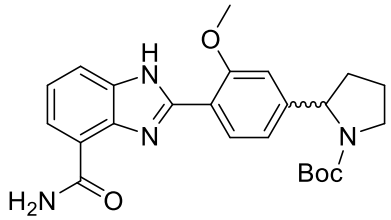


A solution of *tert*-butyl 2-(3-methoxy-4-(methoxycarbonyl)phenyl)pyrrolidine-1-carboxylate (1.545 g, 4.60 mmol, 1.00 eq) and lithium hydroxide monohydrate (0.387 g, 9.21

mmol, 2.00 eq) in THF (15 mL), water (15 mL) and MeOH (15 mL) was stirred at RT for 4 h. LCMS showed still some starting material remaining, so further lithium hydroxide monohydrate (0.194 g, 4.60 mmol, 1.00 eq) was added and the reaction stirred for a further 4 hours. The reaction was then cooled on ice and brought to pH 2 with 1 M HCl before extracting with EtOAc (3 × 20 mL), combined organics washed with brine (60 mL), dried over $MgSO_4$ and concentrated *in vacuo* to give 4-(1-(*tert*-butoxycarbonyl)pyrrolidin-2-yl)-2-methoxybenzoic acid (1.49 g, 100%) as a pale yellow oil, which was used without further purification.

^{1}H NMR (400 MHz, $CDCl_3$) δ 8.12 (d, *J* = 8.1 Hz, 1H), 6.96 (dd, *J* = 8.2, 1.6 Hz, 1H), 6.90 – 6.81 (m, 1H), 4.99 – 4.74 (m, 1H), 4.05 (s, 3H), 3.64 (s, 2H), 2.46 – 2.29 (m, 1H), 1.95 – 1.86 (m, 2H), 1.81 (dt, *J* = 17.4, 6.0 Hz, 1H), 1.45 (s, 3H), 1.20 (s, 6H). **LCMS** (ES+) m/z: $[M+H]^+$ 322.

Tert-butyl 2-(4-(4-carbamoyl-1*H*-benzo[*d*]imidazol-2-yl)-3-methoxyphenyl)pyrrolidine-1-carboxylate (**5d**)



To a solution of 4-(1-(*tert*-butoxycarbonyl)pyrrolidin-2-yl)-2-methoxybenzoic acid (1.13 g, 3.52 mmol, 1.00 eq) in DMF (10 mL) and pyridine (10 mL) was added CDI (0.628 g, 3.87 mmol, 1.10 eq), and the resulting mixture stirred at 45°C for 2.5 h. The reaction was cooled to RT before adding 2,3-diaminobenzamide (0.532 g, 3.52 mmol, 1.00 eq) and stirring at RT for 21 h. The reaction was concentrated *in vacuo* to a thick red oil before adding glacial acetic acid (40 mL) and stirring the reaction at 80°C for 3 h. The reaction was concentrated

in vacuo and resolved in EtOAc (40 mL) before washing with sat. $NaHCO_3$ (aq, 50 mL) and brine (100 mL), dried over $MgSO_4$, and concentrated *in vacuo* to a crude oily yellow solid. The crude was purified by silica gel chromatography, eluting with 0-5% MeOH in DCM, isolating tert-butyl 2-(4-(4-carbamoyl-1*H*-benzo[*d*]imidazol-2-yl)-3-methoxyphenyl)pyrrolidine-1-carboxylate (0.87 g, 57%) as a yellow/beige crystalline solid.

^{1}H NMR (400 MHz, $CDCl_3$) δ 10.75 (s, 1H), 9.90 (s, 1H), 8.50 (d, *J* = 8.1 Hz, 1H), 8.15 (d, *J* = 7.6 Hz, 1H), 7.65 (d, *J* = 7.9 Hz, 1H), 7.35 (t, *J* = 7.8 Hz, 1H), 6.99 (d, *J* = 8.4 Hz, 1H), 6.90 (s, 1H), 5.96 (s, 1H), 5.06 – 4.77 (m, 1H), 4.10 (s, 3H), 3.72 – 3.63 (m, 2H), 2.47 – 2.27 (m, 1H), 1.99 – 1.81 (m, 3H), 1.48 (s, 3H), 1.22 (s, 6H). **LCMS** (ES+) m/z: $[M+H]^+$ 437.

6 Discussion and Future Work

6.1 General review of presented results

With the development of DDR targeted imaging beginning just over a decade ago, this thesis aimed to investigate ATM as a potential new DDR protein target for PET imaging and contribute a new radiotracer to the growing field of PARP targeting imaging. While chapter 2 reported the success in developing the first published ^{18}F-labelled ATM inhibitor, it also highlighted the key challenges that may be faced in trying to image ATM activity. Chapter 3 demonstrated the efforts in developing a second, more clinically applicable and BBB-penetrable ^{18}F-labelled ATMi, [^{18}F]AZD1390, highlighting the challenges faced with the chemistry and radiochemistry in the development of small molecule PET probes. With these difficulties in trying to target the biologically complex ATM, chapter 4 presented the first steps towards a novel PARPi tracer for the purpose of brain tumour imaging, an area where current PARPi radiotracers have faced difficulties.

The key questions raised as a result of this body of work encompass (1) what are the current limitations of ^{18}F-labelling small molecule radiotracers? (2) Is ATM a suitable target for the development of new imaging agents? And (3) could other DDR protein targets benefit from investigation with PET? The following sections provide an extended discussion into these key themes.

6.2 Challenges in designing ^{18}F-radiotracers

Fluorine-18 is often considered the preferred radionuclide for nuclear imaging due to its highly efficient positron decay (97%) allowing PET imaging, pharmaceutically compatible half-life (110 min) allowing distribution across multiple hospital sites, and short tissue diffusion range (< 2.3 mm) giving high spatial resolution. In addition, the frequent occurrence of fluorine in bioactive compounds, normally as a bio-isostere of hydrogen, makes it an attractive target for radionuclide exchange. Several decades of research have expanded the use of ^{18}F thanks to the development of a wide variety of radiolabelling reactions. While electrophilic radiofluorination is possible using [^{18}F]F_2 or newer electrophilic ^{18}F sources such as [^{18}F]Selectfluor, difficulties with regioselectivity and the low maximum molar activity achievable by these reactions have reduced their use in comparison to nucleophilic [^{18}F]fluoride. While classical nucleophilic aromatic radiofluorinations from nitro, halo, and trimethylammonium salt precursors generally require electron withdrawing groups to be present in the aromatic system to promote S_NAr, recent advances in labelling methodologies with [^{18}F]fluoride have focussed on expanding substrate scope beyond electron-deficient precursors to include those that are electronically neutral or electron-rich, often by employing transition metal catalysis.[221] Improvements to radiochemical yield, molar activity, and GMP translatability have also been achieved. More recently, techniques that have previously been used for ^{19}F-fluorinations such as electrochemistry and photochemistry have successfully been applied to radiofluorination.[176,178]

Recent advances in total body PET are estimated to increase in sensitivity of scanners by a factor of 40, meaning that only 1/40th of the radioactivity could be required for the same signal-to-noise ratio.[222,223] With the possibility of requiring only 1/40th of the dose previously needed for ^{18}F PET studies, total body PET could expand the number of radiofluorination reactions that could be used in the synthesis of new tracers by allowing longer reaction times and the potential for multiple additional steps after labelling, beyond simple deprotections. Current reactions with RCYs too low for standard PET could also be utilised if the dose required is reduced. However, an important consideration comes with maintaining suitable molar activities so as to not impede the radiotracer principle, particularly in targeting proteins of low abundance when using tracers with high binding affinities.

Improvements in labelling methodologies and scanner capabilities highlight a bright future for PET and the development of novel tracers. In the progression of novel tracers into clinic, there is however a need for better structuring in the management of radiotracer development, recently highlighted by Campbell *et al.*[224] This article emphasises the need for better, more directed training of radiochemists as a specialist career path, how a better database of suitable molecular imaging targets could save wasted time developing new molecules for irrelevant targets, and the need for an infrastructure similar to that employed in drug development where there are individual teams for e.g. molecule design, HTS, DMPK, process chemistry. The lack of these facilities within radiotracer development currently means that individuals are responsible for multiple processes with less time to focus energies on perfecting each aspect of the development. Within this theme, design of

experiment (DoE) and derisking strategies have recently been employed alongside development of new radiofluorination methods and in the radiosynthesis of complex molecules.[203,225,226] These screening approaches, which share similar parallels seen in fragment-based design of novel therapeutics, can provide more confidence when choosing a specific radiolabelling method and retrosynthetic pathway to a suitable precursor, as well as help to identify any caveats early on in the development of a new probe. All of these factors, in addition to aspects of clinical translatability must be considered when beginning a new radiotracer project.[227]

6.3 ATM vs PARP imaging

The initial aim of this thesis was the investigation of ATM as a new target for molecular imaging, however the results presented in chapter 2 demonstrate the potential drawbacks of ATM as a suitable target. While ATM was discovered in the 1990s and there has been extensive research on the protein in the following decades, there are still important questions to be answered about ATM structure, activation, and its role in cancer. Recent electron microscopy has given excellent insights into the structure of ATM,[26] however its large size has so far precluded a complete crystal structure to be determined. The activation mechanisms of ATM are varied and complex due to the number of key interacting proteins linked to ATM, and this plays into the complexities in understanding its role in cancer development and suppression.

Since ATM activity is controlled post-translationally by phosphorylations and acetylations rather than by increased protein synthesis, imaging active ATM requires a probe that will preferentially bind to the active form compared to the inactive species. With all reported selective small molecule ATMis competing for the ATP-binding pocket of ATM and given the incomplete understanding of ATM structure, it was proposed that ATP-competitive probes may be able to assess whether there are changes in ATP-ATM binding affinity upon ATM activation via readout of ATMi radiotracer binding following ATM activation (i.e. after irradiation). However, following the results of chapter 2 demonstrating no change of tracer uptake in irradiated cells, it is unclear whether imaging probes based on these ATP-competitive inhibitors will be able to selectively distinguish active ATM. Instead, they might only be able to identify total ATM levels, although chapter 2 also demonstrated that identifying different levels of total ATM expression with [^{18}F]**1** was challenging. Given this, to extend the value of radiolabelled ATMis beyond visualisation of ATMi drug pharmacokinetics, further investigation is needed to understand whether it is useful, or indeed possible, to image total ATM expression as opposed to active ATM alone, along with identifying a clear role of ATM expression and activity in cancer.

Aside from directly imaging ATM expression and/or activity, targeting more abundant proteins that are downstream of pATM that could indirectly indicate changes in ATM activity might be explored. As discussed briefly in chapter 2, the development of [^{18}F]FAC that targets dCK (a downstream target of ATM) has the potential to serve as a PET imaging agent that is responsive to ATM activation.[145] Additionally, work by Dr Mathew Veal performed in the Cornelissen group investigated the pATM-dependent target phospho-

KAP1^{S824} (pKAP1) with a radioimmunoconjugate targeted to pKAP1 as a downstream indicator of pATM activity (unpublished). Preliminary results showed good radiolabelling yield, however again lacked statistical significance in cellular uptake when it came to detecting different levels of pKAP1 in the same *in vitro* model system used for [^{18}F]**1**.

While there are hundreds of downstream targets of ATM involved in the DDR, many of them are not uniquely ATM-dependent for activation (i.e. can also be activated by other proteins such as ATR), and their active forms are often simple phosphorylated derivatives. Most PI3K family inhibitors are designed to compete for the ATP-binding pocket where they may not be selective towards the active, phosphorylated proteins, therefore imaging probes designed from these molecules may not be useful to identify specific (e.g. ATM induced) DDR protein interactions. Not all drugs would make useful imaging probes, especially in the case where activity is post-translationally controlled rather than being controlled by increasing protein transcription/expression, as is the case for PARP.

PARP is well-studied family of enzymes, with detailed understanding of how the roles of some PARP isoforms are associated with DNA damage repair and cancer.[228] This contrast in knowledge compared to ATM may be in part due to the earlier discovery of PARP in the 1960s[229] in addition to its high cellular abundance and role in many aspects of cell biology (e.g. aging, reproduction, immunity etc.). Additionally, ATM inhibitors must be designed to be selective against hundreds of other kinases with very similar ATP-binding pockets, whereas designing selective inhibitors of the PARP NAD^+ binding site is more simple, with many more PARP inhibitors published compared to those of ATM. The decision to extend this body of work towards molecular imaging of PARP was prompted by this larger base of

knowledge for PARP and in particular the better-known implications of increased PARP expression in cancer. Several PARPi radiotracers have already demonstrated the ability to detect high levels of PARP *in vivo*[134] and measure drug pharmacokinetics as well as more recently demonstrating their use for monitoring DNA damaging treatments,[230] highlighting its value as a PET imaging target.

The purpose of the work presented in chapter 4 was to build on the current PARPi radiotracer landscape, but specifically to develop a tracer suitable for imaging PARP expression and PARPi pharmacokinetics in the brain. Some PARPi radiotracers have been assessed for brain imaging however poor BBB-penetration has so far impeded suitable brain uptake. Only one clinical trial (NCT04173104) is investigating [^{18}F]F-PARPi for imaging brain cancers following results from preliminary mouse and human studies.[136] Although larger brain tumours often show BBB disruption and may allow penetration of some of the current ^{18}F PARP radiotracers, smaller tumours and brain micrometastases may have more intact BBB and may not be suited to these imaging agents. This highlights the need for BBB-penetrable PARPi radiotracers, particularly in the detection and assessment of PARPi treatment options for smaller brain lesions.

Adjacent to their success as imaging agents, a few PARPi tracers have been adapted to carry therapeutic radionuclides and tested preclinically, such as [^{123}I]MAPi, [^{125}I]KX1, and [^{125}I]PARPi-01 for auger electron therapy,[231-233] [^{131}I]PARPi for beta therapy,[234] and [^{211}At]MM4 for alpha therapy.[235] These PARPi scaffolds are able to deliver damaging radiation to the nucleus of tumour cells and have demonstrated high selectivity and increased survival *in vivo*, and there will likely be further candidates under investigation in

the near future. Notably, two of these radionuclide therapies ([^{123}I]MAPi and [^{131}I]PARPi) had a primary focus on brain tumours (glioblastoma) to tackle the current lack in effective and selective treatments for this indication. To combat potentially poor BBB-penetration, the Reiner group employed convection enhanced delivery (CED) to improve brain tumour uptake of these iodine-based radiotherapies in orthotopic models.[231,234] While CED has demonstrated good results in delivery brain cancer treatments and could potentially be translated for delivering radionuclide therapies, it requires invasive surgery to implant the delivery catheters making it incompatible for an equivalent role in delivering radiotracers for non-invasive imaging. Thus, the development of BBB-penetrable imaging agents remains crucial, and any successful probes may be interesting to investigate for use in radionuclide therapy of brain tumours.

6.4 Future considerations for imaging the DDR

The high levels of DNA damage in cancer has led to the targeting of DDR proteins to inhibit DNA repair and induce cell death. There have been many inhibitors developed against key proteins within the DDR including ATM, ATR, DNA-PK, CHK1, WEE1, and PARP, with a handful reaching clinical trials and/or approval, often with the aim of inducing synthetic lethality.[144] While there are a range of targets with suitable inhibitors becoming available that are anticipated to increase the therapeutic variety for cancer treatment, whether or not these inhibitors would serve as suitable scaffolds for imaging probes is more complex. The attraction of DDR proteins as imaging targets to improve patient stratification is three-

fold, (1) for assessment of drug pharmacokinetics, (2) for assessment of drug-target engagement, and (3) for monitoring response to DNA damaging treatments. While drug radioisotopologues (particularly those labelled with ^{14}C or ^{3}H) have demonstrated their use in understanding DMPK and ADME profiles of novel drugs, their value for PET/SPECT imaging with an appropriate radionuclide can be extended if there is a clear link between tracer-target engagement and if they are able to answer key questions about cancer phenotype/prognosis. Therefore, DDR targets being considered for nuclear imaging should fulfil the criteria of (1) having a clear, clinically relevant role in disease in relation to the protein expression, and (2) have good understanding of inhibitor binding relevant to the design of a suitable radiotracer.

DDR kinases may be less suitable as small molecule nuclear imaging targets due to the post-translational control in their activity. However, one solution to this issue that has demonstrated value is the use of antibody-based imaging with high selectivity towards activated (e.g. phosphorylated) proteins. A γH2AX targeted radioimmunoconjugate demonstrated the ability of [^{111}In]-anti-γH2AX-TAT to measure levels of DNA damage after IR or bleomycin therapy.[236] Although similar preliminary studies in our group using antibody-based imaging probes against pATM and pKAP1 were unsuccessful and were put down to low target expression, it may be that future radioimmunoconjugates targeted towards more abundant, clinically relevant phosphorylated DDR proteins may be more successful, as in the case for γH2AX. One potential target that has shown relevance in a broad range of tumour types is phospho-RAD50^{S635} which has demonstrated significant changes in expression in response to ATM and ATR inhibition, and therefore could be

targeted with PET for the stratification of patients who might respond well to ATM/ATR inhibition.[237] RAD50 expression has also been investigated as a prognostic biomarker for PARPi.[238] Although there are no reported small molecule inhibitors of RAD50, a radioimmunoconjugate approach may be more effective in probing pRAD50 expression.

Small molecule inhibitors of DDR kinases generally inhibit catalytic activity by binding to the ATP-binding pocket of the target kinase, likely in a non-selective manner with regards to binding to the active (phosphorylated) versus the inactive form. This type of ATP-competitive inhibitor is the most common in targeting kinases as the kinase domain pocket across the PIKK family is highly conserved given all PIKK proteins act on serine and threonine residues which makes design of selective inhibitors to this binding site more complex. However, advances in computational modelling and access to accurate kinase structures may reveal alternative binding sites that are specific to the activated (phosphorylated) kinases, and therefore small molecule inhibitors of these sites could propose new scaffolds for selective imaging of active kinases.

6.5 Concluding remarks

Nuclear imaging has the ability to non-invasively probe target expression, drug pharmacokinetics, and monitor treatment response. With many cancer therapies inducing DNA damage to overwhelm tumour cells into arrest, there has been a push to investigate the DNA damage response with regards to understanding the key proteins involved and the development of DDR inhibitors to enhance current DNA damaging therapies. The use of

DDR inhibitor radiotracers with PET or SPECT could allow scientists to quickly collect information on tumour phenotype, DDRi drug interactions and pharmacokinetics, calculate levels of DNA damage as a result of previous therapies, and could ultimately improve patient stratification. With some key targets of the DDR such as γH2AX and PARP already under investigation for nuclear imaging, this thesis aimed to investigate ATM as a potential new target for DDR nuclear imaging, as well as expanding the selection of PARPi radiotracers to allow imaging of tumours in the brain. Ultimately, this body of work highlighted the key challenges faced in the chemistry and radiochemistry of developing new radiotracers and demonstrated the limitations of ATM as an imaging target. It is the hope that this research will pave the way for further development of ATMi radiotracers to verify whether ATM is a suitable molecular imaging target and to promote the development of BBB-penetrable PARPi tracers.

7 References

1. Hanahan D, Weinberg RA. The Hallmarks of Cancer. *Cell.* 2000;100(1):57-70.

2. Hanahan D, Weinberg Robert A. Hallmarks of Cancer: The Next Generation. *Cell.* 2011;144(5):646-674.

3. Hanahan D. Hallmarks of Cancer: New Dimensions. *Cancer Discovery.* 2022;12(1):31-46.

4. Basu AK. DNA Damage, Mutagenesis and Cancer. *Int J Mol Sci.* 2018;19(4):970.

5. Sinha RP, Häder D-P. UV-induced DNA damage and repair: a review. *Photochem Photobiol Sci.* 2002;1(4):225-236.

6. Rastogi RP, Richa, Kumar A, Tyagi MB, Sinha RP. Molecular mechanisms of ultraviolet radiation-induced DNA damage and repair. *J Nucleic Acids.* 2010;2010:592980.

7. Lindahl T, Barnes DE. Repair of endogenous DNA damage. *Cold Spring Harb Symp Quant Biol.* 2000;65:127-133.

8. Hoeijmakers JHJ. DNA Damage, Aging, and Cancer. *N Engl J Med.* 2009;361(15):1475-1485.

9. Ames BN, Shigenaga MK, Hagen TM. Oxidants, antioxidants, and the degenerative diseases of aging. *Proc Natl Acad Sci.* 1993;90(17):7915-7922.

10. Ames BN. Identifying Environmental Chemicals Causing Mutations and Cancer. *Science.* 1979;204(4393):587-593.

11. Seeberg E, Eide L, Bjørås M. The base excision repair pathway. *Trends Biochem Sci.* 1995;20(10):391-397.

12. Lieber MR. The Mechanism of Double-Strand DNA Break Repair by the Nonhomologous DNA End-Joining Pathway. *Annu Rev Biochem.* 2010;79(1):181-211.

13. Filippo JS, Sung P, Klein H. Mechanism of Eukaryotic Homologous Recombination. *Annu Rev Biochem.* 2008;77(1):229-257.

14. Gorodetska I, Kozeretska I, Dubrovska A. BRCA Genes: The Role in Genome Stability, Cancer Stemness and Therapy Resistance. *J Cancer.* 2019;10(9):2109-2127.

15. Olivier M, Hollstein M, Hainaut P. TP53 mutations in human cancers: origins, consequences, and clinical use. *Cold Spring Harb Perspect Biol.* 2010;2(1):a001008.

16. Rivlin N, Brosh R, Oren M, Rotter V. Mutations in the p53 Tumor Suppressor Gene: Important Milestones at the Various Steps of Tumorigenesis. *Genes Cancer.* 2011;2(4):466-474.

17. Vogel WH. Li-Fraumeni Syndrome. *J Adv Pract Oncol.* 2017;8(7):742-746.

18. Reuvers TGA, Kanaar R, Nonnekens J. DNA Damage-Inducing Anticancer Therapies: From Global to Precision Damage. *Cancers (Basel).* 2020;12(8).

19. Yang S-H, Kuo T-C, Wu H, et al. Perspectives on the combination of radiotherapy and targeted therapy with DNA repair inhibitors in the treatment of pancreatic cancer. *World J gastroenterology.* 2016;22(32):7275-7288.

20. Cheng B, Pan W, Xing Y, Xiao Y, Chen J, Xu Z. Recent advances in DDR (DNA damage response) inhibitors for cancer therapy. *Eur J Med Chem.* 2022;230:114109.

21. Kim H, Xu H, George E, et al. Combining PARP with ATR inhibition overcomes PARP inhibitor and platinum resistance in ovarian cancer models. *Nature Commun.* 2020;11(1):3726.

22. Faraoni I, Graziani G. Role of BRCA Mutations in Cancer Treatment with Poly(ADP-ribose) Polymerase (PARP) Inhibitors. *Cancers (Basel).* 2018;10(12).

23. Das S, Camphausen K, Shankavaram U. Pan-Cancer Analysis of Potential Synthetic Lethal Drug Targets Specific to Alterations in DNA Damage Response. *Front Oncol.* 2019;9.

24. Study to Assess the Safety and Preliminary Efficacy of AZD0156 at Increasing Doses Alone or in Combination With Other Anti-cancer Treatment in Patients With Advanced Cancer (AToM). https://clinicaltrials.gov/ct2/show/NCT02588105.

25. Weber AM, Ryan AJ. ATM and ATR as therapeutic targets in cancer. *Pharmacol Ther.* 2015;149:124-138.

26. Warren C, Pavletich NP. Structure of the human ATM kinase and mechanism of Nbs1 binding. *eLife.* 2021;11:e74218.

27. Rothblum-Oviatt C, Wright J, Lefton-Greif MA, McGrath-Morrow SA, Crawford TO, Lederman HM. Ataxia telangiectasia: a review. *Orphanet J Rare Dis.* 2016;11(1):159.

28. Stakyte K, Rotheneder M, Lammens K, et al. Molecular basis of human ATM kinase inhibition. *Nat Struct Mol Biol.* 2021;28(10):789-798.

29. Xiao J, Liu M, Qi Y, et al. Structural insights into the activation of ATM kinase. *Cell Res.* 2019;29(8):683-685.

30. Bekker-Jensen DB, Kelstrup CD, Batth TS, et al. An Optimized Shotgun Strategy for the Rapid Generation of Comprehensive Human Proteomes. *Cell Syst.* 2017;4(6):587-599.e584.

31. Beck M, Schmidt A, Malmstroem J, et al. The quantitative proteome of a human cell line. *Mol Systems Biol.* 2011;7(1):549.

32. Wiśniewski JR, Hein MY, Cox J, Mann M. A "proteomic ruler" for protein copy number and concentration estimation without spike-in standards. *Mol Cell Proteomics.* 2014;13(12):3497-3506.

33. Uziel T, Lerenthal Y, Moyal L, Andegeko Y, Mittelman L, Shiloh Y. Requirement of the MRN complex for ATM activation by DNA damage. *EMBO J.* 2003;22(20):5612-5621.

34. Kozlov SV, Graham ME, Peng C, Chen P, Robinson PJ, Lavin MF. Involvement of novel autophosphorylation sites in ATM activation. *EMBO J.* 2006;25(15):3504-3514.

35. Hartlerode AJ, Morgan MJ, Wu Y, Buis J, Ferguson DO. Recruitment and activation of the ATM kinase in the absence of DNA-damage sensors. *Nat Struct Mol Biol.* 2015;22(9):736-743.

36. Bakkenist CJ, Kastan MB. DNA damage activates ATM through intermolecular autophosphorylation and dimer dissociation. *Nature.* 2003;421(6922):499-506.

37. Sun Y, Xu Y, Roy K, Price BD. DNA damage-induced acetylation of lysine 3016 of ATM activates ATM kinase activity. *Molecular and cellular biology.* 2007;27(24):8502-8509.

38. Daniel JA, Pellegrini M, Lee J-H, Paull TT, Feigenbaum L, Nussenzweig A. Multiple autophosphorylation sites are dispensable for murine ATM activation in vivo. *J Cell Biol.* 2008;183(5):777-783.

39. Pellegrini M, Celeste A, Difilippantonio S, et al. Autophosphorylation at serine 1987 is dispensable for murine Atm activation in vivo. *Nature.* 2006;443(7108):222-225.

40. Paull TT. Mechanisms of ATM Activation. *Annu Rev Biochem.* 2015;84(1):711-738.

41. Baretić D, Pollard HK, Fisher DI, et al. Structures of closed and open conformations of dimeric human ATM. *Science Adv.* 2017;3(5):e1700933.

42. Guo Z, Kozlov S, Lavin MF, Person MD, Paull TT. ATM Activation by Oxidative Stress. *Science.* 2010;330(6003):517-521.

43. Gately DP, Hittle JC, Chan GK, Yen TJ. Characterization of ATM expression, localization, and associated DNA-dependent protein kinase activity. *Mol Biol Cell.* 1998;9(9):2361-2374.

44. Roossink F, Wieringa HW, Noordhuis MG, et al. The role of ATM and 53BP1 as predictive markers in cervical cancer. *Int J Cancer.* 2012;131(9):2056-2066.

45. Bian L, Meng Y, Zhang M, et al. ATM Expression Is Elevated in Established Radiation-Resistant Breast Cancer Cells and Improves DNA Repair Efficiency. *Int J Biol Sci.* 2020;16(7):1096-1106.

46. Choi M, Kipps T, Kurzrock R. ATM Mutations in Cancer: Therapeutic Implications. *Mol Cancer Ther.* 2016;15(8):1781-1791.

47. Dombernowsky SL, Weischer M, Allin KH, Bojesen SE, Tybjjrg-Hansen A, Nordestgaard BG. Risk of Cancer by ATM Missense Mutations in the General Population. *J Clin Oncol.* 2008;26(18):3057-3062.

48. Swift M, Morrell D, Massey RB, Chase CL. Incidence of Cancer in 161 Families Affected by Ataxia–Telangiectasia. *N Engl J Med.* 1991;325(26):1831-1836.

49. Boultwood J. Ataxia telangiectasia gene mutations in leukaemia and lymphoma. *J Clin Pathol.* 2001;54(7):512-516.

50. Randon G, Fucà G, Rossini D, et al. Prognostic impact of ATM mutations in patients with metastatic colorectal cancer. *Scientific Rep.* 2019;9(1):2858-2858.

51. Huang C, Filippone NR, Reiner T, Roberts S. Sensors and Inhibitors for the Detection of Ataxia Telangiectasia Mutated (ATM) Protein Kinase. *Mol Pharm.* 2021;18(7):2470-2481.

52. Jin MH, Oh D-Y. ATM in DNA repair in cancer. *Pharmacol Ther.* 2019;203:107391.

53. Kantidze OL, Velichko AK, Luzhin AV, Petrova NV, Razin SV. Synthetically Lethal Interactions of ATM, ATR, and DNA-PKcs. *Trends Cancer.* 2018;4(11):755-768.

54. A Study to Assess the Safety and Tolerability of AZD1390 Given With Radiation Therapy in Patients With Brain Cancer. https://clinicaltrials.gov/ct2/show/NCT03423628.

55. AZD1390 in Recurrent Grade IV Glioma Patients. https://www.clinicaltrials.gov/ct2/show/NCT05182905.

56. A Platform Study of Novel Agents in Combination With Radiotherapy in NSCLC (CONCORDE). https://clinicaltrials.gov/ct2/show/NCT04550104.

57. Sarcomas and DDR-Inhibition; a Combined Modality Study (SADDRIN-1). https://clinicaltrials.gov/ct2/show/NCT05116254.

58. AZD1390 Administration of a Microdose [^{11}C]AZD1390 to Healthy Volunteers. https://clinicaltrials.gov/ct2/show/NCT03215381.

59. Durant ST, Zheng L, Wang Y, et al. The brain-penetrant clinical ATM inhibitor AZD1390 radiosensitizes and improves survival of preclinical brain tumor models. *Science Adv.* 2018;4(6):eaat1719.

60. Jucaite A, Stenkrona P, Cselényi Z, et al. Brain exposure of the ATM inhibitor AZD1390 in humans - a positron emission tomography study. *Neuro Oncol.* 2021;23(4):687-696.

61. Pike KG, Barlaam B, Cadogan E, et al. The Identification of Potent, Selective, and Orally Available Inhibitors of Ataxia Telangiectasia Mutated (ATM) Kinase: The Discovery of AZD0156 (8-{6-[3-(Dimethylamino)propoxy]pyridin-3-yl}-3-methyl-1-(tetrahydro-2H-pyran-4-yl)-1,3-dihydro-2H-imidazo[4,5-c]quinolin-2-one). *J Med Chem.* 2018;61(9):3823-3841.

62. First-in-human Study of M4076 in Advanced Solid Tumors (DDRiver Solid Tumors 410). https://clinicaltrials.gov/ct2/show/NCT04882917.

63. Fuchss T, Becker A, Kubas H, Graedler U, Inventors; Merck Patent GMBH, assignee. Imidazolonylquinoline compounds and therapeutic uses thereof. US patent WO2020193660A1. 1st October, 2020.

64. Zimmermann A, Zenke FT, Chiu L-Y, et al. A New Class of Selective ATM Inhibitors as Combination Partners of DNA Double-Strand Break Inducing Cancer Therapies. *Mol Cancer Ther.* 2022;21(6):859-870.

65. M3541 in Combination With Radiotherapy in Subjects With Solid Tumors. https://clinicaltrials.gov/ct2/show/NCT03225105.

66. Waqar SN, Robinson C, Olszanski AJ, et al. Phase I trial of ATM inhibitor M3541 in combination with palliative radiotherapy in patients with solid tumors. *Invest New Drugs.* 2022;40(3):596-605.

67. Evaluation of a Promising New Combination of Protein Kinase Inhibitors on Organotypic Cultures of Human Renal Tumors (COMBOREIN). https://clinicaltrials.gov/ct2/show/NCT03571438.

68. Golding SE, Rosenberg E, Valerie N, et al. Improved ATM kinase inhibitor KU-60019 radiosensitizes glioma cells, compromises insulin, AKT and ERK prosurvival signaling, and inhibits migration and invasion. *Mol Cancer Ther.* 2009;8(10):2894-2902.

69. Hickson I, Zhao Y, Richardson CJ, et al. Identification and Characterization of a Novel and Specific Inhibitor of the Ataxia-Telangiectasia Mutated Kinase ATM. *Cancer Res.* 2004;64(24):9152-9159.

70. Batey MA, Zhao Y, Kyle S, et al. Preclinical evaluation of a novel ATM inhibitor, KU59403, in vitro and in vivo in p53 functional and dysfunctional models of human cancer. *Mol Cancer Ther.* 2013;12(6):959-967.

71. Rainey MD, Charlton ME, Stanton RV, Kastan MB. Transient Inhibition of ATM Kinase Is Sufficient to Enhance Cellular Sensitivity to Ionizing Radiation. *Cancer Res.* 2008;68(18):7466-7474.

72. Guo K, Shelat AA, Guy RK, Kastan MB. Development of a cell-based, high-throughput screening assay for ATM kinase inhibitors. *J Biomol Screen.* 2014;19(4):538-546.

73. Morales J, Li L, Fattah FJ, et al. Review of poly (ADP-ribose) polymerase (PARP) mechanisms of action and rationale for targeting in cancer and other diseases. *Crit Rev Eukaryot Gene Expr.* 2014;24(1):15-28.

74. van Beek L, McClay É, Patel S, Schimpl M, Spagnolo L, Maia de Oliveira T. PARP Power: A Structural Perspective on PARP1, PARP2, and PARP3 in DNA Damage Repair and Nucleosome Remodelling. *Int J Mol Sci.* 2021;22(10).

75. Zaniolo K, Desnoyers S, Leclerc S, Guérin SL. Regulation of poly(ADP-ribose) polymerase-1 (PARP-1) gene expression through the post-translational modification of Sp1: a nuclear target protein of PARP-1. *BMC Mol Biol.* 2007;8(1):96.

76. Dréan A, Lord CJ, Ashworth A. PARP inhibitor combination therapy. *Crit Rev Oncolo Hematol.* 2016;108:73-85.

77. Curtin NJ, Szabo C. Therapeutic applications of PARP inhibitors: anticancer therapy and beyond. *Mol Aspects Med.* 2013;34(6):1217-1256.

78. Lal S, Snape TJ. A therapeutic update on PARP inhibitors: implications in the treatment of glioma. *Drug Discovery Today.* 2021;26(2):532-541.

79. Menear KA, Adcock C, Boulter R, et al. 4-[3-(4-Cyclopropanecarbonylpiperazine-1-carbonyl)-4-fluorobenzyl]-2H-phthalazin-1-one: A Novel Bioavailable Inhibitor of Poly(ADP-ribose) Polymerase-1. *J Med Chem.* 2008;51(20):6581-6591.

80. Shen Y, Rehman FL, Feng Y, et al. BMN 673, a Novel and Highly Potent PARP1/2 Inhibitor for the Treatment of Human Cancers with DNA Repair Deficiency. *Clinical cancer research : an official journal of the American Association for Cancer Research.* 2013;19(18):5003-5015.

81. Robillard L, Nguyen M, Harding TC, Simmons AD. Abstract 2475: In vitro and in vivo assessment of the mechanism of action of the PARP inhibitor rucaparib. *Cancer Res.* 2017;77(13_Supplement):2475-2475.

82. Jones P, Altamura S, Boueres J, et al. Discovery of 2-{4-[(3S)-Piperidin-3-yl]phenyl}-2H-indazole-7-carboxamide (MK-4827): A Novel Oral Poly(ADP-ribose)polymerase (PARP) Inhibitor Efficacious in BRCA-1 and -2 Mutant Tumors. *J Med Chem.* 2009;52(22):7170-7185.

83. Xiong Y, Guo Y, Liu Y, et al. Pamiparib is a potent and selective PARP inhibitor with unique potential for the treatment of brain tumor. *Neoplasia.* 2020;22(9):431-440.

84. Miknyoczki S, Chang H, Grobelny J, et al. The selective poly(ADP-ribose) polymerase-1(2) inhibitor, CEP-8983, increases the sensitivity of chemoresistant tumor cells to temozolomide and irinotecan but does not potentiate myelotoxicity. *Mol Cancer Ther.* 2007;6(8):2290-2302.

85. Study to Determine the Maximum Tolerated Dose of the PARP Inhibitor CEP-9722 in Patients With Solid Tumors. https://clinicaltrials.gov/ct2/show/NCT01311713.

86. Study of CEP-9722 in Combination With Gemcitabine and Cisplatin in Patients With Advanced Solid Tumors or Mantle Cell Lymphoma. https://clinicaltrials.gov/ct2/show/NCT01345357.

87. Study of CEP-9722 as Single-Agent Therapy and as Combination Therapy With Temozolomide in Patients With Advanced Solid Tumors. https://clinicaltrials.gov/ct2/show/NCT00920595.

88. Russo AL, Kwon H-C, Burgan WE, et al. In vitro and In vivo Radiosensitization of Glioblastoma Cells by the Poly (ADP-Ribose) Polymerase Inhibitor E7016. *Clinical cancer research : an official journal of the American Association for Cancer Research.* 2009;15(2):607-612.

89. Xu W, Delahanty G, Zhang J, Inventors; MGI GP, INC., assignee. Diazabenzo[de]anthracen-3-one compounds and methods for inhibiting PARP. US patent WO2006078711A2. 27th July, 2006.

90. Study of Poly (ADP-Ribose) Polymerase (PARP) Inhibitor E7016 in Combination With Temozolomide in Subjects With Advanced Solid Tumors. https://clinicaltrials.gov/ct2/show/NCT01127178.

91. Phase 2 Study of the Poly(ADP-Ribose) Polymerase Inhibitor E7016 in Combination With Temozolomide in Subjects With Wild Type BRAF Stage IV or Unresectable Stage III Melanoma. https://clinicaltrials.gov/ct2/show/NCT01605162.

92. Iwashita A, Tojo N, Matsuura S, et al. A Novel and Potent Poly(ADP-Ribose) Polymerase-1 Inhibitor, FR247304 (5-Chloro-2-[3-(4-phenyl-3,6-dihydro-1(2*H*)-pyridinyl)propyl]-4(3*H*)-quinazolinone), Attenuates Neuronal Damage in in Vitro and in Vivo Models of Cerebral Ischemia. *J Pharmacol Exp Ther.* 2004;310(2):425-436.

93. Huang S-H, Xiong M, Chen X-P, Xiao Z-Y, Zhao Y-F, Huang Z-Y. PJ34, an inhibitor of PARP-1, suppresses cell growth and enhances the suppressive effects of cisplatin in liver cancer cells. *Oncol Rep.* 2008;20(3):567-572.

94. Visochek L, Atias D, Spektor I, Castiel A, Golan T, Cohen-Armon M. The phenanthrene derivative PJ34 exclusively eradicates human pancreatic cancer cells in xenografts. *Oncotarget.* 2019;10(58):6269-6282.

95. Penning TD, Zhu GD, Gong J, et al. Optimization of phenyl-substituted benzimidazole carboxamide poly(ADP-ribose) polymerase inhibitors: identification of (S)-2-(2-fluoro-4-(pyrrolidin-2-yl)phenyl)-1H-benzimidazole-4-carboxamide (A-966492), a highly potent and efficacious inhibitor. *J Med Chem.* 2010;53(8):3142-3153.

96. Koosha F, Neshasteh-Riz A, Takavar A, et al. The combination of A-966492 and Topotecan for effective radiosensitization on glioblastoma spheroids. *Biochem Biophy Res Comm.* 2017;491(4):1092-1097.

97. Khan K, Araki K, Wang D, et al. Head and neck cancer radiosensitization by the novel poly(ADP-ribose) polymerase inhibitor GPI-15427. *Head & Neck.* 2010;32(3):381-391.

98. Tentori L, Leonetti C, Scarsella M, et al. Systemic Administration of GPI 15427, a Novel Poly(ADP-Ribose) Polymerase-1 Inhibitor, Increases the Antitumor Activity of Temozolomide against Intracranial Melanoma, Glioma, Lymphoma. *Clinical cancer research : an official journal of the American Association for Cancer Research.* 2003;9(14):5370-5379.

99. Tentori L, Leonetti C, Scarsella M, et al. Oral administration of the PARP-1 inhibitor GPI 15427 increases the anti-tumor activity of temozolomide against melanoma growing at the CNS site. *Cancer Res.* 2004;64(7_Supplement):462-462.

100. Tentori L, Leonetti C, Scarsella M, et al. Brain distribution and efficacy as chemosensitizer of an oral formulation of PARP-1 inhibitor GPI 15427 in experimental models of CNS tumors. *Int J Oncol.* 2005;26(2):415-422.

101. Tentori L, Leonetti C, Scarsella M, et al. Inhibition of poly(ADP-ribose) polymerase prevents irinotecan-induced intestinal damage and enhances irinotecan/temozolomide efficacy against colon carcinoma. *The FASEB Journal.* 2006;20(10):1709-1711.

102. Guo C, Zhang F, Wu X, et al. BTH-8, a novel poly (ADP-ribose) polymerase-1 (PARP-1) inhibitor, causes DNA double-strand breaks and exhibits anticancer activities in vitro and in vivo. *Int J Biol Macromol.* 2020;150:238-245.

103. Wu X, Li Q, Zhang F, et al. Novel poly (ADP-ribose) polymerases inhibitor DHC-1 exhibits in vitro and in vivo anticancer activity on BRCA-deficient pancreatic cancer cells. *Food Chem Toxicol.* 2021;147:111892.

104. Zhou J, Ji M, Wang X, et al. Discovery of Quinazoline-2,4(1H,3H)-dione Derivatives Containing 3-Substituted Piperizines as Potent PARP-1/2 Inhibitors–Design, Synthesis, In Vivo Antitumor Activity, and X-ray Crystal Structure Analysis. *J Med Chem.* 2021;64(22):16711-16730.

105. Noordermeer SM, van Attikum H. PARP Inhibitor Resistance: A Tug-of-War in BRCA-Mutated Cells. *Trends Cell Biol.* 2019;29(10):820-834.

106. Li H, Liu Z-Y, Wu N, Chen Y-C, Cheng Q, Wang J. PARP inhibitor resistance: the underlying mechanisms and clinical implications. *Mol Cancer.* 2020;19(1):107.

107. Mishani E, Abourbeh G, Eiblmaier M, Anderson CJ. Imaging of EGFR and EGFR tyrosine kinase overexpression in tumors by nuclear medicine modalities. *Curr Pharm Des.* 2008;14(28):2983-2998.

108. Vander Heiden MG, Cantley LC, Thompson CB. Understanding the Warburg effect: the metabolic requirements of cell proliferation. *Science.* 2009;324(5930):1029-1033.

109. Love C, Tomas MB, Tronco GG, Palestro CJ. FDG PET of infection and inflammation. *Radiographics.* 2005;25(5):1357-1368.

110. Najjar AM, Johnson JM, Schellingerhout D. The Emerging Role of Amino Acid PET in Neuro-Oncology. *Bioeng (Basel).* 2018;5(4).

111. Huang Y, Fan J, Li Y, Fu S, Chen Y, Wu J. Imaging of Tumor Hypoxia With Radionuclide-Labeled Tracers for PET. *Front Oncol.* 2021;11.

112. Hara T, Kosaka N, Kishi H. Development of ^{18}F-Fluoroethylcholine for Cancer Imaging with PET: Synthesis, Biochemistry, and Prostate Cancer Imaging. *Journal of nuclear medicine : official publication, Society of Nuclear Medicine.* 2002;43(2):187-199.

113. Hennrich U, Eder M. [(68)Ga]Ga-PSMA-11: The First FDA-Approved (68)Ga-Radiopharmaceutical for PET Imaging of Prostate Cancer. *Pharmaceuticals (Basel).* 2021;14(8).

114. Sandhu S, Guo C, Hofman MS. Radionuclide Therapy in Prostate Cancer: From Standalone to Combination PSMA Theranostics. *Journal of nuclear medicine : official publication, Society of Nuclear Medicine.* 2021;62(12):1660-1668.

115. Pauwels E, Cleeren F, Bormans G, Deroose CM. Somatostatin receptor PET ligands - the next generation for clinical practice. *Am J Nucl Med Mol Imaging.* 2018;8(5):311-331.

116. Habbous S, Forster K, Darling G, et al. Incidence and real-world burden of brain metastases from solid tumors and hematologic malignancies in Ontario: a population-based study. *Neuro Oncol Adv.* 2020;3(1).

117. Davis FG, Dolecek TA, McCarthy BJ, Villano JL. Toward determining the lifetime occurrence of metastatic brain tumors estimated from 2007 United States cancer incidence data. *Neuro Oncol.* 2012;14(9):1171-1177.

118. Nayak L, Lee EQ, Wen PY. Epidemiology of Brain Metastases. *Curr Oncol Rep.* 2012;14(1):48-54.

119. Liu Q, Tong X, Wang J. Management of brain metastases: history and the present. *Chin Neurosci J.* 2019;5(1):1.

120. Mayo Clinic - Brain Tumour. https://www.mayoclinic.org/diseases-conditions/brain-tumor/diagnosis-treatment/drc-20350088. Accessed 5th July, 2022.

121. Stamatovic SM, Johnson AM, Keep RF, Andjelkovic AV. Junctional proteins of the blood-brain barrier: New insights into function and dysfunction. *Tissue Barriers.* 2016;4(1):e1154641.

122. Mo F, Pellerino A, Soffietti R, Rudà R. Blood-Brain Barrier in Brain Tumors: Biology and Clinical Relevance. *Int J Mol Sci.* 2021;22(23):12654.

123. O'Reilly MA, Hynynen K. Ultrasound enhanced drug delivery to the brain and central nervous system. *Int J Hyperthermia.* 2012;28(4):386-396.

124. Chowdhury EA, Noorani B, Alqahtani F, et al. Understanding the brain uptake and permeability of small molecules through the BBB: A technical overview. *J Cereb Blood Flow Metab.* 2021;41(8):1797-1820.

125. Zimmer L, Luxen A. PET radiotracers for molecular imaging in the brain: Past, present and future. *NeuroImage.* 2012;61(2):363-370.

126. Pike VW. PET radiotracers: crossing the blood-brain barrier and surviving metabolism. *Trends Pharmacol Sci.* 2009;30(8):431-440.

127. Galldiks N, Lohmann P, Albert NL, Tonn JC, Langen KJ. Current status of PET imaging in neuro-oncology. *Neuro Oncol Adv.* 2019;1(1):vdz010.

128. Albert NL, Weller M, Suchorska B, et al. Response Assessment in Neuro-Oncology working group and European Association for Neuro-Oncology recommendations for the clinical use of PET imaging in gliomas. *Neuro Oncol.* 2016;18(9):1199-1208.

129. Petrirena GJ, Goldman S, Delattre J-Y. Advances in PET imaging of brain tumors: a referring physician's perspective. *Curr Opin Oncol.* 2011;23(6):617-623.

130. Syvänen S, Eriksson J. Advances in PET imaging of P-glycoprotein function at the blood-brain barrier. *ACS Chem Neurosci.* 2013;4(2):225-237.

131. Tu Z, Chu W, Zhang J, Dence CS, Welch MJ, Mach RH. Synthesis and in vivo evaluation of [^{11}C]PJ34, a potential radiotracer for imaging the role of PARP-1 in necrosis. *Nucl Med Biol.* 2005;32(5):437-443.

132. Knight JC, Koustoulidou S, Cornelissen B. Imaging the DNA damage response with PET and SPECT. *EJNMMI.* 2017;44(6):1065-1078.

133. Puentes LN, Makvandi M, Mach RH. Molecular Imaging: PARP-1 and Beyond. *Journal of nuclear medicine : official publication, Society of Nuclear Medicine.* 2021;62(6):765.

134. Wang Q, Zhang J. Current status and progress in using radiolabelled PARP-1 inhibitors for imaging PARP-1 expression in tumours. *Eur J Med Chem.* 2022;242:114690.

135. Lee HS, Schwarz SW, Schubert EK, et al. The Development of ^{18}F Fluorthanatrace: A PET Radiotracer for Imaging Poly (ADP-Ribose) Polymerase-1. *Radiol Imaging Cancer.* 2022;4(1):e210070-e210070.

136. Young RJ, Demétrio De Souza França P, Pirovano G, et al. Preclinical and first-in-human-brain-cancer applications of [^{18}F]poly (ADP-ribose) polymerase inhibitor PET/MR. *Neuro Oncol Adv.* 2020;2(1).

137. Everix L, Nair S, Driver CHS, et al. Perspective on the Use of DNA Repair Inhibitors as a Tool for Imaging and Radionuclide Therapy of Glioblastoma. *Cancers (Basel).* 2022;14(7).

138. Carlucci G, Carney B, Sadique A, Vansteene A, Tang J, Reiner T. Evaluation of [^{18}F]-ATRi as PET tracer for in vivo imaging of ATR in mouse models of brain cancer. *Nucl Med Biol.* 2017;48:9-15.

139. Gao M, Wang M, Miller KD, Zheng Q-H. Simple synthesis of carbon-11-labeled chromen-4-one derivatives as new potential PET agents for imaging of DNA-dependent protein kinase (DNA-PK) in cancer. *Applied Radiation and Isotopes.* 2012;70(8):1558-1563.

140. Wickremsinhe ER, Hynes SM, Payne CD, Guo Y, Cassidy KC. Disposition of [(14)C]LY2606368 following intravenous administration in patients with advanced and/or metastatic solid tumours. *Xenobiotica.* 2020;50(7):793-804.

141. Wickremsinhe ER, Hynes SM, Palmieri MD, et al. Disposition and metabolism of LY2603618, a Chk-1 inhibitor following intravenous administration in patients with advanced and/or metastatic solid tumors. *Xenobiotica.* 2014;44(9):827-841.

142. A Study of [^{14}C]-LY3023414 in Healthy Participants. https://clinicaltrials.gov/ct2/show/NCT02575703.

143. Penner N, Xu L, Prakash C. Radiolabeled absorption, distribution, metabolism, and excretion studies in drug development: why, when, and how? *Chem Res Toxicol.* 2012;25(3):513-531.

144. Minchom A, Aversa C, Lopez J. Dancing with the DNA damage response: next-generation anti-cancer therapeutic strategies. *Ther Adv Med Oncol.* 2018;10:175883591878665.

145. Bunimovich YL, Nair-Gill E, Riedinger M, et al. Deoxycytidine Kinase Augments ATM-Mediated DNA Repair and Contributes to Radiation Resistance. *PLOS ONE.* 2014;9(8):e104125.

146. Fischman AJ, Alpert NM, Rubin RH. Pharmacokinetic Imaging. *Clin Pharmacokinet.* 2002;41(8):581-602.

147. Pike K, Gordon, Barlaam B, Christophe, Hunt T, Anthony, Eatherton A, John, Inventors; Astrazeneca AB, assignee. 8-[6-[3-(amino)propoxy]-3-pyridyl]-1-isopropyl-imidazo[4,5-c]quinolin-2-one derivatives as selective modulators of ataxia telangiectasia mutated (ATM) kinase for the treatment of cancer. US patent WO2017046216A1. 23rd March, 2017.

148. Weber AM, Drobnitzky N, Devery AM, et al. Phenotypic consequences of somatic mutations in the ataxia-telangiectasia mutated gene in non-small cell lung cancer. *Oncotarget.* 2016;7(38):60807-60822.

149. Dollé F. Fluorine-18-labelled fluoropyridines: advances in radiopharmaceutical design. *Curr Pharm Des.* 2005;11(25):3221-3235.

150. Tredwell M, Gouverneur V. ^{18}F Labeling of Arenes. *Angew Chem Int Ed.* 2012;51(46):11426-11437.

151. Dolci L, Dolle F, Jubeau S, Vaufrey F, Crouzel C. 2-[^{18}F]fluoropyridines by no-carrier-added nucleophilic aromatic substitution with [^{18}F]FK-K_{222}—a comparative study. *J Labelled Compd Radiopharm.* 1999;42(10):975-985.

152. Preshlock S, Tredwell M, Gouverneur V. ^{18}F-Labeling of Arenes and Heteroarenes for Applications in Positron Emission Tomography. *Chem Rev.* 2016;116(2):719-766.

153. Björk S, Delisser V, Johnström P, et al., Inventors; Astrazeneca AB, assignee. New Benzofurans Suitable As Precursors To Compounds That Are Useful For Imaging Amyloid Deposits. US patent WO2010024769A1. 4th March, 2010.

154. Smida M, Fece de la Cruz F, Kerzendorfer C, et al. MEK inhibitors block growth of lung tumours with mutations in ataxia-telangiectasia mutated. *Nat Commun.* 2016;7:13701.

155. Degorce SL, Barlaam B, Cadogan E, et al. Discovery of Novel 3-Quinoline Carboxamides as Potent, Selective, and Orally Bioavailable Inhibitors of Ataxia Telangiectasia Mutated (ATM) Kinase. *J Med Chem.* 2016;59(13):6281-6292.

156. Ravi S, Barui S, Kirubakaran S, Duhan P, Bhowmik K. Synthesis and Characterization of Quinoline-3-Carboxamide Derivatives as Inhibitors of the ATM Kinase. *Curr Top Med Chem.* 2020;20(23):2070-2079.

157. Wright JS, Sharninghausen LS, Preshlock S, Brooks AF, Sanford MS, Scott PJH. Sequential Ir/Cu-Mediated Method for the Meta-Selective C–H Radiofluorination of (Hetero)Arenes. *J Am Chem Soc.* 2021;143(18):6915-6921.

158. Chun J-H, Lu S, Pike VW. Rapid and Efficient Radiosyntheses of meta-Substituted [^{18}F]Fluoroarenes from [^{18}F]Fluoride Ion and Diaryliodonium -Tosylates within a Microreactor. *Eur J Org Chem.* 2011;2011(23):4439-4447.

159. Carroll MA, Nairne J, Woodcraft JL. Diaryliodonium salts: a solution to 3-[^{18}F]fluoropyridine. *J Labelled Compd Radiopharm.* 2007;50(5-6):452-454.

160. Quinquer JS, Carlos Piera Peña, Isabel Ramirez De Arellano Serna, Inventor; Cetir Centre Medic, S.A., assignee. Compounds which can be used to diagnose and monitor diseases associated with the formation of amyloid protein fibrils. US patent WO2004045651A1. 3rd June, 2004.

161. Sergeev ME, Morgia F, Lazari M, Wang C, van Dam RM. Titania-Catalyzed Radiofluorination of Tosylated Precursors in Highly Aqueous Medium. *J Am Chem Soc.* 2015;137(17):5686-5694.

162. Tredwell M, Preshlock SM, Taylor NJ, et al. A General Copper-Mediated Nucleophilic ^{18}F Fluorination of Arenes. 2014;53(30):7751-7755.

163. Ishiyama T, Ishida K, Miyaura N. Synthesis of pinacol arylboronates via cross-coupling reaction of bis(pinacolato)diboron with chloroarenes catalyzed by palladium(0)–tricyclohexylphosphine complexes. *Tetrahedron.* 2001;57(49):9813-9816.

164. Barroso S, Joksch M, Puylaert P, et al. Improvement in the Palladium-Catalyzed Miyaura Borylation Reaction by Optimization of the Base: Scope and Mechanistic Study. *J Org Chem.* 2021;86(1):103-109.

165. Matthews RS. 19F NMR spectroscopy of polyhalonaphthalenes. Part IV. Halex reactions of polychloroquinolines. *J Fluorine Chem.* 1998;91(2):203-205.

166. Brömmel K, Konken CP, Börgel F, et al. Synthesis and biological evaluation of PET tracers designed for imaging of calcium activated potassium channel 3.1 (KCa3.1) channels in vivo. *RSC Advances.* 2021;11(48):30295-30304.

167. Neumann CN, Hooker JM, Ritter T. Concerted nucleophilic aromatic substitution with $^{19}F^-$ and $^{18}F^-$. *Nature.* 2016;534(7607):369-373.

168. Preshlock S, Calderwood S, Verhoog S, et al. Enhanced copper-mediated ^{18}F-fluorination of aryl boronic esters provides eight radiotracers for PET applications. *Chem Commun.* 2016;52(54):8361-8364.

169. Gendron T, Destro G, Straathof NJW, et al. Multi-patient dose synthesis of [^{18}F]Flumazenil via a copper-mediated 18F-fluorination. *EJNMMI Radiopharm Chem.* 2022;7(1):5.

170. Zhang Z, Ge J, Jing K, et al. A reliable and automated synthesis of 6-[^{18}F]fluoro-L-DOPA and the clinical application on the imaging of congenital hyperinsulinism of infants. *Med Chem Res.* 2022;31(7):1126-1134.

171. van der Hoek S, Antunes IF, Attia KA, et al. GMP Compliant Synthesis of [^{18}F]Canagliflozin, a Novel PET Tracer for the Sodium–Glucose Cotransporter 2. *J Med Chem.* 2021;64(22):16641-16649.

172. Chen Z, Destro G, Guibbal F, Chan CY, Cornelissen B, Gouverneur V. Copper-Mediated Radiosynthesis of [^{18}F]Rucaparib. *Org Lett.* 2021;23(18):7290-7294.

173. Guibbal F, Isenegger PG, Wilson TC, et al. Manual and automated Cu-mediated radiosynthesis of the PARP inhibitor [^{18}F]olaparib. *Nature Protocols.* 2020;15(4):1525-1541.

174. Ajenjo J, Destro G, Cornelissen B, Gouverneur V. Correction to: Closing the gap between 19F and 18F chemistry. *EJNMMI Radiopharm Chem.* 2022;7(1):1.

175. Blom E, Karimi F, Långström B. [18F]/19F exchange in fluorine containing compounds for potential use in 18F-labelling strategies. *J Labelled Compd Radiopharm.* 2009;52(12):504-511.

176. Chen W, Wang H, Tay NES, et al. Arene radiofluorination enabled by photoredox-mediated halide interconversion. *Nature Chem.* 2022;14(2):216-223.

177. Tay NES, Chen W, Levens A, et al. ^{19}F- and ^{18}F-Arene Deoxyfluorination via Organic Photoredox-Catalysed Polarity-Reversed Nucleophilic Aromatic Substitution. *Nat Catal.* 2020;3(9):734-742.

178. Hernández-Valdés D, Sadeghi S. Electrochemical Radiofluorination of Small Molecules: New Advances. *The Chemical Record.* 2021;21(9):2397-2410.

179. Teare H, Robins EG, Kirjavainen A, et al. Radiosynthesis and evaluation of [^{18}F]Selectfluor bis(triflate). *Angew Chem Int Ed Engl.* 2010;49(38):6821-6824.

180. Oberdorfer F, Hofmann E, Maier-Borst W. Preparation of ^{18}F-labelled *N*-fluoropyridinium triflate. *J Labelled Compd Radiopharm.* 1988;25(9):999-1005.

181. Teare H, Robins EG, Arstad E, Luthra SK, Gouverneur V. Synthesis and reactivity of [^{18}F]-*N*-fluorobenzenesulfonimide. *Chem Commun (Cambridge, UK).* 2007(23):2330-2332.

182. Veal M. *Optimisation and evaluation of antibody-based immuno-PET/SPECT imaging of intranuclear epitopes*: Department of Oncology, University of Oxford; 2021.

183. Ning J, Wakimoto H. Therapeutic Application of PARP Inhibitors in Neuro-Oncology. *Trends Cancer.* 2020;6(2):147-159.

184. Parrish KE, Cen L, Murray J, et al. Efficacy of PARP Inhibitor Rucaparib in Orthotopic Glioblastoma Xenografts Is Limited by Ineffective Drug Penetration into the Central Nervous System. *Mol Cancer Ther.* 2015;14(12):2735-2743.

185. Sun K, Mikule K, Wang Z, et al. A comparative pharmacokinetic study of PARP inhibitors demonstrates favorable properties for niraparib efficacy in preclinical tumor models. *Oncotarget.* 2018;9(98):37080-37096.

186. Vaidyanathan A, Sawers L, Gannon A-L, et al. ABCB1 (MDR1) induction defines a common resistance mechanism in paclitaxel- and olaparib-resistant ovarian cancer cells. *Br J Cancer.* 2016;115(4):431-441.

187. Halford SER, Cruickshank G, Dunn L, et al. Results of the OPARATIC trial: A phase I dose escalation study of olaparib in combination with temozolomide (TMZ) in patients with relapsed glioblastoma (GBM). *J Clin Oncol.* 2017;35(15_suppl):2022-2022.

188. Hanna C, Kurian KM, Williams K, et al. Pharmacokinetics, safety, and tolerability of olaparib and temozolomide for recurrent glioblastoma: results of the phase I OPARATIC trial. *Neuro Oncol.* 2020;22(12):1840-1850.

189. Cruz C, Castroviejo-Bermejo M, Gutiérrez-Enríquez S, et al. RAD51 foci as a functional biomarker of homologous recombination repair and PARP inhibitor resistance in germline BRCA-mutated breast cancer. *Ann Oncol.* 2018;29(5):1203-1210.

190. Pilié PG, George A, Yap TA. Patient selection biomarker strategies for PARP inhibitor therapy. *Ann Oncol.* 2020;31(12):1603-1605.

191. Ossovskaya V, Koo IC, Kaldjian EP, Alvares C, Sherman BM. Upregulation of Poly (ADP-Ribose) Polymerase-1 (PARP1) in Triple-Negative Breast Cancer and Other Primary Human Tumor Types. *Genes Cancer.* 2010;1(8):812-821.

192. Huang Y-H, Yin S-J, Gong Y-Y, et al. PARP1 as a prognostic biomarker for human cancers: a meta-analysis. *Biomarkers in Medicine.* 2021;15(16):1563-1578.

193. Gajdzis M, Theocharis S, Klijanienko J, et al. The Prognostic Values of PARP-1 Expression in Uveal Melanoma. *Cells.* 2021;10(2).

194. Bertucci F, Finetti P, Monneur A, et al. PARP1 expression in soft tissue sarcomas is a poor-prognosis factor and a new potential therapeutic target. *Mol Oncol.* 2019;13(7):1577-1588.

195. Wang L, Liang C, Li F, et al. PARP1 in Carcinomas and PARP1 Inhibitors as Antineoplastic Drugs. *Int J Mol Sci.* 2017;18(10).

196. Reiner T, Keliher EJ, Earley S, Marinelli B, Weissleder R. Synthesis and In Vivo Imaging of a ^{18}F-Labeled PARP1 Inhibitor Using a Chemically Orthogonal Scavenger-Assisted High-Performance Method. *Angew Chem Int Ed.* 2011;50(8):1922-1925.

197. Ambur Sankaranarayanan R, Kossatz S, Weber W, Beheshti M, Morgenroth A, Mottaghy FM. Advancements in PARP1 Targeted Nuclear Imaging and Theranostic Probes. *J Clin Med.* 2020;9(7):E2130. doi:10.3390/jcm9072130. Accessed 2020/07//.

198. Michel LS, Dyroff S, Brooks FJ, et al. PET of Poly (ADP-Ribose) Polymerase Activity in Cancer: Preclinical Assessment and First In-Human Studies. *Radiology.* 2017;282(2):453-463.

199. Makvandi M, Pantel A, Schwartz L, et al. A PET imaging agent for evaluating PARP-1 expression in ovarian cancer. *J Clin Invest.* 2018;128(5):2116-2126.

200. Schöder H, França PDDS, Nakajima R, et al. Safety and Feasibility of PARP1/2 Imaging with ^{18}F-PARPi in Patients with Head and Neck Cancer. *Clinical cancer research : an official journal of the American Association for Cancer Research.* 2020;26(13):3110-3116.

201. Wilson TC, Xavier M-A, Knight J, et al. PET Imaging of PARP Expression Using ^{18}F-Olaparib. *Journal of nuclear medicine : official publication, Society of Nuclear Medicine.* 2019;60(4):504-510.

202. Chan CY, Chen Z, Destro G, et al. Imaging PARP with ^{18}F-rucaparib. *Journal of nuclear medicine : official publication, Society of Nuclear Medicine.* 2021;62(supplement 1):1516.

203. Bowden GD, Stotz S, Kinzler J, et al. DoE Optimization Empowers the Automated Preparation of Enantiomerically Pure [18F]Talazoparib and its In Vivo Evaluation as a PARP Radiotracer. *J Med Chem.* 2021;64(21):15690-15701.

204. Zhou D, Chen H, Mpoy C, et al. Radiosynthesis and Evaluation of Talazoparib and Its Derivatives as PARP-1-Targeting Agents. *Biomedicines.* 2021;9(5):565.

205. Guibbal F, Hopkins SL, Pacelli A, et al. [^{18}F]AZD2461, an Insight on Difference in PARP Binding Profiles for DNA Damage Response PET Imaging. *Mol Imaging Biol.* 2020;22(5):1226-1234.

206. Reilly S, MaKvandi M, Weng C-C, et al. Development of a PARP-1 Selective [^{18}F]-PET Probe for Brain Imaging Studies. *Journal of nuclear medicine : official publication, Society of Nuclear Medicine.* 2018;59(supplement 1):619.

207. Reilly SW, Puentes LN, Schmitz A, et al. Synthesis and evaluation of an AZD2461 [^{18}F]PET probe in non-human primates reveals the PARP-1 inhibitor to be non-blood-brain barrier penetrant. *Bioorg Chem.* 2019;83:242-249.

208. Barker G, O'Brien P, Campos KR. Diamine-Free Lithiation−Trapping of N-Boc Heterocycles using s-BuLi in THF. *Org Lett.* 2010;12(18):4176-4179.

209. Campos KR, Klapars A, Waldman JH, Dormer PG, Chen C-y. Enantioselective, Palladium-Catalyzed α-Arylation of N-Boc-pyrrolidine. *J Am Chem Soc.* 2006;128(11):3538-3539.

210. Salinas B, Irwin CP, Kossatz S, et al. Radioiodinated PARP1 tracers for glioblastoma imaging. *EJNMMI Res.* 2015;5(1):123.

211. Dun MD, Chalkley RJ, Faulkner S, et al. Proteotranscriptomic Profiling of 231-BR Breast Cancer Cells: Identification of Potential Biomarkers and Therapeutic Targets for Brain Metastasis. *Mol Cell Proteomics.* 2015;14(9):2316-2330.

212. Yoneda T, Williams PJ, Hiraga T, Niewolna M, Nishimura R. A bone-seeking clone exhibits different biological properties from the MDA-MB-231 parental human breast cancer cells and a brain-seeking clone in vivo and in vitro. *J Bone Miner Res.* 2001;16(8):1486-1495.

213. Wanner KT, Weber U. A convenient synthesis of 1,3-oxazolidin-4-ones and 1,3-oxazin-4-ones. *J Heterocycl Chem.* 1997;34(2):681-683.

214. Burkhard C. Notes - Trimethylsilyl Derivatives of Hydroxy Aromatic Acids. *J Org Chem.* 1957;22(5):592-593.

215. Gu Z-S, Chen W-X, Shao L-X. N-Heterocyclic Carbene-Palladium(II)-1-Methylimidazole Complex-Catalyzed Direct C–H Bond Arylation of (Benz)imidazoles with Aryl Chlorides. *J Org Chem.* 2014;79(12):5806-5811.

216. Shaw MH, Shurtleff VW, Terrett JA, Cuthbertson JD, MacMillan DWC. Native functionality in triple catalytic cross-coupling: sp^3 C–H bonds as latent nucleophiles. *Science.* 2016;352(6291):1304-1308.

217. Zuo Z, Ahneman DT, Chu L, Terrett JA, Doyle AG, MacMillan DWC. Merging photoredox with nickel catalysis: Coupling of α-carboxyl sp3-carbons with aryl halides. *Science.* 2014;345(6195):437-440.

218. Beyzavi H, Mandal D, Strebl MG, et al. 18F-Deoxyfluorination of Phenols via Ru π-Complexes. *ACS Central Science.* 2017;3(9):944-948.

219. Dakin L, Daly K, Del Valle D, et al., Inventors; Astrazeneca AB, assignee. Chemical Compounds. US patent WO2008056148A1. 15th May, 2008.

220. Liu L, Norman MH, Lee M, et al. Structure-Based Design of Novel Class II c-Met Inhibitors: 2. SAR and Kinase Selectivity Profiles of the Pyrazolone Series. *J Med Chem.* 2012;55(5):1868-1897.

221. Liu Z, Sun Y, Liu T. Recent Advances in Synthetic Methodologies to Form C-^{18}F Bonds. *Front Chem.* 2022;10:883866.

222. Cherry SR, Jones T, Karp JS, Qi J, Moses WW, Badawi RD. Total-Body PET: Maximizing Sensitivity to Create New Opportunities for Clinical Research and Patient Care. *Journal of nuclear medicine : official publication, Society of Nuclear Medicine.* 2018;59(1):3-12.

223. Badawi RD, Shi H, Hu P, et al. First Human Imaging Studies with the EXPLORER Total-Body PET Scanner. *Journal of nuclear medicine : official publication, Society of Nuclear Medicine.* 2019;60(3):299-303.

224. Campbell MG, Mercier J, Genicot C, Gouverneur V, Hooker JM, Ritter T. Bridging the gaps in 18F PET tracer development. *Nature Chem.* 2017;9(1):1-3.

225. Bowden GD, Pichler BJ, Maurer A. A Design of Experiments (DoE) Approach Accelerates the Optimization of Copper-Mediated 18F-Fluorination Reactions of Arylstannanes. *Scientific Rep.* 2019;9(1):11370.

226. Taylor NJ, Emer E, Preshlock S, et al. Derisking the Cu-Mediated ^{18}F-Fluorination of Heterocyclic Positron Emission Tomography Radioligands. *J Am Chem Soc.* 2017;139(24):8267-8276.

227. Allott L, Aboagye EO. Chemistry Considerations for the Clinical Translation of Oncology PET Radiopharmaceuticals. *Mol Pharm.* 2020;17(7):2245-2259.

228. Demény MA, Virág L. The PARP Enzyme Family and the Hallmarks of Cancer Part 1. Cell Intrinsic Hallmarks. *Cancers (Basel).* 2021;13(9):2042.

229. Kraus WL. PARPs and ADP-Ribosylation: 50 Years … and Counting. *Mol Cell.* 2015;58(6):902-910.

230. Zhang H, Abou D, Lu P, et al. [^{18}F]-Labeled PARP-1 PET imaging of PSMA targeted alpha particle radiotherapy response. *Scientific Rep.* 2022;12(1):13034.

231. Pirovano G, Jannetti SA, Carter LM, et al. Targeted Brain Tumor Radiotherapy Using an Auger Emitter. *Clinical cancer research : an official journal of the American Association for Cancer Research.* 2020;26(12):2871-2881.

232. Lee H, Riad A, Martorano P, et al. PARP-1-Targeted Auger Emitters Display High-LET Cytotoxic Properties In Vitro but Show Limited Therapeutic Utility in Solid Tumor Models of Human Neuroblastoma. *Journal of nuclear medicine : official publication, Society of Nuclear Medicine.* 2020;61(6):850-856.

233. Ambur Sankaranarayana R, Florea A, Allekotte S, et al. PARP targeted Auger emitter therapy with [^{125}I]PARPi-01 for triple-negative breast cancer. *EJNMMI Res.* 2022;12(1):60.

234. Jannetti SA, Carlucci G, Carney B, et al. PARP-1–Targeted Radiotherapy in Mouse Models of Glioblastoma. *Journal of nuclear medicine : official publication, Society of Nuclear Medicine.* 2018;59(8):1225-1233.

235. Makvandi M, Lee H, Puentes LN, et al. Targeting PARP-1 with Alpha-Particles Is Potently Cytotoxic to Human Neuroblastoma in Preclinical Models. *Mol Cancer Ther.* 2019;18(7):1195-1204.

236. Cornelissen B, Kersemans V, Darbar S, et al. Imaging DNA damage in vivo using γH2AX-targeted immunoconjugates. *Cancer Res.* 2011;71(13):4539-4549.

237. Jones GN, Rooney C, Griffin N, et al. pRAD50: a novel and clinically applicable pharmacodynamic biomarker of both ATM and ATR inhibition identified using mass spectrometry and immunohistochemistry. *Br J Cancer.* 2018;119(10):1233-1243.

238. Zhang M, Liu G, Xue F, et al. Copy number deletion of RAD50 as predictive marker of BRCAness and PARP inhibitor response in BRCA wild type ovarian cancer. *Gynecol Oncol.* 2016;141(1):57-64.